

---

Electronic Thesis and Dissertation Repository

---

9-23-2016 12:00 AM

## The Application of Geophysical Inversion Techniques to the Nechalacho Rare Earth Element Deposit, NT

Derek W. Kouhi, *The University of Western Ontario*

Supervisor: Kristy Tiampo, *The University of Western Ontario*

Joint Supervisor: Bob Linnen, *The University of Western Ontario*

A thesis submitted in partial fulfillment of the requirements for the Master of Science degree in Geophysics

© Derek W. Kouhi 2016

Follow this and additional works at: <https://ir.lib.uwo.ca/etd>



Part of the [Geology Commons](#), and the [Geophysics and Seismology Commons](#)

---

### Recommended Citation

Kouhi, Derek W., "The Application of Geophysical Inversion Techniques to the Nechalacho Rare Earth Element Deposit, NT" (2016). *Electronic Thesis and Dissertation Repository*. 4164.  
<https://ir.lib.uwo.ca/etd/4164>

This Dissertation/Thesis is brought to you for free and open access by Scholarship@Western. It has been accepted for inclusion in Electronic Thesis and Dissertation Repository by an authorized administrator of Scholarship@Western. For more information, please contact [wlsadmin@uwo.ca](mailto:wlsadmin@uwo.ca).

## Abstract

The Nechalacho deposit is a world-class rare earth element deposit located in the Thor Lake region approximately 100 kilometers southwest of Yellowknife, NT, Canada. Located within the Blatchford Lake Intrusion Complex, this deposit has the potential to be a large-scale economic asset due to its relatively shallow and sub-horizontal geometry. In this study, geophysical inversion techniques are used to model subsurface magnetic susceptibility and density in order to delineate the deposit. Isolated and joint inversion of both magnetic and gravity data provide similar models. Each inversion procedure delineates a shallow, sub-horizontal layer of high susceptibility and density in approximately the same location. This layer is interpreted to be the Nechalacho deposit and it extends further north than previously determined. Finally, magnetic susceptibilities were measured on selected samples using laboratory instruments to check the quality of previous field measurements as well as to validate and derive relationships between geophysical and mineralogical properties in the deposit.

## Keywords

Inverse theory, joint inversion, magnetic susceptibility, geophysical modelling, Nechalacho, Thor Lake, Blatchford Lake Intrusion Complex

## Co-Authorship Statement

This thesis was compiled in integrated article format and the following manuscripts were written by Derek Kouhi:

Kouhi, D.W., and Tiampo, K.F., 2016a. Current Status of Magnetic Inversion Project at Thor Lake, N.W.T.; Open-File Report 2016-06, Northwest Territories Geological Survey, Yellowknife.

Kouhi, D.W., and Tiampo, K.F., 2016b. Implementation of Gravity Data for Isolated and Joint Inversion Methods at Thor Lake, N.W.T.; Pending Open-File Report, Northwest Territories Geological Survey, Yellowknife.

The research for these studies was completed under the supervision and financial support of Dr. Kristy Tiampo.

The Northwest Territories Geological Survey supplied the data and additional financial support.

## Acknowledgments

Time flies when you're having fun. I cannot honestly say that every minute of this journey was fun by the traditional use of the word, but each moment was definitely special. There are so many people that supported me and left an everlasting impression.

First and foremost, I would like to thank my supervisor Dr. Kristy Tiampo. Her support and encouragement have made this experience a great one. While communicating at a distance for much of my project, I cannot think of anyone I could count on more for timely comments, words of encouragement or general advice. Her broad knowledge in the field of geophysics has been an integral asset and her stories are enough to make even the worst days a little brighter. She is the reason I chose to stay at Western for my Master's degree and I don't regret it for a second.

In addition, I would like to thank my co-supervisor, Dr. Bob Linnen for his support in the latter half of my research. His knowledge in the field of economic geology has infinitely helped bridge the gap between geology and geophysics in this work. I would also like to thank Dr. Phil McCausland for his contributions to my research through revising manuscripts and general discussion of the project. I also express gratitude to geoscientists at the Northwest Territories Geological Survey, Hendrik Falck and Asif Mirza, as well as Avalon geologist Bill Mercer for their meaningful comments, suggestions and support throughout my research.

This work was funded by the Northwest Territories Geological Survey, while work by Dr. Tiampo was supported through NSERC Discovery Grants.

I'd like to extend appreciation to the invaluable administrative staff at the University of Western Ontario for their on-going assistance throughout my time here. Many thanks to the Department of Earth Sciences, who helped me find my home in geophysics back when I was a lost second year undergrad.

Finally, I need to thank all of my friends and family, both within the department and at home. My parents and grandmother at home have shown unwavering support in good times and bad. My department family has grown significantly with the addition of new incoming graduate students each year. They have never failed to keep things upbeat and I owe many thanks to them for that. Last but certainly not least, I would like to thank my significant other, Emma-Dawn for her loving support and endless patience over the past two years.

# Table of Contents

Abstract .....	i
Co-Authorship Statement.....	ii
Acknowledgments.....	iii
Table of Contents .....	v
List of Tables .....	ix
List of Figures .....	x
List of Appendices .....	xxiii
Chapter 1 .....	1
1 Introduction .....	1
1.1 Objectives .....	1
1.2 Outline.....	5
1.3 Background.....	7
1.3.1 General Inverse Theory.....	7
1.3.2 Geophysical Inversion Facility Software.....	8
1.3.3 Previous Studies.....	11
1.3.4 Programs Written .....	13
1.4 References .....	15
Chapter 2 .....	18
2 Current Status of Magnetic Inversion Project at Thor Lake, N.W.T. ....	18
2.1 Introduction.....	18
2.2 Geological Background .....	20
2.2.1 Regional Geology .....	20
2.2.2 Local Geology.....	22
2.2.3 Mineralization .....	24

2.3	Data .....	26
2.4	Software and Inversion Setup .....	28
2.5	Magnetic Inversions and Discussion .....	32
2.5.1	Unconstrained Inversion .....	32
2.5.2	Adding Boundary Conditions .....	35
2.5.3	Upward Continuation.....	39
2.5.4	Gradient Attenuation and Enhancement .....	43
2.6	Geological Interpretation and Implications .....	45
2.7	Future Work .....	50
2.7.1	Gravity Implementation .....	50
2.7.2	Joint Inversion.....	52
2.7.3	Caribou Lake.....	53
2.8	Conclusions .....	53
2.9	References .....	54
	Appendices .....	56
	Appendix A: Step-by-Step Cross-Sections Facing North.....	57
	Appendix B: Step-by-Step Cross-Sections Facing West.....	68
	Chapter 3 .....	77
3	Implementation of Gravity Data for Isolated and Joint Inversion Methods at Thor Lake, N.W.T.....	77
3.1	Introduction.....	77
3.1.1	Background Geology .....	79
3.1.2	Background Geophysics .....	82
3.2	Methods.....	85
3.2.1	Gravity .....	85
3.2.2	Lateral Interpolation.....	87

3.2.3	Joint Inversion.....	93
3.3	Results.....	96
3.3.1	Gravity .....	96
3.3.2	New Magnetic Results .....	101
3.3.3	Joint Inversion.....	105
3.4	Discussion .....	114
3.4.1	Lateral Interpolation vs. Kriging.....	114
3.4.2	Comparison Between Gravity and Magnetics .....	120
3.4.3	Validity of Joint Inversion .....	121
3.5	Conclusions.....	124
3.6	References.....	125
Chapter 4	.....	128
4	Relating Magnetic Susceptibility of Deep-Hole Samples to Mineralogy in Thor Lake, N.W.T.....	128
4.1	Introduction.....	128
4.1.1	Previous Measurements .....	129
4.1.2	Off-Cut Blocks.....	130
4.1.3	This Study .....	132
4.2	Methods.....	133
4.2.1	Magnetic Susceptibility Measurements .....	133
4.2.2	Mass- to Volume-Based Susceptibility Conversion .....	134
4.3	Results.....	135
4.3.1	Mass-Based Magnetic Susceptibility .....	135
4.3.2	Volume-Based Magnetic Susceptibility .....	136
4.4	Discussion .....	138
4.4.1	Geophysical Implications of the Mineralogy.....	138



4.4.2	Systematic Bias .....	144
4.4.3	Colour Analysis .....	147
4.4.4	Future Work .....	155
4.5	Conclusion .....	156
4.6	References.....	157
Chapter 5	.....	159
5	General Discussion and Conclusions .....	159
5.1	Model Improvements .....	159
5.2	Structural Joint Inversion.....	161
5.3	Newly Developed Techniques .....	161
5.4	Future Work .....	162
5.5	References.....	163
Appendices	.....	164
Appendix A: Matlab Code .....		164
UBC-GIF_Conversion.m .....		164
upward_cont.m.....		169
grad_attenuate.m .....		173
lat_interp.m .....		176
joint.m	190	
geo_analysis.m.....		196
pixel_test.m.....		202
Curriculum Vitae .....		207

## List of Tables

Table 4.1: Brief summary of off-cut samples from drillhole L09-194 .....	131
Table 4.2: A summary of the minerals included in RGB colour analysis methods.....	150

## List of Figures

Figure 2.1: Location map showing the Thor Lake area in the Northwest Territories. Blue shaded area in the red inset map shows the inversion area in this study. Adapted from Google Earth, 2015. ....	21
Figure 2.2: Regional geology of the Blatchford Lake Complex, NWT Canada (modified from Mumford, 2010 after Davidson, 1978). The yellow dots signify sample locations from the study by Mumford (2010) and are not mentioned in this study. ....	22
Figure 2.3: Cross-section of the Nechalacho deposit from current geological methods (modified from Ciuculescu et al., 2013). The Nechalacho nepheline syenite (NNS) is in green and includes the upper and basal zones, while the Thor Lake syenite (TLS) is represented in orange. The blue lithology is the roof sodalite. The vertical scale is in metres above sea level (ASL). ....	24
Figure 2.4: Map of the residual magnetic field from the aeromagnetic survey completed by NRCan (2011) of the Blatchford Lake Complex. The eastern large positive elliptical anomaly is the Thor Lake deposit while the western elongated anomaly is associated with the Caribou Lake gabbro that hosts Cu-Ni-PGE mineralization. Units are in nanoTeslas. The inset plot is an enlarged in view of the inversion area with drill-holes plotted in black. Drillhole locations obtained from Avalon Rare Metals (2014). ....	27
Figure 2.5: Program workflow for MAG3D. GRAV3D follows a similar workflow by substituting the gravity programs for their magnetic counterparts (UBC-GIF, 2013). ....	29
Figure 2.6: The original magnetic field anomaly dataset for the Thor Lake region selected for this study. UTM coordinates shown in all figures and cross sections are NAD 83, Zone 11N. There are 5265 datapoints with magnetic inclination (I) and declination (D) also specified. ....	33
Figure 2.7: A north-south (N-S) cross-section for the preliminary, unconstrained magnetic inversion of the Thor Lake study area along line 416550 Easting (UTM), looking west. Units	

on the right side represent susceptibility in SI units. Scale on the left is elevation above sea level (ASL) in metres. .... 34

Figure 2.8: Mesh grid in the x and y directions and the locations of the drillholes. Drillhole locations from Avalon Rare Metals (2014). Northing and Easting are shown on the axes (UTM). .... 36

Figure 2.9: An N-S sample cross-section of the three-dimensional model created by binning magnetic susceptibility measurements. Units on the right side represent susceptibility in SI units. Scale on the left is elevation above sea level (ASL) in metres. Drillholes numbers are labelled and their approximate orientation within the model are shown (Avalon Rare Metals, 2014). Note the scaling with maximum values at approximately 0.217 SI. .... 36

Figure 2.10: Magnetic inversion constrained using maximum and minimum boundaries derived from borehole susceptibility measurements (N-S line 416550 Easting (UTM), looking west). Units on the right side represent susceptibility in SI units. Scale on the left is elevation above sea level (ASL) in metres. .... 38

Figure 2.11: Plan view of the inversion area showing transformation of data from the subtraction of upward continued data. Top left is the original anomaly data, top right is the upward continued data and the bottom right is the residual data. Note the different scales; all in nanoTeslas. .... 41

Figure 2.12: Magnetic inversion of the Thor Lake region with long wavelength signal subtracted and upper and lower bounds applied (N-S line 416550 Easting (UTM), looking west). Units on the right side represent susceptibility in SI units. Scale on the left is elevation above sea level (ASL) in metres. .... 43

Figure 2.13: Magnetic model (N-S line 416550 Easting (UTM), looking west) with three iterations of gradient enhancement and attenuation. Units on the right side represent susceptibility in SI units. Scale on the left is elevation above sea level (ASL) in metres. .... 45

Figure 2.14: Plan view of the inversion area comparing the data (a) to the forward modeled data from the model (b). The residuals at the bottom (c). Units are in nanoTeslas. .... 46

Figure 2.15: Comparison of the current geological model (top, along line 416800 Easting (UTM), looking west) with the best magnetic geophysical model (bottom, along line 416550 Easting (UTM), looking west). The red line in the magnetic model is an early delineation of the deposit. Yellow lines are to indicate depth intervals. Units on the right side represent susceptibility in SI units. Scale on the left is elevation above sea level (ASL) in metres. Geological model adapted from Ciuculescu et al., 2013. .... 47

Figure 2.16: A projection looking north of a smoothed isosurface of the high susceptibility region displaying all cells that have susceptibilities greater than 0.1 SI to show the lateral extent. Note that even with smoothing, the model is still somewhat discontinuous. UTM Eastings are labeled along the bottom while elevation in metres ASL are labeled on the left side. Units on the right side represent susceptibility in SI units. .... 49

Figure 2.17: A preliminary gravity model of the Thor Lake region with no constraints at N-S line 416550 Easting (UTM), facing west. Units are in  $\text{g/cm}^3$  density contrast. Scale on the left is elevation above sea level (ASL) in metres. .... 51

Figure 2.18: Cross-section of the best current geophysical model along E-W line 6885000 Northing (UTM), looking north. Units on the right side represent susceptibility in SI units. Scale on the left is elevation above sea level (ASL) in metres. .... 57

Figure 2.19: Cross-section of the best current geophysical model along E-W line 6885200 Northing (UTM), looking north. Units on the right side represent susceptibility in SI units. Scale on the left is elevation above sea level (ASL) in metres. .... 58

Figure 2.20: Cross-section of the best current geophysical model along E-W line 6885400 Northing (UTM), looking north. Units on the right side represent susceptibility in SI units. Scale on the left is elevation above sea level (ASL) in metres. .... 58

Figure 2.21: Cross-section of the best current geophysical model along E-W line 6885600 Northing (UTM), looking north. Units on the right side represent susceptibility in SI units. Scale on the left is elevation above sea level (ASL) in metres. .... 59

Figure 2.22: Cross-section of the best current geophysical model along E-W line 6885800 Northing (UTM), looking north. Units on the right side represent susceptibility in SI units. Scale on the left is elevation above sea level (ASL) in metres. ....	59
Figure 2.23: Cross-section of the best current geophysical model along E-W line 6886000 Northing (UTM), looking north. Units on the right side represent susceptibility in SI units. Scale on the left is elevation above sea level (ASL) in metres. ....	60
Figure 2.24: Cross-section of the best current geophysical model along E-W line 6886200 Northing (UTM), looking north. Units on the right side represent susceptibility in SI units. Scale on the left is elevation above sea level (ASL) in metres. ....	60
Figure 2.25: Cross-section of the best current geophysical model along E-W line 6886400 Northing (UTM), looking north. Units on the right side represent susceptibility in SI units. Scale on the left is elevation above sea level (ASL) in metres. ....	61
Figure 2.26: Cross-section of the best current geophysical model along E-W line 6886600 Northing (UTM), looking north. Units on the right side represent susceptibility in SI units. Scale on the left is elevation above sea level (ASL) in metres. ....	61
Figure 2.27: Cross-section of the best current geophysical model along E-W line 6886800 Northing (UTM), looking north. Units on the right side represent susceptibility in SI units. Scale on the left is elevation above sea level (ASL) in metres. ....	62
Figure 2.28: Cross-section of the best current geophysical model along E-W line 6887000 Northing (UTM), looking north. Units on the right side represent susceptibility in SI units. Scale on the left is elevation above sea level (ASL) in metres. ....	62
Figure 2.29: Cross-section of the best current geophysical model along E-W line 6887200 Northing (UTM), looking north. Units on the right side represent susceptibility in SI units. Scale on the left is elevation above sea level (ASL) in metres. ....	63
Figure 2.30: Cross-section of the best current geophysical model along E-W line 6887400 Northing (UTM), looking north. Units on the right side represent susceptibility in SI units. Scale on the left is elevation above sea level (ASL) in metres. ....	63

Figure 2.31: Cross-section of the best current geophysical model along E-W line 6887600 Northing (UTM), looking north. Units on the right side represent susceptibility in SI units. Scale on the left is elevation above sea level (ASL) in metres. ....	64
Figure 2.32: Cross-section of the best current geophysical model along E-W line 6887800 Northing (UTM), looking north. Units on the right side represent susceptibility in SI units. Scale on the left is elevation above sea level (ASL) in metres. ....	64
Figure 2.33: Cross-section of the best current geophysical model along E-W line 6888000 Northing (UTM), looking north. Units on the right side represent susceptibility in SI units. Scale on the left is elevation above sea level (ASL) in metres. ....	65
Figure 2.34: Cross-section of the best current geophysical model along E-W line 6888200 Northing (UTM), looking north. Units on the right side represent susceptibility in SI units. Scale on the left is elevation above sea level (ASL) in metres. ....	65
Figure 2.35: Cross-section of the best current geophysical model along E-W line 6888400 Northing (UTM), looking north. Units on the right side represent susceptibility in SI units. Scale on the left is elevation above sea level (ASL) in metres. ....	66
Figure 2.36: Cross-section of the best current geophysical model along E-W line 6888600 Northing (UTM), looking north. Units on the right side represent susceptibility in SI units. Scale on the left is elevation above sea level (ASL) in metres. ....	66
Figure 2.37: Cross-section of the best current geophysical model along E-W line 6888800 Northing (UTM), looking north. Units on the right side represent susceptibility in SI units. Scale on the left is elevation above sea level (ASL) in metres. ....	67
Figure 2.38: Cross-section of the best current geophysical model along E-W line 6889000 Northing (UTM), looking north. Units on the right side represent susceptibility in SI units. Scale on the left is elevation above sea level (ASL) in metres. ....	67
Figure 2.39: Cross-section of the best current geophysical model along N-S line 414800 Easting (UTM), looking west. Units on the right side represent susceptibility in SI units. Scale on the left is elevation above sea level (ASL) in metres. ....	68

Figure 2.40: Cross-section of the best current geophysical model along N-S line 415000 Easting (UTM), looking west. Units on the right side represent susceptibility in SI units. Scale on the left is elevation above sea level (ASL) in metres. ....	69
Figure 2.41: Cross-section of the best current geophysical model along N-S line 415200 Easting (UTM), looking west. Units on the right side represent susceptibility in SI units. Scale on the left is elevation above sea level (ASL) in metres. ....	69
Figure 2.42: Cross-section of the best current geophysical model along N-S line 415400 Easting (UTM), looking west. Units on the right side represent susceptibility in SI units. Scale on the left is elevation above sea level (ASL) in metres. ....	70
Figure 2.43: Cross-section of the best current geophysical model along N-S line 415600 Easting (UTM), looking west. Units on the right side represent susceptibility in SI units. Scale on the left is elevation above sea level (ASL) in metres. ....	70
Figure 2.44: Cross-section of the best current geophysical model along N-S line 415800 Easting (UTM), looking west. Units on the right side represent susceptibility in SI units. Scale on the left is elevation above sea level (ASL) in metres. ....	71
Figure 2.45: Cross-section of the best current geophysical model along N-S line 416000 Easting (UTM), looking west. Units on the right side represent susceptibility in SI units. Scale on the left is elevation above sea level (ASL) in metres. ....	71
Figure 2.46: Cross-section of the best current geophysical model along N-S line 416200 Easting (UTM), looking west. Units on the right side represent susceptibility in SI units. Scale on the left is elevation above sea level (ASL) in metres. ....	72
Figure 2.47: Cross-section of the best current geophysical model along N-S line 416400 Easting (UTM), looking west. Units on the right side represent susceptibility in SI units. Scale on the left is elevation above sea level (ASL) in metres. ....	72
Figure 2.48: Cross-section of the best current geophysical model along N-S line 416600 Easting (UTM), looking west. Units on the right side represent susceptibility in SI units. Scale on the left is elevation above sea level (ASL) in metres. ....	73



Figure 2.49: Cross-section of the best current geophysical model along N-S line 416800 Easting (UTM), looking west. Units on the right side represent susceptibility in SI units. Scale on the left is elevation above sea level (ASL) in metres. ....	73
Figure 2.50: Cross-section of the best current geophysical model along N-S line 417000 Easting (UTM), looking west. Units on the right side represent susceptibility in SI units. Scale on the left is elevation above sea level (ASL) in metres. ....	74
Figure 2.51: Cross-section of the best current geophysical model along N-S line 417200 Easting (UTM), looking west. Units on the right side represent susceptibility in SI units. Scale on the left is elevation above sea level (ASL) in metres. ....	74
Figure 2.52: Cross-section of the best current geophysical model along N-S line 417400 Easting (UTM), looking west. Units on the right side represent susceptibility in SI units. Scale on the left is elevation above sea level (ASL) in metres. ....	75
Figure 2.53: Cross-section of the best current geophysical model along N-S line 417600 Easting (UTM), looking west. Units on the right side represent susceptibility in SI units. Scale on the left is elevation above sea level (ASL) in metres. ....	75
Figure 2.54: Cross-section of the best current geophysical model along N-S line 417800 Easting (UTM), looking west. Units on the right side represent susceptibility in SI units. Scale on the left is elevation above sea level (ASL) in metres. ....	76
Figure 2.55: Cross-section of the best current geophysical model along N-S line 418000 Easting (UTM), looking west. Units on the right side represent susceptibility in SI units. Scale on the left is elevation above sea level (ASL) in metres. ....	76
Figure 3.1: A north-south (N-S) cross-section of the best magnetic susceptibility model from the earlier Thor Lake study area, <i>Kouhi and Tiampo</i> (2016). The figure displays easting line 416550 (UTM), looking west. Units on the right side represent susceptibility in SI units. Scale on the left is elevation above sea level (ASL) in metres. ....	79

Figure 3.2: Location map showing the Thor Lake area, the Northwest Territories. Blue shaded area in the red inset map shows the inversion area in this study ( <i>Kouhi and Tiampo, 2016; adapted from Google Earth, 2015</i> ). .....	80
Figure 3.3: A basic geological model of the Nechalacho deposit (modified from <i>Ciuculescu et al., 2013</i> ). The Nechalacho nepheline syenite (NNS, green) includes the upper and basal zones, while the Thor Lake syenite (TLS) is represented in orange. The blue lithology is the roof sodalite. The vertical scale is in metres ASL. ....	82
Figure 3.4: Map of the airborne magnetic field anomaly for the inversion area. UTM coordinates shown in all figures and cross sections are NAD 83, Zone 11N. There are 5265 data points with magnetic inclination (I) and declination (D) specified as well. ....	83
Figure 3.5: Map of the airborne gravity anomaly for the inversion area. There are 5265 data points. A gravitational high can be seen in the centre of the region, likely from a region of high density associated with the Nechalacho deposit. ....	85
Figure 3.6: The mesh for the geophysical inversion, shown here, spans 4000 metres in the north-south direction and 3200 metres in the east-west direction. Cell dimensions are 20x20x10 metres in the <i>x,y</i> and <i>z</i> directions. The mesh contains 6,044,577 cells in total (191x231x137). ....	87
Figure 3.7: Sample cross-section from the three-dimensional reference model for core density data created from binning measured values into the cells without any interpolation (northing line 6885900 [UTM], facing north). All density models display units on the right in +/- g/cm <sup>3</sup> with respect to the average density (2.67g/cm <sup>3</sup> ) and depths on the left in metres ASL. ....	89
Figure 3.8: A simple diagram describing the assignment of uncertainty values for the lateral interpolation technique. The star represents a cell with drillhole data and is assigned an uncertainty value of 4. From here, uncertainty values decrease the further a given cell is away from the centre cell up to a maximum distance of 3 cells away. ....	90
Figure 3.9: Sample cross-section from the three-dimensional reference model for core density data created using lateral interpolation methods (northing line 6885900 [UTM],	

facing north). The reference model contains much more data than the previous three-dimensional model. ....	93
Figure 3.10: Cross-section of the preliminary, unconstrained gravity inversion for the Thor Lake study area (northing line 6885890, facing north). Units on the right side represent density in $\text{g/cm}^3$ above or below $2.67 \text{ g/cm}^3$ . Scale on the left is elevation ASL in metres. .	97
Figure 3.11: Cross-section of the constrained gravity inversion for the Thor Lake study area (northing line 6885270, facing north). A laterally interpolated reference model was used in the inversion. Units on the right side represent density in $\text{g/cm}^3$ above or below $2.67 \text{ g/cm}^3$ . Scale on the left is elevation ASL in metres. The approximate interpretation of the Thor Lake syenite, Nechalacho nepheline syenite and Upper/Basal Zones have been included. ...	98
Figure 3.12: A density isosurface of the shallow, high density anomaly. The figure displays densities greater than $+0.1 \text{ g/cm}^3$ within the top 400 metres. Units on the right side represent density in $\text{g/cm}^3$ above or below $2.67 \text{ g/cm}^3$ .....	99
Figure 3.13: The isosurface for the shallow density anomaly approximately overlain on a geological model from <i>Ciuculescu et al.</i> (2013) to show the geometrical and geographical similarities. Northing values range from line 6885500 to line 6888000 and easting values range from line 415500 to line 418000.....	100
Figure 3.14: Sample cross-section from the three-dimensional reference model for core magnetic susceptibility data created using lateral interpolation methods (northing line 6885890 [UTM], facing north). Units on the right side represent magnetic susceptibility in SI units. Scale on the left is elevation ASL in metres.....	102
Figure 3.15: Cross-section of the new constrained magnetic inversion for the Thor Lake study area (northing line 6885890, facing north). A laterally interpolated reference model was used in the inversion. Units on the right side represent magnetic susceptibility in SI units. Scale on the left is elevation ASL in metres. The approximate interpretation of the Thor Lake syenite, Nechalacho nepheline syenite and Upper/Basal Zones have been included.....	102

Figure 3.16: An isosurface of the shallow high magnetic susceptibility anomaly. The figure displays susceptibilities greater than 0.04 SI within the top 400 metres. Units on the right side represent magnetic susceptibility in SI units. .... 104

Figure 3.17: A view of the new magnetic susceptibility model from above, looking at the surface. There are northeast trending lines in the centre of the model and a northwest trending line north of the deposit which may delineate subsurface dykes. .... 105

Figure 3.18: Cross-sections of the northing line 6885890 [UTM] obtained through joint inversion. The joint inversion included all cells with no threshold and a low intensity factor. The top figure is a density model with units displayed in  $\text{g/cm}^3$  above or below  $2.67 \text{ g/cm}^3$  and the bottom figure is a magnetic susceptibility model with units displayed in SI units. Units on the left side represent depths in metres ASL. .... 107

Figure 3.19: Cross-sections of the northing line 6885890 [UTM] obtained through joint inversion. The joint inversion included all cells with no threshold and a high intensity factor. The top figure is a density model with units displayed in  $\text{g/cm}^3$  above or below  $2.67 \text{ g/cm}^3$  and the bottom figure is a magnetic susceptibility model with units displayed in SI units. Units on the left side represent depths in metres ASL. .... 109

Figure 3.20: Cross-sections of the northing line 6885890 [UTM] obtained through joint inversion. The joint inversion included only cells in the top 400 metres with no threshold and a high intensity factor. The top figure is a density model with units displayed in  $\text{g/cm}^3$  above or below  $2.67 \text{ g/cm}^3$  and the bottom figure is a magnetic susceptibility model with units displayed in SI units. Units on the left side represent depths in metres ASL. .... 111

Figure 3.21: An isosurface of the shallow high magnetic susceptibility anomaly from the joint inversion using only the top 400 metres, no threshold and a high intensity factor. The figure displays susceptibilities greater than 0.04 SI within the top 400 metres. Units on the right side represent magnetic susceptibility in SI units. .... 112

Figure 3.22: Cross-section from the joint inversion using only the top 400 metres, no threshold and a high intensity factor (northing line 6885690 [UTM]). This figure shows the effects of over-influencing the model in the joint inversion process. If the intensity factor is

too high, the model is forced closer to the reference model, which results in cells where the influence a drillhole is evident. .... 113

Figure 3.23: Magnetic cross-section of northing line 6885890 [UTM] obtained through joint inversion. The joint inversion included only cells in the top 400 metres with a threshold of 0.25 and a high intensity factor. The figure is a magnetic susceptibility model with units displayed in SI units. Units on the left side represent depths in metres ASL. Note that model susceptibilities no longer contain negative values. .... 114

Figure 3.24: A sample variogram showing the fit of the data to a Gaussian trend. Created with code modified from *Schwanghart* (2010). .... 116

Figure 3.25: Sample cross-section from the three-dimensional reference model for core density data created using ordinary kriging methods (northing line 6885890 [UTM], facing north). The reference model shows evidence of lateral over-smoothing. Units on the right side represent density in  $\text{g/cm}^3$  above or below  $2.67 \text{ g/cm}^3$ . Scale on the left is elevation ASL in metres. .... 117

Figure 3.26: Comparison cross-sections of constrained gravity inversions for the Thor Lake study area (northing line 6885270, facing north). In the top figure, a reference model obtained via ordinary kriging was used while in the bottom figure, the laterally interpolated model has been rescaled for comparison. Units on the right side represent density in  $\text{g/cm}^3$  above or below  $2.67 \text{ g/cm}^3$ . Scale on the left is elevation ASL in metres. .... 119

Figure 3.27: Isosurfaces comparing shallow density anomalies to shallow magnetic susceptibility anomalies (top 400 metres). Cells that have density values greater than  $+0.1 \text{ g/cm}^3$  are considered density anomalies while cells that have magnetic susceptibility values greater than 0.4 SI are considered susceptibility anomalies. Figure (a) shows all cells that are considered anomalies. Cells that are only considered susceptibility anomalies are in pink (b), cells that are only considered density anomalies are in blue (c) and cells that are anomalous for both fields are in green (d). .... 121

Figure 3.28: Comparison isomaps of anomalous cells for the final joint inversion (top) and the final individual inversions (bottom). Green cells are cells where both density and

magnetic susceptibility are considered anomalous, blue are only density and pink are only susceptibility. Both maps are nearly identical. ....	123
Figure 4.1: Comparison of the magnetic susceptibilities measured on the core from drillhole L09-160 by Avalon (2013) and <i>Nichols</i> (2014) using KT-9 and KT-10 instruments, respectively. Note the slight offset in the depth domain.....	130
Figure 4.2: Mass-based magnetic susceptibilities measured using the in-lab magnetic susceptibility meter. Lithological units are based from work by <i>Möller and Williams-Jones</i> (2016). Note there are no error bars because only two measurements were taken on each sample, therefore a reliable estimate of the error could not be assigned. ....	136
Figure 4.3: Volume-based magnetic susceptibilities measured using the in-lab magnetic susceptibility meter (red circles). Green circles represent the susceptibilities using a constant density of 2.67 g/cm <sup>3</sup> for sensitivity analysis. Lithological units are based from work by <i>Möller and Williams-Jones</i> (2016). ....	138
Figure 4.4: Comparison of the visual mineralogy of a sample from 93.75 metres depth (top) and a sample from 118.5 metres depth (bottom). The top sample is from unit NLS-4 between the upper and basal zones while the bottom sample is from the basal zone (NLS-6). The bottom sample appears to contain significantly more magnetite by visual inspection. This is confirmed by the magnetic susceptibility measurements. ....	140
Figure 4.5: A moderately susceptible sample from 1044.9 metres depth that shows potential evidence of aegirine altering to magnetite. ....	142
Figure 4.6: Plot of density versus volume-based magnetic susceptibility for each sample. The approximate REE concentrations are represented by the sizes of the markers and the different colours represent the different lithological units.....	143
Figure 4.7: Volume-based magnetic susceptibilities measured using the in-lab magnetic susceptibility meter, scaled down by a factor of 1.5. Lithological units are based from work by <i>Möller and Williams-Jones</i> (2016). ....	145

Figure 4.8: The only sample from within the upper zone (NLS-5). The measured magnetic susceptibility for this off-cut block is anomalously higher than previously measured by *Avalon* (2013). While most samples appear to be approximately 1.5 times higher in susceptibility than previously measured, this sample measured at values more than 3 times higher. Magnetite can be identified by visual inspection. .... 146

Figure 4.9: Scaled down volume-based susceptibility measurements with REE abundance overlain below (modified from *Möller and Williams-Jones* (2016)). .... 147

Figure 4.10: Plot of magnetic susceptibility with depth for drillhole L09-194. Marker colours were determined by the average red, green and blue values extracted from each image. Darker shades of grey represent minerals that were generally dominated by darker coloured minerals such as magnetite while lighter shades represent minerals that were dominated by minerals such as albite. .... 148

Figure 4.11: The original high resolution photograph (above) of a sample at 118.5 metres depth, and the reproduced image via computational colour analysis (below). This method uses colours to distinguish between different minerals. Black represents magnetite, green represents aegirine, white represents albite, blue represents sodalite, yellow represents eudialyte and red represents pixels that are unassigned. .... 151

Figure 4.12: Mineral abundances as calculated from the computational colour analysis technique (coloured lines) versus depth for each sample are plotted on the right-hand y-axis. Magnetic susceptibilities are plotted (circles) versus depth on the left-hand y-axis. The filling colours for the circles represent the average RGB values for that sample unless the sample was dominated by a specific red, green or blue value (i.e. blue circles represent samples that had an average blue value significantly higher than its red or green values). . 154

Figure 4.13: Plot of the magnetic susceptibility (left-hand axis, circles, in SI units) and magnetite abundance (right-hand axis, dashed line) versus depth for the samples from drillhole L09-194. Abundances were calculated using computational colour analysis and exclude the four data points that were deemed outliers during the process. .... 155

## List of Appendices

Appendix A: Matlab Code .....	164
-------------------------------	-----



# Chapter 1

## 1 Introduction

### 1.1 Objectives

Geophysical measurement techniques have become staples in the mineral exploration industry. These techniques are relatively quick and cost-effective methods to quantify the physical properties of the surface and subsurface. In addition, airborne surveying methods allow for the acquisition of large datasets in remote regions, often acquiring multiple fields of data simultaneously. The raw data obtained can be used to analyze spatial trends without further significant processing. Therefore, geophysical datasets are an excellent starting point to target anomalous signals that may be the result of economic bodies. Furthermore, geophysical inversion techniques use these datasets, as well as a physical understanding of geophysical properties, to solve for one or more subsurface parameters which may be linked to such bodies.

Two of the most common geophysical properties in the mineral exploration industry are magnetic susceptibility and density. This is because many minerals and parent rocks associated with mineral deposits yield anomalously high gravitational or magnetic field signals. Magnetic susceptibility is a value that describes the ability of a mineral to emit an induced field when under the influence of an inducing magnetic field such as that of Earth (*Pratt, 2005*). Depending on the strength and orientation of magnetic moments within a mineral, the inducing field may be enhanced by the alignment of these moments with the direction of the external field. Therefore, minerals that have high magnetic susceptibilities produce small anomalies in the natural magnetic field in that region.

Magnetic susceptibility is related to magnetic field through a series of equations and assumptions. The magnetization,  $M$ , is broken into two components, the induced magnetization,  $M_i$ , and the remanent magnetization,  $M_r$ :

$$M = M_i + M_r \quad (1)$$

$$M_i = kH$$

where  $k$  is the magnetic susceptibility and  $H$  is the inducing magnetic field intensity (Pratt, 2005). Induced magnetization is magnetization that occurs due to an external inducing field, while remanent magnetization is magnetization that is imprinted in the rock from when it formed that does not need an external field to be magnetized. Often small amounts of remanent magnetism are associated with iron, however, in order to simplify the problem, this magnetism is assumed to be small enough to be negligible. Therefore, the magnetization can be simplified to:

$$M = kH \quad (2)$$

Therefore, magnetic susceptibility is related to the magnetic field,  $B$  via the equation:

$$B = \mu_0(1 + k)H \quad (3)$$

where  $\mu_0$  is the magnetic constant or the permeability of free space (Pratt, 2005).

Similarly, the density of rocks and minerals in the region affect the gravitational field in the area due to changes in the mass per unit volume. A positive gravitational anomaly

suggests that excess mass is contributing to the signal. The density is related to the vertical component of the gravitational field,  $g_z$ , via the equation:

$$g_z(r_0) = G \int_V \rho(r) \frac{z - z_0}{|r - r_0|^3} dv \quad (4)$$

where  $r_0 = (x_0, y_0, z_0)$  is the position vector of the observation,  $r = (x, y, z)$  is the position vector of the source,  $G$  is the gravitational constant, and  $\rho$  is the density (*UBC-GIF*, 2013b).

The Nechalacho deposit is a world class rare earth element (REE) deposit located at Thor Lake, approximately 100 kilometers southeast of Yellowknife, NT, Canada. The site is of particular interest because of its high proportions of heavy rare earth elements (HREE) and relatively shallow, sub-horizontal geometry (*Ciuculescu et al.*, 2013). Several key geological studies have been completed on the deposit including mineralogical work by *Sheard et al.* (2012) and mineralogical petrogenesis work by *Möller and Williams-Jones* (2016). In addition to this geological research, geophysical data was collected by Natural Resources Canada (NRCan) for Avalon Rare Metals Inc. (Avalon), who owns the rights to the property. This data consists of airborne gravitational and magnetic field data from the region as well as density and magnetic susceptibility measurements taken on core samples from over 400 drill holes (*Avalon*, 2013). The magnetic susceptibility measurements were taken with a portable KT-9 kappameter on the cores at 1 metre intervals, while density measurements were taken on small samples from the core at approximately 5 metre intervals.

The goal of this work was to improve on preliminary geophysical inversions completed for the Nechalacho deposit by *Tiampo and Nichols* (2014) through the implementation of geological constraints and cooperative inversion techniques. The core geophysical property measurements can be coupled with their respective field data to act as constraints for geophysical inversion. A common problem with inverse theory is non-uniqueness, as there theoretically are infinitely many solutions to a given inverse problem (*Aster et al.*, 2013). By implementing information from measured parameters and structures from the subsurface, this issue can be mitigated by reducing the total number of possible solutions and forcing the solution to converge to a subsurface model that agrees with known features. Additionally, inverse models can be improved by the incorporation of multiple datasets. A secondary aim of this study was to implement joint inversion techniques to incorporate gravity and magnetic results into a more robust model. Such a model would display characteristics from density models as well as magnetic susceptibility models to obtain a clearer picture of subsurface lithology, and thus help further delineate the Nechalacho deposit.

These goals were accomplished through innovative inversion techniques and codes that were written as a part of this thesis. This required a thorough understanding of the physics and methods behind the previously written software in order to write and implement self-authored, supplementary code. This new code is used in a variety of ways, including data filtering, interpolating reference models and implementing joint inversion methods. In addition to the supplementary code, this thesis developed multiple innovative techniques. The first of these techniques was a method for interpolating between drill hole data points to increase the influence of known geophysical properties

in the inversion process. This technique could have further applications as a substitute for standard methods of interpolation in the mineral exploration industry. The second technique developed was used to obtain preliminary modal percentages for samples using colour analysis on a pixel-by-pixel basis. This method could play an important role in large-scale modal analysis for simplified systems given its automated potential.

## 1.2 Outline

The following section in this chapter covers a brief introduction to inverse theory as it applies to geophysical inverse modelling, as well as a description of the programs used in this study. The primary inversion programs used were obtained from the Geophysical Inversion Facility of the University of British Columbia (UBC-GIF). The section will also overview programs written to supplement the UBC-GIF software.

Chapter 2 presents preliminary geophysical inversions completed using magnetic field data in the Thor Lake region. This work focused on the shallow subsurface where the deposit lies. A three-dimensional reference model was calculated using a self-written program that sorted and averaged the core magnetic susceptibility measurements into respective model cells. This reference model then was used to constrain subsequent inversions by implementing upper and lower bounds on each cell while also acting as a starting model. A deep-seated, long wavelength signal overprinted much of the shallow detail in the model, therefore coded wavenumber filtering techniques also were implemented. Results showed significant improvement over preliminary models by *Tiampo and Nichols* (2014). Models displayed a shallow sub-horizontal layer of high susceptibility that corresponded well with prior geological models despite a lack of lateral continuity within the layer.

Chapter 3 is an extension of the previous chapter and focuses on incorporating gravitational field data into the problem in order to better constrain the inversions. A similar workflow was followed to solve for subsurface density models. In this chapter, a new method of lateral interpolation between subsurface geophysical measurements is developed and proposed to increase the lateral continuity of the three-dimensional reference model. This technique is compared with more traditional kriging methods and proves effective for this dataset. As a result, additional magnetic susceptibility modelling is described in this section as well as preliminary joint inversion results. The results of density and magnetic susceptibility modelling correlate well spatially and geometrically, while the joint inversions result in minor improvements to the model.

Chapter 4 presents preliminary findings from a study on the magnetic susceptibilities of samples and the relation to the mineralogy within the deposit. The objective in this chapter was to check the validity of measured magnetic susceptibilities using laboratory instruments and comparing these measurements to those taken using field instruments. A further extension of this work involved a comparison of the findings to mineralogical work by *Möller and Williams-Jones (2016)* in order to investigate the relationship between the mineralogy and geophysics in detail. As expected, magnetic susceptibility measurements corresponded to increased hydrothermal alteration that resulted in secondary magnetite mineralization. Further study is needed to analyze the potential differences in geophysical signature between primary magmatic magnetite and secondary hydrothermal magnetite. High-definition images were also analyzed computationally, using software written as a part of this thesis, as an experimental first-pass method of approximating mineral percentages and geophysical trends with respect to colour.

Results of the latter study showed promise, however future work is necessary to assess any further potential for such methods.

## 1.3 Background

### 1.3.1 General Inverse Theory

The generalized inverse problem can be broken down to a trivial equation:

$$G(m) = d \tag{5}$$

where  $d$  is the data, such as airborne magnetic field data,  $G$  is a model or system of equations that describe the physics of the problem, such as those governing the relationship between magnetic susceptibility and magnetic field, and  $m$  is the set of model parameters that are being solved for (Aster *et al.*, 2013). While this generalized equation is trivial, inverse problems are normally very complex. A major obstacle when inverse modelling arises when solving for a three-dimensional model using a two-dimensional dataset. In geophysical modelling, the subsurface is broken up into a finite number of three-dimensional cells. The inversion process solves for a parameter value for each of these cells that collectively result in the reproduction of the data. In rank-deficient problems, each given solution is one of infinitely many solutions that can solve the system of equations. Therefore, since there are many more cells than data points, there are infinitely many parameter models that fit the data. As a result, cells in which the geophysical model parameter has been measured, and is therefore known within some error bounds, can be used to constrain the problem and reduce the number of possible solutions, forcing the solution toward a model that agrees with independently known subsurface measurements.

Joint inversion describes an inversion that uses two or more different types of datasets cooperatively to reach a solution that satisfies both. Structural joint inversion describes a joint inversion method where the solution from the inversion of one dataset is used to influence the solution of the other dataset. Therefore, the structure of one model, such as magnetic susceptibility influences the structure of another model, such as density. The structure of the density model simultaneously influences the structure of the magnetic susceptibility model in an iterative manner. The methods used for this structural joint inversion method are describe in section 1.3.3.

### 1.3.2 Geophysical Inversion Facility Software

The University of British Columbia Geophysical Inversion Facility (UBC-GIF) software package consists of several programs used for the inversion of geophysical data. The magnetic (mag3d) and gravity (grav3d) packages were the main programs used in this study. Both programs invert for their respective geophysical parameter in a similar manner. A three-dimensional mesh is defined by the user that describes the cell dimensions as well as the total extent of the model in each of the three dimensions. This mesh, along with the geophysical field data is used to calculate a sensitivity matrix. That sensitivity matrix is used to provide forward mapping from the current model to the input data throughout the iterative inverse process (*UBC-GIF*, 2013a). In other words, the sensitivity matrix is an  $i$  by  $j$  matrix where  $i$  is the dimension of the data,  $d$ , and  $j$  is the dimension of the model,  $m$ , that represents  $G$  in **Equation 5**. Therefore, the sensitivity matrix can be multiplied by  $m$  to forward model for an estimate of the data, given the current model. The inverse problem relies on the minimization of an objective function,



$\varphi$ , which is comprised of two components: the model objective function,  $\varphi_m$ , and the data misfit function,  $\varphi_d$ . The function is then minimized according to the equation:

$$\min\{\varphi\} = \varphi_d + \beta \varphi_m \quad (6)$$

where  $\beta$  is the trade-off parameter that influences the accepted misfit allowed by the expected  $\varphi_d$  value. This parameter is determined using the L-curve criterion (*UBC-GIF*, 2013a). The L-curve is a log-log plot of the norm of the residuals versus the norm of the model or solution which was named due to the shape of the resulting plot (*Hansen*, 2000). The L-curve criterion is based on Tikhonov regularization techniques where the norm of the model is minimized such that the norm of the residuals is less than some threshold,  $\delta$  (*Aster et al.*, 2013):

$$\min(\|m\|_2) \text{ s.t. } \|Gm - d\|_2 \leq \delta \quad (7)$$

In this case, the trade-off parameter,  $\beta$  is the regularization parameter. The problem can also be considered by minimizing the norm of the residuals such that the norm of the model is less than a separate threshold,  $\varepsilon$  (*Aster et al.*, 2013):

$$\min(\|Gm - d\|_2) \text{ s.t. } \|m\|_2 \leq \varepsilon \quad (8)$$

The L-curve criterion suggests that the most appropriate regularization parameter,  $\beta$  is the value that yields a solution closest to the corner of the L-curve (*Hansen*, 2000). This coincides with the solution where  $\delta$  and  $\varepsilon$  are equivalent (*Aster et al.*, 2013).

The first component of the inverse problem is the model objective function, defined by the equation:

$$\begin{aligned}
\varphi_m(\kappa) = & \alpha_s \int_V \omega_s \{ \omega(r) [\kappa(r) - \kappa_0] \}^2 dv \\
& + \alpha_x \int_V \omega_x \left\{ \frac{\partial \omega(r) [\kappa(r) - \kappa_0]}{\partial x} \right\}^2 dv \\
& + \alpha_y \int_V \omega_y \left\{ \frac{\partial \omega(r) [\kappa(r) - \kappa_0]}{\partial y} \right\}^2 dv \\
& + \alpha_z \int_V \omega_z \left\{ \frac{\partial \omega(r) [\kappa(r) - \kappa_0]}{\partial z} \right\}^2 dz
\end{aligned} \tag{9}$$

where  $\alpha$  are coefficients that affect the relative importance of each component,  $\kappa_0$  is the reference model,  $\omega(r)$  is the depth weighting function, and  $\omega$  are spatially dependent weighting coefficients (*UBC-GIF*, 2013a). This objective function is then discretized over the mesh using the finite difference approximation given by:

$$\varphi_m(\kappa) = \|W_m(\kappa - \kappa_0)\|^2 \tag{10}$$

where the model sensitivity matrix,  $W_m$ , is calculated for the defined mesh, depth weighting function and weighting coefficients (*UBC-GIF*, 2013a). The depth weighting function is included to counteract geometrical decay experienced by a deep, long-wavelength signal that originates further from the point of measurement. Essentially, this function assumes that potential fields decay at a rate proportional to the inverse of distance cubed and enhances the weight of deeper cells to account for loss of signal.

The second component of the objective function is simply the  $L_2$ -norm of the residuals that describes how well the observed data are reproduced:

$$\varphi_d = \|W_d(Gm - d)\|^2 \quad (11)$$

$W_d$  is a diagonal matrix where the  $i^{th}$  element is the inverse of the standard deviation for that data point. If the noise is assumed to be random and a Gaussian distribution with zero mean is assumed, then  $\varphi_d$  represents a chi-squared distribution with  $N$  degrees of freedom (*UBC-GIF*, 2013a). Therefore the optimal data misfit can provide a target misfit for the inversion via:

$$E[\chi^2] = N \quad (12)$$

Once both components ( $\varphi_m$  and  $\varphi_d$ ) and the trade-off parameter ( $\beta$ ) are defined, the optimization problem can be solved using the projected gradients method (*UBC-GIF*, 2013a). This method is a conjugate gradient method that projects the gradient into a subspace that forces the gradient to zero if the proposed step would cause the parameter to exceed the bound constraints (*Calamai and Moré*, 1987). Essentially this is a way of constraining the conjugate gradient method of optimization by allowing the model to reach the bounds, but not exceed them (*UBC-GIF*, 2013a). The result is an inverse modelling technique that can easily be influenced by geophysical measurements in order to constrain the models on a cell-by-cell basis.

### 1.3.3 Previous Studies

Several case studies have been completed by authors at UBC-GIF using a variety of similar geophysical inversion methods. *Li and Oldenburg* (1998) investigated two approaches to geophysical inversion of gravity data using similar depth weighting and objective function optimization. The first inversion method used Poisson's relation in

order to invert via a three-dimensional magnetic inversion algorithm, while the second method inverted the gravity data directly. This study was performed on both synthetic and field data and showed that reasonable results can be obtained without the use of Poisson's relation with an appropriate objective function (**Equation 9**) (*Li and Oldenburg, 1998*).

*Li and Oldenburg* (2003) implemented sparse matrix representation of the sensitivity matrix that allowed for efficient forward modelling. In this study, a three-dimensional wavelet transform, along with thresholding are applied to the sensitivity matrix in order to decrease computation time. A conjugate gradient method then was used in order to take advantage of efficient forward modelling and further improve computation rates to allow for larger problems to be solved (*Li and Oldenburg, 2003*). These updates were tested on a synthetic magnetic dataset and produced results that agreed well with the true susceptibility model.

An approach for incorporating knowledge of structural trends in subsurface geology as well as geophysical constraints based on drillhole measurements was proposed by *Lelièvre et al.* (2009). This case study solved for a synthetic model using drillhole magnetic susceptibility and density measurements to set upper and lower bounds on individual cells to constrain the inversion. Weighting coefficients were used in order to influence known structural trends in the geology and to better define boundaries of geologically realistic models (*Lelièvre et al., 2009*). Lastly, a method of combining structural trends from both susceptibility and density models to jointly influence subsequent inversions was proposed as a method of cooperative inversion between two data fields.

### 1.3.4 Programs Written

In addition to the programs from the UBC-GIF software package, several supplementary programs were written as a part of this thesis (see **Appendix A**). These programs were used for a variety of tasks from statistical analysis to data manipulation and filtering. Coding was completed using the Matlab computing environment by MathWorks. *UBC-GIF\_Conversion.m* was written as a conversion tool to sort, bin and average geophysical core measurements based on a user-defined mesh to be used in the UBC-GIF software. This program was used to format the core data correctly into the appropriate cells in order to create a three-dimensional reference model, which was then used to calculate a starting model, as well as the maximum and minimum boundary models used to constrain the inversions. *Upward\_cont.m* is a script written to perform wavenumber filtering techniques on airborne potential field data. This program takes input potential field data and filters out long wavelength signal in the frequency domain via upward continuation. Upward continuation methods are used to obtain a dataset of long-wavelength signal, which is then subtracted from the original dataset in order to remove signal produced by deep anomalous bodies. *Grad\_attenuate.m* implements a method of solving for more geologically realistic models proposed by *Lelièvre et al.* (2009). This script removes padding cells from the current best model and calculates the gradient in three dimensions. These gradients are then normalized and used to create an input file of weighting coefficients for subsequent inversions. Weighting factors are increased between cells with lower gradients to promote smoothing while factors are decreased between cells where the gradients are high to penalize smoothness to promote more defined lithological boundaries.

*Lat\_interp.m* is a program that calculates a three-dimensional reference model similar to that produced by *UBC-GIF\_Conversion.m*, but with the implementation of the proposed lateral interpolation method. This creates reference, starting and boundary models for both magnetic and gravity datasets where significantly more cells contain data than the previous three-dimensional reference model. The implementation of the lateral interpolation method led to a comparison between these results and those obtained through the more traditional interpolation method of kriging. *Krig\_test.m* employs code written by Schwanghart (2010) to apply ordinary kriging to the core data on each  $x$ - $y$  plane for a total of  $z$  iterations to obtain a three-dimensional reference model. This model is used in a similar manner to the other three-dimensional models, however the variance is used to determine the ranges for the maximum and minimum boundary models. The final script written for chapter 3 is *joint.m*. This program removes padding cells and calculates the gradient between cells in three dimensions similar to *grad.attenuate.m*, but for both magnetic susceptibility and density models. These gradients then are normalized and added together as proposed by Lelièvre *et al.* (2009) and used to adjust weighting factors as in the gradient attenuation and enhancement method. This method is described in detail in Chapter 2, but essentially promotes more smoothing where the gradient of the current model is low and penalizes smoothing where the gradient is high. The addition of a second normalized dataset results in subsequent inversions being influenced by the lithological boundaries of both geophysical parameter models.

Work in Chapter 4 is completed using one robust program *geo\_analysis.m* as well as a secondary program, *pixel\_test.m*. The main function of the first few sections of this code is to plot magnetic susceptibility, density and REE concentrations within their respective

lithological unit as defined by *Möller and Williams-Jones* (2016), given their depth. This part of the script was used mainly to analyze any geological trends in relation to their geophysical characteristics. *Pixel\_test.m* is a program written that takes a high definition image of a sample and breaks it down to a sequence of numerical RGB values. These values are used in preliminary proposed colour analysis of samples through assigning mineral types to each pixel based on a set of conditions that govern the RGB values of each mineral. These conditions were assigned based on experimentation through the collection of several different mineral subsets of RGB values.

## 1.4 References

- Aster, R. C., Borchers, B., and Thurber, C., 2004.** Parameter Estimation and Inverse Problems. Academic Press, Oxford, UK, 355p.
- Avalon Rare Metals Inc., 2014.** Lithology and Magnetic Susceptibility Data. Prepared by Ben Webb.
- Calamai, P.H., and Moré, J.J., 1987.** Projected Gradient Methods for Linearly Constrained Problems; Mathematical Programming, v. 39, p. 93-116.
- Ciuculescu, T., Foo, B., Gowans, R., Hawton, K., Jacobs, C., and Spooner, J., 2013.** Technical Report Disclosing the Results of the Feasibility Study on the Nechalacho Rare Earth Elements Project. Micon International Limited, Toronto, Canada, 307p.
- Hansen, P.C., 2000.** The L-Curve and its Use in the Numerical Treatment of Inverse Problems; Department of Mathematical Modelling, Technical University of Denmark Research.
- Lelièvre, P. G., Oldenburg, D. W., and Williams, N. C., 2009.** Integrating Geological and Geophysical Data Through Advanced Constrained Inversions; Exploration Geophysics, v. 40, p. 334-341.

**Li, Y., and Oldenburg, D.W., 1998.** 3-D Inversion of Gravity Data; *Geophysics*, v. 63, p. 109-119.

**Li, Y., and Oldenburg, D.W., 2003.** Fast Inversion of Large-Scale Magnetic Data Using Wavelet Transforms and a Logarithmic Barrier Method; *Geophysics Journal International*, v. 152, p. 251-265.

**Möller, V., and Williams-Jones, A.E., 2016.** Petrogenesis of the Nechalacho Layered Suite, Canada: Magmatic Evolution of a REE-Nb-rich Nepheline Syenite Intrusion; *Journal of Petrology*, v. 57, p. 229-276.

**Pratt, G. R., 2005.** Induced Magnetization and Magnetic Susceptibility; *in* Applied Geophysics, Department of Geological Sciences and Geological Engineering, Queen's University, Kingston, Ontario, Canada, p. 65-69.

**Schwanghart, W., 2010.** Ordinary Kriging; Variogramfit; Experimental (Semi) Variogram; MathWorks File Exchange, Matlab, retrieved March 1, 2016.

**Sheard, E. R., Williams-Jones, A.E., Heiligmann, M., Pederson, C., and Trueman, D. L., 2012.** Controls on the Concentration of Zirconium, Niobium, and the Rare Earth Elements in the Thor Lake Rare Metal Deposit, Northwest Territories, Canada; *Economic Geology*, v. 107, p. 51-104.

**Tiampo, K.F. and Nichols, N., 2014.** Preliminary Inversion, Blatchford Lake Intrusive Suite; Accelerated Masters Project Report by Nolan Nichols, University of Western Ontario, London, Canada.

**UBC-Geophysical Inversion Facility, 2013a.** A Program Library for Forward Modelling and Inversion of Magnetic Data over 3D Structures, version 5.0; Developed under the consortium research project, *Joint/Cooperative Inversion of Geophysical and Geological Data*, Department of Earth and Ocean Sciences, University of British Columbia, Vancouver, British Columbia.

**UBC-Geophysical Inversion Facility, 2013b.** A Program Library for Forward Modelling and Inversion of Gravity Data over 3D Structures, version 5.0; Developed



under the consortium research project, *Joint/Cooperative Inversion of Geophysical and Geological Data*, Department of Earth and Ocean Sciences, University of British Columbia, Vancouver, British Columbia.

## Chapter 2

### 2 Current Status of Magnetic Inversion Project at Thor Lake, N.W.T.

*This section was written and submitted as an open-file report for the Northwest Territories Geological Survey. In this study, magnetic field data, coupled with magnetic susceptibility measurements from core drilled through the Nechalacho deposit and in the Thor Lake area, are used to create three-dimensional susceptibility models through geophysical inversion techniques. The deposit has been examined extensively in order to identify the extent of the rare earth element mineralization. Beneath the Thor Lake syenite, hydrothermal alteration of a cumulate sequence within the Nechalacho syenite acts as a host for rare earth element-bearing minerals. Preliminary results presented here agree with current geological models which suggest that an extensive, sub-horizontal layer of increased alteration and mineralization lies at approximate depths of 150-200 metres. This layer extends for over 1500 metres laterally and potentially represents a layer of increased heavy rare earth element mineralization referred to as the basal zone. Early findings suggest that the basal zone extends further north than predicted from previous understanding.*

#### 2.1 Introduction

Inverse theory as applied to geophysical datasets has applications to engineering problems as well as both petroleum and mineral exploration. Making use of modern computational power, inversions represent a novel method for studying the subsurface in order to pinpoint a variety of target bodies. Inversion is reasonably straightforward, following the equation:

$$G(m) = d \quad (1)$$

where  $d$  is the dataset,  $G$  is the geophysical source or set of equations to describe the system and  $m$  is the model or set of parameters that are to be modeled (*Aster et al.*, 2004). In practice, the solutions can become very complex and the major barrier to overcome is the problem of non-uniqueness.

Geological studies can produce very extensive data acquisitions from a given area. However, when it comes to mapping the boundaries of ore bodies that lie deep in the subsurface, there will always be unknowns. The goal of an inversion is to resolve some of these unknowns using plausible constraints based on geological and geophysical data from the region. These constraints aid in solving the non-uniqueness problem by limiting the number of possible results that will fit the system. Information from surface geology maps and borehole data are ideal for use as model constraints.

In the mineral exploration industry, surveying gravity and magnetic fields via airborne techniques is a fast and relatively cost efficient way of obtaining physical data on a large scale. As a result, airborne techniques are preferable to boreholes as a first pass because they provide useful information about an entire area of interest. Borehole data, however, offer the opportunity to thoroughly sample a target region in three dimensions on a more local scale. Thus, the combination of these two techniques reduces the need for more drillholes while still obtaining an improved and more complete picture of the subsurface.

Magnetic field data are widely used in the mineral exploration industry to utilize contrasting magnetic susceptibilities in host-rocks in relation to the surrounding rock.

This allows for the mapping of ore bodies by solving for the volumetric distribution of magnetic susceptibility given the magnetic field anomaly in the area.

Inversions can be further constrained by using additional datasets that contain different physical signals such as gravitational field data. Gravity anomaly data can be used to invert for changes in density beneath the surface allowing for lithological units to be separated from one another based on their densities. When these results are paired with lithological units that are separated based on magnetic susceptibility in a joint inversion, the result can provide an accurate image of the lithological distribution beneath the surface.

## 2.2 Geological Background

### 2.2.1 Regional Geology

The region of interest at Thor Lake is located approximately 100 kilometres southeast of Yellowknife in the Northwest Territories, Canada (**Figure 2.1**). The area is underlain by the Blatchford Lake Intrusive Complex (BLIC), a Proterozoic alkaline intrusion divided into two main zones (**Figure 2.2**). The eastern lobe contains the Grace Lake granite and the Thor Lake syenite which contains the Nechalacho deposit. With peralkaline characteristics, the Thor Lake syenite is enclosed by the 2176.2 Ma Grace Lake granite, and has been dated at 2176  $\pm$  1.6 Ma (*Mumford*, 2013). In comparison, the western lobe is less alkaline and contains the Caribou Lake gabbro (*Davidson*, 1978). The BLIC is cross-cut by numerous diabase dykes, including several east-northeast trending dykes believed to be a part of the 1901 Ma Hearne swarm. The Thor Lake syenite itself is

cross-cut by a northwest trending dyke with a strong magnetic signal that has recently been re-classified as a 2126-2108 Ma Indin diabase dyke (*Mumford, 2013*).

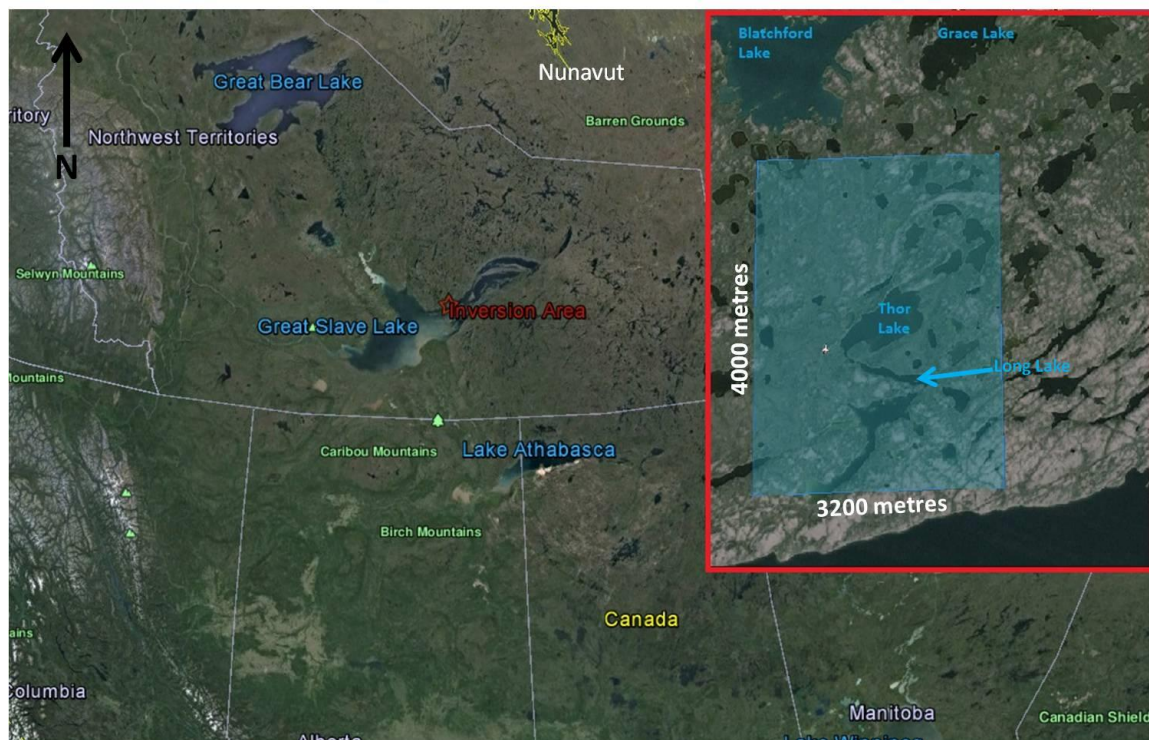


**Figure 2.1:** Location map showing the Thor Lake area in the Northwest Territories. Blue shaded area in the red inset map shows the inversion area in this study. Adapted from Google Earth, 2015.

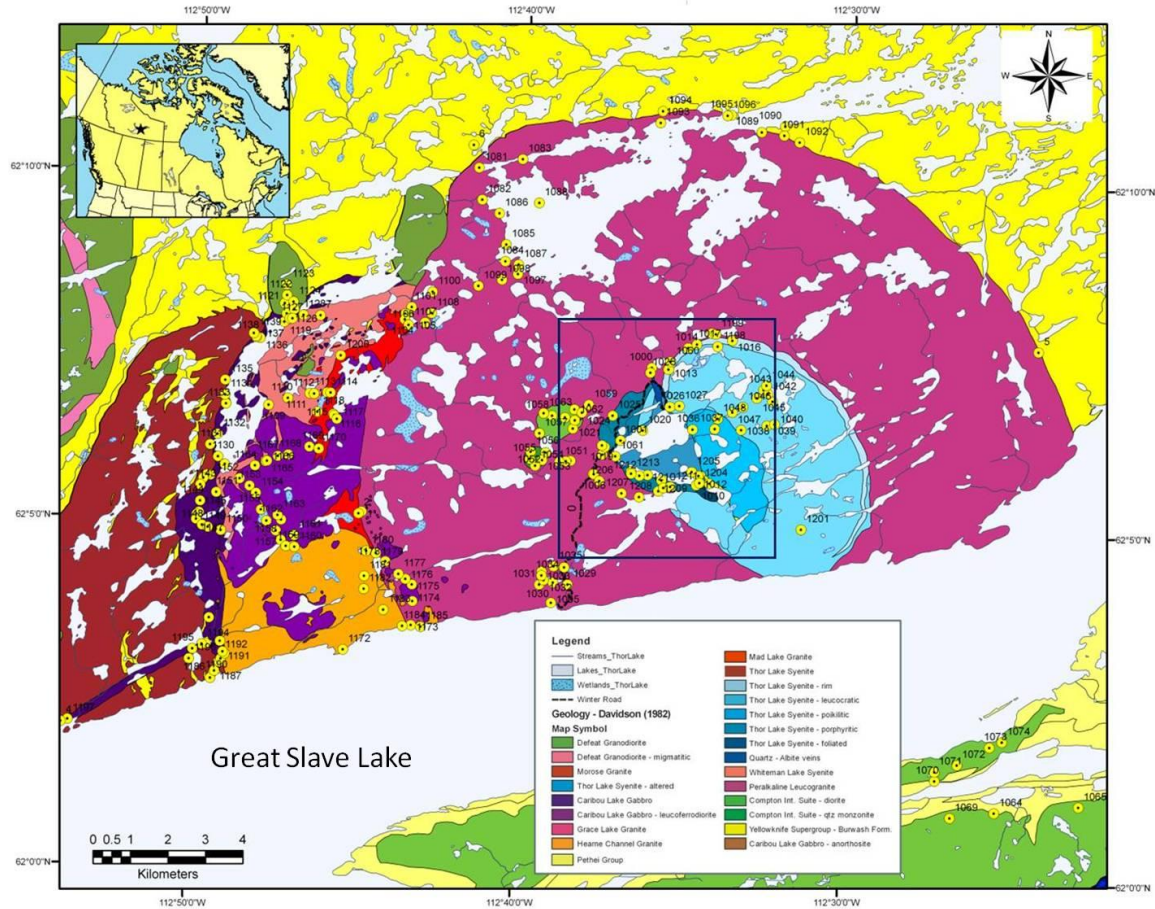


**Figure 2.2: Regional geology of the Blatchford Lake Complex, NWT Canada (modified from Mumford, 2010 after Davidson, 1978). The yellow dots signify sample locations from the study by Mumford (2010) and are not mentioned in this study.**

### 2.2.2 Local Geology

The Nechalacho deposit, known for its high concentrations of rare earth elements (REE), is the primary focus of this study. It is hosted by the Nechalacho nepheline syenite (NNS), a layered intrusion with peralkaline characteristics that increase with depth (Sheard *et al.*, 2012). Based on current drilling, it has been speculated that the intrusion dips beneath the Thor Lake syenite in all directions (Ciuculescu *et al.*, 2013). Located within the Thor Lake syenite, small isolated outcrops of the NNS are exposed at the

surface between Long Lake and Thor Lake which display strong hydrothermal alteration but appear to be relatively undeformed with textures generated by both magmatic and hydrothermal processes (*Sheard et al.*, 2012). This alteration zone is located in the apex of the syenite dome-like feature and divided into the upper zone and basal zone (**Figure 2.3**). The upper zone is defined as the volume between the top of the basal zone and the bottom of the overburden and lakes while the basal zone is constrained by the contact with the Grace Lake granite and roof-top sodalite (*Ciuculescu et al.*, 2013). Originally thought to extend just beneath Thor and Long Lakes, drilling to the north in 2010 found evidence that the deposit may extend beneath Cressy Lake as well (*Pilkington et al.*, 2012). The greatest potential for further mineralization and increased value of the deposit apparently lies to the north, although the western boundary is not well defined (*Ciuculescu et al.*, 2013). Presently there are no known dykes from the Mackenzie swarm that cross cut the deposit. However, east-northeast trending 1901 Ma Hearne swarm dykes do cross cut the deposit, but no significant displacement is seen along faults (*Mumford and Cousens*, 2014).

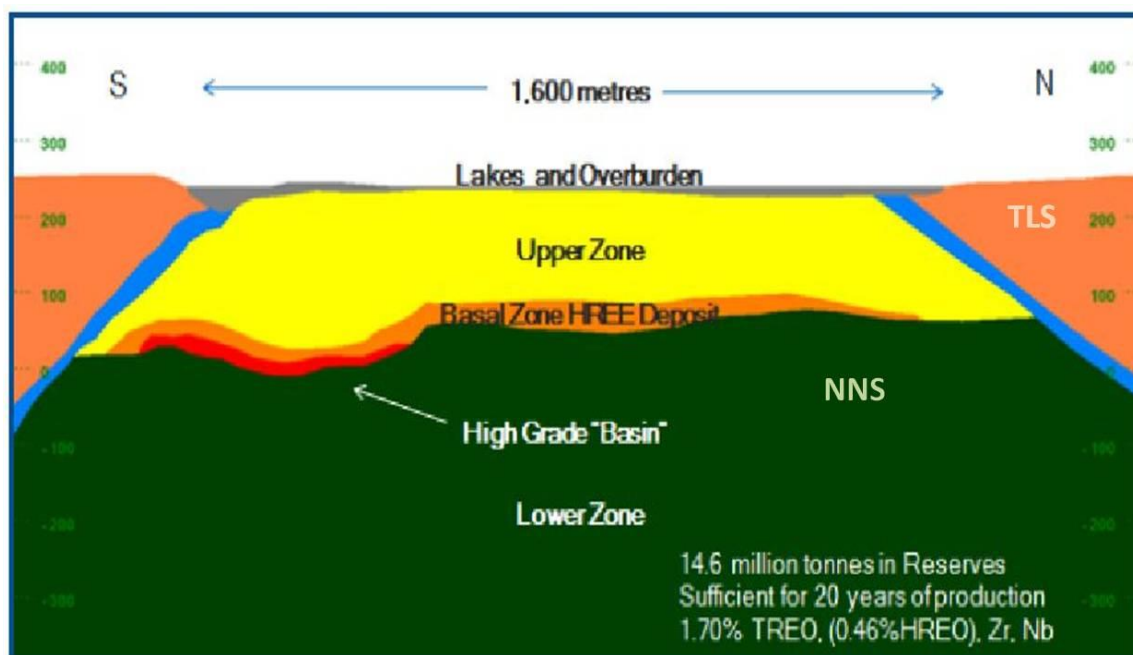


**Figure 2.3: Cross-section of the Nechalacho deposit from current geological methods (modified from Ciuculescu et al., 2013). The Nechalacho nepheline syenite (NNS) is in green and includes the upper and basal zones, while the Thor Lake syenite (TLS) is represented in orange. The blue lithology is the roof sodalite. The vertical scale is in metres above sea level (ASL).**

### 2.2.3 Mineralization

The mineralization of the Nechalacho deposit is generally sub-horizontal and has been traced for over 1500 metres (*Sheard et al.*, 2012). The primary elements of interest are: light rare earth elements (LREE) contained in allanite, monazite, bastnaesite and synchysite; heavy rare earth elements (HREE), niobium and tantalum contained in fergusonite; niobium contained in ferrocolumbite; and HREE, niobium, tantalum and zirconium contained in zircon (*Pinckston and Smith*, 1995; *Ciuculescu et al.*, 2013). The proportion of HREE to LREE increases from the top of the deposit to the bottom. HREE account for 30% of the total REE in the high grade basin within the bottom of the basal



zone (*Ciuculescu et al.*, 2013). Sheard et al. (2012) described the progression from the hanging wall sodalite cumulates, down through the upper zone which contains coarse-grained nepheline aegirine syenites locally enriched with zircon silicates, to the basal zone which is comprised of a foyaitic syenite within a zone of altered eudialyte cumulates. This sequence of rocks was intensely altered by sodium and iron rich hydrothermal fluids which resulted in magnetite and hematite as a few of the major alteration minerals (*Sheard et al.*, 2012). The alteration zone extends from the surface down to approximately 80 metres depth, with some regions extending as far down as 200 metres (*Ciuculescu et al.*, 2013). The original mineralogy of the deposit consisted of a rooftop sodalite, enclosing layers of aegirine nepheline syenite with cumulate zircon, followed by more syenite layering and finally cumulate inferred eudialyte. Extensive alteration by what is thought to have been a fluorine bearing hydrothermal fluid resulted in the breakdown of eudialyte to secondary minerals that contain HREE, such as zircon and fergusonite, and leaving behind alteration minerals such as magnetite, which has a highly anomalous magnetic signature. As the fluid altered the zircon cumulates, REE were leached from the cores of the crystals and deposited along fractures and crystal boundaries. LREE were remobilized further and form the high degree of LREE in the upper portion of the deposit (*Sheard et al.*, 2012).

The goal of this study is to use the knowledge collected in the exploration process, including previous geological research and geophysical survey data, to further delineate the boundaries of the upper and lower zones of mineralization. The initial steps in the process, reported here, involve inverting magnetic field data to produce a magnetic susceptibility model and constraining it with magnetic susceptibility measurements

collected from boreholes as boundary conditions. Future steps will incorporate gravitational field data to further constrain the model and enhance important lithological boundaries. The anticipated end result is a model that improves on existing interpretation of the lateral and vertical extents of the deposit.

## 2.3 Data

The data used in this study are airborne total magnetic field data obtained by Natural Resources Canada (*NRCan*, 2011). The survey was flown by Fugro GeoServices Ltd. at an altitude of 100 metres above ground level with a traverse line spacing of 250 metres and covered a total area of approximately 250 square kilometres (**Figure 2.4**). The survey collected total magnetic field data with a fixed-wing aircraft, using a single cell cesium vapour magnetic system. When examining the survey result on a regional basis, the east-northeast trending signature of the Hearne dyke swarms is apparent, as well as a highly magnetic northwest trending anomaly presumed to be related to the Indin dyke swarm (*Mumford and Cousens*, 2014). Full-tensor airborne gradiometry and gravity anomaly surveys were collected of the same area by NRCan and will play a larger role in future work.

There has also been extensive subsurface exploration through the drilling of boreholes in the area. Magnetic susceptibility measurements were collected from the cores of over 400 holes on the Thor Lake property. These measurements were taken directly on the core with a handheld KT-9 instrument at 1 metre intervals by Avalon Rare Metals (*Avalon Rare Metals*, 2014).

A region of interest was defined based on the drilling pattern. The resulting Thor Lake inversion region is a 12.8 square kilometre area that is centered on the Thor Lake Syenite, chosen for its proximity to a prominent magnetic high and the large number of boreholes concentrated in this area (**Figure 2.4**).

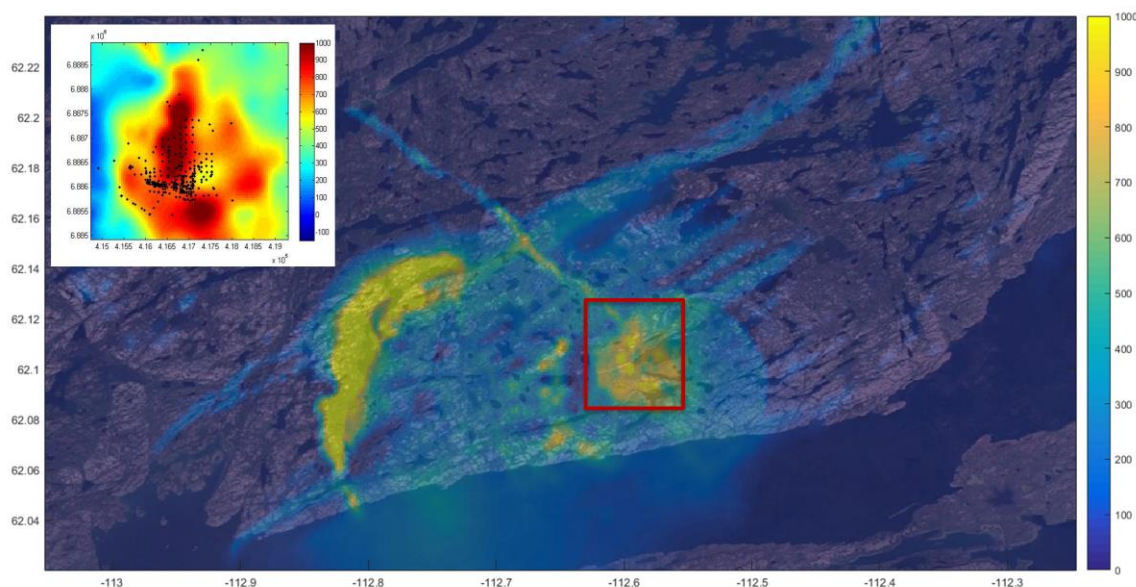


**Figure 2.4:** Map of the residual magnetic field from the aeromagnetic survey completed by NRCan (2011) of the Blatchford Lake Complex. The eastern large positive elliptical anomaly is the Thor Lake deposit while the western elongated anomaly is associated with the Caribou Lake gabbro that hosts Cu-Ni-PGE mineralization. Units are in nanoTeslas. The inset plot is an enlarged in view of the inversion area with drill-holes plotted in black. Drillhole locations obtained from Avalon Rare Metals (2014).

It is expected that the source of this large magnetic signal is the abundance of alteration minerals such as magnetite and hematite that are associated with REE mineralization within the Nechalacho deposit. It is important to note that the anomalies, while indicative of REE deposits, are not caused by the REE but the mineralogy of the intrusions that are

associated with them (*Verplanck and Van Gosen, 2011*). Therefore regions of high magnetic susceptibility will likely be associated with regions where primary minerals such as eudialyte and aegirine have been altered to magnetite. In the case of the Nechalacho deposit, this occurs mainly within the basal zone, thus anomalous densities and magnetic susceptibilities are expected where the REE mineralization is present in larger concentrations (*Sheard et al., 2012*).

## 2.4 Software and Inversion Setup

The software used in this study is the University of British Columbia Geophysical Inversion Facility (UBC-GIF) software suite. This suite is comprised of forward modelling and inversion software for electromagnetic, induced polarization, magnetic and gravity data in 3-dimensions (*UBC- Geophysical Inversion Facility, 2013*). The main program used in this study is the magnetic (mag3d) code (details provided below). This program runs with important user inputs including mesh, topography, data, model, and weighting files (**Figure 2.5**).

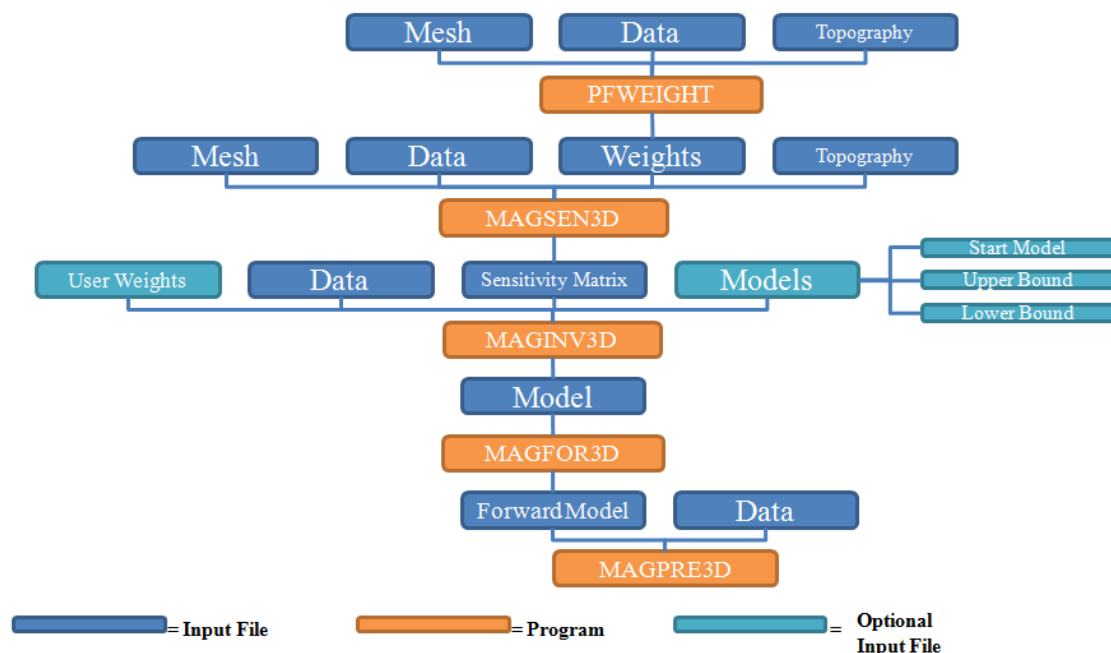


**Figure 2.5: Program workflow for MAG3D. GRAV3D follows a similar workflow by substituting the gravity programs for their magnetic counterparts (UBC-GIF, 2013).**

The mesh file defines the desired model resolution as a series of three-dimensional cells, with each dimension specified. These dimensions need to be chosen in advance with a few guidelines in mind. The first, as mentioned above, is the resolution that is desired for the inverted model. Smaller cells will result in the model calculating susceptibilities or densities for more individual points, making it possible to detect changes in physical properties on a smaller scale. The tradeoff is that the more cells the model has, the more computational power it uses and the more time-consuming the inversion. Also, there is some tradeoff between the lateral dimensions of the cells and the vertical dimension. The vertical z-dimension of the cell should be approximately half of the horizontal x-y-dimensions (UBC- *Geophysical Inversion Facility*, 2013). Another important consideration is the resolution of discrete geological information such as borehole

readings or core sample measurements. In this case, magnetic susceptibility measurements were taken every 1 metre on the core. However the horizontal positions of the drillholes are unequally distributed with a high density of holes in the centre of the region.

With all of these guidelines in mind, cells were chosen to be 25 metres in the x and y-dimensions and 10 metres in the z-dimension. This results in two cells per magnetic field data point as the 250 metre line spacing has been grid interpolated to 50 metre intervals between data points. This provides a vertical resolution sufficient such that the resolution of the borehole magnetic susceptibility data remains useful, without the inversion being too computationally expensive. Different meshes used in magnetic inversions of the region ranged from 70 000 cells to more than one million cells with run times of 20 minutes to 36 hours, respectively. While grid resolution is important, an additional factor that affects the computation time is how tight the constraints are on parameters such as measured susceptibilities. Meshes with larger numbers of cells can run faster if the starting model is closer to the converging point and the inversion is given room for error.

The inversion itself works by calculating a model objective function  $\phi$ , which is then minimized in order to find a geophysical model that best fits the data. The objective function is defined by:

$$\begin{aligned} \phi_m(\kappa) = & \alpha_s \int_V \omega_s \{ \omega(r) [\kappa(r) - \kappa_0] \}^2 dx + \alpha_x \int_V \omega_x \left\{ \frac{\partial \omega(r) [\kappa(r) - \kappa_0]}{\partial x} \right\}^2 dv \\ & + \alpha_y \int_V \omega_y \left\{ \frac{\partial \omega(r) [\kappa(r) - \kappa_0]}{\partial y} \right\}^2 dv + \alpha_z \int_V \omega_z \left\{ \frac{\partial \omega(r) [\kappa(r) - \kappa_0]}{\partial z} \right\}^2 dv, \end{aligned} \quad (2)$$

where  $\omega_x$ ,  $\omega_y$ ,  $\omega_z$  and  $\omega_s$  are weighting functions used make the model smoother or coarser in the specific directions,  $\kappa_o$  is the reference model and  $\omega(r)$  is the depth weighting function (*UBC-GIF*, 2013).

As mentioned previously, a major challenge in the inversion process is non-uniqueness. The minimization of the objective function is an optimization problem for which there are potentially an infinite number of minima. Therefore, constraints from real physical measurements within the region can help the optimization converge to an optimal solution or model. A variety of model input files can be included in the inversion including an elevation file, a starting model, upper bounds, and lower bounds files (*UBC-Geophysical Inversion Facility*, 2013). The elevation file is important because it allows the program to omit cells that are above the topography of the region. This keeps the model from including extra signals from cells that are actually located above the surface. The starting model is used to help the inversion start off on the right track, or to set a starting point from a previous inversion in iterative processes. Upper and lower bounds files place constraints on each individual cell, allowing for some flexibility to account for error in cells where the susceptibility values are known.

The final important type of input file is the weighting file. This makes use of the weighting functions ( $\omega_x$ ,  $\omega_y$ ,  $\omega_z$  and  $\omega_s$ ) and allows the enhancement or attenuation of gradients at each point to result in smoother or more abrupt changes in the model (*Lelièvre et al.*, 2009). This is an important tool that can be used to smooth homogeneous packages of rocks while allowing for abrupt changes in physical properties that coincide with changes in lithology.

## 2.5 Magnetic Inversions and Discussion

Most inversions on this scale are iterative processes. A basic inversion is completed without any constraints and with each consecutive inversion more information is added to the problem until a reasonable result is reached that obeys all of the requirements (*Lelièvre et al.*, 2009). In this case, the magnetic field data alone is used in the first inversion to solve for a subsurface magnetic susceptibility model. The results are then analyzed to determine which additional datasets are needed to constrain the following iterations.

### 2.5.1 Unconstrained Inversion

The first inversion performed on the data was a basic unconstrained inversion. This involved taking the magnetic anomaly data (**Figure 2.6**) and the selected mesh and fitting an answer to the problem in the form of a subsurface model. This elementary inversion allows for the calculation of the simplest model that fits the data. While not usually a good representation of the true subsurface, it is a useful starting point for subsequent inversions. Even in areas with simple subsurface geology, one inversion or iteration is never enough and subsequent revisions are implemented to improve the solution.



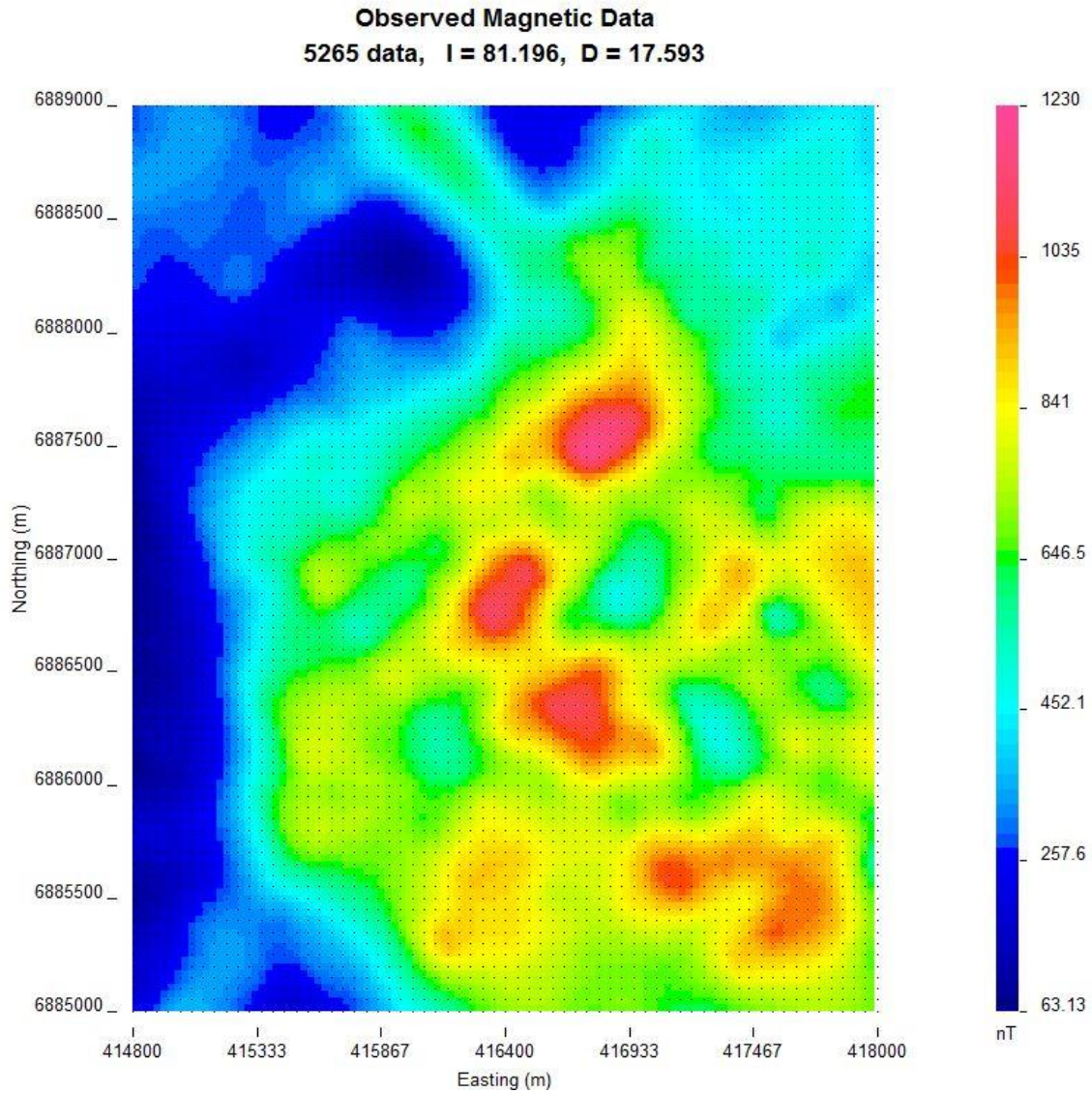


**Figure 2.6:** The original magnetic field anomaly dataset for the Thor Lake region selected for this study. UTM coordinates shown in all figures and cross sections are NAD 83, Zone 11N. There are 5265 datapoints with magnetic inclination ( $I$ ) and declination ( $D$ ) also specified.

**Figure 2.7** shows a cross-section of the unconstrained inversion. This inversion included input files for the mesh, the magnetic field anomaly data, and the elevation. The distance

between the point at which the measurement is taken and the ground is included in the magnetic data and accounted for in the inversion. However, an elevation file is still preferable because it omits extra padded cells at the top of the mesh to account for topography or lack thereof.

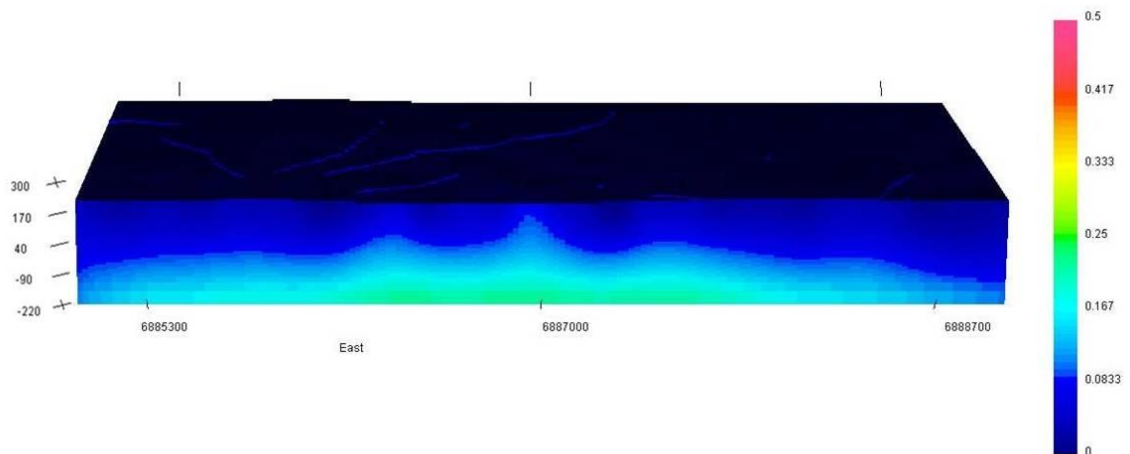


**Figure 2.7: A north-south (N-S) cross-section for the preliminary, unconstrained magnetic inversion of the Thor Lake study area along line 416550 Easting (UTM), looking west. Units on the right side represent susceptibility in SI units. Scale on the left is elevation above sea level (ASL) in metres.**

This inversion produces a simple, smooth result with a large anomaly along the base of the modeled region. While this appears to have the sub-horizontal structure expected in the deposit, the anomaly is much deeper than the geologic structure would predict with much larger susceptibilities than those measured in the drillhole data. This demonstrates the weakness of an unconstrained inversion. The simplest model fits the long wavelength signal, resulting in the estimation of a large, deep anomaly at the lowest possible depth that, in amplitude, overwhelms the shallower, shorter-wavelength anomalies. This is

evidenced in this model by the fact that the largest magnetic susceptibility values are those along the x-y plane at maximum depth. A larger anomaly that lies deeper than the model allows could also produce this result but it is unlikely as several different maximum model depths were tested and each produced a similar model with a maximum anomaly at the lowest possible depth. Since magnetic susceptibility data are available for boreholes in the region and current geological models lead to the expectation of a shallower deposit, the next logical step is to attempt to constrain the inversion with discrete magnetic susceptibility data.

## 2.5.2 Adding Boundary Conditions

The first step in constraining an inversion is to apply the information known from physical measurements to the problem. In this case, the physical measurements are magnetic susceptibility readings from over 400 boreholes in the region (**Figure 2.8**). These measurements were collected at one metre depth intervals for a variety of vertical and angled boreholes. In order to account for non-vertical and deviated boreholes, these measurements are taken as data points and binned into their respective cells based on their x, y and z locations. Each cell that contained more than one measurement was then averaged over all measurements whose locations lied within the 25x25x10 metre cell. The averaged results produce a three-dimensional representation of the susceptibility values that includes every cell in the mesh, even if the cell value is zero (**Figure 2.9**). It is important to note that the susceptibility model contains the measurements averaged over ten metre intervals of depth due to the resolution of the mesh. Cells that did not contain any measurements were left null at this stage.

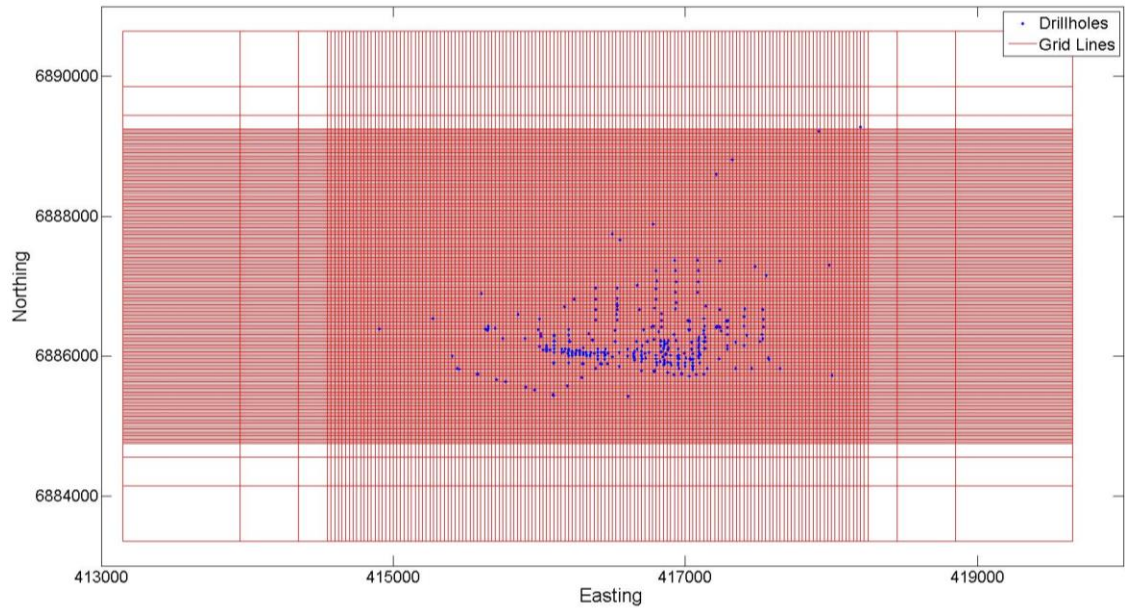


**Figure 2.8: Mesh grid in the x and y directions and the locations of the drillholes. Drillhole locations from Avalon Rare Metals (2014). Northing and Easting are shown on the axes (UTM).**

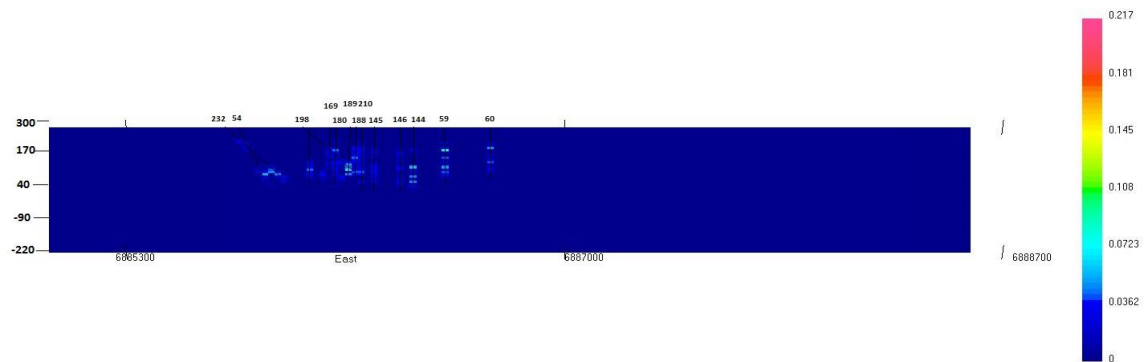


**Figure 2.9: An N-S sample cross-section of the three-dimensional model created by binning magnetic susceptibility measurements. Units on the right side represent susceptibility in SI units. Scale on the left is elevation above sea level (ASL) in metres. Drillholes numbers are labelled and their approximate orientation within the model are shown (Avalon Rare Metals, 2014). Note the scaling with maximum values at approximately 0.217 SI.**

The magnetic susceptibility reference model can be used in several different ways to constrain the data. The model can be included as an input to the inversion as a reference model described in **Equation 2** as  $\kappa_0$ , causing the inversion process to attempt to find a model as close to the given reference model as possible; this approach normally is used if the data are considered extremely reliable (*UBC-GIF*, 2013). The reference model can be supplemented by an active cell matrix, which provides the program an estimate of the reliability of the values within each cell. The active cell matrix is an input file in the same format as the model file and tells the program whether the cells are known or not and whether they should be included in the calculation of the objective function. In this initial constrained inversion, the three-dimensional model was used as a reference model, along with an active cell matrix identifying all cells containing data; these accurate measurements were incorporated in the calculation. However, the method produced an inversion that did not converge to a model that fit all of the given criteria within certain error bounds. The lack of convergence likely is due to the combination of not allowing the data points any margin for error and the loss of resolution that occurred when binning the magnetic susceptibility measurements into the mesh cells. Since reducing the cell size further would cost too much computational power, the best option is to allow the data cells a range to account for error and loss of resolution.

In order to allow a range in measured data, maximum and minimum boundary input files are used. These files contain data in each cell, similar to the model file but in this case with each cell containing a ceiling or floor for the possible solution for that cell (Lelièvre et al., 2009). Adding 0.2 to each model cell where there is a value establishes a maximum boundary file and subtracting 0.2 from each model cell with data makes a

minimum boundary file. Each valued cell therefore has  $\pm 0.2$  susceptibility, and all cells that did not contain data were given a large range with a standard minimum value of 0 and a maximum of 0.6 to avoid the model predicting unrealistically high susceptibilities. Upon utilizing these boundary conditions for the inversion, as well as using the three-dimensional model as a starting model, a result similar to that of the unconstrained inversion is obtained (**Figure 2.10**).

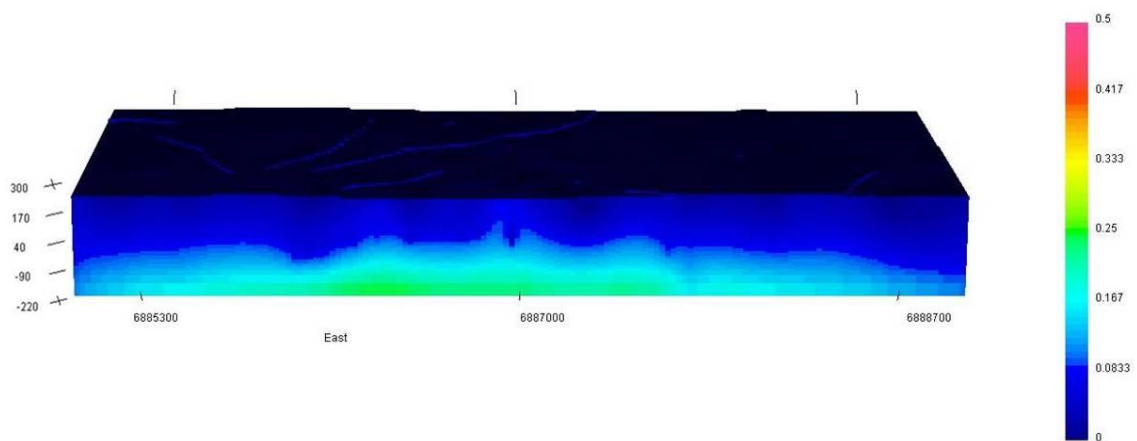


**Figure 2.10: Magnetic inversion constrained using maximum and minimum boundaries derived from borehole susceptibility measurements (N-S line 416550 Easting (UTM), looking west). Units on the right side represent susceptibility in SI units. Scale on the left is elevation above sea level (ASL) in metres.**

As in the case of the unconstrained inversion, a large anomaly with susceptibilities larger than those of the anomalous cells in the three-dimensional model appears at the maximum depth. Since this large anomaly occurs even with boundary conditions implemented, it suggests that there must be large signal from deep within the subsurface interfering with the shallower signal that is the primary interest of this study. Thus the

identification and removal of this deep-seated signal is necessary before a reliable resulting model can be obtained.

### 2.5.3 Upward Continuation

Deeper anomalies that influence the data are characterized by longer wavelength signals. Consequently, in order to remove the large excess long wavelength signal, some wavenumber filtering must be applied. The wavenumber is defined by:

$$k = \frac{2\pi}{\lambda} \quad (3)$$

where  $k$  is the wavenumber and  $\lambda$  is the wavelength (*Blakely, 1995*). A process called upward continuation can transform the field measured from one surface into a field as measured from another surface. This is useful because smaller wavelength signals are attenuated over shorter distances than longer wavelength signals, so increasing the distance between the measurement and the surface will attenuate the larger wavenumbers (*Blakely, 1995*). The data can be continued upward to identify smoother, deeper signals in the data. While it may seem that this is contrary for the problem at hand, where shallow features are of interest, this methodology also can be used to filter out the smaller wavenumber, larger wavelength signals.

The continuation itself is a complex process of adjusting the potential field to a new height and integrating it over the  $x$  and  $y$ -dimensions. This process can be simplified by transforming the problem to the Fourier domain. By converting the data to the frequency domain, the upward continuation can be carried out by multiplying it by a filter operator:

$$T(u, v) = e^{-\Delta z |k|}, \quad \Delta z > 0 \quad (4)$$

where  $\Delta z$  is the positive value by which the data will be upward continued in the  $z$ -dimension and  $k$  is the wavenumber (*Blakely, 1995*). Downward continuation is not easily implemented. From this equation, a negative  $\Delta z$  would result in larger wavenumbers being amplified rather than attenuated. However, while the smaller wavelength signal is of interest here, it is important to note that any noise will be contained in the smaller wavelengths as well and therefore also will be amplified. Depending on the noise, this can result in the process becoming unstable. For this reason, it is a much simpler problem to first upward continue the data to obtain the larger wavelength signal, and then subtract this signal from the original data to filter it out. The results of this transformation are shown in **Figure 2.11**.



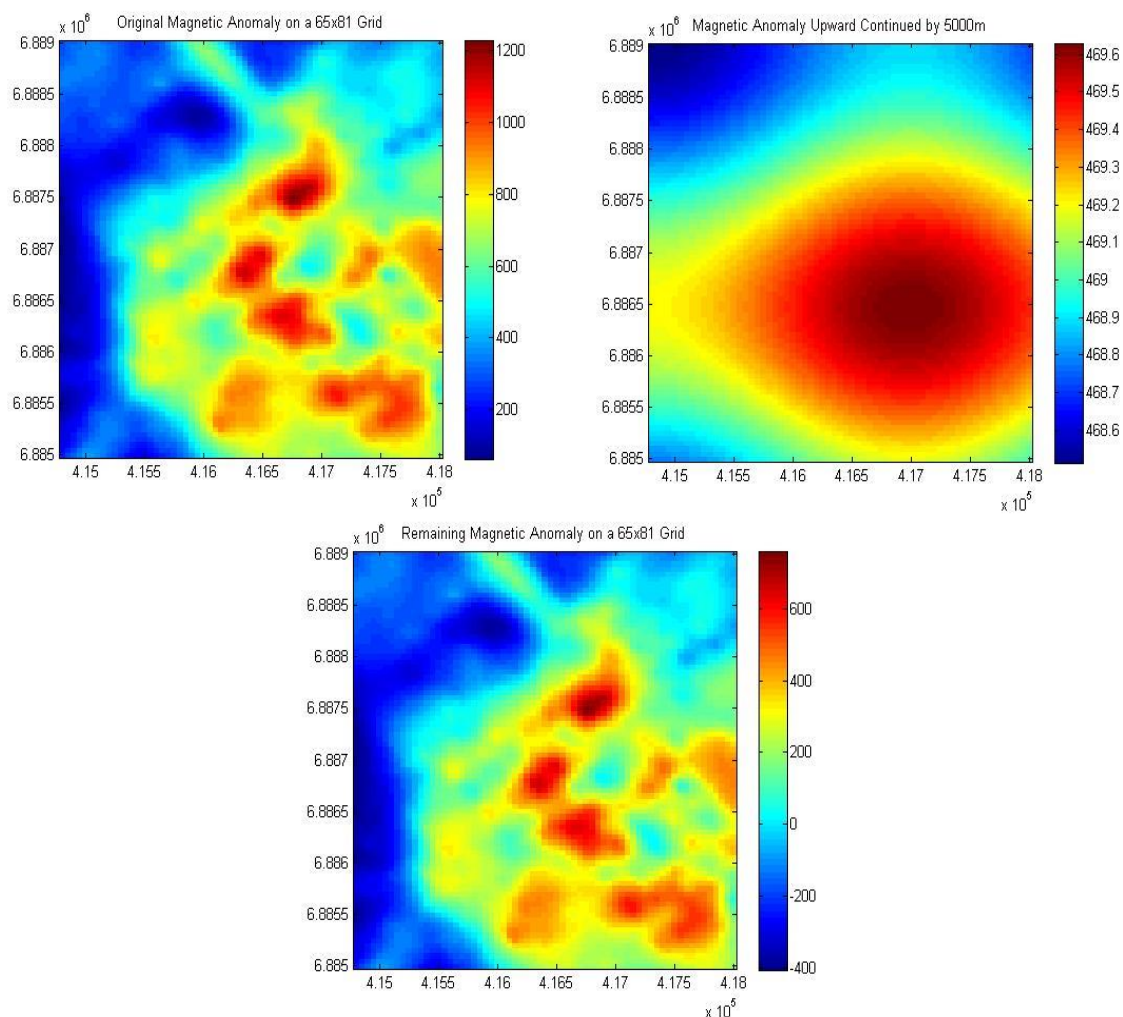


**Figure 2.11: Plan view of the inversion area showing transformation of data from the subtraction of upward continued data. Top left is the original anomaly data, top right is the upward continued data and the bottom right is the residual data. Note the different scales; all in nanoTeslas.**

This downward continuation produces a dataset that contains the same features as the original, but with a large decrease in amplitude. Maximum susceptibilities have gone from approximately 1200 to 750 SI units. In the upward continued dataset (before subtraction) there is some evidence for cycle wrap-around associated with the Fourier transform. This aliasing is likely due to undersampling of data which causes high

frequency signals to wrap around producing multiples of the signal (*Pratt, 2015*).

However, the magnitude of this wrap-around was deemed to be small enough to have a negligible effect on the inversion.

The resultant dataset was then used in place of the original dataset, along with the mesh, elevation, and boundary input files in an inversion. This next iteration of the inversion process can be seen in **Figure 2.12**. Successful implementation of the upward continuation process leads to removal of the large, smooth anomaly at the bottom of the model. The resulting features resemble the structures expected from the local geology in the subsurface in this region. Most of the large susceptibility cells lie on a sub-horizontal plane that ranges from approximately 100 metres below sea level to 50 metres above sea level. While more reflective of the known geology than the result of the previous constrained inversion, this model still has room for improvement as the anomaly appears discontinuous and choppy, more than expected from the geological setting. However the model is converging to a more geologically appropriate representation of the smaller scale features after filtering. The weighting coefficients mentioned above could produce a smoother, more continuous model and provide a more accurate and detailed result.

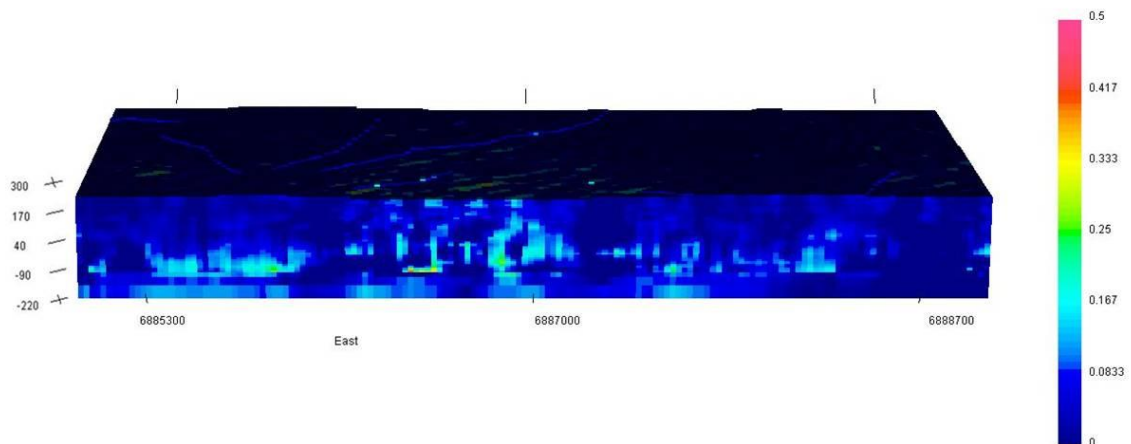


**Figure 2.12: Magnetic inversion of the Thor Lake region with long wavelength signal subtracted and upper and lower bounds applied (N-S line 416550 Easting (UTM), looking west). Units on the right side represent susceptibility in SI units. Scale on the left is elevation above sea level (ASL) in metres.**

#### 2.5.4 Gradient Attenuation and Enhancement

Adaptations to the model by adjusting the weighting function in each direction can enhance large changes in magnetic susceptibility and thus, potential lithology changes, while smoothing regions of homogenous lithology to allow for a more geologically plausible model. This method, developed by Lelièvre et al. (2009), relies on a reasonably accurate starting model. The gradient is calculated at each cell within the current best model in all three dimensions. Weighting model files then are created for each dimension separately, assigning weighting values that are inversely proportional to the magnitude of the gradient at that cell. Cell volumes exhibiting high gradients are given lower weighting values, to allow the model to be less smooth, resulting in abrupt changes in magnetic susceptibility in these regions during the inversion and simulating cleaner lithological contacts in the model. Volumes with low gradient suggest a common

lithology, leading to these regions being smoothed by higher weighting values (*Lelièvre et al.*, 2009). This is an iterative process where the weighting file is calculated after each inversion and then used in the subsequent inversion.

Input files for these inversions include the model from the previous iteration (used as a starting model), the weighting file calculated from said model, the traditional mesh used in all inversions as well as the standard data and elevation files. A preliminary result after the third iteration can be seen in **Figure 2.13**.

From the gradient smoothing technique, the model has become noticeably less discontinuous. In regions where the anomaly once appeared choppy, it is now smoother and bears a closer resemblance to the continuous structure expected based on the geological setting. Additional iterations in this manner could prove to be an excellent way to allow the model to better reproduce the actual geological conditions that occur in the subsurface.

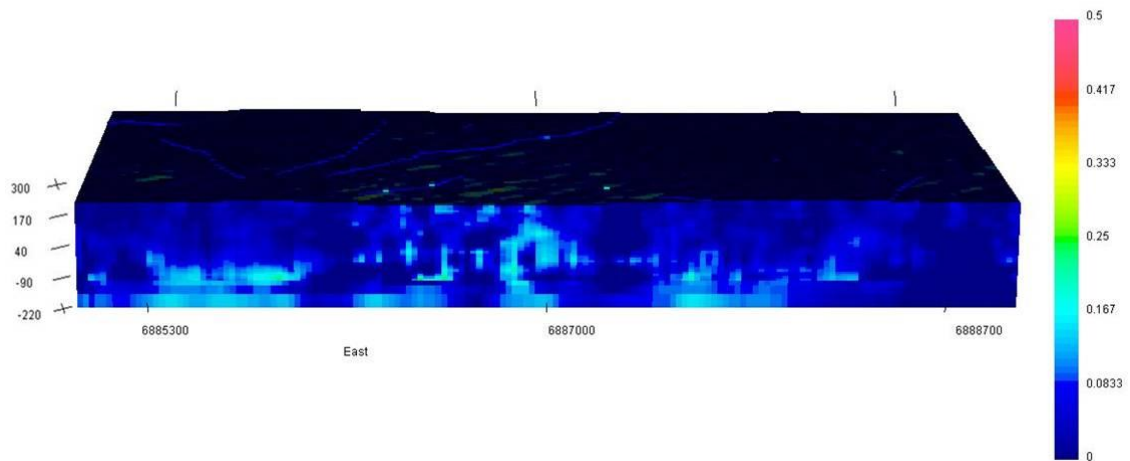


**Figure 2.13: Magnetic model (N-S line 416550 Easting (UTM), looking west) with three iterations of gradient enhancement and attenuation. Units on the right side represent susceptibility in SI units. Scale on the left is elevation above sea level (ASL) in metres.**

## 2.6 Geological Interpretation and Implications

In order to assess the validity of a model obtained from an inversion, forward modeling was used to calculate an estimated data field using the model. This field then was compared to the original data in order to get a prediction of how well the new model truly fits the data. **Figure 2.14** shows the original data compared with predicted data from the best inversion to date as well as the residuals. In analyzing the residuals, the data fits within approximately  $\pm 5$  nanoTeslas everywhere in the region of interest. It is also important to note that the distribution of these differences is relatively random throughout the region and does not have a coherent spatial pattern. The lack of a spatial pattern implies that the inversion is not systematically biasing susceptibilities in certain parts of the region, but represents random error.

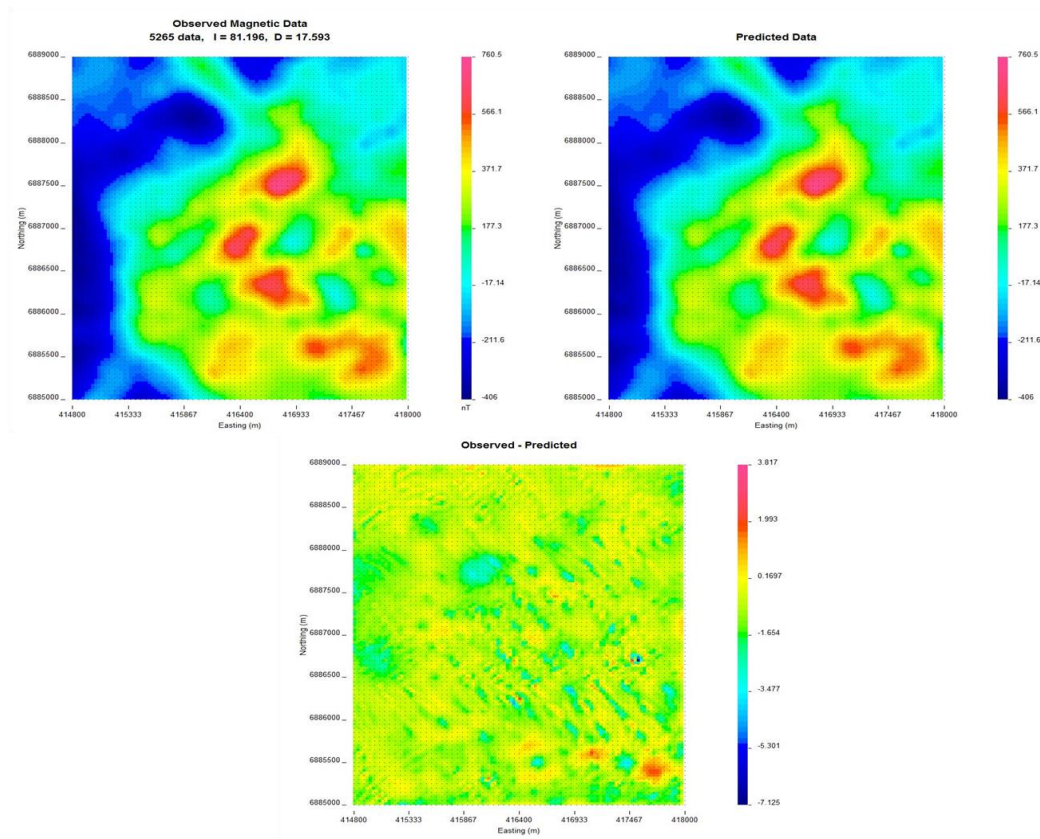


**Figure 2.14: Plan view of the inversion area comparing the data (a) to the forward modeled data from the model (b). The residuals at the bottom (c). Units are in nanoTeslas.**

The model shows a sub-horizontal layer of high magnetic susceptibility that ranges in depth between approximately 200 metres above sea level to sea level (0 metres) (**Figure 2.15**). This anomaly is located near the centre of the inversion area in the vicinity of Thor Lake and appears to extend laterally for approximately 2500 metres along the north-south line at 416550E. While the anomalous body is not laterally continuous in its entirety, there is an overall flat-lying trend. The lateral continuity could be improved by implementing smoothing in the horizontal directions. The anomaly also forms a gently sloping dome-like structure which could represent the expected form of the NNS. The

magnetic susceptibilities tend to increase with depth until they reach the sub-horizontal structure, after which they start to decrease gradually. This reinforces geological studies that suggest increasing mineralization of iron-rich alteration minerals, such as magnetite, with depth to the bottom of the basal zone, followed by a gradual decrease. This implies that the largest susceptibility layer is, in fact, the basal zone where higher proportions of HREE are associated with magnetite (Sheard *et al.*, 2012).

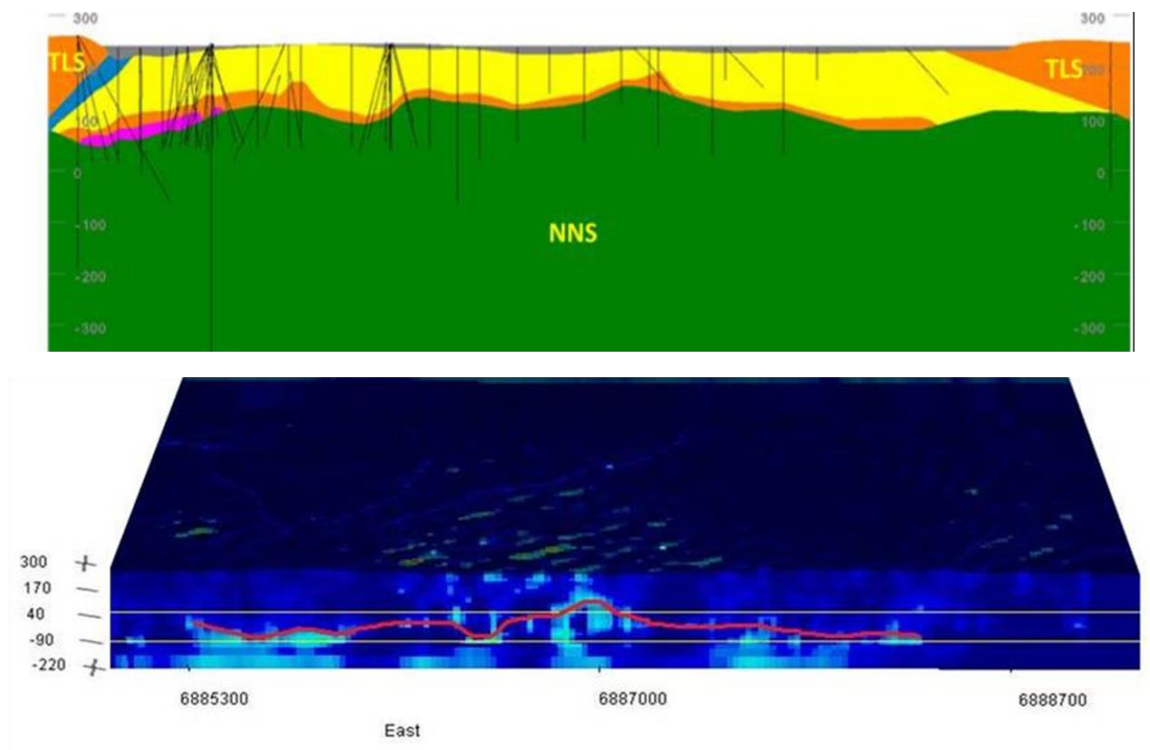


**Figure 2.15: Comparison of the current geological model (top, along line 416800 Easting (UTM), looking west) with the best magnetic geophysical model (bottom, along line 416550 Easting (UTM), looking west). The red line in the magnetic model is an early delineation of the deposit. Yellow lines are to indicate depth intervals. Units on the right side represent susceptibility in SI units. Scale on the left is elevation above sea level (ASL) in metres. Geological model adapted from Ciuculescu *et al.*, 2013.**

Comparing these results with the current geological model, the depths and approximate structure of the anomaly coincide reasonably well with the basal zone top and bottom layers (**Figure 2.15**). The approximate depths to the inferred basal zone of 30-220 metres coincide with the thicknesses of the alteration zone estimated from current exploration methods to be between 80 and 200 metres. However, the lateral extent of the deposit towards the north direction appears to extend farther under the hanging wall of the Thor Lake Syenite than predicted by the current exploration methods (**Figure 2.16**). While these results are preliminary, the potential for future constraint of this northern edge could provide better estimates of additional mineralization in this direction. The model also shows additional magnetically susceptible regions which are deeper than the defined mineralized zone in the NNS. Although these could be artifacts in the model that may be removed by further constraints, they could be signal produced by packages of abundant mineralization of iron oxides. A third possibility is that they are produced by underlying aegirine nepheline syenite which is apparent in the drillhole logs. Due to lack of constraining measurements beneath the basal zone, the deeper, long wavelength signal is difficult to model with sufficient confidence. Another data source such as gravity measurements could help determine whether these anomalous cells are indeed artifacts or caused by subsurface geology.



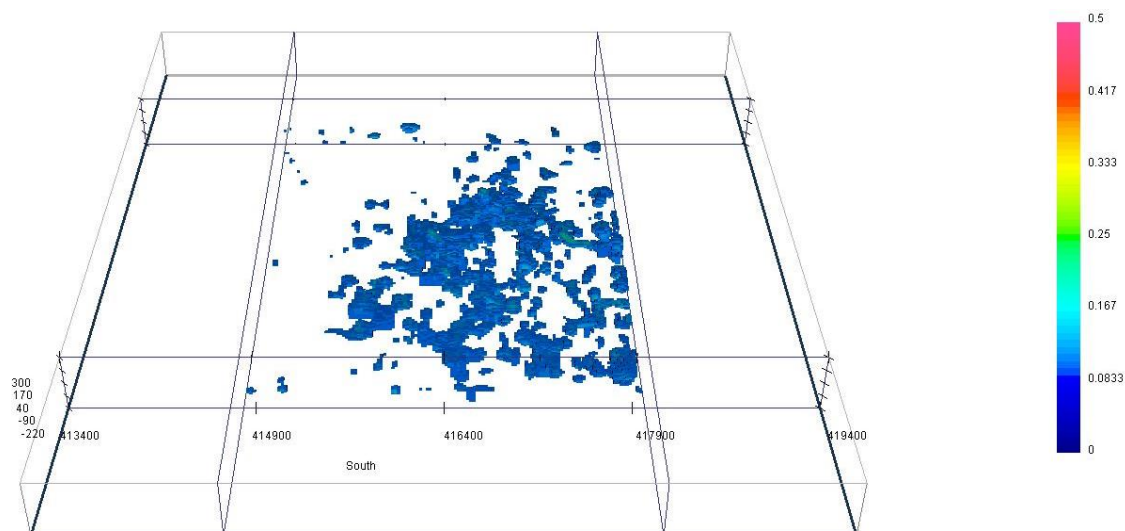


**Figure 2.16: A projection looking north of a smoothed isosurface of the high susceptibility region displaying all cells that have susceptibilities greater than 0.1 SI to show the lateral extent. Note that even with smoothing, the model is still somewhat discontinuous. UTM Eastings are labeled along the bottom while elevation in metres ASL are labeled on the left side. Units on the right side represent susceptibility in SI units.**

While the current best model does not show clear indications of the dykes known to be in the area, complex structural features may become apparent with the implementation of another data source. There are some shallower features that could be glimpses of the north-east trending Hearne dykes, however there is not enough evidence at this point to infer this with any reliability. Strategic drilling has targeted dykes with some magnetic signature cross-cutting the deposit, however no signal within the model is clear enough to be designated a Hearne dyke. This could be caused, in part, by the horizontal cell dimensions of 25 metres in either direction averaging out the signal from these relatively narrow structural features into broader cells. On the magnetic dataset there is a northwest trending arm at the north end of the inversion field which is likely related to the Indin

dykes, known for their prominent magnetic signals (*Mumford and Cousens, 2014*). This could account for some of the apparent extra lateral extension of the deposit signature to the north within the model. There is a relatively strong signal further north and west of the cross-section shown that may be related to this dyke. Further modeling is necessary in order to conclude whether or not these signals are, in fact, related to that dyke. Cross sections of the best current geophysical model of the Thor Lake inversion study area are provided in the appendices.

## 2.7 Future Work

### 2.7.1 Gravity Implementation

The conclusions from this study could be tested by the implementation of gravitational field data. The association of iron-oxide alteration minerals with REE mineralization results in prominent magnetic signals produced within the deposit. However, this is not the only signal produced within the deposit that has the potential to be better characterized. The inversion region also contains a spike in the vertical component of the gravitational field. This signifies that there is excess mass caused by a high density body in this region, likely associated with the higher density cumulate minerals which contain the REE. Gravity inversions of the region could provide some insight into the subsurface geology, as changes in density would represent potential lithology differences that may not be accompanied by a change in magnetic susceptibility. For this reason, the next step in this research is to investigate the anomalous gravity signal and invert for a density contrast model. This can be carried out with UBC-GIF's grav3d program which works very similarly to mag3d. While no extensive modeling has been completed on this aspect

yet, a preliminary model without any constraints or boundary conditions has been obtained (**Figure 2.17**).

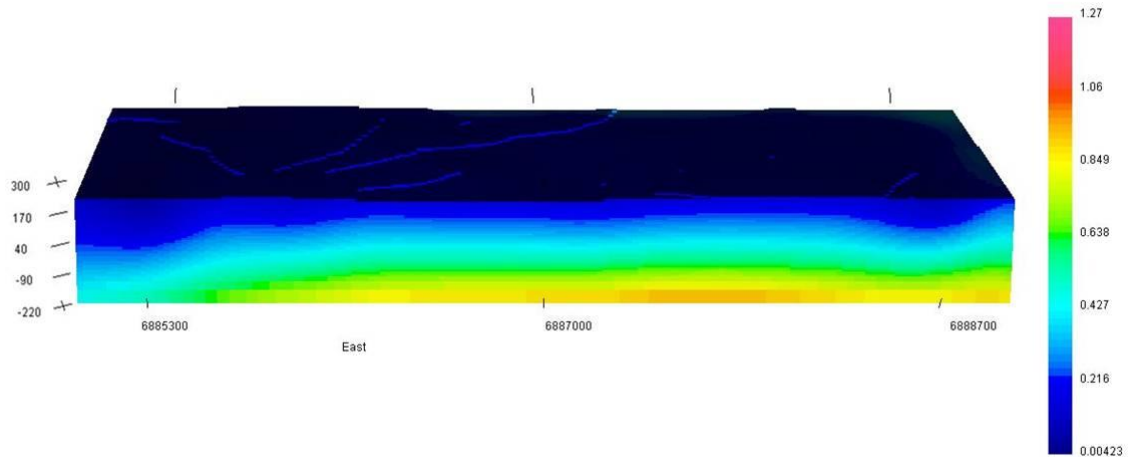


**Figure 2.17: A preliminary gravity model of the Thor Lake region with no constraints at N-S line 416550 Easting (UTM), facing west. Units are in  $\text{g/cm}^3$  density contrast. Scale on the left is elevation above sea level (ASL) in metres.**

Similar to the first magnetic inversion, the model shows a high density anomaly in the deepest cells in the centre of the model. Again, this likely is caused by lack of constraining parameters, resulting in the simplest possible model that fits the long-wavelength signal. However, a new problem arises that was not encountered in the magnetic inversions; the lack of physical measurements to constrain the inversion. The magnetic inversions could be constrained using borehole magnetic susceptibility measurements, so a similar workflow will be necessary for a gravity inversion.

Future study on creating a density model will assess the validity of using a gradient enhancement and attenuation technique to use the current best magnetic model to constrain a gravity model. The methodology behind this approach remains the same as

the smoothing technique used in magnetic modeling. By enhancing the gradient in regions of potential lithological contacts, it will allow for sharp density contrasts. Attenuating the gradient in regions of constant lithology can encourage constant densities throughout those cells (*Lelièvre et al.*, 2009). If successful, the gravity model could prove to be extremely beneficial to the current magnetic model through cooperative inversion methods.

### 2.7.2 Joint Inversion

The idea behind joint or cooperative inversion is to sense the Earth in as many ways as possible and incorporate this into one accurate model. Different types of geophysical surveys are able to sense different characteristics of the true subsurface to different degrees of accuracy (*Lelièvre et al.*, 2009). For example, magnetic field data can sense high concentrations of magnetic elements beneath the surface while gravitational field data can sense high or low density rock types. In some cases, these anomalous densities can occur within the same rock type that contains magnetic elements. However, a magnetic anomaly can be caused by a completely different rock type than those that result in a gravitational anomaly. For this reason, a wider range of geophysical data results in a more integrated view of the subsurface.

Implementation of a density model into the current susceptibility model is a direct extension of the gradient work completed in magnetic smoothing processes. The method developed and implemented by Lelievre et al. (2009) to combine the lateral efficiency of gravity inversions with the depth efficiency of tomography inversions. The end goal of this study is to implement such a technique by adding and normalizing gradients from

meaningful density and susceptibility models and using these to inversely determine the smoothing weights in subsequent inversions.

### 2.7.3 Caribou Lake

Thor Lake is one of two regions of interest due to the mineralization within the Nechalacho site. The other is located at Caribou Lake, to the west of Thor Lake. The Caribou Lake gabbro, located in the western lobe of the BLC, is a host for Cu-Ni-PGE mineralization (*Mumford, 2013*), and can be seen in the airborne magnetic field survey (**Figure 2.3**) as the prominent anomaly to the west. Upon completing the inversions for the Thor Lake region, a similar workflow will be extended to Caribou Lake. Gravity and magnetic anomalies are expected to assist in the identification of mineralization in this area. However gravity is the preferred dataset due to the potential for remanent magnetization associated with these deposits (*King, 2007*).

## 2.8 Conclusions

Thus far, magnetic field inversion has proved to be a useful tool for subsurface mapping of the Nechalacho deposit at Thor Lake. To date, the overall structure of the best three-dimensional models appears to be a flat lying, highly magnetic deposit with the largest signals up to depths of approximately 200 metres beneath the surface. This agrees well with the understood subsurface geology. Laterally, the inversions show higher susceptibilities extending further to the north, suggesting that there may be possible extensions of the magnetite-bearing alteration zones associated with REE mineralization. The models also show potential evidence for the Hearne dykes that are known to cross-cut the deposit, although the east-northeast trending anomalies currently cannot currently

be traced clearly enough to make any such conclusions at this time. The magnetic field data also shows clear indication of a northwest trending dyke associated with the Indin swarm. This dyke could be the cause of the increased magnetic susceptibilities to the north, although there is some indication that it also appears in the model further to the northwest. Cooperative inversion with the gravity dataset is expected to help define those features that cannot be clearly delineated from the magnetic models.

## 2.9 References

- Aster, R. C., Borchers, B., and Thurber, C., 2004.** Parameter Estimation and Inverse Problems. Academic Press, Oxford, UK, 355p.
- Avalon Rare Metals Inc., 2014.** Lithology and Magnetic Susceptibility Data. Prepared by Ben Webb.
- Blakely, R. J., 1995.** Potential Theory in Gravity and Magnetic Applications. Cambridge University Press, Cambridge, UK, 464p.
- Ciuculescu, T., Foo, B., Gowans, R., Hawton, K., Jacobs, C., and Spooner, J., 2013.** Technical Report Disclosing the Results of the Feasibility Study on the Nechalacho Rare Earth Elements Project. Micon International Limited, Toronto, Canada, 307p.
- Davidson, A., 1978.** The Blatchford Lake Intrusive Suite, an Aphebian Plutonic Complex in the Slave Province, Northwest Territories; Paper 78-1A, Geological Survey of Canada, Ottawa, p. 119-122.
- King, A., 2007.** Review of Geophysical Technology for Ni-Cu-PGE Deposits; Proceedings of Exploration 07: Fifth Decennial International Conference on Mineral Exploration, p. 647-665.
- Lelièvre, P. G., Oldenburg, D. W., and Williams, N. C., 2009.** Integrating Geological and Geophysical Data Through Advanced Constrained Inversions; Exploration Geophysics, v. 40, p. 334-341.

**Mumford, T., 2013.** Petrology of the Blatchford Lake Intrusive Suite, Northwest Territories, Canada; PH.D., Carleton University.

**Mumford, T. R., and Cousens, B. L., 2014.** Constraints on the Relationships Between Paleoproterozoic Intrusions and Dyke Swarms, East Arm of Great Slave Lake, N.W.T., Canada; Canadian Journal of Earth Science, v. 51, p. 419-438.

**NRCan (Natural Resources Canada), 2011.** Blatchford Lake Grav-Mag Survey.

**Pilkington, M., Thomas, M. D., and Mumford, T. R., 2012.** Geological Significance of a New High Resolution Gravity Gradiometric and Magnetic Survey over the Blatchford Lake Complex, Northwest Territories; Open-File 7084, Geological Survey of Canada, Ottawa.

**Pinckston, D. R., and Smith, D. G., 1995.** Mineralogy of the Lake Zone, Thor Lake Rare-Metals Deposit, N.W.T., Canada; Canadian Journal of Earth Science, v. 32, p. 516-532.

**Pratt, G. R., 2015.** The Implications of Frequency Domain Modelling – Sampling and Wrap-Around; *in* Waveform Tomography: An Introduction to Theory and Practice, Western University, London, Canada, p. 39-44.

**Sheard, E. R., Williams-Jones, A.E., Heiligmann, M., Pederson, C., and Trueman, D. L., 2012.** Controls on the Concentration of Zirconium, Niobium, and the Rare Earth Elements in the Thor Lake Rare Metal Deposit, Northwest Territories, Canada; Economic Geology, v. 107, p. 51-104.

**UBC-Geophysical Inversion Facility, 2013.** A Program Library for Forward Modelling and Inversion of Magnetic Data over 3D Structures, version 5.0; Developed under the consortium research project, *Joint/Cooperative Inversion of Geophysical and Geological Data*, Department of Earth and Ocean Sciences, University of British Columbia, Vancouver, British Columbia.

**Verplanck, P. L., and Van Gosen, B. S., 2011.** Carbonatite and Alkaline Intrusion-Related Rare Earth Element Deposits – A Deposit Model; Open-File Report 2011-1256, U.S. Geological Survey, 8 pages.

## Appendices

The appendices contain cross sections of the best current geophysical model of the Thor Lake inversion study area. The scale on the right indicates magnetic susceptibilities in SI units. The left axis shows elevation in metres above sea level. Coordinates for the sections are all UTM Datum NAD 83, Zone 11N.



## Appendix A: Step-by-Step Cross-Sections Facing North

Appendix A contains cross sections at 200 metre intervals along UTM northing lines (east-west sections facing north), with each section spanning 3200 metres across. See figures A1-A20.

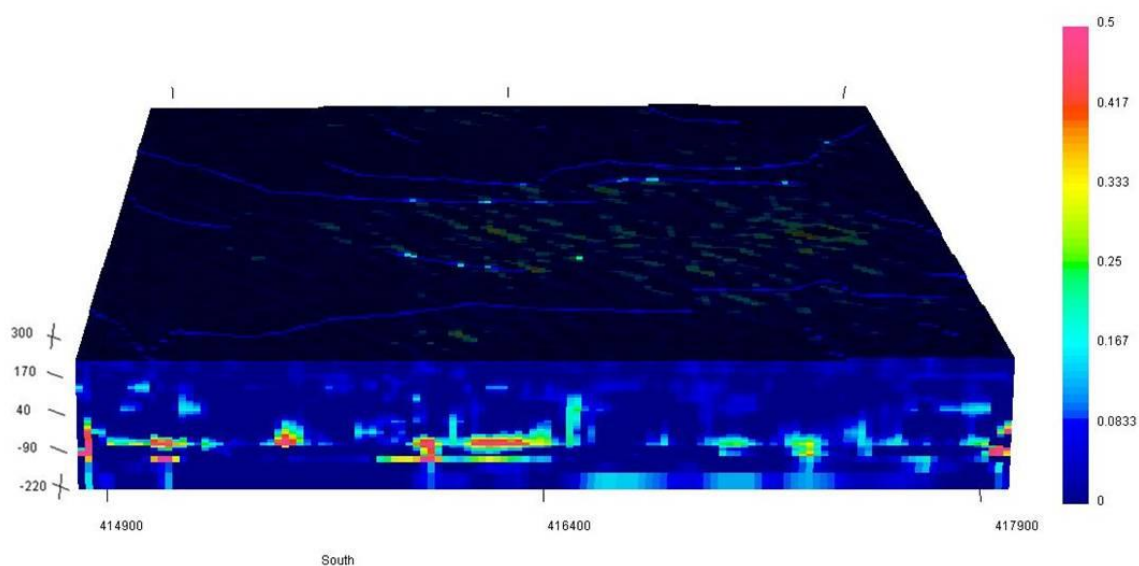


**Figure 2.18: Cross-section of the best current geophysical model along E-W line 6885000 Northing (UTM), looking north. Units on the right side represent susceptibility in SI units. Scale on the left is elevation above sea level (ASL) in metres.**

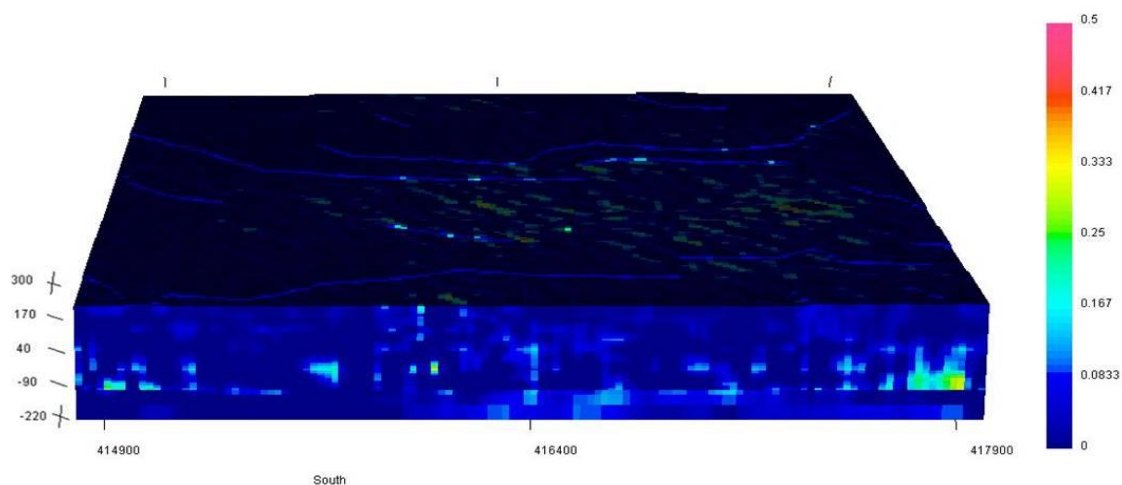


**Figure 2.19:** Cross-section of the best current geophysical model along E-W line 6885200 Northing (UTM), looking north. Units on the right side represent susceptibility in SI units. Scale on the left is elevation above sea level (ASL) in metres.

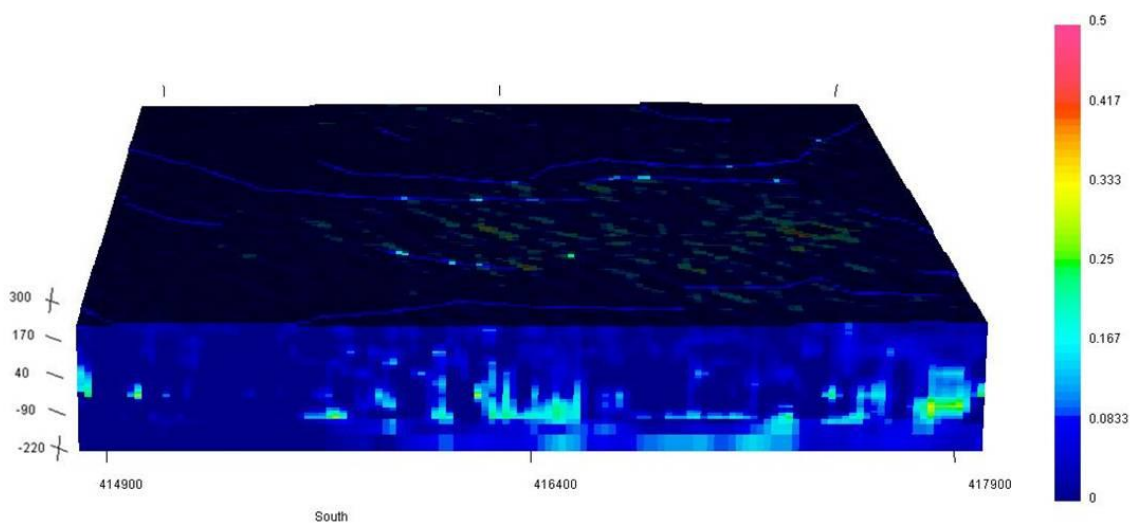


**Figure 2.20:** Cross-section of the best current geophysical model along E-W line 6885400 Northing (UTM), looking north. Units on the right side represent susceptibility in SI units. Scale on the left is elevation above sea level (ASL) in metres.

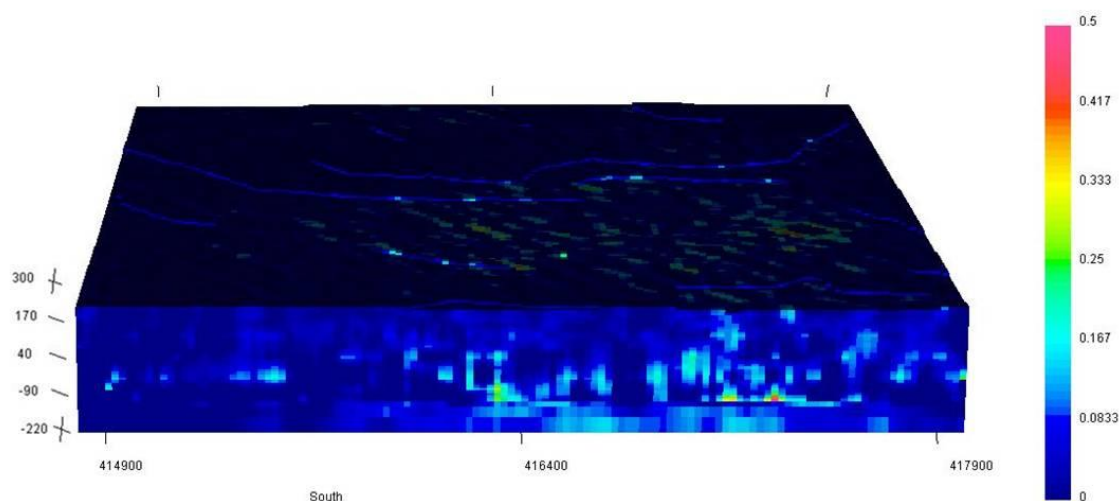


**Figure 2.21:** Cross-section of the best current geophysical model along E-W line 6885600 Northing (UTM), looking north. Units on the right side represent susceptibility in SI units. Scale on the left is elevation above sea level (ASL) in metres.

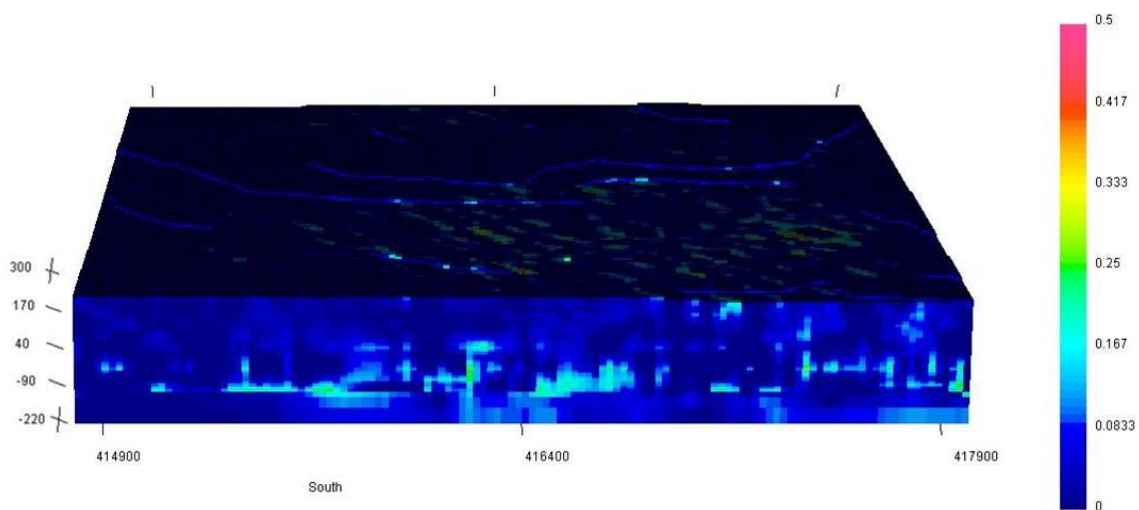


**Figure 2.22:** Cross-section of the best current geophysical model along E-W line 6885800 Northing (UTM), looking north. Units on the right side represent susceptibility in SI units. Scale on the left is elevation above sea level (ASL) in metres.

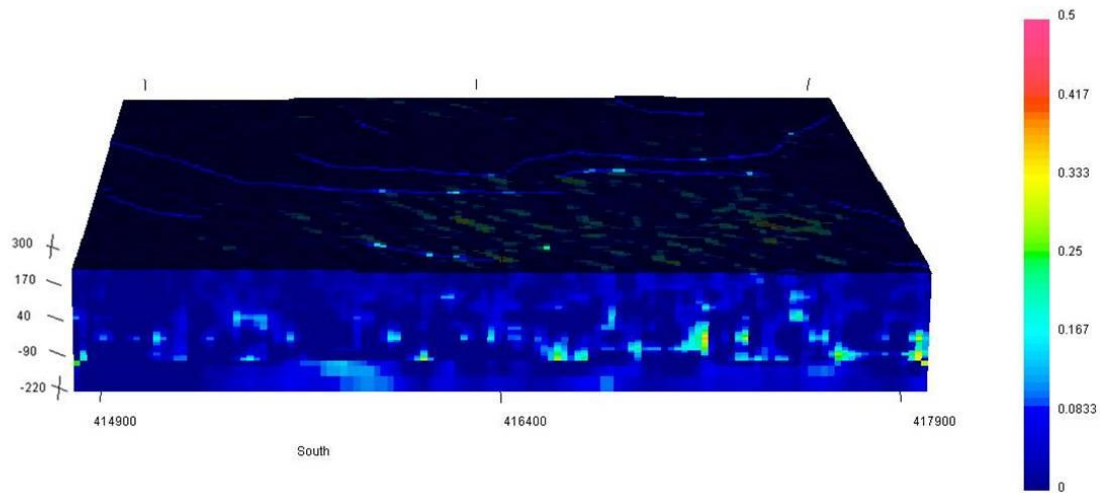


**Figure 2.23: Cross-section of the best current geophysical model along E-W line 6886000 Northing (UTM), looking north. Units on the right side represent susceptibility in SI units. Scale on the left is elevation above sea level (ASL) in metres.**

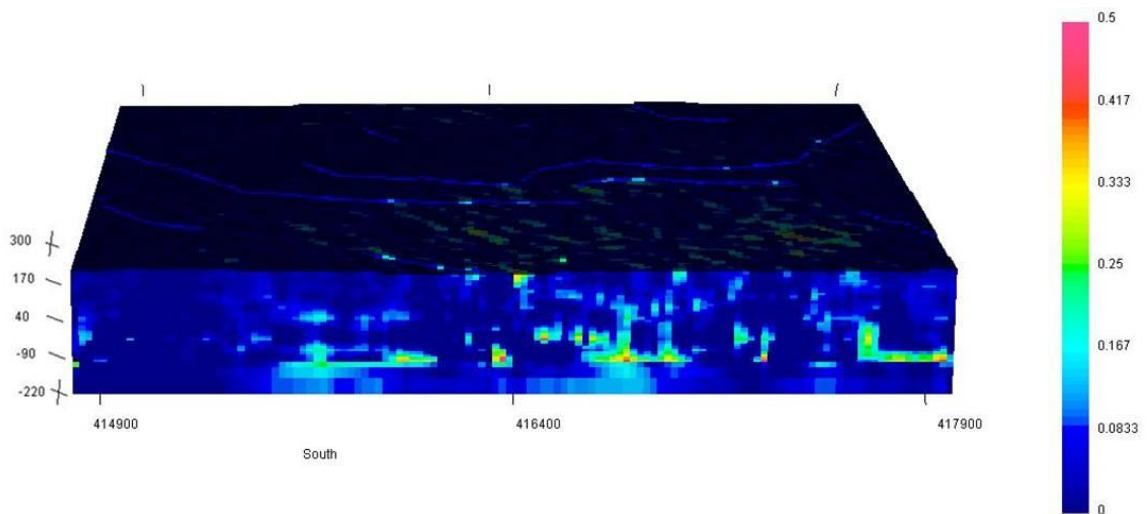


**Figure 2.24: Cross-section of the best current geophysical model along E-W line 6886200 Northing (UTM), looking north. Units on the right side represent susceptibility in SI units. Scale on the left is elevation above sea level (ASL) in metres.**

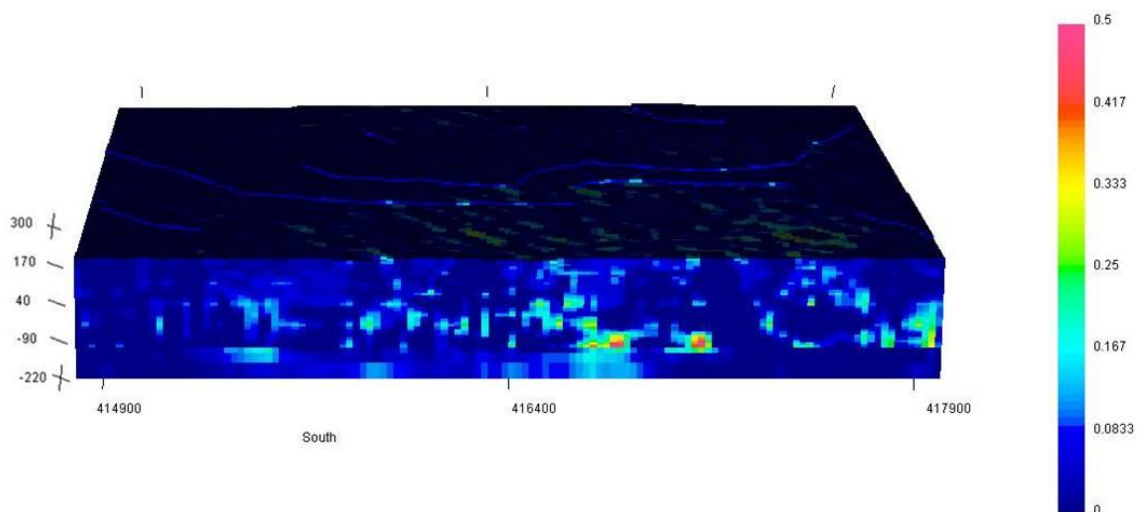


**Figure 2.25: Cross-section of the best current geophysical model along E-W line 6886400 Northing (UTM), looking north. Units on the right side represent susceptibility in SI units. Scale on the left is elevation above sea level (ASL) in metres.**

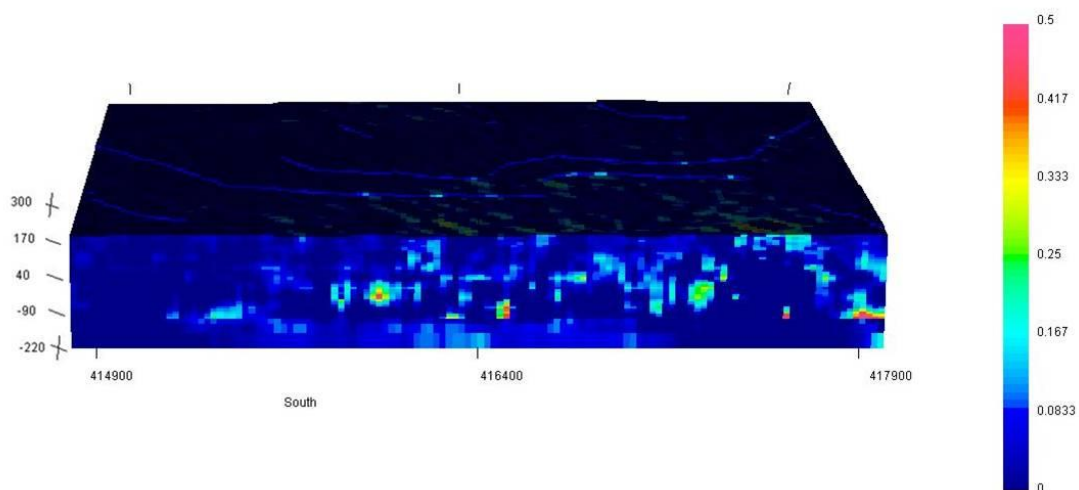


**Figure 2.26: Cross-section of the best current geophysical model along E-W line 6886600 Northing (UTM), looking north. Units on the right side represent susceptibility in SI units. Scale on the left is elevation above sea level (ASL) in metres.**

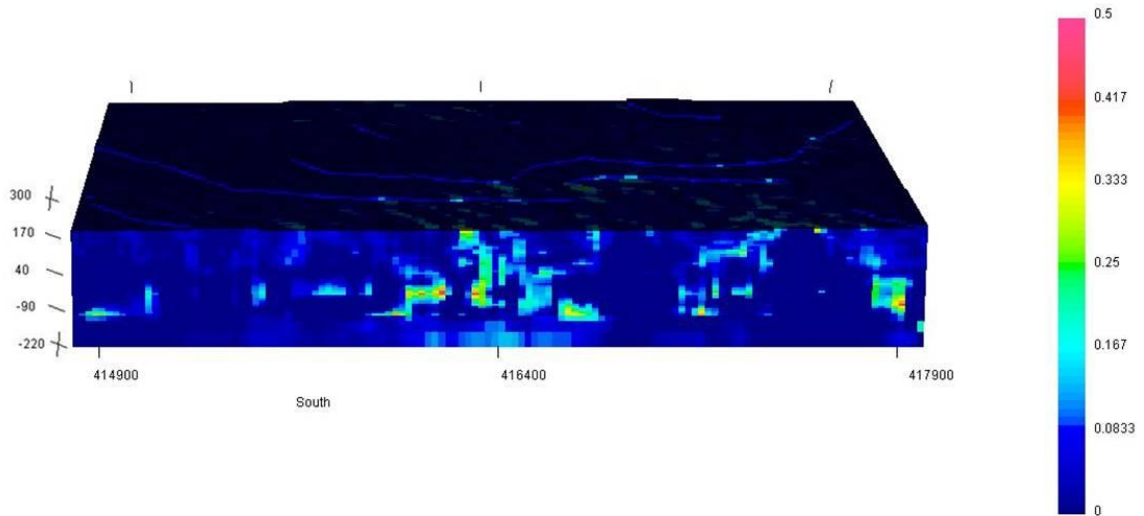


**Figure 2.27: Cross-section of the best current geophysical model along E-W line 6886800 Northing (UTM), looking north. Units on the right side represent susceptibility in SI units. Scale on the left is elevation above sea level (ASL) in metres.**

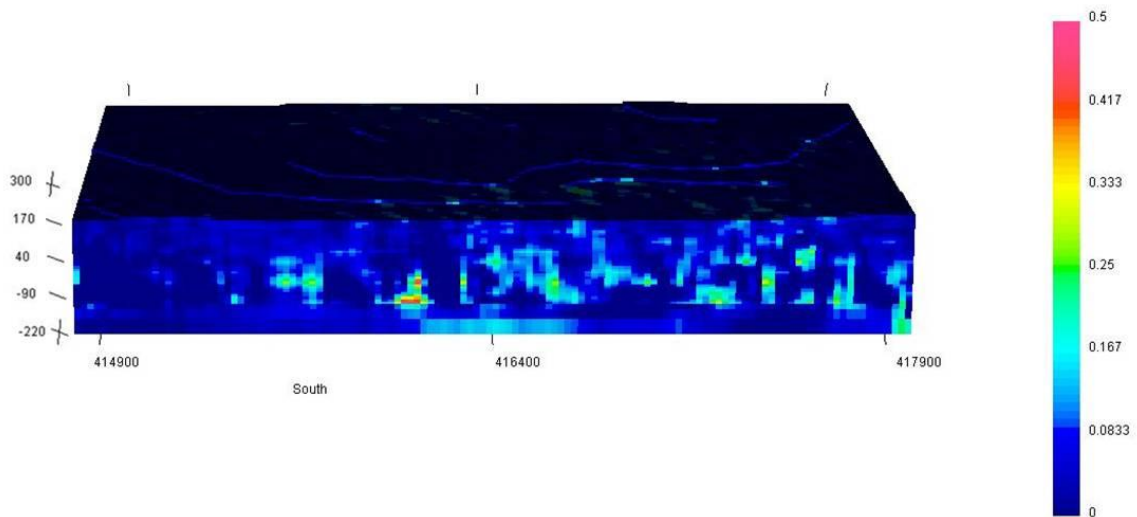


**Figure 2.28: Cross-section of the best current geophysical model along E-W line 6887000 Northing (UTM), looking north. Units on the right side represent susceptibility in SI units. Scale on the left is elevation above sea level (ASL) in metres.**



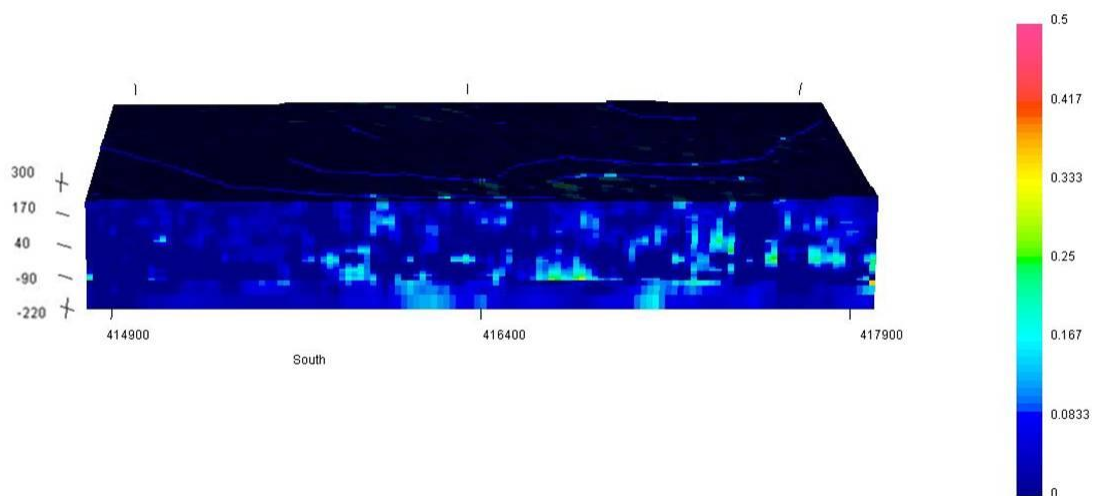


**Figure 2.29: Cross-section of the best current geophysical model along E-W line 6887200 Northing (UTM), looking north. Units on the right side represent susceptibility in SI units. Scale on the left is elevation above sea level (ASL) in metres.**

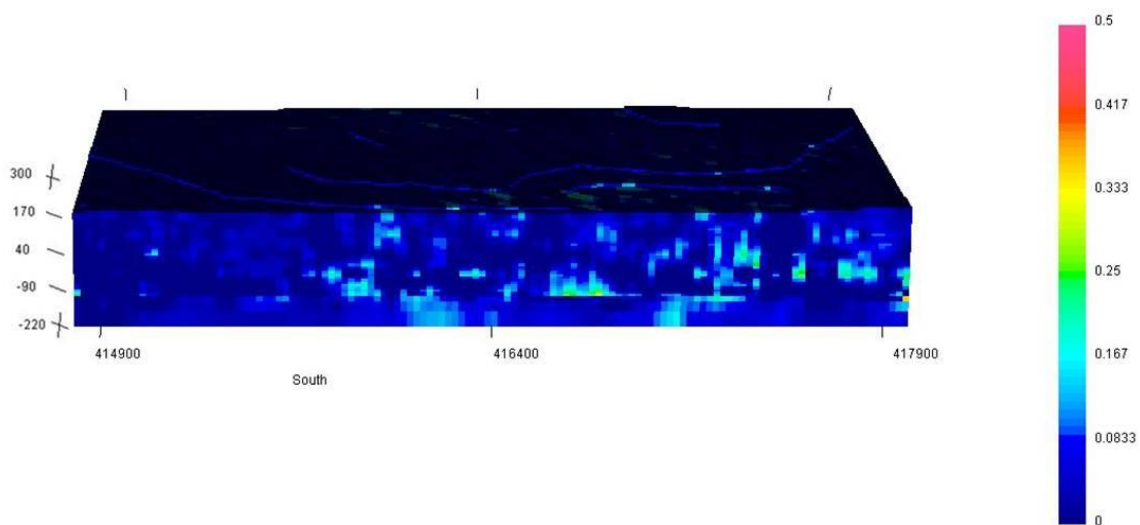


**Figure 2.30: Cross-section of the best current geophysical model along E-W line 6887400 Northing (UTM), looking north. Units on the right side represent susceptibility in SI units. Scale on the left is elevation above sea level (ASL) in metres.**

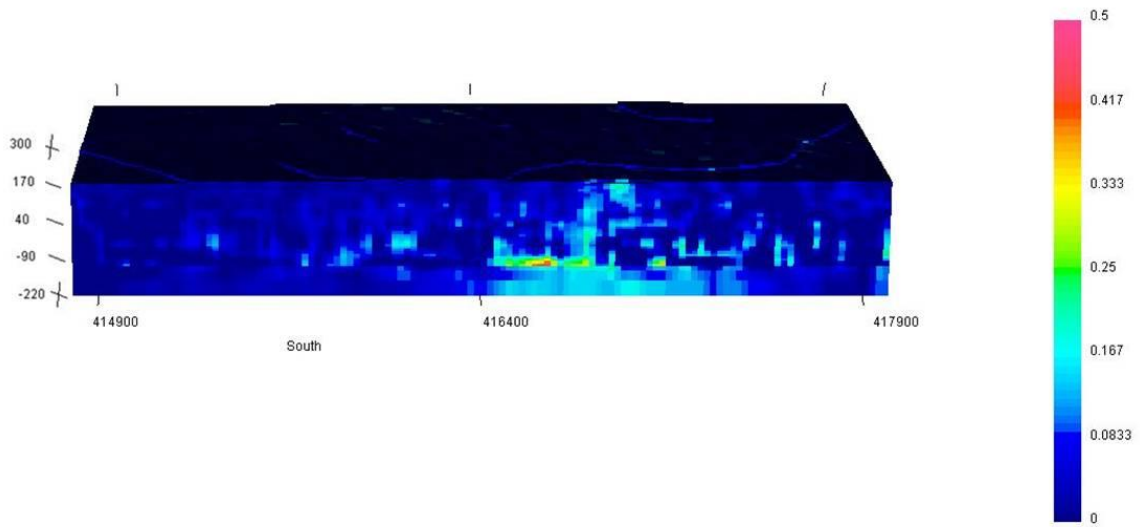


**Figure 2.31: Cross-section of the best current geophysical model along E-W line 6887600 Northing (UTM), looking north. Units on the right side represent susceptibility in SI units. Scale on the left is elevation above sea level (ASL) in metres.**

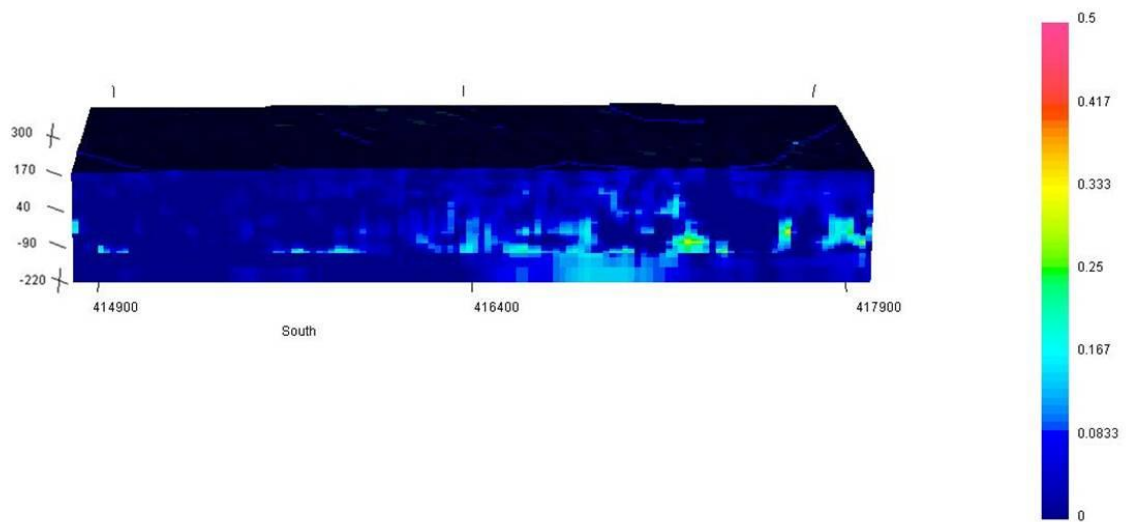


**Figure 2.32: Cross-section of the best current geophysical model along E-W line 6887800 Northing (UTM), looking north. Units on the right side represent susceptibility in SI units. Scale on the left is elevation above sea level (ASL) in metres.**



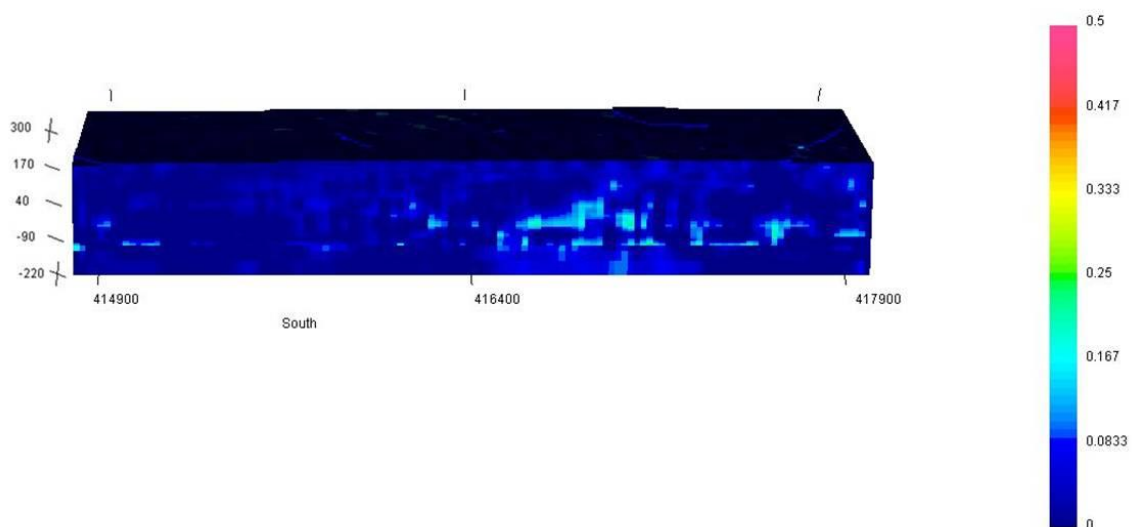


**Figure 2.33: Cross-section of the best current geophysical model along E-W line 6888000 Northing (UTM), looking north. Units on the right side represent susceptibility in SI units. Scale on the left is elevation above sea level (ASL) in metres.**

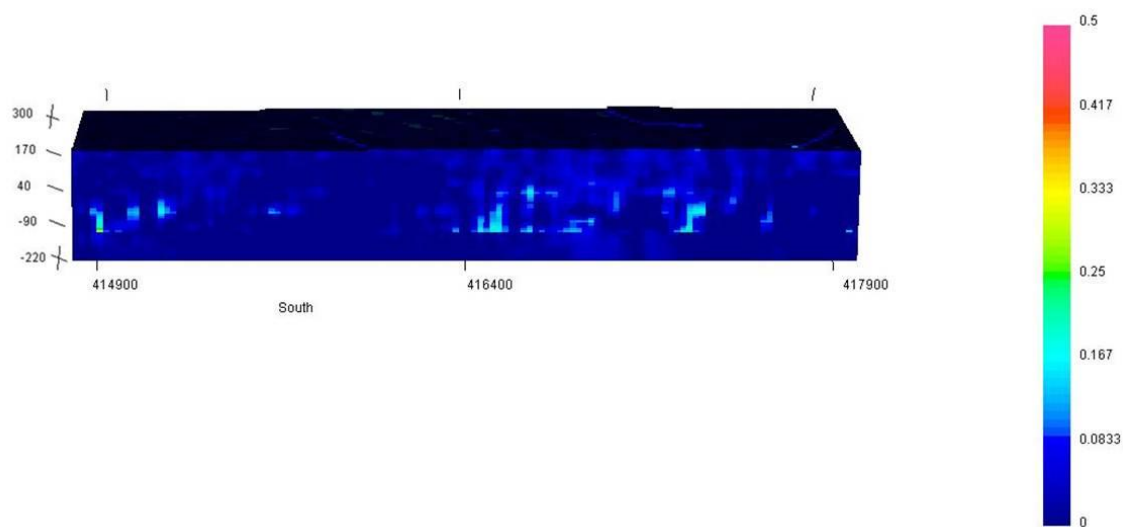


**Figure 2.34: Cross-section of the best current geophysical model along E-W line 6888200 Northing (UTM), looking north. Units on the right side represent susceptibility in SI units. Scale on the left is elevation above sea level (ASL) in metres.**

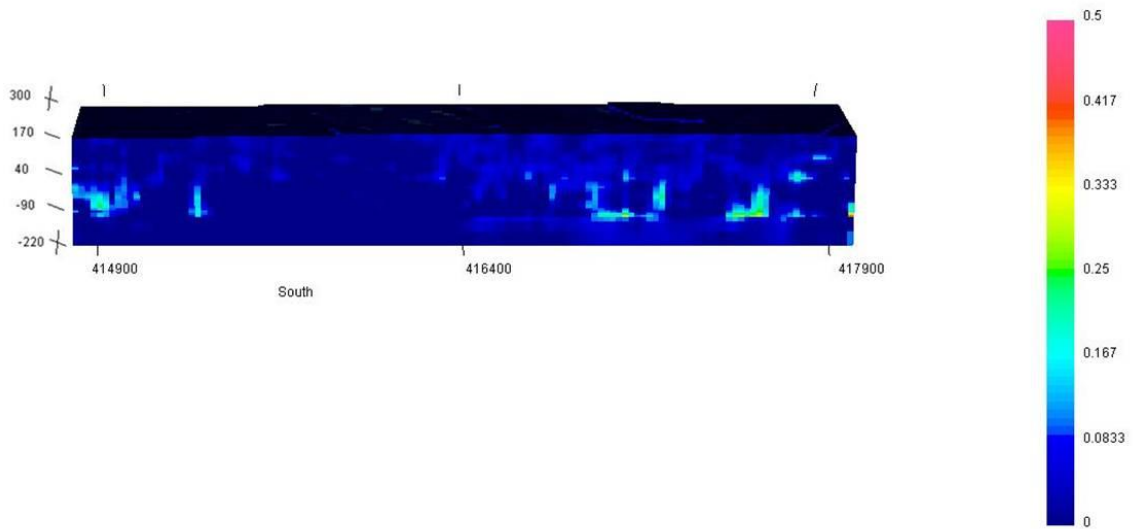


**Figure 2.35: Cross-section of the best current geophysical model along E-W line 6888400 Northing (UTM), looking north. Units on the right side represent susceptibility in SI units. Scale on the left is elevation above sea level (ASL) in metres.**

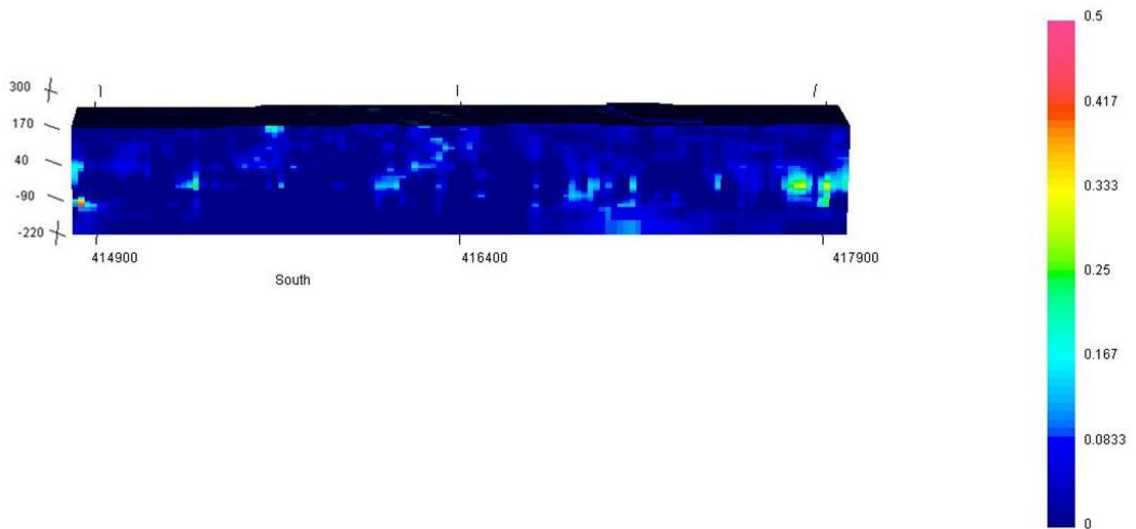


**Figure 2.36: Cross-section of the best current geophysical model along E-W line 6888600 Northing (UTM), looking north. Units on the right side represent susceptibility in SI units. Scale on the left is elevation above sea level (ASL) in metres.**

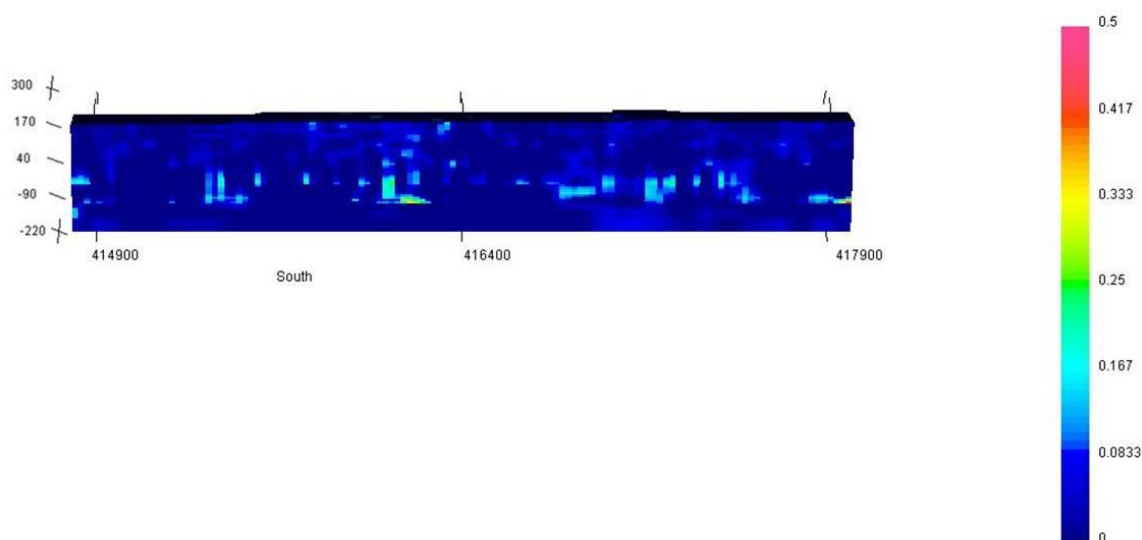


**Figure 2.37: Cross-section of the best current geophysical model along E-W line 6888800 Northing (UTM), looking north. Units on the right side represent susceptibility in SI units. Scale on the left is elevation above sea level (ASL) in metres.**

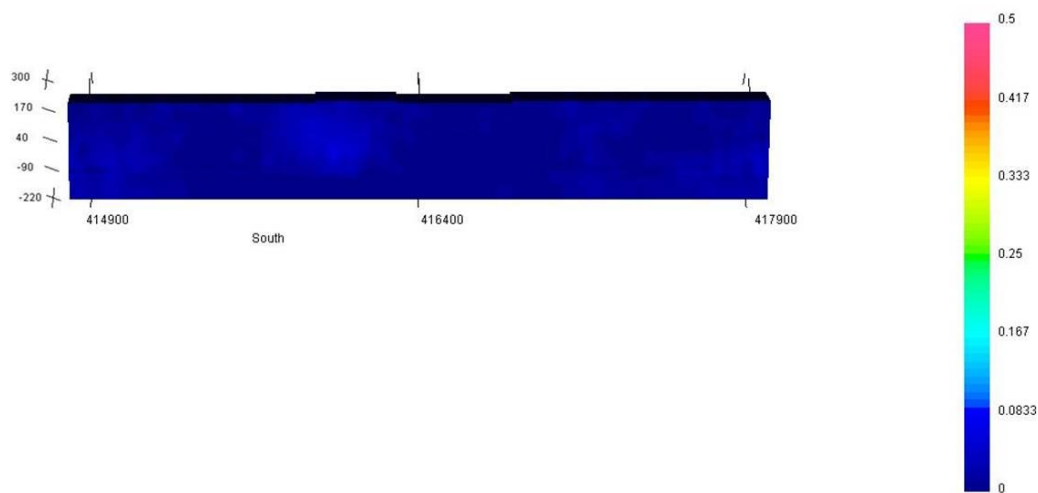


**Figure 2.38: Cross-section of the best current geophysical model along E-W line 6889000 Northing (UTM), looking north. Units on the right side represent susceptibility in SI units. Scale on the left is elevation above sea level (ASL) in metres.**

## Appendix B: Step-by-Step Cross-Sections Facing West

Appendix B contains cross sections spaced every 200 metres along UTM easting lines (north-south sections facing west), with each section spanning 4000 metres across. See figures A21-A37.

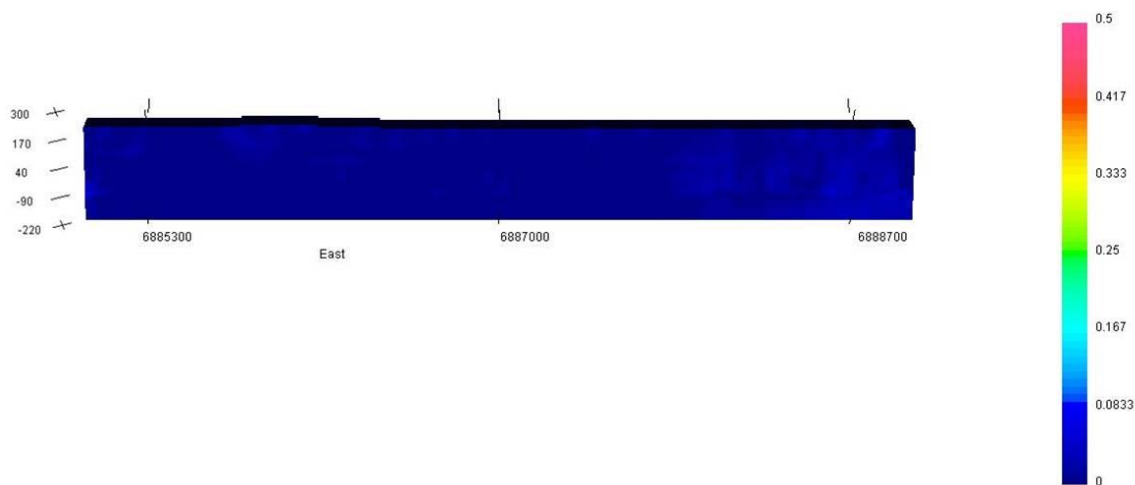


**Figure 2.39: Cross-section of the best current geophysical model along N-S line 414800 Easting (UTM), looking west. Units on the right side represent susceptibility in SI units. Scale on the left is elevation above sea level (ASL) in metres.**

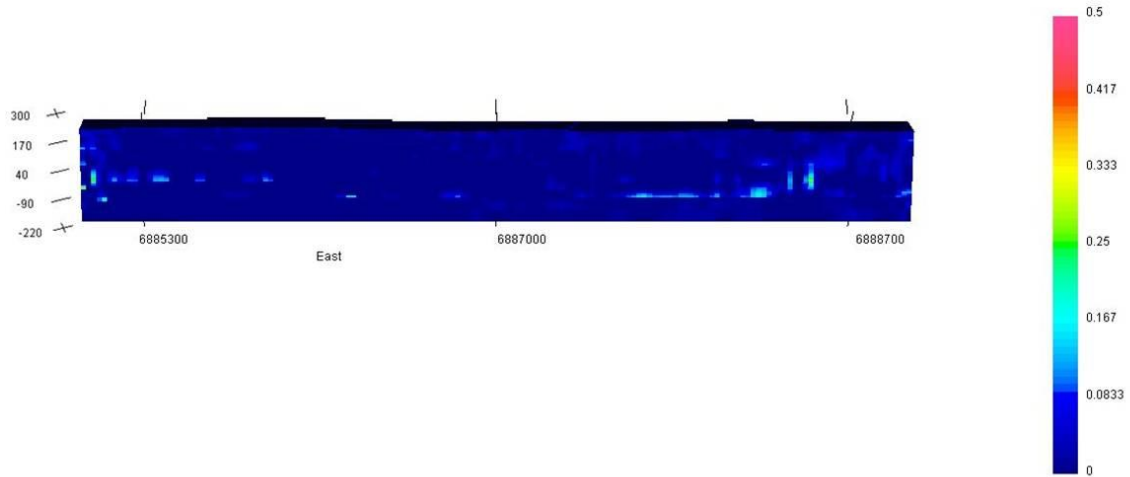


**Figure 2.40: Cross-section of the best current geophysical model along N-S line 415000 Easting (UTM), looking west. Units on the right side represent susceptibility in SI units. Scale on the left is elevation above sea level (ASL) in metres.**

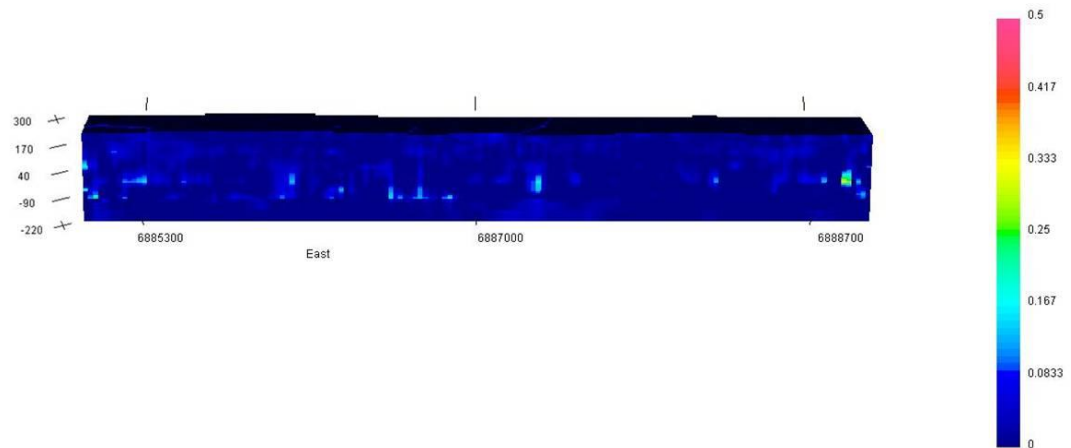


**Figure 2.41: Cross-section of the best current geophysical model along N-S line 415200 Easting (UTM), looking west. Units on the right side represent susceptibility in SI units. Scale on the left is elevation above sea level (ASL) in metres.**

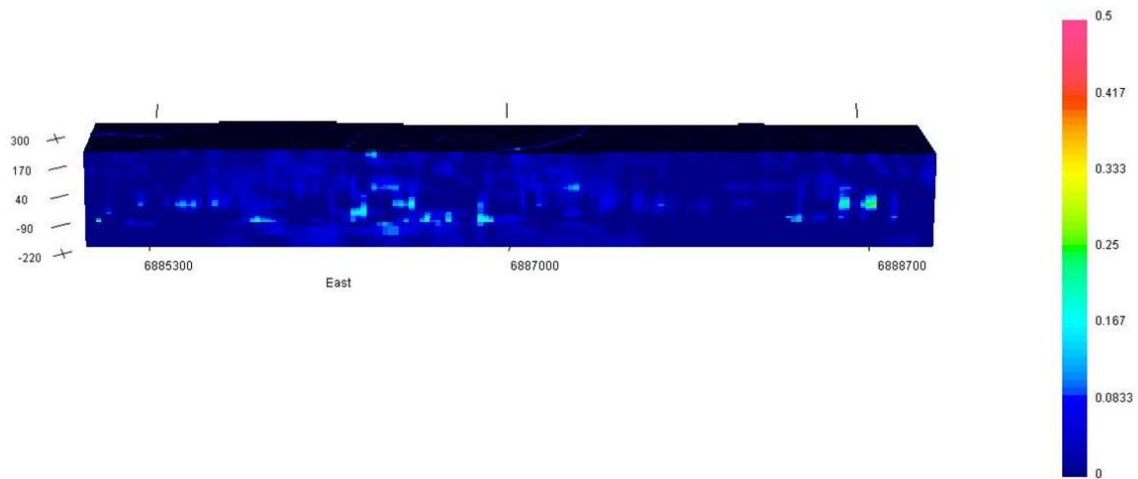


**Figure 2.42: Cross-section of the best current geophysical model along N-S line 415400 Easting (UTM), looking west. Units on the right side represent susceptibility in SI units. Scale on the left is elevation above sea level (ASL) in metres.**

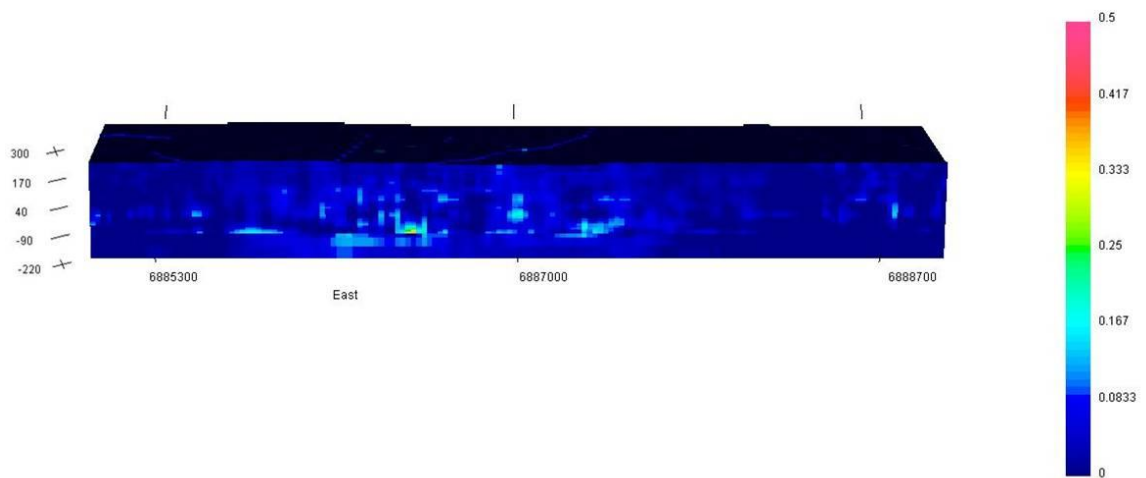


**Figure 2.43: Cross-section of the best current geophysical model along N-S line 415600 Easting (UTM), looking west. Units on the right side represent susceptibility in SI units. Scale on the left is elevation above sea level (ASL) in metres.**

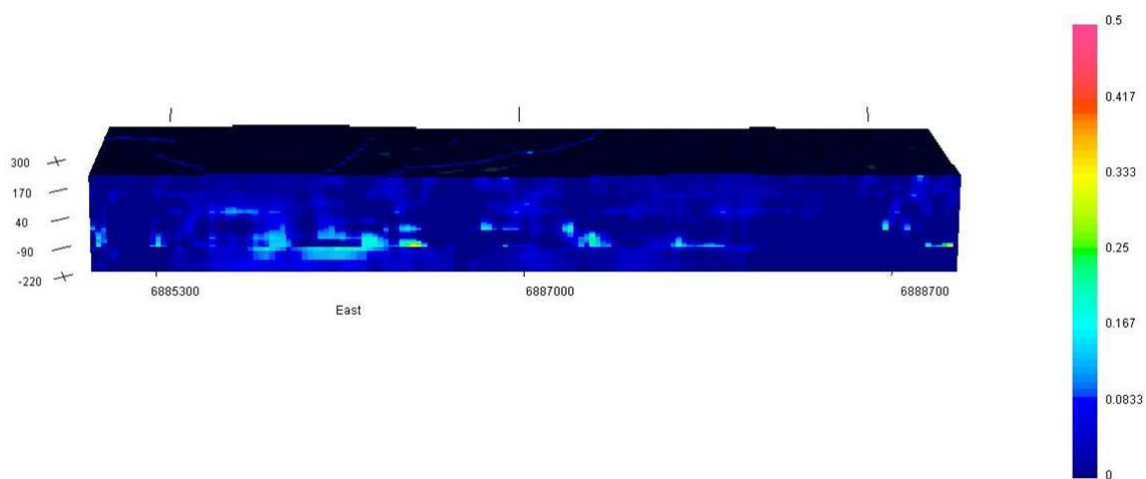


**Figure 2.44:** Cross-section of the best current geophysical model along N-S line 415800 Easting (UTM), looking west. Units on the right side represent susceptibility in SI units. Scale on the left is elevation above sea level (ASL) in metres.

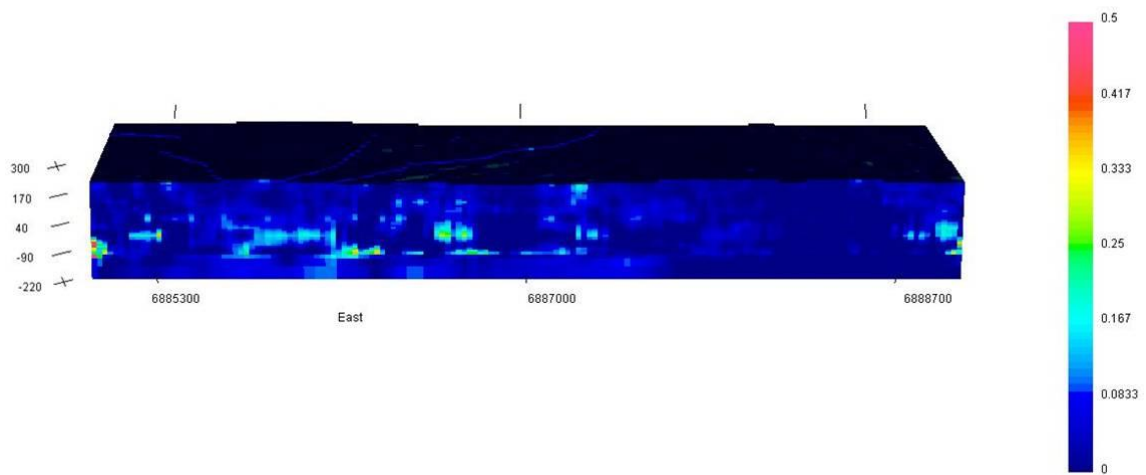


**Figure 2.45:** Cross-section of the best current geophysical model along N-S line 416000 Easting (UTM), looking west. Units on the right side represent susceptibility in SI units. Scale on the left is elevation above sea level (ASL) in metres.

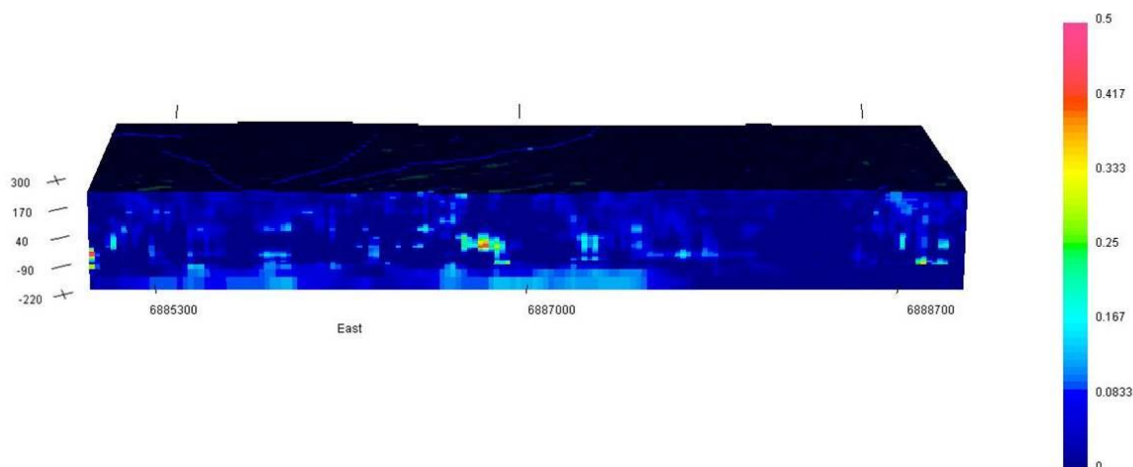


**Figure 2.46:** Cross-section of the best current geophysical model along N-S line 416200 Easting (UTM), looking west. Units on the right side represent susceptibility in SI units. Scale on the left is elevation above sea level (ASL) in metres.

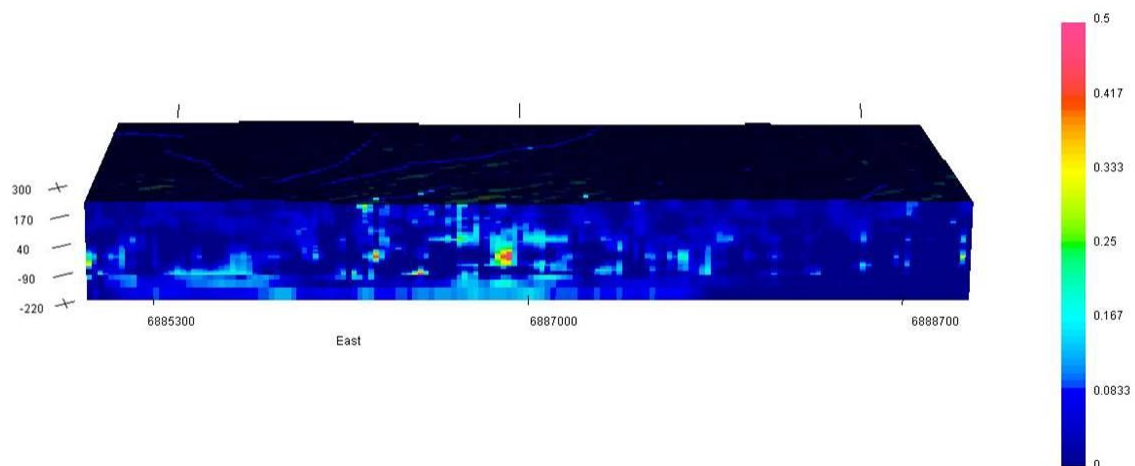


**Figure 2.47:** Cross-section of the best current geophysical model along N-S line 416400 Easting (UTM), looking west. Units on the right side represent susceptibility in SI units. Scale on the left is elevation above sea level (ASL) in metres.



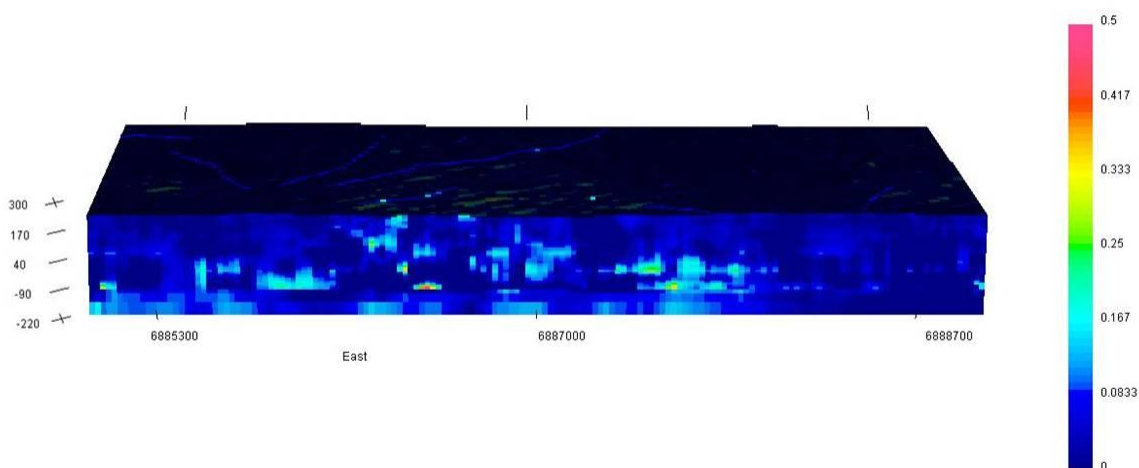


**Figure 2.48:** Cross-section of the best current geophysical model along N-S line 416600 Easting (UTM), looking west. Units on the right side represent susceptibility in SI units. Scale on the left is elevation above sea level (ASL) in metres.

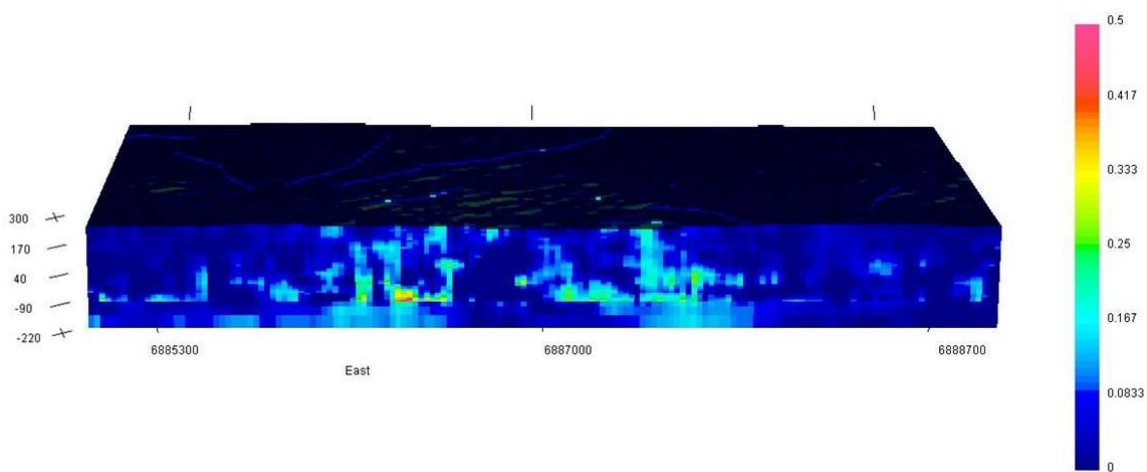


**Figure 2.49:** Cross-section of the best current geophysical model along N-S line 416800 Easting (UTM), looking west. Units on the right side represent susceptibility in SI units. Scale on the left is elevation above sea level (ASL) in metres.

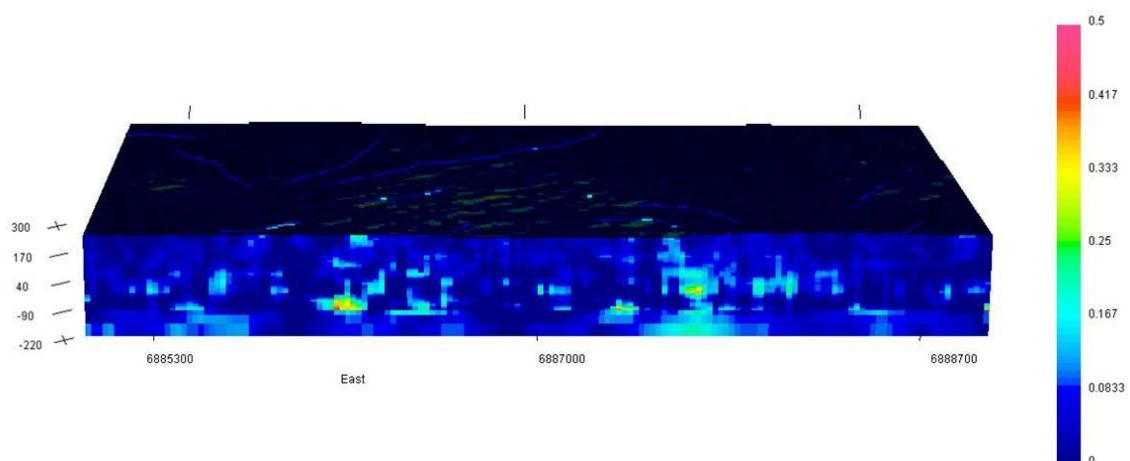


**Figure 2.50: Cross-section of the best current geophysical model along N-S line 417000 Easting (UTM), looking west. Units on the right side represent susceptibility in SI units. Scale on the left is elevation above sea level (ASL) in metres.**

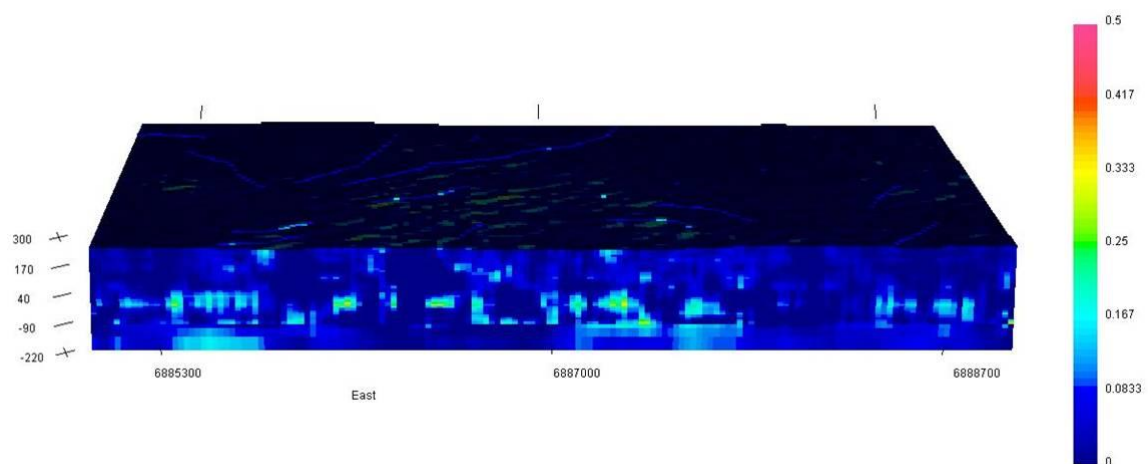


**Figure 2.51: Cross-section of the best current geophysical model along N-S line 417200 Easting (UTM), looking west. Units on the right side represent susceptibility in SI units. Scale on the left is elevation above sea level (ASL) in metres.**

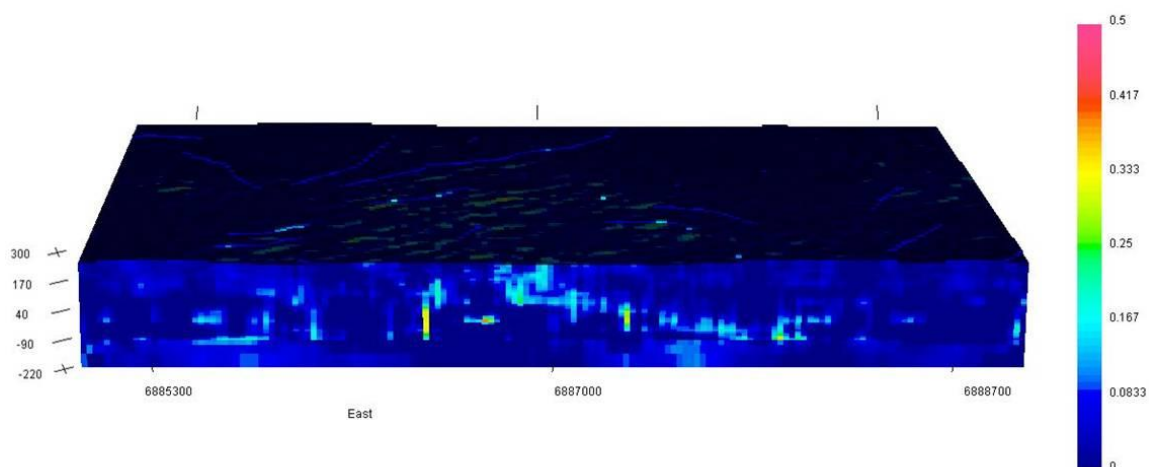


**Figure 2.52:** Cross-section of the best current geophysical model along N-S line 417400 Easting (UTM), looking west. Units on the right side represent susceptibility in SI units. Scale on the left is elevation above sea level (ASL) in metres.

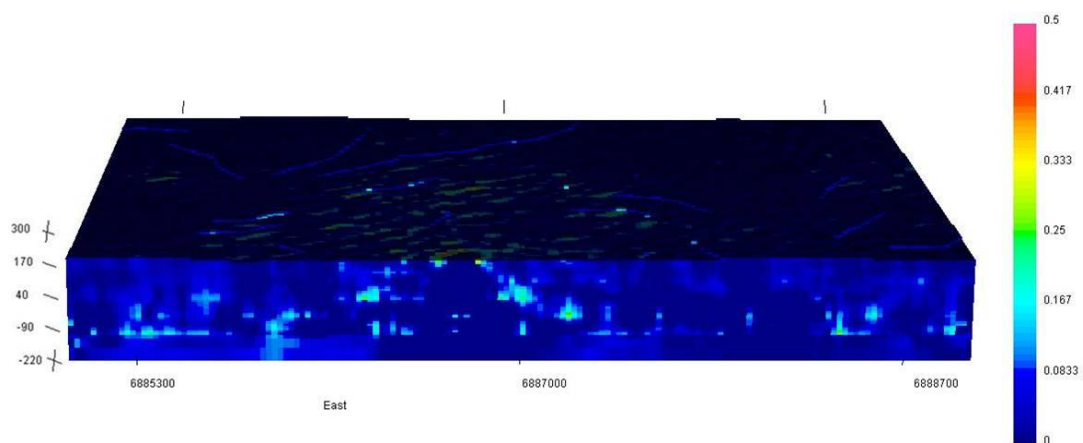


**Figure 2.53:** Cross-section of the best current geophysical model along N-S line 417600 Easting (UTM), looking west. Units on the right side represent susceptibility in SI units. Scale on the left is elevation above sea level (ASL) in metres.

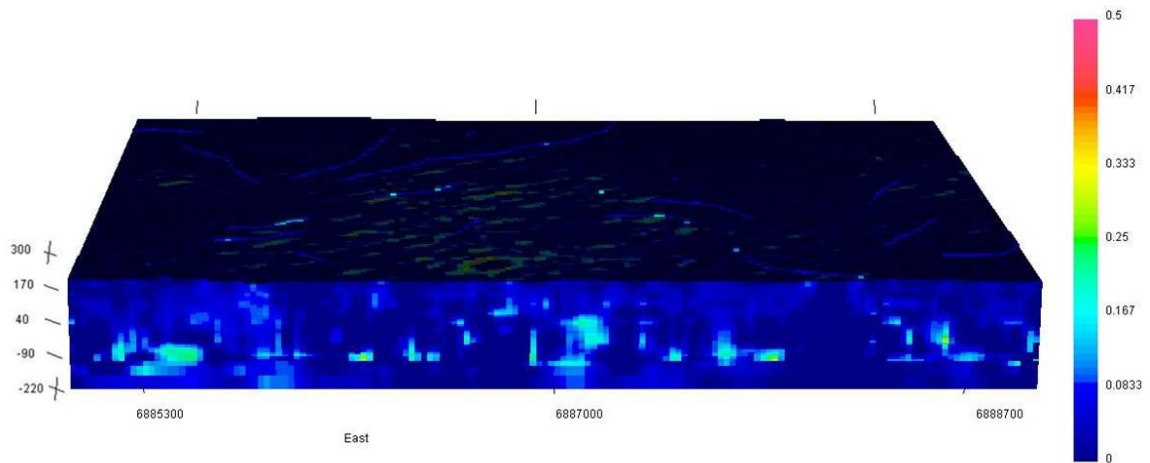


**Figure 2.54: Cross-section of the best current geophysical model along N-S line 417800 Easting (UTM), looking west. Units on the right side represent susceptibility in SI units. Scale on the left is elevation above sea level (ASL) in metres.**

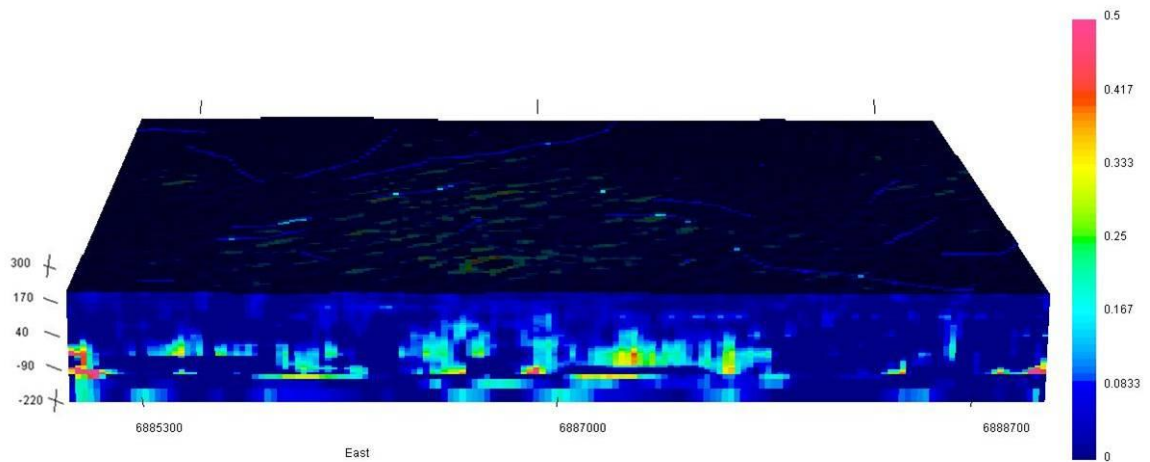


**Figure 2.55: Cross-section of the best current geophysical model along N-S line 418000 Easting (UTM), looking west. Units on the right side represent susceptibility in SI units. Scale on the left is elevation above sea level (ASL) in metres.**

## Chapter 3

### 3 Implementation of Gravity Data for Isolated and Joint Inversion Methods at Thor Lake, N.W.T.

*This section was written and submitted as a follow up open-file report to Chapter 2 for the Northwest Territories Geological Survey. This study implements airborne gravitational field data and new techniques for obtaining reference models via lateral interpolation to create an updated subsurface density model for the Thor Lake region. These techniques also have been implemented on the magnetic data in order to improve the previous model. Both potential fields can be used to track the same anomalous layer that acts as a host to the Nechalacho rare earth element deposit. Using structural cooperative inversion methods to influence the individual models, joint inversions were completed with the goal of further delineating the deposit. Density models agree well with geological findings as well as the magnetic susceptibility models for both the geometry and location of the deposit. It is shown that the method of lateral interpolation used here is an effective way to increase the amount of data in the reference model for a deposit of this geometry. Joint inversion techniques help to resolve some logistic issues with the earlier magnetic modelling and produce models with anomalous layers similar to those of the isolated inversions, but with greater confidence due to the incorporation of multiple datasets.*

#### 3.1 Introduction

Geophysical inversion is an excellent technique to supplement geological findings in regions where subsurface geophysical measurements may vary systematically with changes in lithology or subsurface material. This applies to a wide range of disciplines

from the petroleum and mineral exploration industries to infrastructure planning and construction. Making use of potential field data that is relatively inexpensive and commonly acquired, as well as observations made by geologists such as core logs, a geophysical inversion can be extremely useful for mapping the subsurface. In some scenarios, the lithological variations can be sensed by multiple different types of potential field. This special circumstance bears with it the opportunity to look at the subsurface from multiple points of view.

In this report, previous work with magnetic field data from Chapter 2 (*Kouhi and Tiampo* (2016)) will be used as a starting point and built upon with the addition of gravitational field data from the Thor Lake region in Northwest Territories, Canada. Previous magnetic inversions revealed a deep-seated magnetic signal which was removed with the use of wavenumber filtering techniques in order to better characterize a shallow, sub-horizontal region of high magnetic susceptibility that ranges from approximately 50 to 200 metres depth (*Kouhi and Tiampo*, 2016) (**Figure 3.1**). The model shows this high susceptibility region extends for over 1500 metres and likely represents a lithology with high concentrations of magnetite.

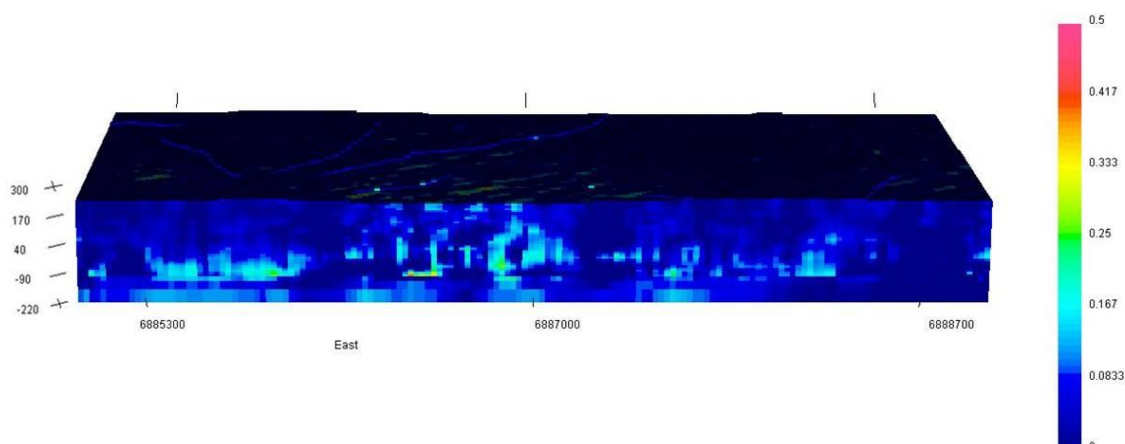


**Figure 3.1: A north-south (N-S) cross-section of the best magnetic susceptibility model from the earlier Thor Lake study area, *Kouhi and Tiampo (2016)*. The figure displays easting line 416550 (UTM), looking west. Units on the right side represent susceptibility in SI units. Scale on the left is elevation above sea level (ASL) in metres.**

### 3.1.1 Background Geology

The Thor Lake property is located approximately 100 kilometres southeast of Yellowknife, NT within the Blatchford Lake Igneous Complex (BLIC) (**Figure 3.2**). The BLIC is divided into the eastern lobe and the western lobe and then further subdivided into six units based on lithology (*Davidson, 1978, 1982*). The eastern lobe is comprised of the  $2176.2 \pm 1.3$  Ma Grace Lake granite (*Sinclair et al., 1994*) and the  $2176.8 \pm 1.6$  Ma Thor Lake syenite (TLS) (*Mumford, 2013*) which have a gradational contact and are interpreted to have been part of the same intrusive event (*Davidson, 1982*). Within the TLS lies the Nechalacho Layered Suite (NLS), formerly known as the Lake Zone (*Pinckston and Smith, 1995*), which is a sequence of silica-undersaturated intrusive layers which display increasing alkaline characteristics with depth (*Sheard et al., 2012*). The



NLS is contained within the Thor Lake property and hosts the world class Nechalacho deposit, one of the world's largest undeveloped heavy rare earth element deposits.

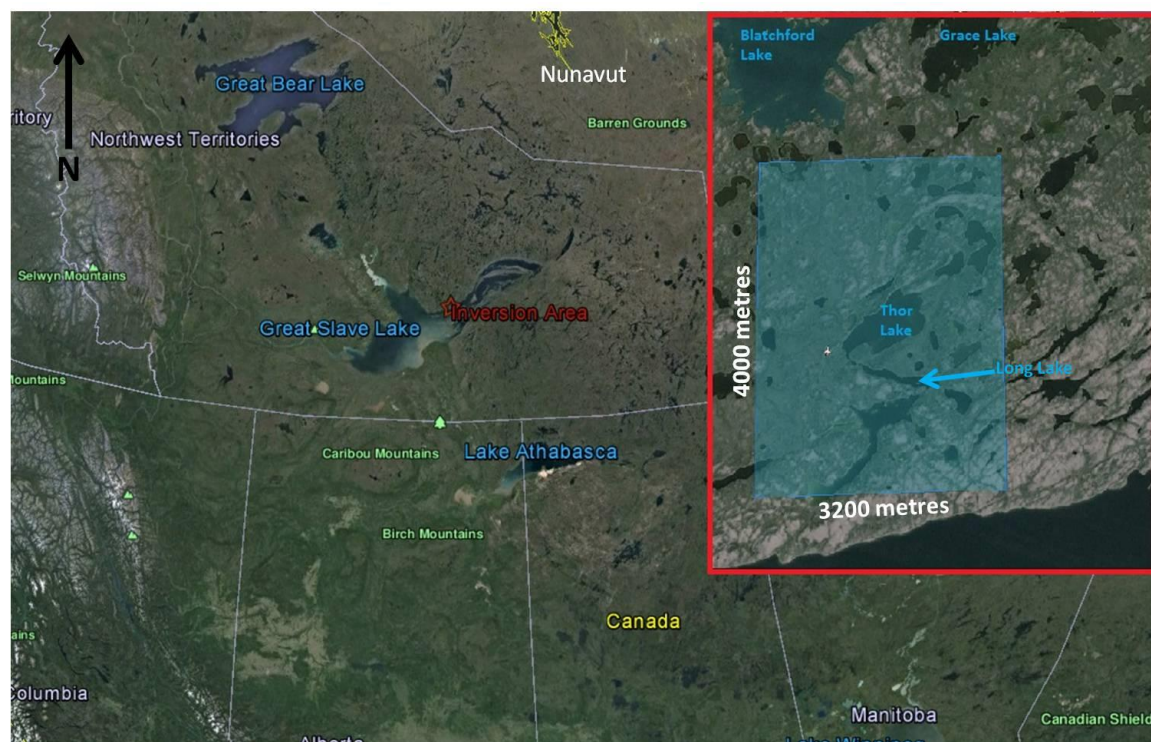


**Figure 3.2: Location map showing the Thor Lake area, the Northwest Territories. Blue shaded area in the red inset map shows the inversion area in this study (Kouhi and Tiampo, 2016; adapted from Google Earth, 2015).**

The NLS is a hydrothermally altered intrusion that spans approximately 1.8 kilometres in the north-south direction and 2.1 kilometres in the east-west direction and reaches depths of at least 1000 metres based on current drilling (Möller and Williams-Jones, 2016). The Nechalacho rare metal deposit is hosted within a highly altered region in the upper 300 metres of the intrusion and is comprised of the upper zone and basal zone (Sheard *et al.*, 2012)(**Figure 3.3**). Both zones are comprised of a sequence of layers hosted within an aegirine-rich foyaite and pinch out toward the edges of the intrusion (Möller and



*Williams-Jones, 2016*). The upper zone is characterized by its abundance of interstitial eudialyte within the foyaite and the basal zone is characterized by densely packed eudialyte cumulate and eudialyte syenite (*Möller and Williams-Jones, 2016*). The upper zone is approximately 15 to 30 metres thick and contains high concentrations of light rare earth elements (LREE) while the basal zone ranges from 15 to 60 metres in thickness and hosts large concentrations of heavy rare earth elements (HREE) (*Sheard et al., 2012*).

*Möller and Williams-Jones (2016)* interpreted the NLS to have formed from the bottom-up and top-down, meeting at the foyaite that hosts the upper and basal zones, resulting in a horizon sandwiched between the two different crystallization sequences. Minerals such as sodalite and nepheline formed first, followed by potassium feldspar which led to increasing iron enrichment upward from the bottom and downward from the top, culminating in the densely packed eudialyte cumulate (*Möller and Williams-Jones, 2016*). The later hydrothermal alteration that overprinted the previous mineralogy resulted in the abundance of magnetite as the main alteration mineral in the deposit, with hematite prevailing as the alteration mineral below the basal zone (*Sheard et al., 2012*).

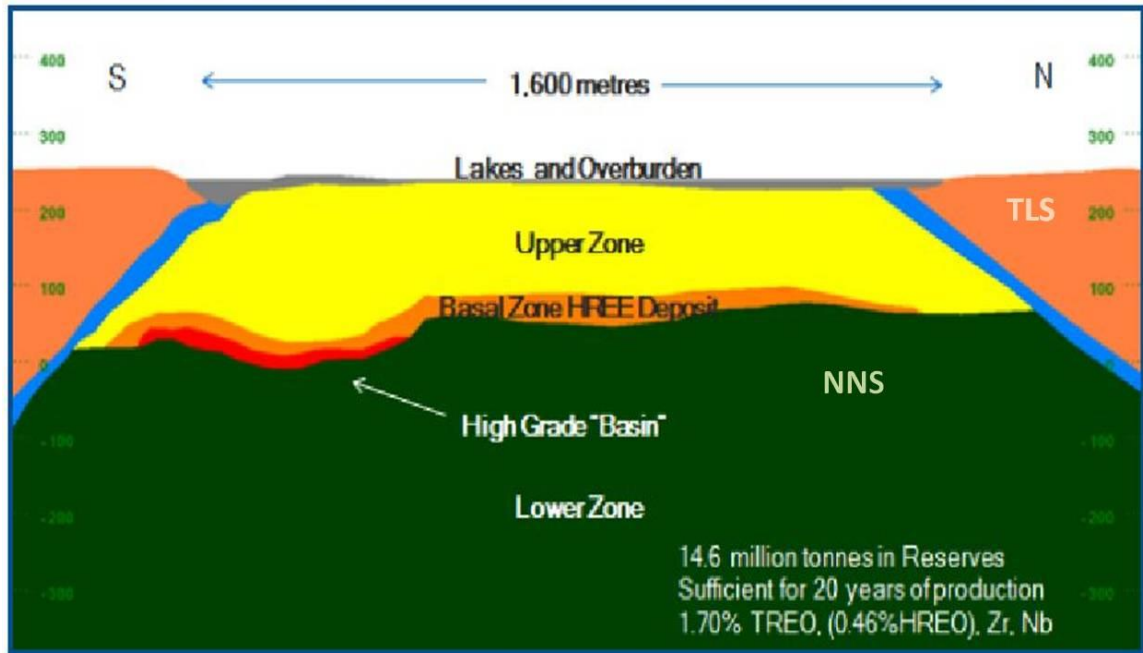


**Figure 3.3:** A basic geological model of the Nechalacho deposit (modified from *Ciuculescu et al., 2013*). The Nechalacho nepheline syenite (NNS, green) includes the upper and basal zones, while the Thor Lake syenite (TLS) is represented in orange. The blue lithology is the roof sodalite. The vertical scale is in metres ASL.

### 3.1.2 Background Geophysics

As stated above, previous models for subsurface magnetic susceptibility were obtained through constrained geophysical inversion (*Kouhi and Tiampo, 2016*). All inversions were completed using the mag3d component of the University of British Columbia Geophysical Inversion Facility (UBC-GIF) software which allows for the final model to be constrained based on subsurface geophysical measurement and regional geological trends (UBC-GIF). The airborne total magnetic field data used was obtained for Natural Resources Canada (NRCan) by Fugro GeoServices Ltd. with a linespacing of 250 metres and flown at an altitude of 100 metres (*NRCan, 2011*)(**Figure 3.4**). *Kouhi and Tiampo*

(2016) treated the data using wavenumber filtering techniques to remove long wavelength signal in order to concentrate the study on the shallow anomalies (*Blakely, 1995*). This study produced a preliminary magnetic susceptibility model based on geophysics that displayed many of the characteristics expected for the deposit based on previous geological work (*Sheard et al., 2012; Möller and Williams-Jones, 2016*). While this model corresponds well with previous geological models both spatially and geometrically, it lacks the lateral continuity expected in the highly anomalous layer. The purpose of this study is to improve and refine the magnetic susceptibility model using a second potential field dataset.

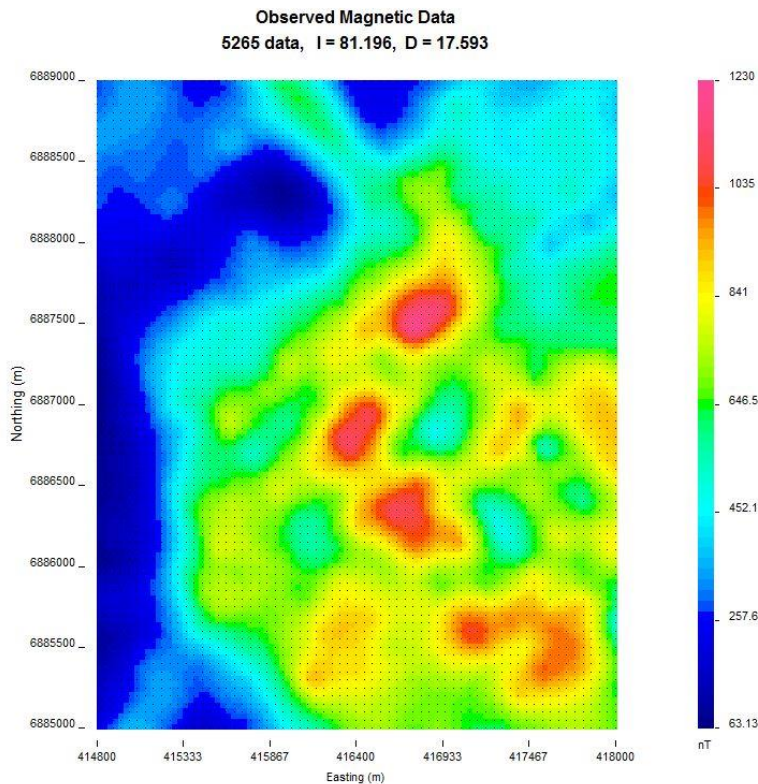


**Figure 3.4: Map of the airborne magnetic field anomaly for the inversion area.**  
UTM coordinates shown in all figures and cross sections are NAD 83, Zone 11N.

**There are 5265 data points with magnetic inclination (I) and declination (D) specified as well.**

In addition to total magnetic field data, the survey also simultaneously collected gravitational field data (*NRCan*, 2011)(**Figure 3.5**). This data, coupled with density measurements taken on core samples at approximately 5 metre intervals, allows for a constrained inversion of gravity data to create a subsurface density model. This inversion is run using the grav3d program that inverts for a subsurface density model within the UBC-GIF software in a similar fashion to mag3d. The density model then can be used cooperatively with the previous magnetic susceptibility model in an attempt to further delineate the boundaries of the deposit and refine both models.

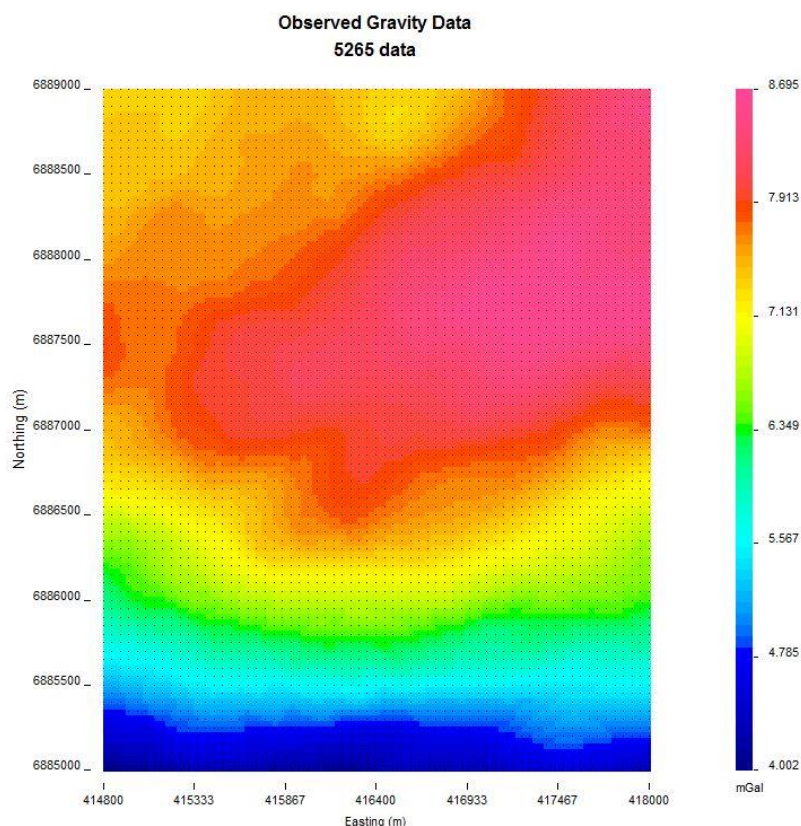


**Figure 3.5: Map of the airborne gravity anomaly for the inversion area. There are 5265 data points. A gravitational high can be seen in the centre of the region, likely from a region of high density associated with the Nechalacho deposit.**

## 3.2 Methods

### 3.2.1 Gravity

The rock paragenesis for the Nechalacho deposit makes for an ideal scenario for inversion of gravity data. The region of interest is located at a local high gravity anomaly, suggesting that there is excess mass beneath the surface. Due to the nature of the formation of the intrusion, with minerals forming from the bottom up beneath the deposit and from the top down above the deposit, a large proportion of the high gravity signal likely stems from the sandwich layer that hosts the majority of the REE (*Möller*

and Williams-Jones, 2016). Due to its high relative density, this densely packed layer of secondary minerals altered from eudialyte acts as an excellent target to model through the inversion of airborne gravity data. As a result, the high density layers modelled at this depth can be used as a proxy for rare element mineralization, and thus the deposit.

The general workflow for previous magnetic inversions consisted of solving for an unconstrained model, then constraining cells where subsurface data has been obtained, followed by wavenumber filtering of airborne data and finally, gradient smoothing (Kouhi and Tiampo, 2016). While the overall process remains similar, a few major adaptations from this workflow have been implemented for this study.

The first of these adaptations is the exclusion of wavenumber filtering in favour of a deeper mesh. The mesh for the previous magnetic model consisted of cells of 25 metres in the north-south and east-west directions and 10 metres in thickness, ranging to depths of approximately 400 metres. The approach in this study was to mitigate additional error introduced in the wavenumber filtering process by eliminating it altogether and allowing for the deep-seated signal to be modelled in the subsurface. Therefore, the mesh for the gravity inversions was changed as suggested by *UBC-GIF* (2013), to include cells of size 20 metres in both lateral directions and 10 metres in thickness, ranging down to depths of 2000 metres (**Figure 3.6**). Ideally, this removes the need to wavenumber filter the data. However, it adds a degree of uncertainty because only one drillhole (L09-194) reaches to depths of more than 400 metres as it extends down to approximately 1000 metres (*Avalon Rare Metals*, 2014). Therefore, only the top 400 metres are reasonably well constrained and cells below suffer from lack of uniqueness.



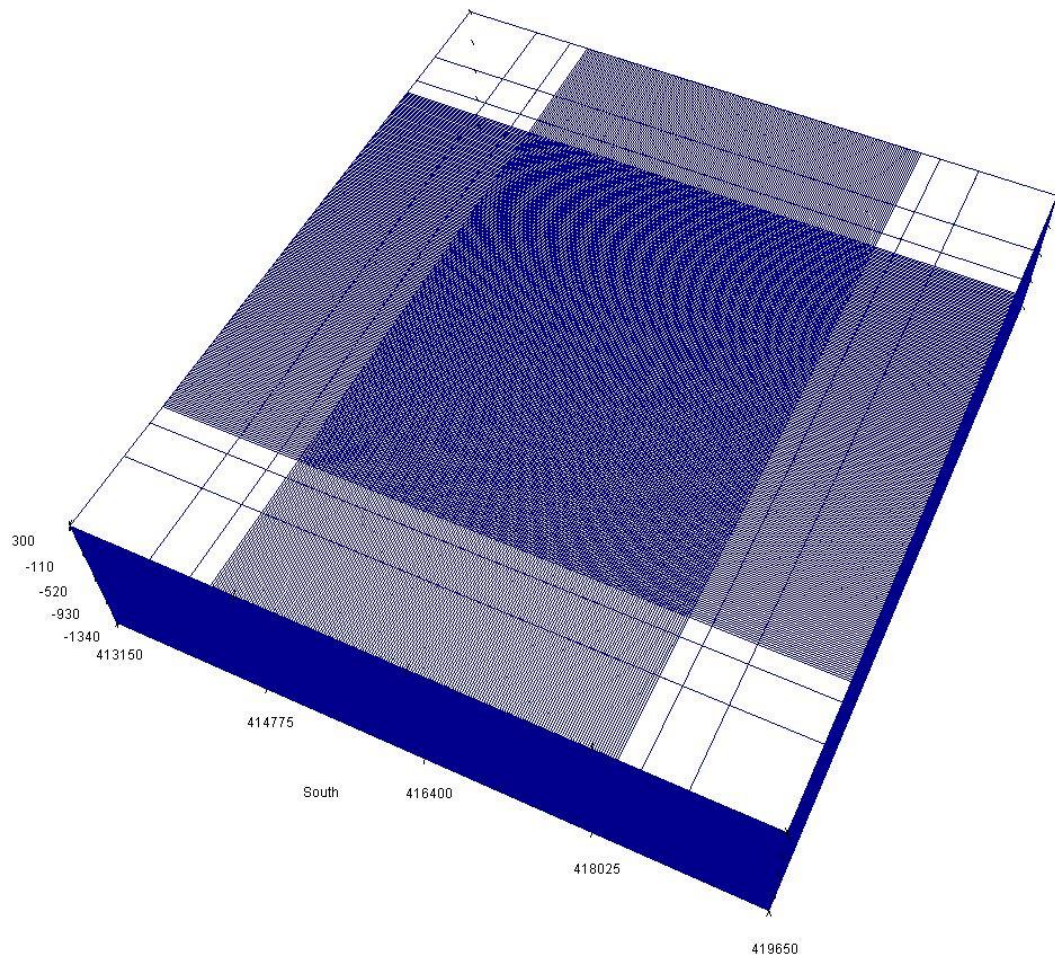


**Figure 3.6:** The mesh for the geophysical inversion, shown here, spans 4000 metres in the north-south direction and 3200 metres in the east-west direction. Cell dimensions are 20x20x10 metres in the  $x$ ,  $y$  and  $z$  directions. The mesh contains 6,044,577 cells in total (191x231x137).

The other major adaptation from previous inversions is the implementation of a lateral interpolation method to the three-dimensional constraining model.

### 3.2.2 Lateral Interpolation

One of the major issues with any inversion is the problem of non-uniqueness. This is generally overcome by implementing constraints or binding values on individual cells in

order to supplement the inverse problem with information that is already known. In the inverse problem at hand, the airborne data is supplemented with geophysical measurements taken on core samples. *Kouhi and Tiampo* (2016) use these measurements as upper and lower bounding constraints on cells that contain drillhole information by creating a three-dimensional model file (**Figure 3.7**). This model file is obtained by binning and averaging values that are contained within the same cell. While this method proved to be effective for modeling the approximate location and geometry of the deposit, the model obtained was discontinuous and lacked the relatively smooth lateral trend expected in the deposit. Further examination of the three-dimensional model file shows that while data was taken from over 400 drillholes, only approximately 0.169% of the total number of cells actually contain values. A large portion of these null cells can be attributed to the new mesh mentioned above. Since drillhole L09-194 is the only data available that reaches depths greater than 400 metres, the majority of the cells below this point do not contain any data. While this greatly affects the amount of uncertainty involved in modeling the deeper anomalies, the true region of interest for this study is contained within the top 400 metres (*Ciuculescu et al.*, 2013). A glance at the top 400 metres of the three-dimensional model shows that approximately 0.552% of the cells contain data. Although this is a significant improvement, a method of lateral interpolation between cells with data points was developed to enhance the amount of data in order to further smooth the inversion models.



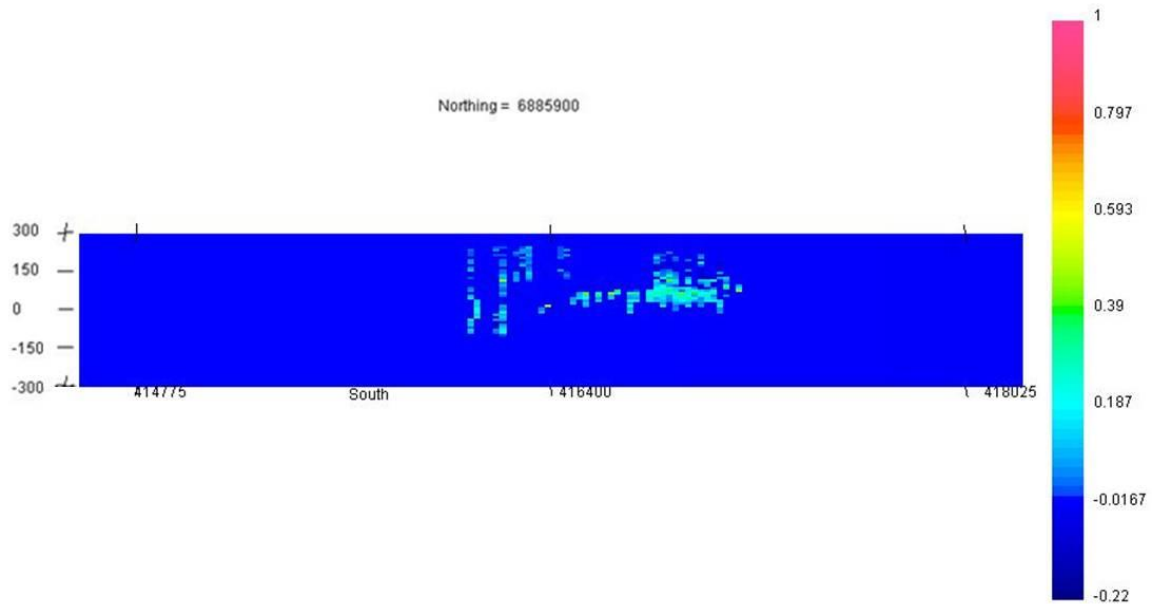


**Figure 3.7: Sample cross-section from the three-dimensional reference model for core density data created from binning measured values into the cells without any interpolation (northing line 6885900 [UTM], facing north). All density models display units on the right in +/- g/cm<sup>3</sup> with respect to the average density (2.67g/cm<sup>3</sup>) and depths on the left in metres ASL.**

Different interpolation and lateral modeling techniques such as kriging were investigated in order to enhance the boundary models for inversion. However, a more specialized approach to the problem was developed and used to create three-dimensional models to be used as reference and boundary constraining models in the inversion. In this interpolation method, the north-south and east-west dimensions of the cells are used as a two-dimensional grid. Any cell in the grid that contains a drillhole directly in it is assigned an arbitrary numerical value, referred to as the uncertainty value. In this case the value assigned is four. This point is then taken as the centre where the geophysical property value is relatively well-known. From this centre, decreasing values are assigned as adjacent cells grow further from the centre (**Figure 3.8**). For example, any cells

touching the centre cell (four) either diagonally or adjacently are assigned an uncertainty value of three. Then any cells touching this first ring of adjacent cells (three) are assigned a value of two. The final third ring of cells are assigned a value of one.

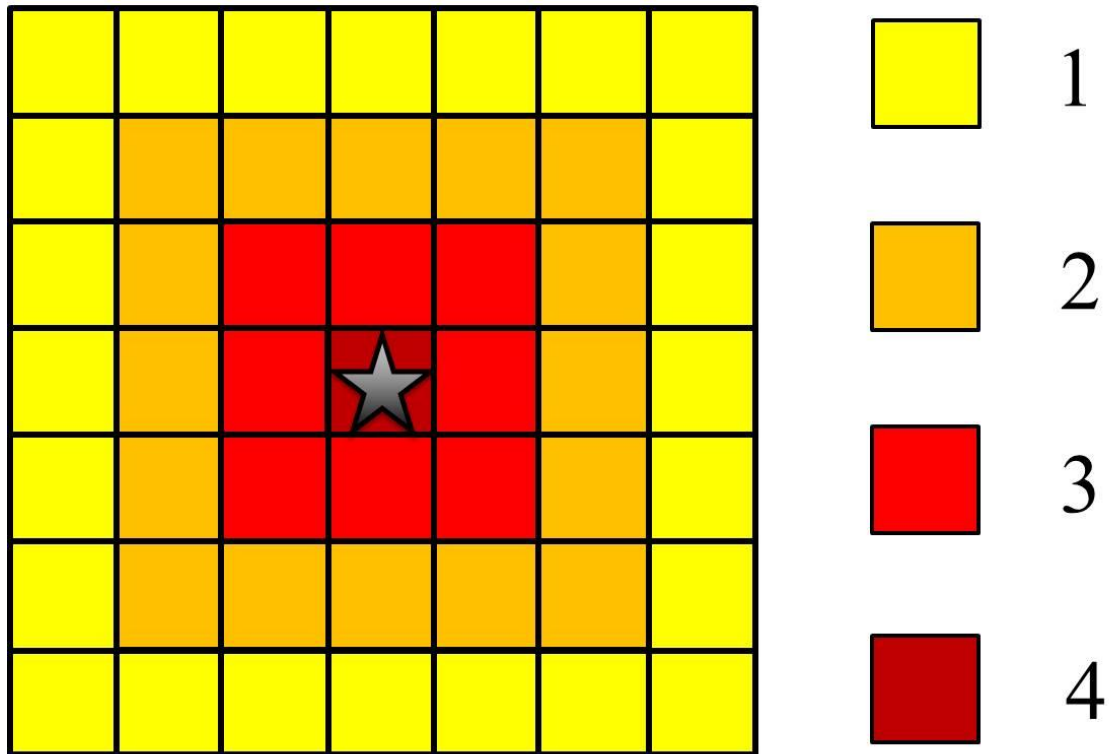


**Figure 3.8: A simple diagram describing the assignment of uncertainty values for the lateral interpolation technique. The star represents a cell with drillhole data and is assigned an uncertainty value of 4. From here, uncertainty values decrease the further a given cell is away from the centre cell up to a maximum distance of 3 cells away.**

These uncertainty values are used when evaluating the value of the geophysical measurement and when assigning a maximum and minimum value range for each cell. First, it is used when binning the geophysical measurement values. The measurement value from the centre cell is binned into each cell surrounding it as described above,

however using the uncertainty value in each individual cell as a weighting factor for the measurement value. Once all values are binned on all x-y planes, the averages in each cell are used as a three-dimensional reference model similar to *Kouhi and Tiampo (2016)*. However, each cell now contains a weighted average based on its proximity to the centre cell. Given a 7-by-7 grid where the centre cell, a cell where there is known drillhole data, is taken as the origin, mathematically the reference value for each cell can be described by:

$$\varphi = \frac{\sum U_{ij} \varphi_0}{\sum U_{ij}}, \quad \begin{aligned} &\{i \in \mathbb{Z} \mid -3 \leq i \leq 3\} \\ &\{j \in \mathbb{Z} \mid -3 \leq j \leq 3\} \end{aligned} \quad (1)$$

where  $\varphi$  is the geophysical reference value assigned to the cell,  $U$  is the set of uncertainty values for the cell,  $i$  and  $j$  are the distances in number of cells from a given geophysical measurement value (set as the origin) in the  $x$  and  $y$  directions respectively, and  $\varphi_0$  is the subset of geophysical measurement values that satisfy the conditions of  $i$  and  $j$ . This is a weighted average based on uncertainty values described by the equation:

$$U_{ij} = 4 - \max(\text{abs}(i, j)), \quad \begin{aligned} &\{i \in \mathbb{Z} \mid -3 \leq i \leq 3\} \\ &\{j \in \mathbb{Z} \mid -3 \leq j \leq 3\} \end{aligned} \quad (2)$$

Once the reference model is calculated, uncertainty values are also used to determine the range of the values allowed when creating maximum and minimum boundary files.

Ranges are assigned as constant values based on the weighted average uncertainty value in each cell. These constant values are added to or subtracted from the reference model value in a specific cell to create a maximum or minimum boundary file:

$$\max(\varphi) = \varphi + \bar{U} \quad (3)$$

$$\min(\varphi) = \varphi - \bar{U}$$

where  $\bar{U}$  is the weighted average of the set of uncertainty values,  $U$ . This technique of using measured geophysical data points takes advantage of the knowledge of the geological trend of the deposit. Since the deposit is expected to be subhorizontal and contained within the top 400 metres (*Ciuculescu et al.*, 2013), it can be assumed that the geophysical values are relatively continuous in both lateral directions and therefore may benefit from interpolation in these directions. The three-dimensional reference model produced by this interpolation method is a vast improvement in terms of the quantity of cells that contain data (**Figure 3.9**). Overall approximately 2.186% of the cells now contain data, and the top 400 metres reveals that approximately 7.129% of these cells are filled. By inverse theory standards, this is a significant amount of data that can be used to constrain the model and remove ambiguity. However, as with all interpolation methods, it must be used with caution as error in these values is created as a by-product of these assumptions. A statistical variation of this method, as well as a comparison to classic kriging methods are discussed in section 3.5.1.

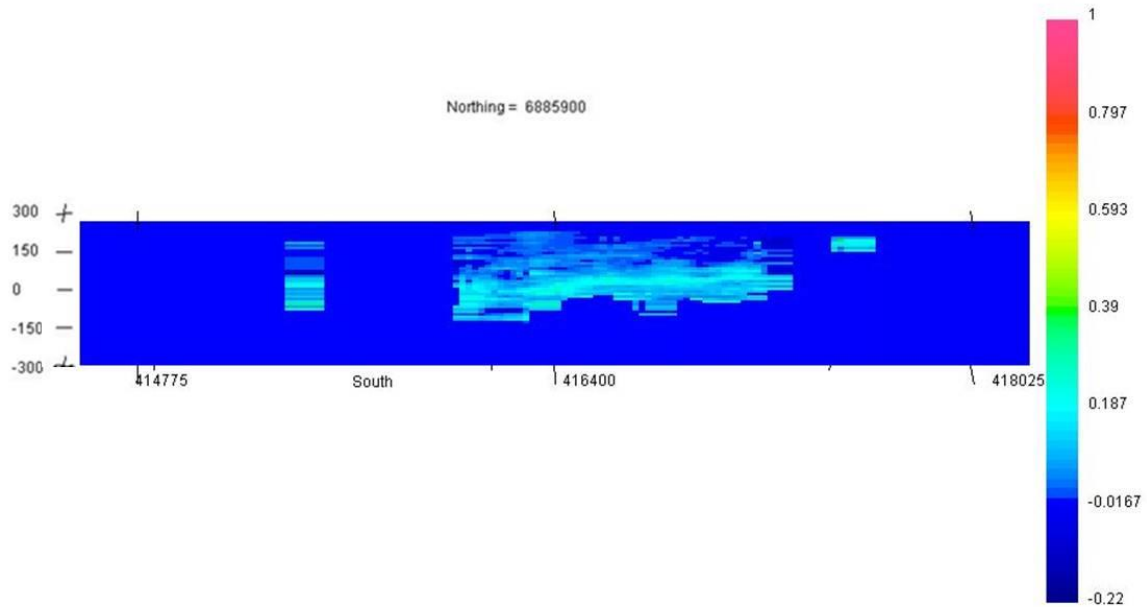


**Figure 3.9: Sample cross-section from the three-dimensional reference model for core density data created using lateral interpolation methods (northing line 6885900 [UTM], facing north). The reference model contains much more data than the previous three-dimensional model.**

### 3.2.3 Joint Inversion

Geophysical measurements can be used to sense and differentiate a variety of different geological structures and trends. For example, in the work by *Kouhi and Tiampo* (2016), subsurface magnetic susceptibility was used as a proxy for the degree of alteration as suggested by *Möller and Williams-Jones* (2016). Total magnetic field anomalies are directly related to the volume of susceptible minerals beneath the surface. Similarly, gravitational field anomalies are directly related to the density of the materials beneath the surface. While these two potential fields track different variations in the subsurface, often there are correlations between minerals that display high magnetic susceptibilities and minerals that have high density.

The Nechalacho deposit represents an interesting case study for the use of joint inversion due to its complex paragenesis. As summarized above, the magmatic layering from both the top and bottom of the intrusion resulted in a high density layer that hosts the deposit (*Möller and Williams-Jones, 2016*). A later hydrothermal event altered the majority of the original mineralogy with magnetite being the major alteration mineral (*Sheard et al., 2012*). Due to the high iron content in the densely packed eudialyte, the largest proportions of magnetite, and thus the highest susceptibilities, are expected in the same region as the high density layers. Therefore supplementing gravity inversions with knowledge of the lithological changes sensed by magnetic inversions and vice versa can be an effective way to help further delineate the boundaries of the deposit. Each of these potential fields is sensing different geophysical properties of the subsurface lithology, therefore the technique is analogous to investigating beneath the surface from two different perspectives.

The joint inversion methodology used in this study is adapted from the work by *Lelièvre et al. (2009)*. The method requires reliable models for all datasets based on knowledge of the geology. For this study, this relies on having obtained reasonable results from individual gravity and magnetic inversions. *Lelièvre et al. (2009)* described an  $L^2$ -norm based approach in which the magnitude of the spatial model gradient of the best current model was used to adjust inversion smoothness weights. The magnitude of the gradient given by:

$$\|\nabla m\| = \sqrt{(\nabla_x m)^2 + (\nabla_y m)^2 + (\nabla_z m)^2} \quad (4)$$

where  $m$  is the current best model, and is used to inversely weight the smoothing weights (*Lelièvre et al.*, 2009). Where the gradient is high, smoothness is penalized to suggest a change in lithology and where the gradient is low, smoothness weights are increased to promote a smoother model in regions that are assumed to be homogeneous lithology. This method was first introduced as a way to encourage sharp boundaries between rock units. However its application to cooperative inversion techniques was also addressed (*Lelièvre et al.*, 2009). Models from different potential field datasets can be used to influence the lithological structure of one another by calculating the magnitude of the spatial model gradient for each dataset, as described above. The magnitudes are then normalised, summed and used to adjust inversion smoothness weights for the subsequent individual inversions and then the process is repeated (*Lelièvre et al.*, 2009). This iterative process converges structural characteristics from each individual field into one weighting file that is then used as an equal influence in both subsequent individual inversions.

A variation of this procedure, used in this study, makes use of an updated software package by UBC-GIF. Rather than calculating the magnitude of the spatial model gradient, gradient tensors can be implemented into a smoothness weighting file. In essence, this allows for the smoothness to be promoted or penalized depending on the changes in geophysical properties with direction. Updates to both mag3d and grav3d allow for an input weighting file which contains data for each individual cell in the  $x$ ,  $y$  and  $z$  directions (*UBC-GIF*, 2013). The technique described above is then carried out without the use of the  $L^2$ -norm, in an iterative fashion with the goal of refining the boundaries of the Nechalacho deposit.

### 3.3 Results

#### 3.3.1 Gravity

Initial inversions of airborne gravity data were completed using basic input files. These files are the mesh file which defines the cell sizes as well as the number of cells in each of the three dimensions (**Figure 3.6**), the airborne data file, and an elevation file. The purpose behind starting with an inversion without any constraints is to analyze the problem in its simplest form before the complexity of constraining models and other such knowledge is included. **Figure 3.10** shows a cross-section that summarizes the results of the basic inversion. The model has some structure that could be interpreted as layering. That layering could agree with a partial melting process in which denser crystals underwent gravitational settling first, followed by lighter, less dense crystals. However, similar to unconstrained magnetic inversion results obtained by *Kouhi and Tiampo* (2016), the majority of the high anomaly in the gravitational field data is attributed to a source deep within the subsurface. This is often a problem associated with the ambiguity of the inversion process. As there are infinitely many solutions to the problem, inversion processes tend to place anomalies deeper, with higher geophysical property contrasts unless constraining parameters promote a more complex model.



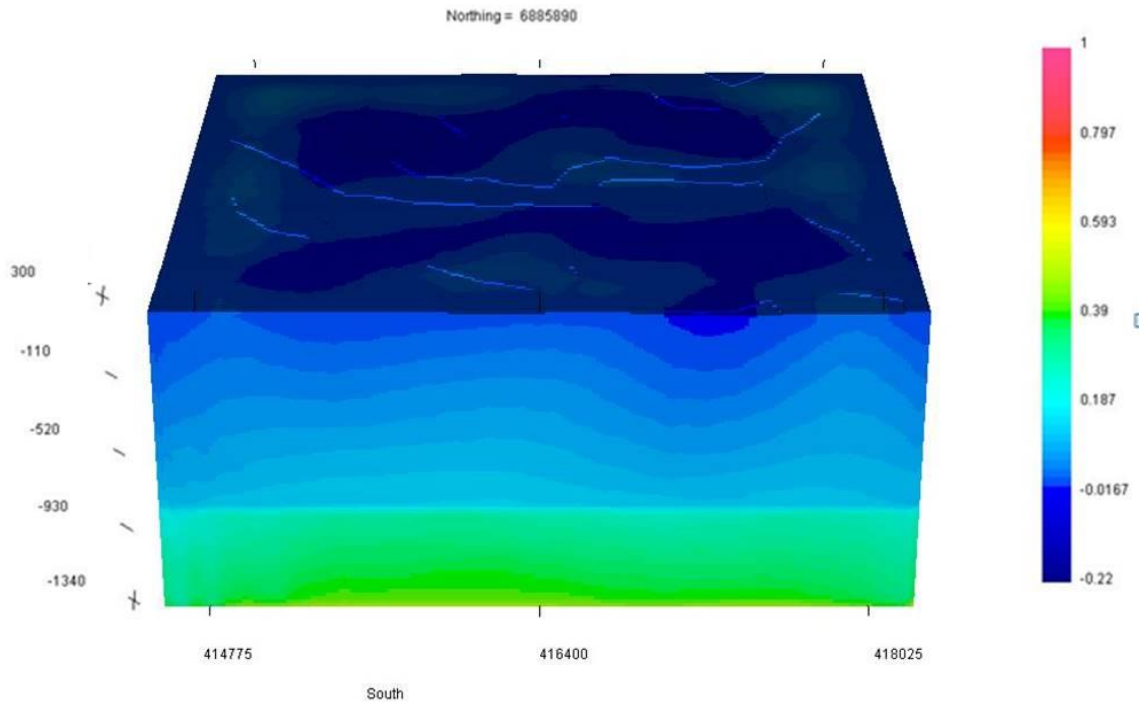


**Figure 3.10: Cross-section of the preliminary, unconstrained gravity inversion for the Thor Lake study area (northing line 6885890, facing north). Units on the right side represent density in  $\text{g/cm}^3$  above or below  $2.67 \text{ g/cm}^3$ . Scale on the left is elevation ASL in metres.**

By incorporating additional information about the subsurface that is known within reasonable error bounds through geophysical measurements, the problem of non-uniqueness can be mitigated. **Figure 3.11** is a cross-section of the model and geological interpretation obtained through the addition of laterally interpolated maximum and minimum boundary files and reference models. The contrast between the constrained model and the unconstrained model is immediately evident. Similar layering structure can be seen beneath the deposit. However this new model contains a large, highly dense layer within the top 400 metres. Unlike the unconstrained model, this inversion had access to more information about the structure and expected values within the subsurface.

The result is a model where much of the signal that was assumed to originate deep beneath the surface in previous models is allocated to a relatively shallow region.

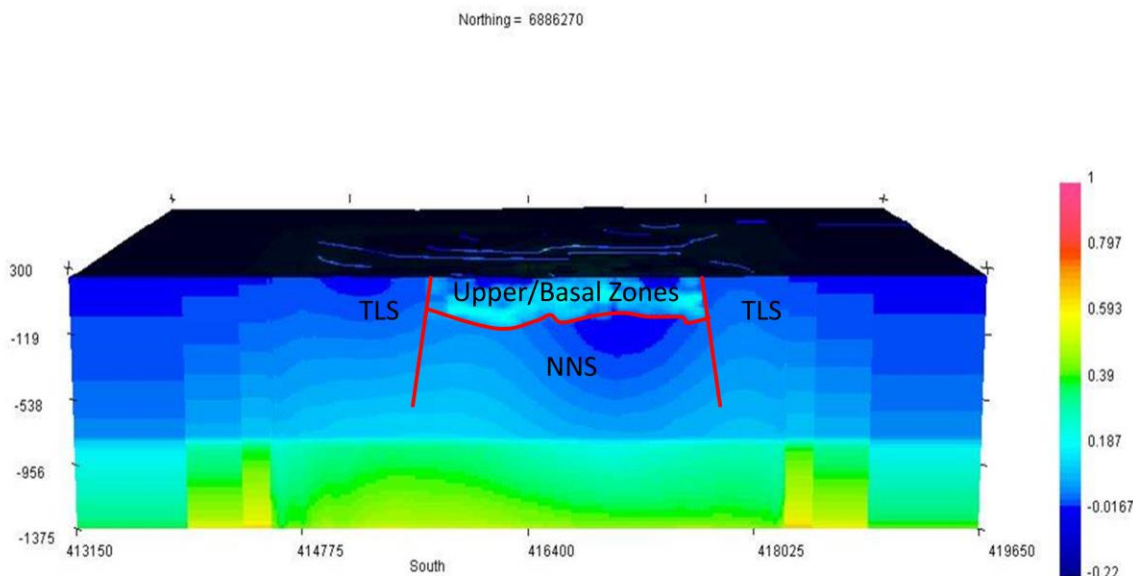


**Figure 3.11: Cross-section of the constrained gravity inversion for the Thor Lake study area (northing line 6885270, facing north). A laterally interpolated reference model was used in the inversion. Units on the right side represent density in  $\text{g/cm}^3$  above or below  $2.67 \text{ g/cm}^3$ . Scale on the left is elevation ASL in metres. The approximate interpretation of the Thor Lake syenite, Nechalacho nepheline syenite and Upper/Basal Zones have been included.**

The layer of high density forms a dome-like structure that extends from the surface at the apex down to depths of approximately 300 metres. The anomaly extends for approximately 1800 metres in the east-west direction and approximately 2000 metres in the north-south direction. Therefore, based on its geometry and location, it can be inferred that this represents the densely packed layer of secondary minerals after eudialyte that hosts the Nechalacho deposit. Another way to evaluate the reliability of a model is to assess not only whether it agrees with known geological processes in the

region, but also if the model as a whole is geologically plausible. An effective way to do this is through the representation of the anomaly as an isosurface (**Figure 3.12**).

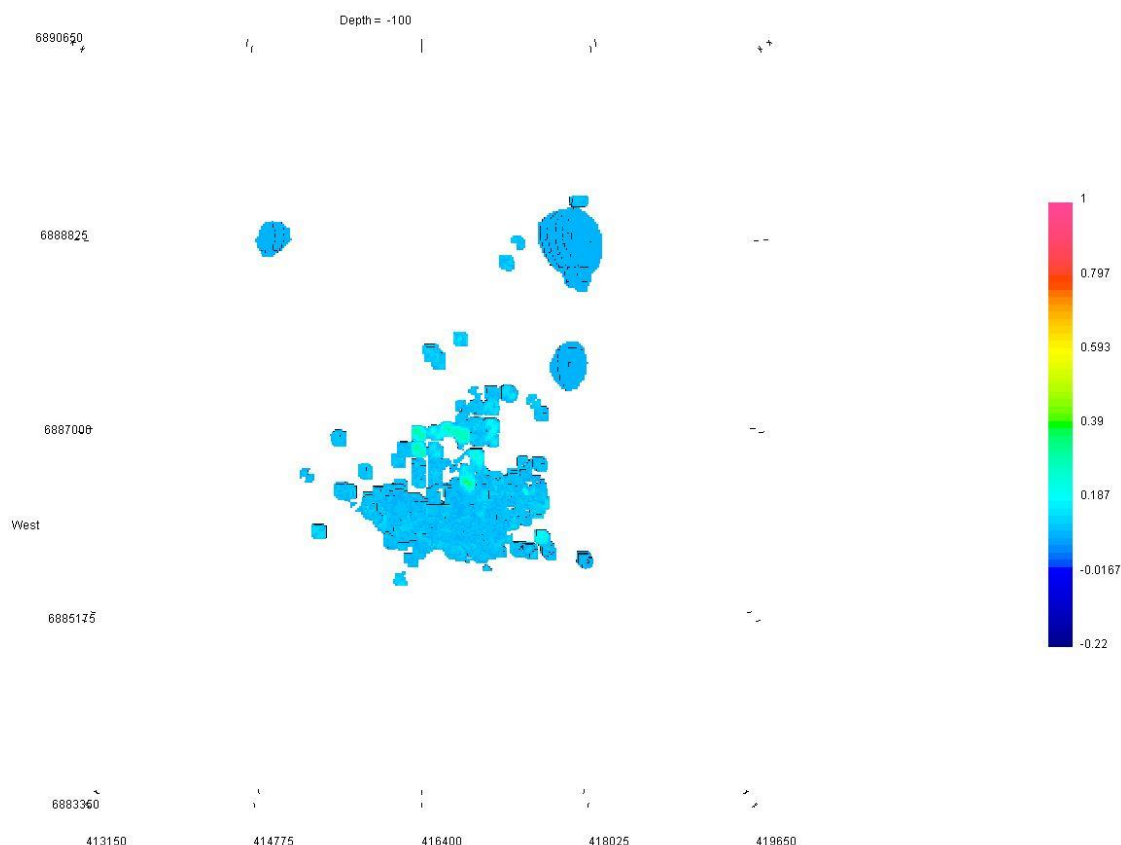


**Figure 3.12: A density isosurface of the shallow, high density anomaly. The figure displays densities greater than  $+0.1 \text{ g/cm}^3$  within the top 400 metres. Units on the right side represent density in  $\text{g/cm}^3$  above or below  $2.67 \text{ g/cm}^3$ .**

The isosurface representation of the modelled deposit shows a relatively smooth layer of highly dense material. Aside from the bulk mass near the centre of the inversion area, there are other small zones where highly dense material has been modelled. These zones could represent pockets of densely packed mineralization or artifacts of inversion.

However, it is also possible that they represent further extensions of the deposit that have been modelled as isolated features rather than a continuation of the main body. **Figure**

**3.13** shows a geological model by *Ciuculescu et al.* (2013) with the density isosurface approximately positioned as an overlay. This geological model was created based on drillhole measurements and knowledge of subsurface geological trends. The figure shows the difference in interpretation of the small isolated body just north of the main body. In the geological model, this drillhole measurement data point was assumed to be a continuation of the main body, where in the geophysical model, the inversion has modelled it as a separate entity. A future exploration goal to drill between these two bodies would help discern between these two possibilities and help to better evaluate the potential increase in REE mineralization to the north.

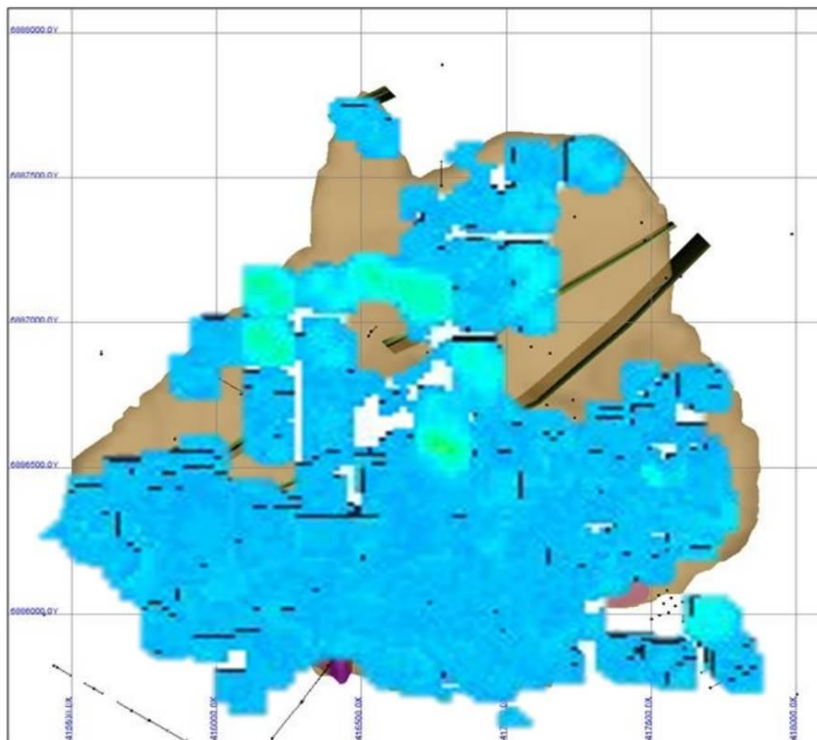


**Figure 3.13:** The isosurface for the shallow density anomaly approximately overlain on a geological model from *Ciuculescu et al.* (2013) to show the geometrical and

**geographical similarities. Northing values range from line 6885500 to line 6888000 and easting values range from line 415500 to line 418000.**

### 3.3.2 New Magnetic Results

Improvements to the inversion workflow as well as the similarities in the geometry of the density anomaly to the magnetic susceptibility anomaly lead to a second pass at the inversion of magnetic data. As discussed above, the previous magnetic susceptibility model by *Kouhi and Tiampo* (2016) resolved a subhorizontal, yet relatively discontinuous highly susceptible layer (**Figure 3.1**). The model is a by-product of the wavenumber filtered data inverted using constraining data in cells where core magnetic susceptibility measurements were taken.

To avoid the increase in potential error that arises from manipulating the airborne data using filtering techniques, the inversion was rerun for the deeper mesh that was used in the inversion of gravity data. Additionally, a new three-dimensional magnetic reference model was calculated with the goal to increase lateral continuity in the final model (**Figure 3.14**). When creating the minimum boundary model file, small negative susceptibilities were allowed in order to allow the inversion more freedom to resolve the structure of the deposit and match the reference model. While this is unphysical, these small negative susceptibilities will not greatly alter the result, and may allow the freedom necessary to resolve the bottom of the anomaly. **Figure 3.15** shows a cross-section and geological interpretations from the new magnetic model.

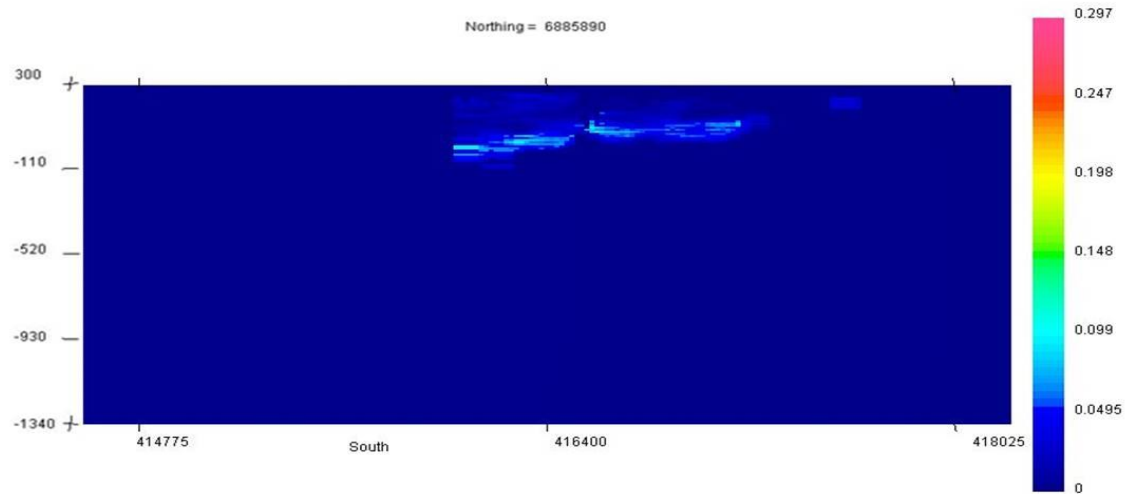


**Figure 3.14:** Sample cross-section from the three-dimensional reference model for core magnetic susceptibility data created using lateral interpolation methods (northing line 6885890 [UTM], facing north). Units on the right side represent magnetic susceptibility in SI units. Scale on the left is elevation ASL in metres.

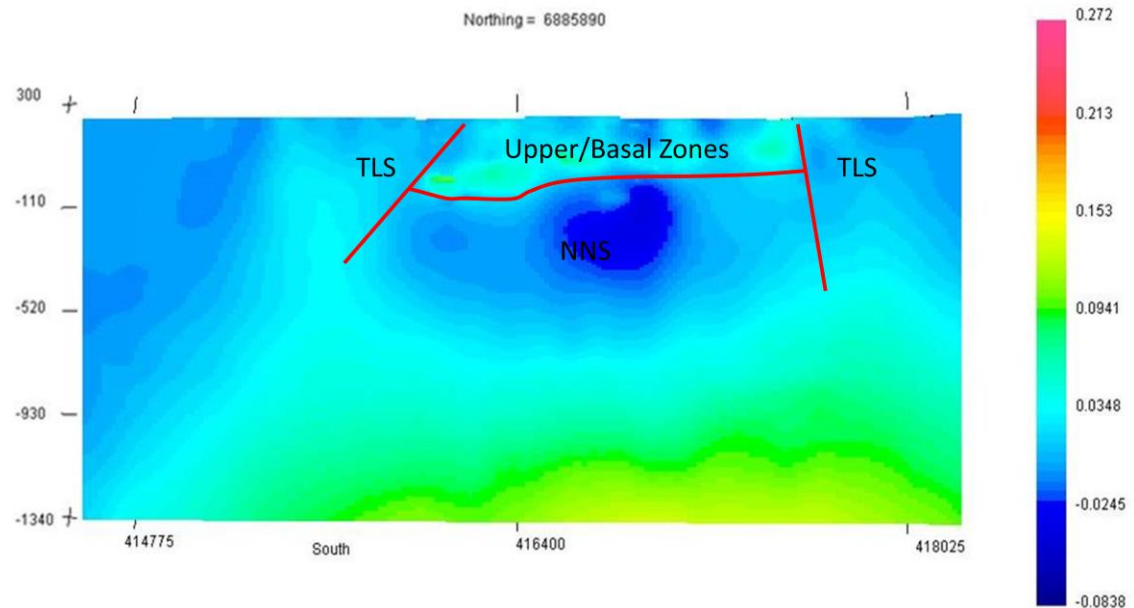


**Figure 3.15:** Cross-section of the new constrained magnetic inversion for the Thor Lake study area (northing line 6885890, facing north). A laterally interpolated reference model was used in the inversion. Units on the right side represent

**magnetic susceptibility in SI units. Scale on the left is elevation ASL in metres. The approximate interpretation of the Thor Lake syenite, Nechalacho nepheline syenite and Upper/Basal Zones have been included.**

The first major distinction between this model and previous models is the apparent lateral continuity that was lacking in earlier models (**Figure 3.16**). Aside from the continuity, the general shape of the anomaly agrees well with both previous susceptibility models as well as the density model. However, the issue of negative magnetic susceptibilities does arise in the centre cells of the two small pockets beneath the anomaly. While this is geophysically unrealistic, the main takeaway from the model is the structure of the deposit. Cooperative inversion methods will ideally help to maintain this structure when susceptibilities are forced above zero in future models.

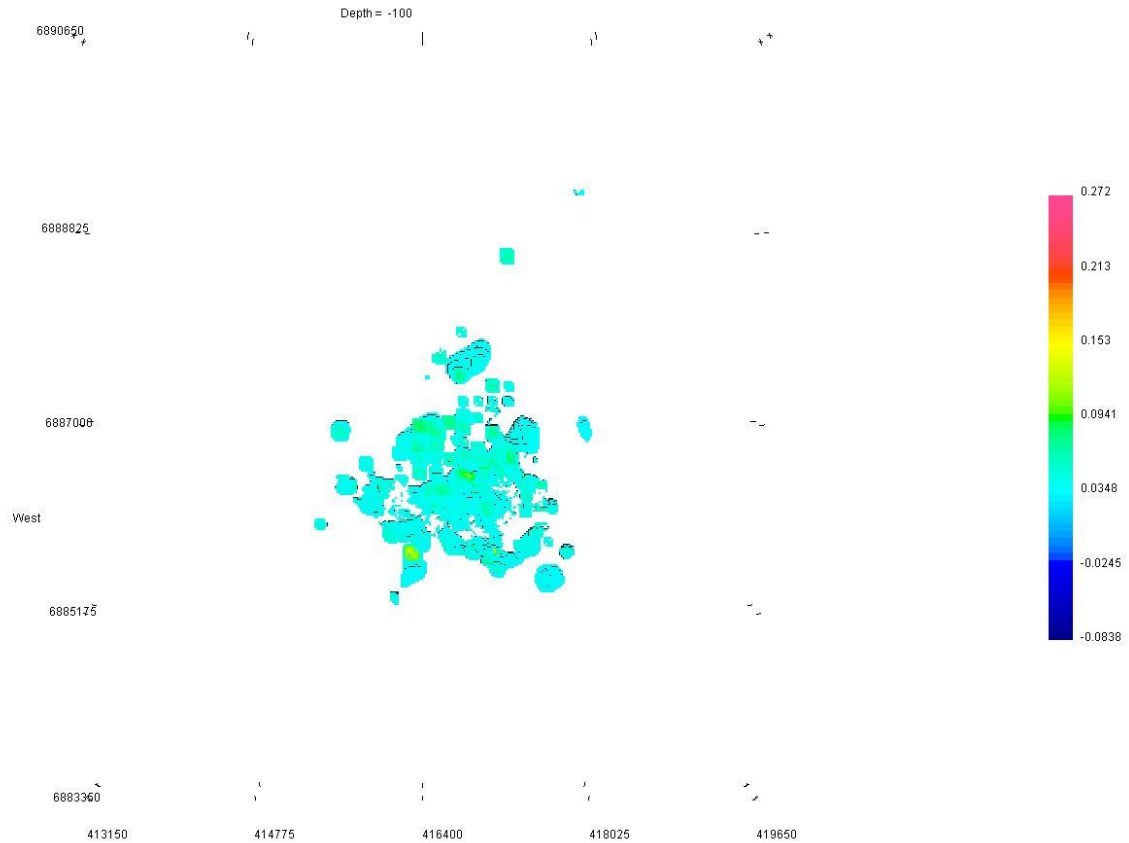


**Figure 3.16: An isosurface of the shallow high magnetic susceptibility anomaly. The figure displays susceptibilities greater than 0.04 SI within the top 400 metres. Units on the right side represent magnetic susceptibility in SI units.**

Structure and lateral continuity are two of the main improvements of the new magnetic model over previous versions. More potentially overlooked differences include the surface trends. **Figure 3.17** shows the surface magnetic susceptibilities from the improved magnetic model. There is a north-west trending structure with higher susceptibilities north of the deposit and a few north-east trending features with slightly increased susceptibilities running over top of the deposit. These could be the first appearance in these inversions of the Indin swarm and the Hearne swarm dykes, respectively, that are known to cross-cut the region (*Mumford and Cousens, 2014*).



These features were not discernable in the previous magnetic model, although their magnetic signatures were evident in the airborne data (*Kouhi and Tiampo, 2016*).

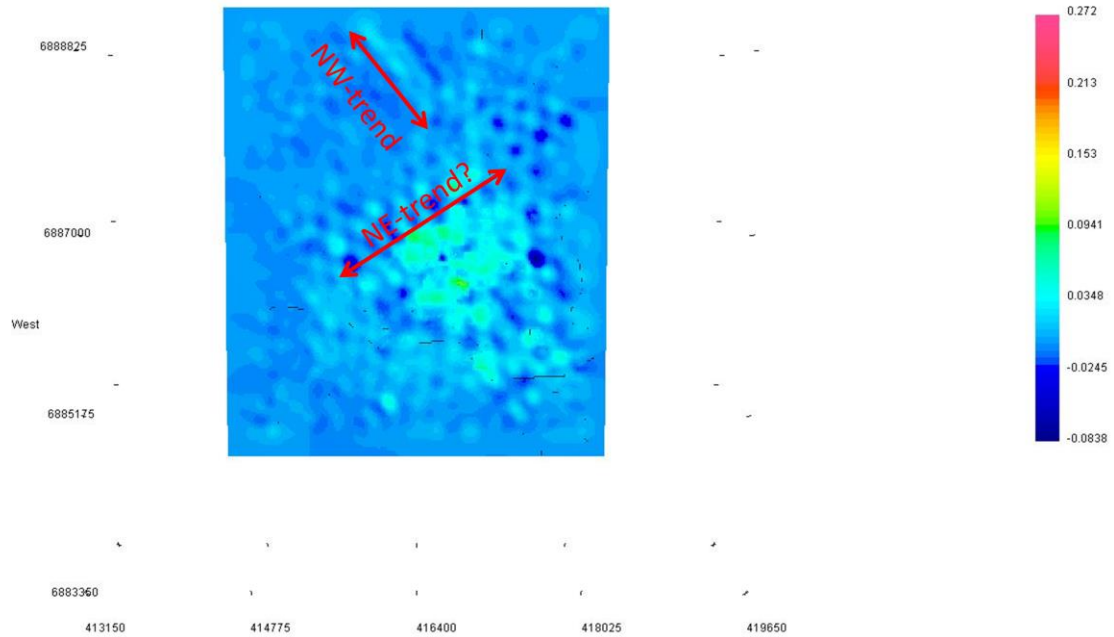


**Figure 3.17: A view of the new magnetic susceptibility model from above, looking at the surface. There are northeast trending lines in the centre of the model and a northwest trending line north of the deposit which may delineate subsurface dykes.**

### 3.3.3 Joint Inversion

Joint inversion techniques described in the previous section were applied to the density model and the new magnetic susceptibility model with the goal of improving the resolution of the true boundaries of the deposit. There are several key parameters involved in implementing the joint technique. First, the cut-off parameters for the normalized gradient must be estimated. The sum of the normalized gradients ranges from 0 to 1. One must decide whether to incorporate all gradients, even those that are

relatively low, in order to determine smoothing weights or decide to only include gradients that are larger than a certain threshold. Once a threshold is in place, the intensity with which the smoothness weights are scaled with the gradient is the next important decision. A high intensity factor means that cells with high gradients will have their smoothness greatly penalized while cells with low gradients will have the smoothness greatly promoted. Finally, the choice of which cells to include in the structure-based cooperative inversion can have a significant impact on the final model.

The first set of joint inversions were carried out using smoothness weights that were scaled across all gradients with a low intensity scaling factor. All cells in the volume were included, with the exception of the padding cells, and five iterations were run.

**Figure 3.18** is a cross-section from both the density and magnetic susceptibility models.

The density model displays little to no change from previous models and it does not appear to have influenced the magnetic susceptibility model. This is likely caused by using too low of an intensity scaling factor, as the influence of the joint method is not significant enough to see changes in the results. The susceptibility model appears to have lost structure.

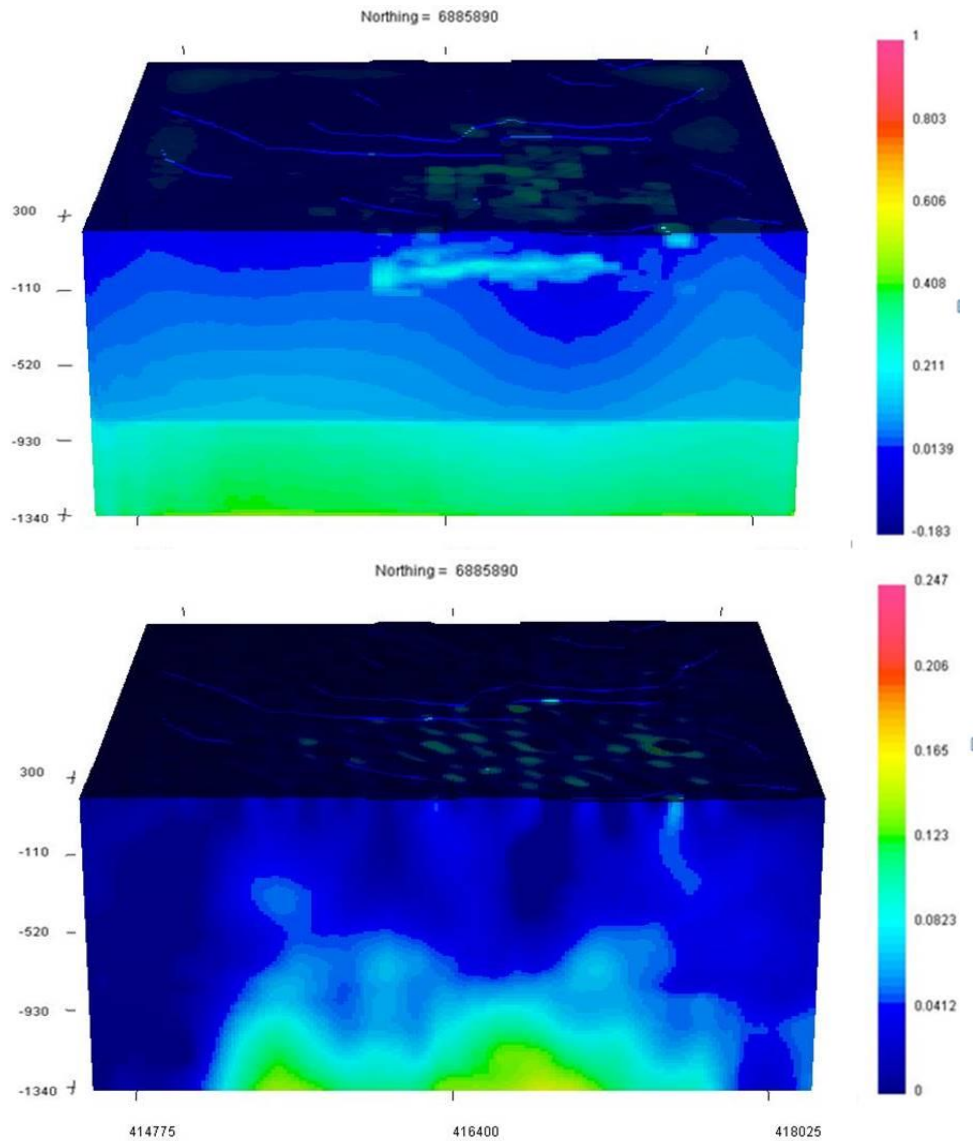


**Figure 3.18:** Cross-sections of the northing line 6885890 [UTM] obtained through joint inversion. The joint inversion included all cells with no threshold and a low intensity factor. The top figure is a density model with units displayed in  $\text{g/cm}^3$  above or below  $2.67 \text{ g/cm}^3$  and the bottom figure is a magnetic susceptibility model with units displayed in SI units. Units on the left side represent depths in metres ASL.

The next joint inversion attempt was run including all cells with a high intensity factor for 3 iterations. **Figure 3.19** shows a sample cross-section of the best results. The

magnetic susceptibility model is beginning to display some of the structure that the density model displays at shallow depths again but, the density model has now been influenced by the magnetic data. This influence has greatly smoothed the moderate to large depths while almost completely erasing the shallow anomaly. The effect of the joint process are evident in these models, however signs of over-influence are apparent. Over-influence occurs when the inversion is run with an intensity factor that is too high. As the intensity factor increases, the smoothness of the model is penalized greatly and cells are increasingly forced toward reference model values, resulting in discontinuous, non-geological artifacts. It appears as if the deeper structure of the magnetic model is influencing the density model in a negative way, although the shallow structure in the magnetic model seems to be improving. These results are likely a product of trying to influence the same structure on both models, even in deeper cells where density anomalies are not necessarily expected to coincide with anomalies in magnetic susceptibility. It should be noted that an important distinction between the gravity and magnetic signals is their origin and the processes by which their sources were formed. While both anomalies are expected in the host rock for the deposit, the rest of the structure may differ quite significantly. The secondary magnetite that is being modelled as magnetic susceptibility was formed through hydrothermal processes and was an overprint on preliminary lithology. On the other hand, the highly dense layer that hosts the deposit was formed through magmatic processes. Therefore, while both signals should correspond with similar structures in the shallow subsurface, there is no such guarantee deeper beneath the surface.

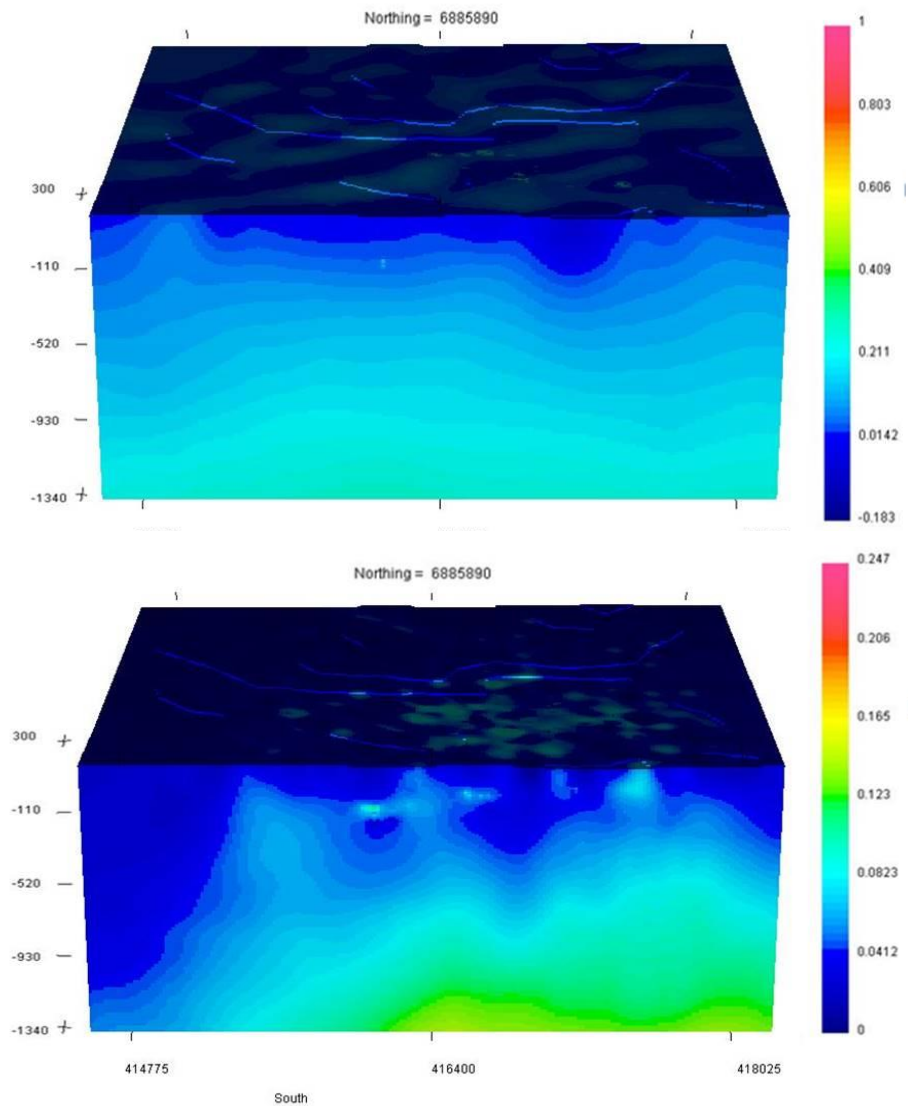


**Figure 3.19: Cross-sections of the northing line 6885890 [UTM] obtained through joint inversion. The joint inversion included all cells with no threshold and a high intensity factor. The top figure is a density model with units displayed in  $\text{g/cm}^3$  above or below  $2.67 \text{ g/cm}^3$  and the bottom figure is a magnetic susceptibility model with units displayed in SI units. Units on the left side represent depths in metres ASL.**

With the different processes that form the structure in mind, the next joint inversion included only the cells contained within the top 400 metres. The rest of the cells were set

to default smoothing weights so changes in the density structure in these cells are not projected on the susceptibility model, and vice versa. A high intensity factor was used and sample cross-sections from the second iteration are shown in **Figure 3.20**. The density model once again looks quite similar to past models, however the susceptibility model appears relatively smooth with subhorizontal features that coincide with predicted subsurface geology. The long wavelength signal is contributing to a magnetic high deep within the mesh and the short wavelength signal is contributing to subhorizontal magnetic high similar to the isolated magnetic model.

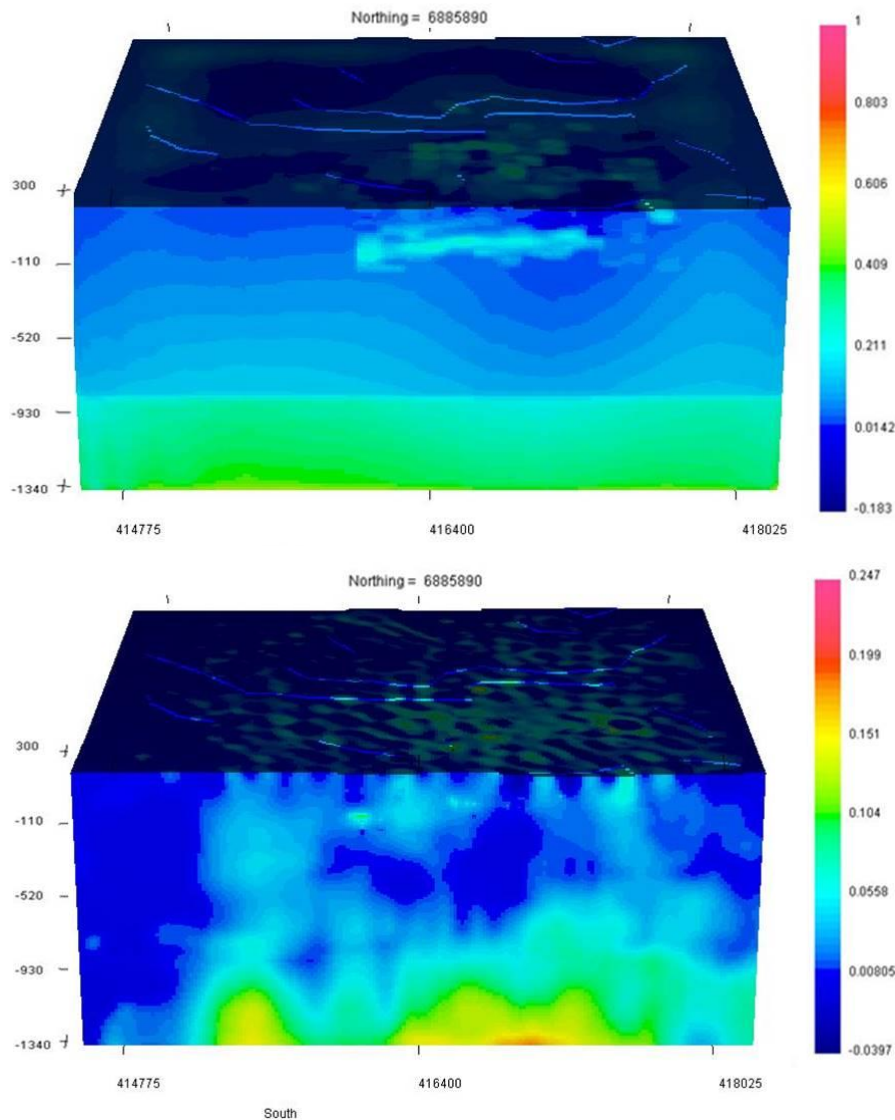


**Figure 3.20: Cross-sections of the northing line 6885890 [UTM] obtained through joint inversion. The joint inversion included only cells in the top 400 metres with no threshold and a high intensity factor. The top figure is a density model with units displayed in  $\text{g/cm}^3$  above or below  $2.67 \text{ g/cm}^3$  and the bottom figure is a magnetic susceptibility model with units displayed in SI units. Units on the left side represent depths in metres ASL.**

The isosurface (**Figure 3.21**) shows that this susceptibility model is similar in shape and size to isolated models, although it is more discontinuous laterally. This is likely because

the intensity factor is too high. Other evidence of its over-influence can be seen in **Figure 3.22**. The cells that are influenced by the drillhole also are clearly visible in the model. This is because as per **Equation 5** in chapter 1, as smoothness factors decrease, more emphasis is placed on the smallest component. Therefore smoothness penalties are forcing the cells closer to the reference model.

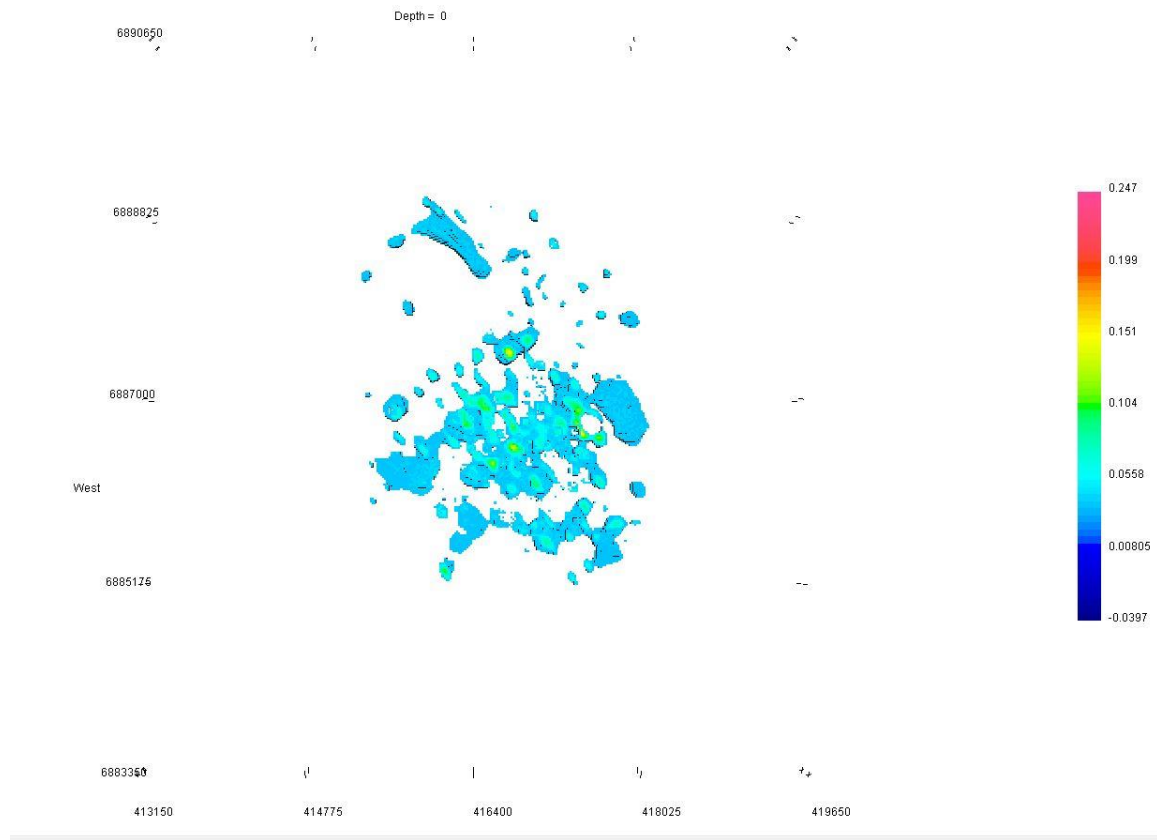


**Figure 3.21:** An isosurface of the shallow high magnetic susceptibility anomaly from the joint inversion using only the top 400 metres, no threshold and a high intensity factor. The figure displays susceptibilities greater than 0.04 SI within the top 400 metres. Units on the right side represent magnetic susceptibility in SI units.



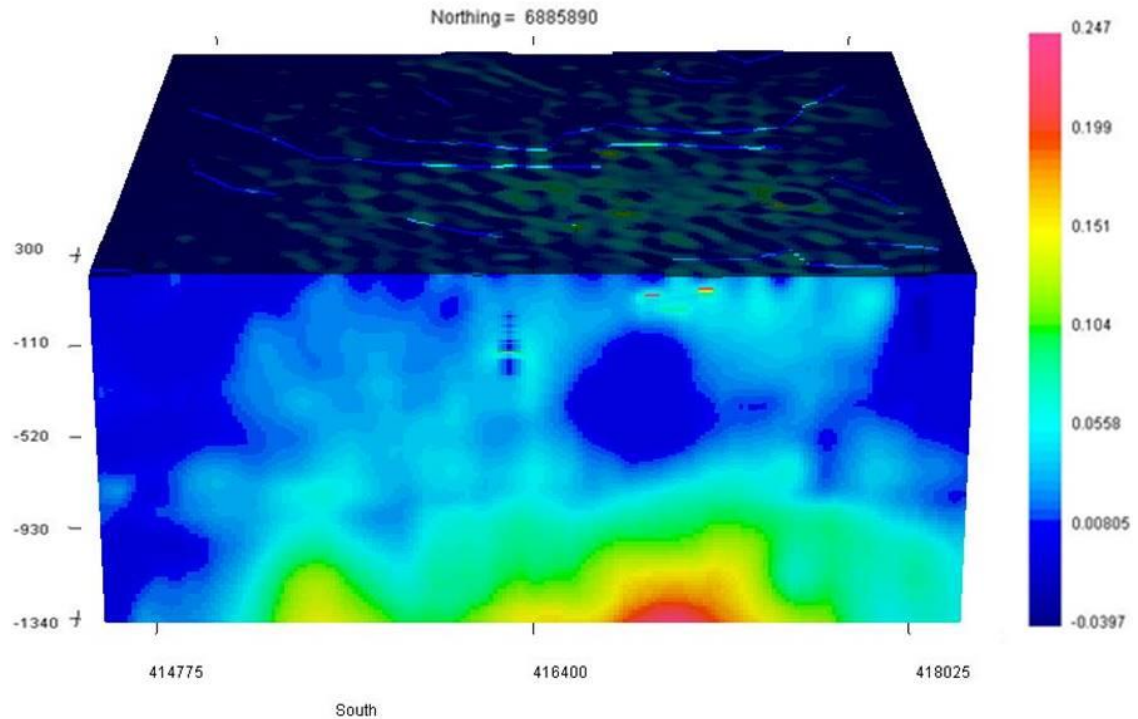


**Figure 3.22: Cross-section from the joint inversion using only the top 400 metres, no threshold and a high intensity factor (northing line 6885690 [UTM]). This figure shows the effects of over-influencing the model in the joint inversion process. If the intensity factor is too high, the model is forced closer to the reference model, which results in cells where the influence a drillhole is evident.**

The final parameter that has not been discussed is the threshold value. A final joint inversion was run using a threshold value of 0.25. This means that only cells that have gradients large enough (normalised value greater than 0.25) will affect the smoothness weights. All other cells are set to the default. Similar to the last inversion, only the top 400 metres will be considered as influencing cells and a moderate intensity factor was used. The magnetic susceptibility cross-section (**Figure 3.23**) shows a relatively smooth shallow subhorizontal anomaly. This model is similar to the isolated magnetic inversion

but, the issue resulting from the negative susceptibilities has now been removed, representing a more realistic model.

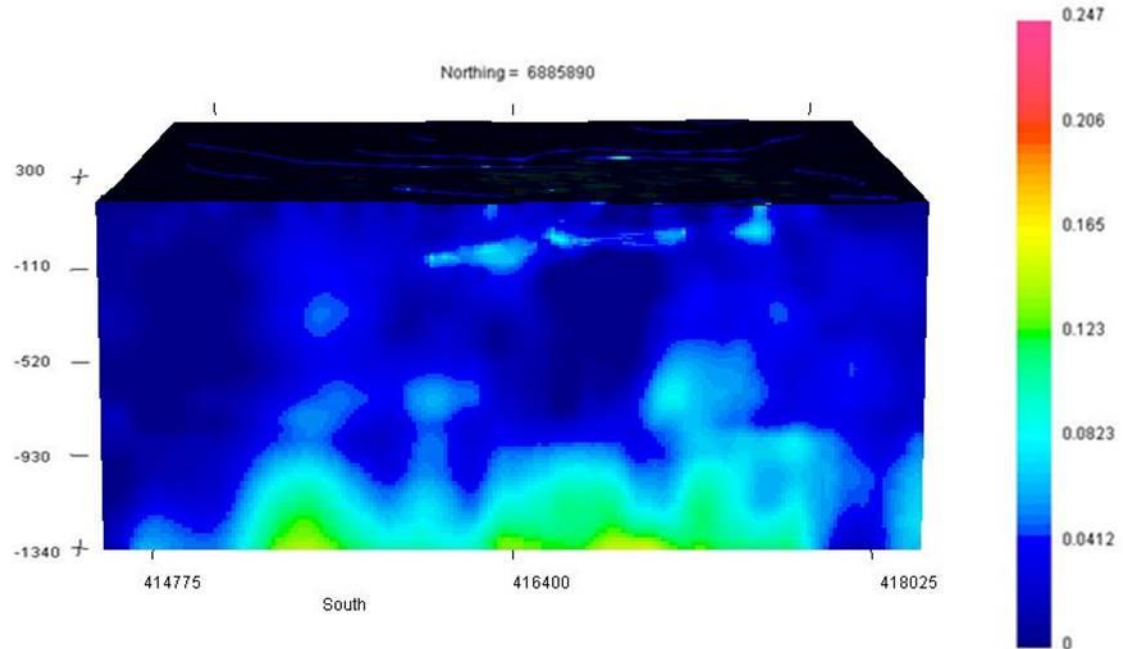


**Figure 3.23: Magnetic cross-section of northing line 6885890 [UTM] obtained through joint inversion. The joint inversion included only cells in the top 400 metres with a threshold of 0.25 and a high intensity factor. The figure is a magnetic susceptibility model with units displayed in SI units. Units on the left side represent depths in metres ASL. Note that model susceptibilities no longer contain negative values.**

## 3.4 Discussion

### 3.4.1 Lateral Interpolation vs. Kriging

The lateral interpolation method for enhancing subsurface geophysical datasets proved to be quite effective. In order to test its validity against more traditional methods, a three-dimensional reference model was calculated using a method of ordinary kriging. Kriging is a statistical approach to solving scarce sampling issues through interpolation using the

variability of known data points in the vicinity (*Samsonov, 2007*). Ordinary kriging is a method of geostatistical interpolation that does not rely on knowing the mean of the data and thus it is the simplest application to this problem (*Chilès and Delfiner, 2012*). The kriging approach fits a variogram to nearby points to assess the variability and interpolates a model that fits the statistical trend of the variogram as well as the known data points (*Journel, 1974*). For comparison to the lateral interpolation model, two-dimensional interpolation using ordinary kriging was carried out on each of the layers of the  $x$ - $y$  plane. While three-dimensional kriging is possible, this two-dimensional method provides a simple, computationally inexpensive way to directly compare the results of the two techniques.

A Gaussian variogram was chosen because it had the best correlation with the data (**Figure 3.24**). Kriging was completed layer-by-layer in Matlab, using code adapted from *Schwanghart (2010)*. A sample cross-section of the resulting three-dimensional reference model is displayed in **figure 3.25**. Even before this reference model is used in a geophysical inversion, it displays some interesting characteristics that the laterally interpolated model did not. It is clear that the kriging method is over-smoothing the data points across the full extent of the mesh, creating a layer of high susceptibility approximately 400 metres thick. While it seems that the kriging method has smoothed out the high susceptibility region over entire  $x$ - $y$  planes at shallow depths, some of the structure seen in the lateral interpolation model is still prevalent. The issue with smoothing could be the result of the minimization of the estimation variance which often causes the kriging process to smooth true spatial fluctuations (*Journel, 1974*). The deposit was targeted strategic drilling, therefore a large proportion of the drillholes cross-

cut the anomalous region. Since the deposit is subhorizontal, the variance for values is going to be relatively small, resulting in the overestimation of densities outside of the boundaries of the deposit due to smoothing. Another interesting point to consider is the sensitivity of the ordinary kriging process to the specification of the variogram (*Chilès and Delfiner, 2012*). An inappropriately chosen variogram fit can result in kriging estimates that differ from the ideal estimates. While the Gaussian variogram fit the data reasonably well, there will be some error contributed from this part of the process.

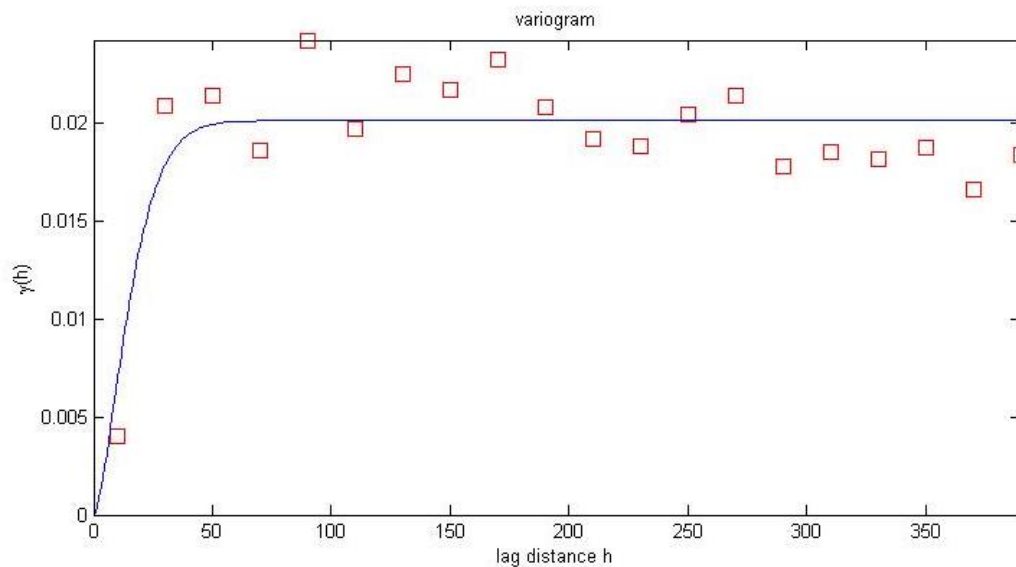


**Figure 3.24:** A sample variogram showing the fit of the data to a Gaussian trend. Created with code modified from *Schwanghart (2010)*.

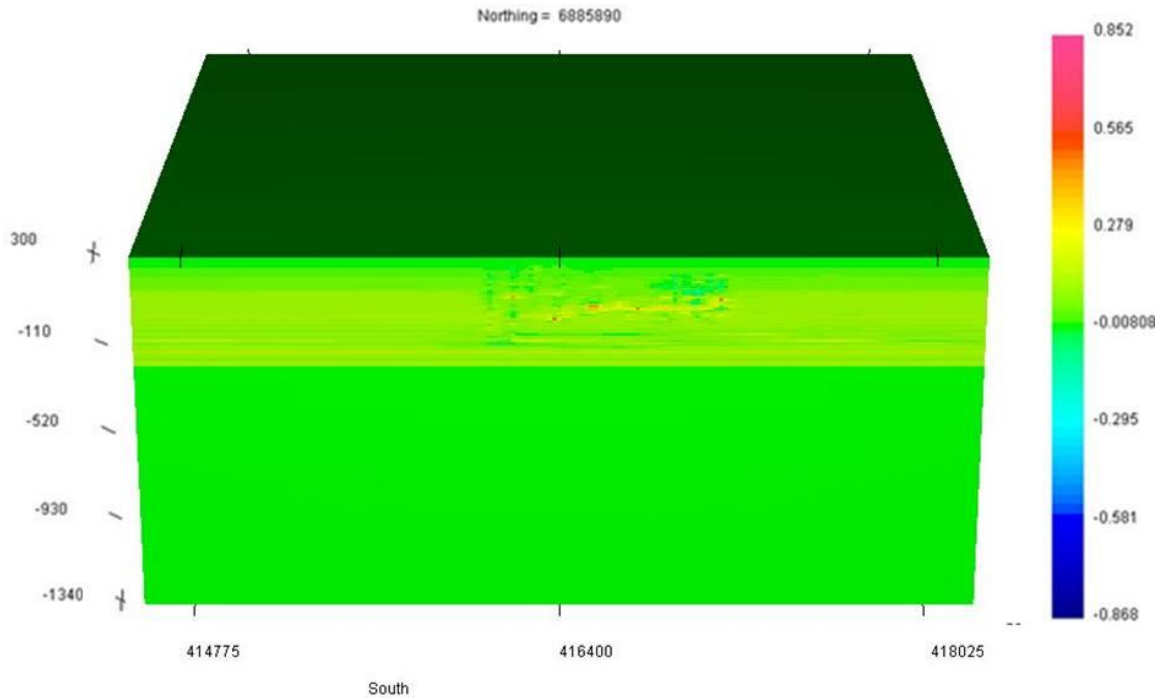


**Figure 3.25: Sample cross-section from the three-dimensional reference model for core density data created using ordinary kriging methods (northing line 6885890 [UTM], facing north). The reference model shows evidence of lateral over-smoothing. Units on the right side represent density in  $\text{g}/\text{cm}^3$  above or below  $2.67 \text{ g}/\text{cm}^3$ . Scale on the left is elevation ASL in metres.**

The kriging model was then used as a reference model and its variances were used to calculate the maximum and minimum boundary constraints for an inversion of gravity data. **Figure 3.26a** shows a cross-section from the resulting inversion. The shallow regions of this model display some of the features of the subhorizontal high density layer seen in the lateral interpolation model as well as some of the layering seen at moderate depths. However, the over-smoothing overprints a large portion of the shallow structure and results in an overall smooth model. **Figure 3.26b** is a cross-section of the previous laterally interpolated model with the same density scaling as the kriging model for comparison. The lateral interpolation technique proposed earlier appears to do a better

job of resolving a reliable reference model for the given drillhole geometry and subsurface structure. A modified, more statistically robust version of the lateral interpolation method described in the previous sections was also tested for its validity. Rather than assign ranges for the maximum and minimum boundary models based solely on the uncertainty value for a given cell, the weighted standard deviation plays a role in this method. The weighted standard deviation was based on the deviations of each of the values binned into each cell and combined with the uncertainty value to assign error tolerances. This method did not appear to enhance the resulting inversions; rather it appeared to hinder them due to not allowing a large enough range for the cells. This method could be investigated further by increasing the role that the uncertainty value plays in the range, although it also might be due to the fact that individual cells generally do not have large enough populations of data to calculate a reliable standard deviation.

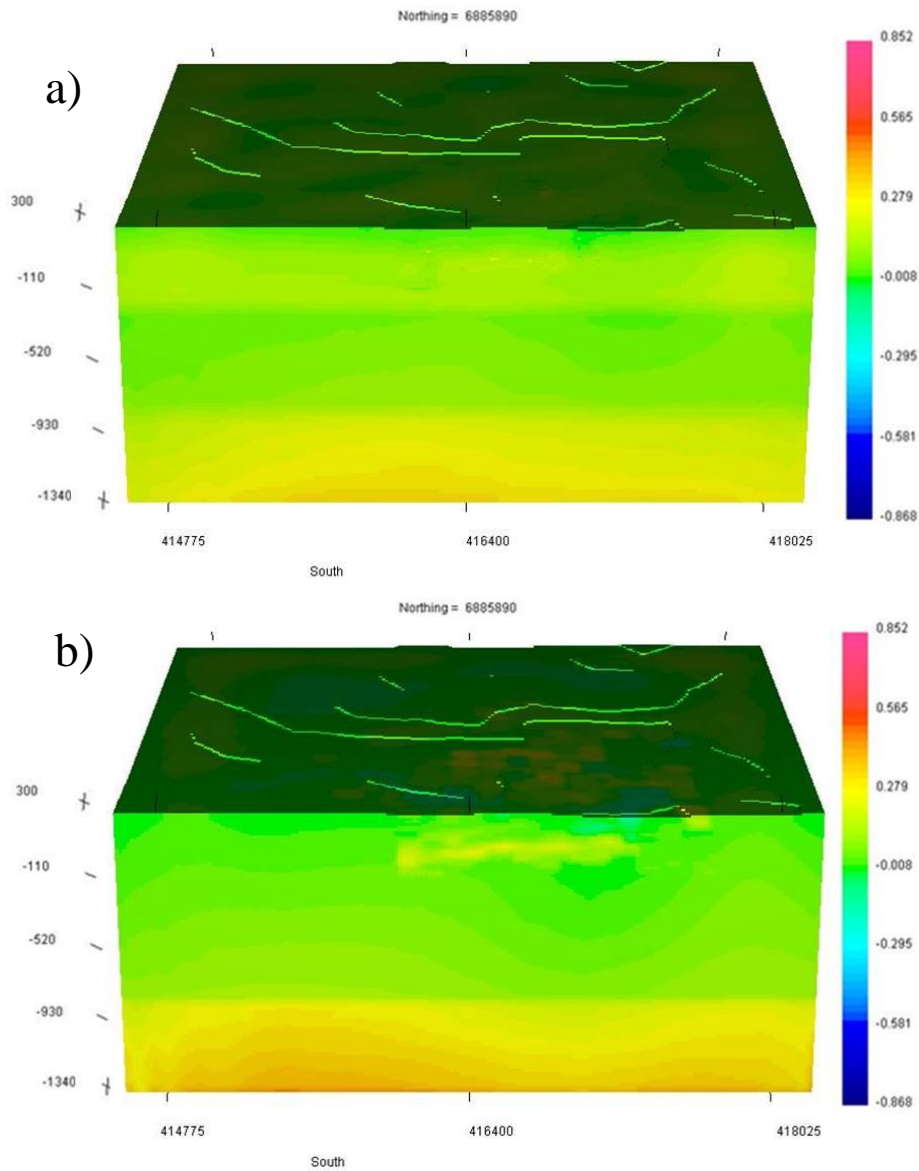


**Figure 3.26: Comparison cross-sections of constrained gravity inversions for the Thor Lake study area (northing line 6885270, facing north). In the top figure, a reference model obtained via ordinary kriging was used while in the bottom figure, the laterally interpolated model has been rescaled for comparison. Units on the right side represent density in  $\text{g/cm}^3$  above or below  $2.67 \text{ g/cm}^3$ . Scale on the left is elevation ASL in metres.**

### 3.4.2 Comparison Between Gravity and Magnetism

In the case of the Nechalacho deposit, a layer of densely packed minerals also is expected that is heavily altered and with a high magnetic signature. Based on geological modelling from drillhole data, initial magnetic susceptibility models were reasonably successful in approximating the boundaries of the deposit. However, these models lacked geological plausibility. Density models presented in this work appear to have been the most successful in providing a geologically realistic model that agrees with previous research. Improved magnetic susceptibility models displayed better continuity that resembles both previous geologic models as well as the density models obtained in this work. Overall, the shallow high density anomaly and the shallow high susceptibility anomaly are geographically and geometrically similar. **Figure 3.27** is a set of isosurface maps that show the correspondence of the anomalies from each dataset. With the cut-off for a density anomaly set at  $+0.1 \text{ g/cm}^3$  and the cut-off for magnetic susceptibility at 0.04 SI, the cells that contain both anomalies form a relatively flat surface extending for almost 2000 metres in each direction. The individual density and susceptibility components are systematically similar in shape and size with small but significant differences. In the magnetic susceptibility component the north-west trending Indin dyke is clearly visible north of the deposit while, in the density component there is a semi-spherical body northeast of the deposit. It is important to note that this is focusing on the top 400 metres and that the bottom layers of the models differ more significantly.



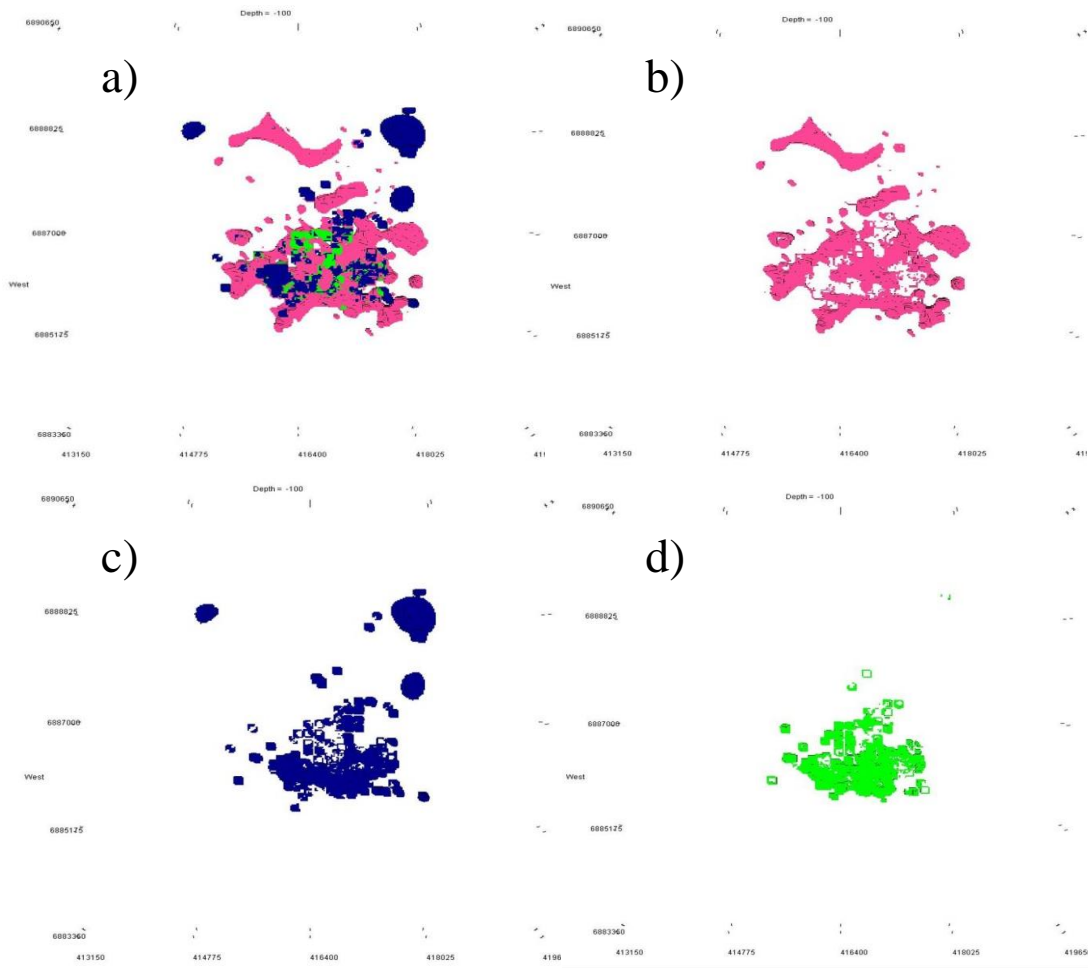


**Figure 3.27: Isosurfaces comparing shallow density anomalies to shallow magnetic susceptibility anomalies (top 400 metres). Cells that have density values greater than  $+0.1 \text{ g/cm}^3$  are considered density anomalies while cells that have magnetic susceptibility values greater than  $0.4 \text{ SI}$  are considered susceptibility anomalies. Figure (a) shows all cells that are considered anomalies. Cells that are only considered susceptibility anomalies are in pink (b), cells that are only considered density anomalies are in blue (c) and cells that are anomalous for both fields are in green (d).**

### 3.4.3 Validity of Joint Inversion

As discussed above, the different processes by which the sources of the gravity and magnetic signals were created has a large impact on the validity of a joint inversion to

solve the problem. This is where the key parameters make a large difference in how effective the joint inversion is. Preliminary joint inversion parameters resulted in the over or under-influence of the individual models in the result, while the choice of cells used to influence the joint model also proved to be vital. Results shown here demonstrate the potential, and the complexity, of using cooperative techniques to better resolve a model. Best model results for both datasets in this study were the result of using prior geological knowledge to choose the region within the inversion area where the geophysical sources should align. From there, it is a matter of trial and error to find suitable influence factors and thresholds.

Another technique is to increase the threshold with each subsequent inversion as more inversions are run (*Lelièvre et al.*, 2009). This means that with each iteration the number of cells that influence the final model is decreasing resulting in later iterations and only taking very large changes in geophysical properties into account. This technique could help further resolve boundaries of the deposit and result in more definitive edges, but at the risk of promoting further discontinuity in certain cells within the deposit. Overall, the joint inversion process obtained a more geologically realistic magnetic susceptibility model. However, when comparing the isosurface maps from individual and joint inversion techniques, it is difficult to discern any significant differences in the shape or size of the anomaly (**Figure 3.28**).

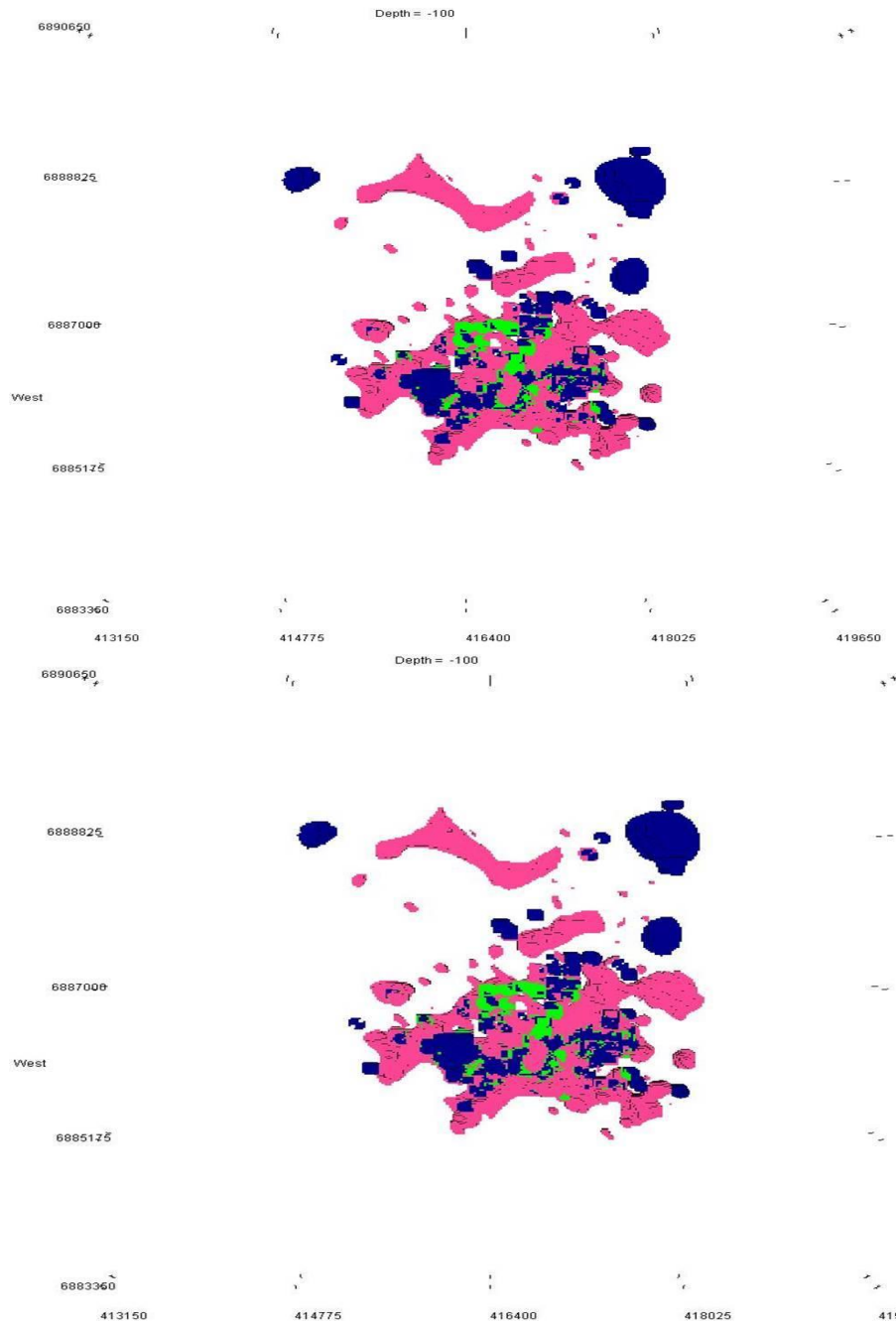


**Figure 3.28: Comparison isomaps of anomalous cells for the final joint inversion (top) and the final individual inversions (bottom). Green cells are cells where both density and magnetic susceptibility are considered anomalous, blue are only density and pink are only susceptibility. Both maps are nearly identical.**

### 3.5 Conclusions

When it comes to inverse modelling, each step in the inversion workflow from starting models to inversion parameters can be crucial. In this study, a new technique in laterally interpolating measured geophysical properties has proven to be an effective method to help constrain an inversion. Airborne gravity data was successfully inverted to obtain a subsurface density model that agrees with prior geophysical work with magnetics, as well as geological modelling. Similar techniques were also successful in improving the magnetic susceptibility model from the previous study (*Kouhi and Tiampo, 2016*). While effective here, this method relies on the assumption that the subsurface geology that contributes to the signal is relatively subhorizontal in structure and should be used with caution in other regions. This is similar to all geophysical inversion constraints in that, while inverse modelling is a robust technique, each parameter, constraint or method must be tailored to the specific problem at hand.

The validity of joint inversion techniques was investigated for the Nechalacho deposit with limited, but overall positive results. While definitive boundaries of the deposit are not any clearer after cooperative inversion techniques than they were prior, both models have incorporated the multiple potential field results. The magnetic susceptibility model benefited from the density structure to better separate the magnetic high at shallow depths from the deeper signal as well as to eliminate negative susceptibilities. Overall, the boundaries of the deposit did not undergo significant change, however the fact that both joint and individual inversion techniques delineated similar bodies can speak to the confidence in the modelled results.

### 3.6 References

**Avalon Rare Metals Inc., 2014.** Lithology and Magnetic Susceptibility Data. Prepared by Ben Webb.

**Blakely, R. J., 1995.** Potential Theory in Gravity and Magnetic Applications. Cambridge University Press, Cambridge, UK, 464p.

**Chilès, J.P. and Delfiner, J., 2012.** Kriging with an Unknown Mean; in Geostatistics: Modeling Spatial Uncertainty, Second Edition. John Wiley and Sons Inc., New York, United States, p. 164-182.

**Ciuculescu, T., Foo, B., Gowans, R., Hawton, K., Jacobs, C., and Spooner, J., 2013.** Technical Report Disclosing the Results of the Feasibility Study on the Nechalacho Rare Earth Elements Project. Micon International Limited, Toronto, Canada, 307p.

**Davidson, A., 1978.** The Blatchford Lake Intrusive Suite, an Aphebian Plutonic Complex in the Slave Province, Northwest Territories; Paper 78-1A, Geological Survey of Canada, Ottawa, p. 119-122.

**Davidson, A., 1982.** Petrochemistry of the Blachford Lake Complex Near Yellowknife, Northwest Territories; in Uranium in Granites, ed. Y.T. Maurice; Paper 81-23, Geological Survey of Canada, Ottawa, p. 71-79.

**Journel, A.G., 1974.** Geostatistics for Conditional Simulation of Ore Bodies; Economic Geology, v. 69, p. 673-687.

**Kouhi, D.W., and Tiampo, K.F., 2016.** Current Status of Magnetic Inversion Project at Thor Lake, N.W.T.; Open-File Report 2016-06, Northwest Territories Geological Survey, Yellowknife.

**Lelièvre, P. G., Oldenburg, D. W., and Williams, N. C., 2009.** Integrating Geological and Geophysical Data Through Advanced Constrained Inversions; Exploration Geophysics, v. 40, p. 334-341.

**Möller, V., and Williams-Jones, A.E., 2016.** Petrogenesis of the Nechalacho Layered Suite, Canada: Magmatic Evolution of a REE-Nb-rich Nepheline Syenite Intrusion; *Journal of Petrology*, v. 57, p. 229-276.

**Mumford, T., 2013.** Petrology of the Blatchford Lake Intrusive Suite, Northwest Territories, Canada; PH.D., Carleton University.

**Mumford, T. R., and Cousens, B. L., 2014.** Constraints on the Relationships Between Paleoproterozoic Intrusions and Dyke Swarms, East Arm of Great Slave Lake, N.W.T., Canada; *Canadian Journal of Earth Science*, v. 51, p. 419-438.

**NRCan (Natural Resources Canada), 2011.** Blatchford Lake Grav-Mag Survey.

**Pinckston, D. R., and Smith, D. G., 1995.** Mineralogy of the Lake Zone, Thor Lake Rare-Metals Deposit, N.W.T., Canada; *Canadian Journal of Earth Science*, v. 32, p. 516-532.

**Samsonov, S.V., 2007.** Integration of Differential InSAR and GPS measurements for studying of surface deformation; PH.D., University of Western Ontario.

**Schwanghart, W., 2010.** Ordinary Kriging; Variogramfit; Experimental (Semi) Variogram; MathWorks File Exchange, Matlab, retrieved March 1, 2016.

**Sheard, E. R., Williams-Jones, A.E., Heiligmann, M., Pederson, C., and Trueman, D. L., 2012.** Controls on the Concentration of Zirconium, Niobium, and the Rare Earth Elements in the Thor Lake Rare Metal Deposit, Northwest Territories, Canada; *Economic Geology*, v. 107, p. 51-104.

**Sinclair, W.D., Hunt, P.A., and Birkett, T.C., 1994.** U-Pb Zircon and Monazite Ages of the Grace Lake Granite, Blatchford Lake Intrusive Suite, Slave Province, Northwest Territories; in *Radiogenic Age and Isotopic Studies: Report 8*; Geological Survey of Canada, Current Research 1994-F, p. 15-20.

**UBC-Geophysical Inversion Facility, 2013.** A Program Library for Forward Modelling and Inversion of Magnetic Data over 3D Structures, version 5.0; Developed under the

consortium research project, *Joint/Cooperative Inversion of Geophysical and Geological Data*, Department of Earth and Ocean Sciences, University of British Columbia, Vancouver, British Columbia.

## Chapter 4

### 4 Relating Magnetic Susceptibility of Deep-Hole Samples to Mineralogy in Thor Lake, N.W.T.

*In this section, magnetic susceptibility values for drill core from the Nechalacho deposit at Thor Lake, NT were measured and validated using field instruments in previous research. These measurements also were used as constraints for magnetic inversions in the region. In this study, in-lab techniques for measuring the magnetic susceptibility of off-cut blocks were used to once again validate the measurements taken in the past. These measurements on specific samples also were used to relate their geophysical properties to their mineralogy. It is shown that rare earth element mineralization increases proportionally with magnetic susceptibility in the Nechalacho deposit. In addition, there is evidence that density may also play a role in REE mineralization if the sample displays even small amounts of magnetic susceptibility. Finally, the use of computational colour analysis to identify minerals shows the potential for use as a preliminary method for designating mineral abundances in a simplified mineral system.*

#### 4.1 Introduction

Magnetic susceptibility is an important geophysical property that helps to distinguish different lithological units within the Blatchford Lake Intrusive Complex (BLIC). The upper zone and the basal zone that host the large concentrations of rare earth elements (REE) associated with the Nechalacho deposit formed through a combination of magmatic and hydrothermal processes. Magmatically, the layered intrusion was formed from the top downward and the bottom upward, resulting in the layering associated with the upper and basal zones crystallizing last (Möller and Williams-Jones, 2016). Sodalite



and nepheline crystallized early, followed by potassium-feldspar resulting in higher iron concentrations in these densely-packed layers. Further enrichment with iron due to the lack of primary magnetite and olivine phases associated with the high concentrations of sodium in the melt compounded to produce the host layers that were highly enriched in aegirine and eudialyte (*Möller and Williams-Jones, 2016*). The extensive hydrothermal alteration that then overprinted the majority of the original mineralogy in the deposit left behind an abundance of magnetite as the principal alteration mineral, specifically in these regions of high iron content (*Sheard et al., 2012*). Therefore magnetic susceptibility can be used as a proxy for the intensity of the alteration in the deposit due to the strong signal associated with magnetite.

#### 4.1.1 Previous Measurements

Avalon Rare Metals Inc. (Avalon) has drilled core for more than 400 holes in the region. Previous magnetic susceptibility measurements were taken on each of the cores at 1 metre intervals using a KT-9 Kappameter hand-held instrument (*Avalon, 2013*). These measurements provide excellent spatial coverage of the region and were used in the geophysical inversions described in previous sections to constrain the models. A second set of measurements were taken on a subset of the cores with a KT-10 instrument by *Nichols (2014)*. The cores chosen for these secondary measurements were based on targeting known subsurface geology. The measurements were taken by holding the stub of the instrument up against the rounded outer edge of the core. Measurements were then used to constrain preliminary magnetic and gravity inversions of the region (*Tiampo and Nichols, 2014*). Before the data from *Avalon (2013)* was used in the work in Chapter 2 (*Kouhi and Tiampo (2016a)*) mentioned above, it was compared with the updated KT-10

measurements to ensure its accuracy and reproducibility (**Figure 4.1**). While there are some slight variations in the magnitudes of the magnetic susceptibility, the overall peaks in both datasets appear to coincide, but with a slight offset in the depth domain. This can potentially be attributed to human error in the recorded depths for each measurement on the core. Any small offsets in measurements on the scale of a few metres depth will not affect the inversion results, as this is too fine resolution compared to the cell size. Otherwise, the original measurements by Avalon appear to be of reasonable quality.

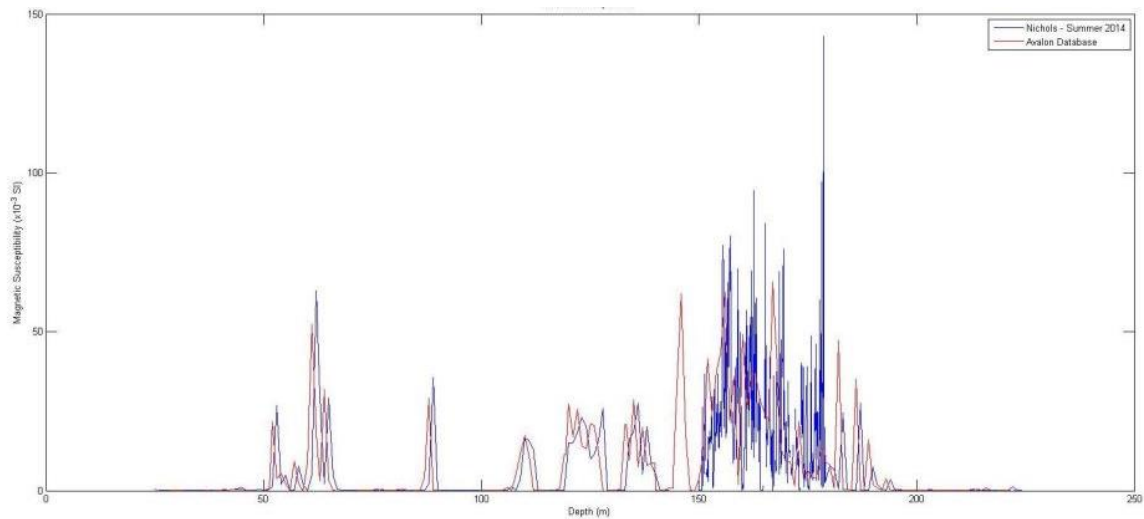


**Figure 4.1: Comparison of the magnetic susceptibilities measured on the core from drillhole L09-160 by Avalon (2013) and Nichols (2014) using KT-9 and KT-10 instruments, respectively. Note the slight offset in the depth domain.**

#### 4.1.2 Off-Cut Blocks

The majority of the drillholes extend to depths between 250 metres and 400 metres in order to target the Nechalacho deposit. However, drillhole L09-194 was drilled to approximately 1065 metres depth and therefore allows for the analysis of the intrusion as a whole (Avalon, 2013). Extensive mineralogical work has been completed by Möller

and Williams-Jones (2016) on the entire intrusion and its petrogenesis while Sheard *et al.* (2012) focused mainly on those shallow depths where the deposit itself is hosted. Off-cut block samples that remained from the research by Möller and Williams-Jones (2016) where available for further study of the magnetic susceptibility of the intrusion. The set of samples consists of 70 off-cut blocks that were left over from the creation of thin-sections. Although they vary in total volume, most samples are approximately rectangular in shape and have one smooth face. The depths of the core from which the samples were taken vary in distribution and extend from 46.4 metres to 1065.4 metres depth. Möller and Williams-Jones (2016) subdivided the intrusion into fourteen different lithological units based on mineralogy and textural properties (NLS-1 to NLS-14). The distribution of the off-cut blocks throughout these units can be seen in **Table 4.1**.

**Table 4.1: Brief summary of off-cut samples from drillhole L09-194**

Unit	Description	Depth Range	Number of Samples
NLS-4	Foyaite – host of upper and basal zones	Top 135m	1
NLS-5	Upper Zone	15-60m	1
NLS-6	Basal Zone	95-135m	7
NLS-8	Microlayered Aegirine-Nepheline Syenite	150-300m	12
NLS-9	Rhythmically Layered Syenite	300-450m	22
NLS-11	Microlayered Annite-K-Feldspar-Sodalite-Aegirine Syenite	480-720m	4
NLS-12	Trachytoidal Annite-Sodalite Syenite	720-870m	12
NLS-13	Aegirine-Sodalite Foyaite	870-1065m	10

<b>NLS-14</b>	K-Feldspare-Sodalite-Aegirine Syenite	1065-?? m	1
<b>Total</b>			<b>70</b>
<b>Table summarized from Möller and Williams-Jones (2016)</b>			

#### 4.1.3 This Study

The primary purpose of this study was to analyze the variability between the portable magnetic susceptibility measurements and the in-lab susceptibility measurements. This is important to the geophysical inversions in the previous sections because it provides an idea of the accuracy of the values used in the reference models. It is expected that both methods of measuring the magnetic susceptibility will yield peaks in signal at similar depths, however the magnitudes of the susceptibility values may vary. If the values vary with a systematic bias, the results could play an important role in future geophysical inversions.

A second research goal was to further tie the mineralogy of the deposit to the geophysical properties observed in the magnetic susceptibility measurements, as well as the modelled susceptibility values obtained through inversion. Work by *Sheard et al.* (2012) found that the principal alteration mineral associated with the deposit is magnetite, while work by *Möller and Williams-Jones* (2016) breaks down the deep hole (L09-194) into specific units including the REE mineralized upper zone and basal zone. The samples have been intensely studied from a mineralogical standpoint and can be assigned specific magnetic susceptibility values and then analyzed based on their lithological unit. The effect of the

mineralogy on the geophysical properties in each unit can be assessed in detail and related back to the models obtained in the geophysical inversions above.

Lastly, this study is a preliminary step toward analyzing the geophysical differences between hydrothermal and magmatic magnetite. Due to high activity of sodium in the melt, the magnetite phase is absent and thus there is no magmatic magnetite in the intrusion (*Möller and Williams-Jones, 2016*). While this does not bode well for a direct comparison of magmatic and hydrothermal magnetite in the deposit, it presents the opportunity to directly relate the effects of the abundance secondary magnetite to the magnetic susceptibility values.

## 4.2 Methods

### 4.2.1 Magnetic Susceptibility Measurements

The masses of each of the 70 samples were taken prior to magnetic susceptibility measurements. Each of the samples was weighed individually, using an analytical balance. Magnetic susceptibility measurements were performed using a benchtop Sapphire Instruments SI2b susceptibility meter. Before any measurements were made, the susceptibility meter was calibrated using a  $\text{MnO}_2$  sample with known magnetic susceptibility for reference. Susceptibilities were measured as mass-based susceptibilities with SI output units in  $\text{m}^3/\text{kg}$ . Each measurement was corrected for instrument drift by running the susceptibility meter without a sample before and after the sample measurement. The process was then repeated, once again correcting for instrument drift in order to ensure the repeatability of each measurement. The software outputs the average of the two measurements as well as the standard deviation of all measurements

on the same sample. While the standard deviation of a population of two cannot be considered statistically significant, checking this value ensures that the measurement was reproducible. If the two measurements differed significantly, a third measurement was taken and the standard deviation was reassessed.

#### 4.2.2 Mass- to Volume-Based Susceptibility Conversion

Once the mass-based magnetic susceptibility measurements were taken, the values were compared to each other. However, in order to compare these values to the susceptibilities measured using the KT-9 and -10 instruments from the geophysical inversions, they must be converted to dimensionless, volume-based susceptibilities. The conversion is trivial if the density values are known for each sample, using the equation:

$$\chi_v = \chi_m \rho \quad (1)$$

where  $\chi_v$  is the volume-based susceptibility in SI units,  $\chi_m$  is the mass-based susceptibility and  $\rho$  is the density of the sample in  $\text{kg/m}^3$  (Hinze *et al.*, 2013). For the drillhole L09-194, core density measurements are available at approximately 5 metre intervals for the length of the core. For the purpose of this study, density measurements at depths that most closely matched sample depths were assumed for the density of each sample. It also should be noted that the magnetic susceptibility meter is capable of performing direct volume-based susceptibility measurements if the volumes of each sample are known initially. However, this study makes use of alternative methods of measuring magnetic susceptibility due to the solubility of the original sample label in water. Therefore traditional methods of measuring volume such as wet-dry techniques were not attempted here. Because the interpolation of densities from the core logs

potentially incorporates an additional error in the volume-based susceptibility calculations, a simple sensitivity analysis was conducted on the results (see Results section below).

## 4.3 Results

### 4.3.1 Mass-Based Magnetic Susceptibility

The results of the mass-based magnetic susceptibility measurements yielded values that span four orders of magnitude (**Figure 4.2**). It is important to note that these values are mass-based and, as a result, a relatively constant density must be assumed throughout all samples in order to compare values to one another. Also note there are no error bars because only two measurements were taken on each sample, therefore a reliable estimate of the error could not be assigned. Geophysical inverse modelling shows that density values range from approximately  $2.57 \text{ g/cm}^3$  to  $3.07 \text{ g/cm}^3$  (*Kouhi and Tiampo, 2016b*). This represents a percentage difference of approximately 17.7% between the two endpoint values. While significant, this difference is small enough to assume a relatively constant density in order to perform a relative comparison of the susceptibility values.

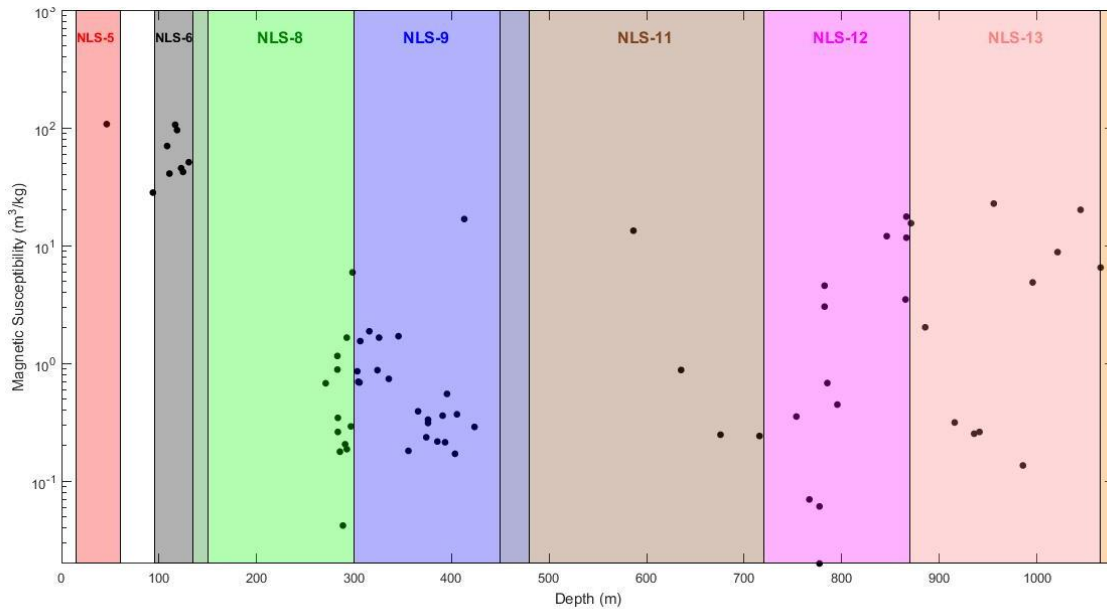


**Figure 4.2: Mass-based magnetic susceptibilities measured using the in-lab magnetic susceptibility meter. Lithological units are based from work by Möller and Williams-Jones (2016). Note there are no error bars because only two measurements were taken on each sample, therefore a reliable estimate of the error could not be assigned.**

Susceptibilities from the shallow units that are associated with the upper zone (NLS-5) and the basal zone (NLS-6) have the highest values and very little variance with depth. As depth increases down hole, the variability in the measured values appears to increase with relatively low susceptibility in the middle units (NLS-8 and -9) and a wide range of high and low susceptibility in the deeper units (NLS-11 to -14) (**Figure 4.2**).

#### 4.3.2 Volume-Based Magnetic Susceptibility

Converted volume-based susceptibility values are plotted over the previous measurements from Avalon (2013) in **Figure 4.3**. The in-lab susceptibility measurements and the field susceptibility measurements have corresponding peaks at similar depths for



the entire drillhole. While these high susceptibility regions occur at the same depth in both datasets, the in-lab measurements appear to be systematically higher in magnitude. The difference between the red and green data points can be considered a simple sensitivity analysis for the density values. This is important due to the large margin of error associated with using density measurements, which could be up to 2.5 metres deeper or shallower than the true sample depth. The green data points represent the volume-based susceptibilities assuming a constant density of  $2.67 \text{ g/cm}^3$  throughout the entire intrusion. The susceptibilities remain largely unchanged with the exception of the shallow data points, where the values decrease. This is because these units are truly much denser than the average density of  $2.67 \text{ g/cm}^3$ , therefore assuming the average density results in the under-estimation in susceptibility via **Equation 1** (*Kouhi and Tiampo, 2016b*). However, assuming a lower density value for these samples still results in the measured magnetic susceptibilities being higher than those measured on the cores.

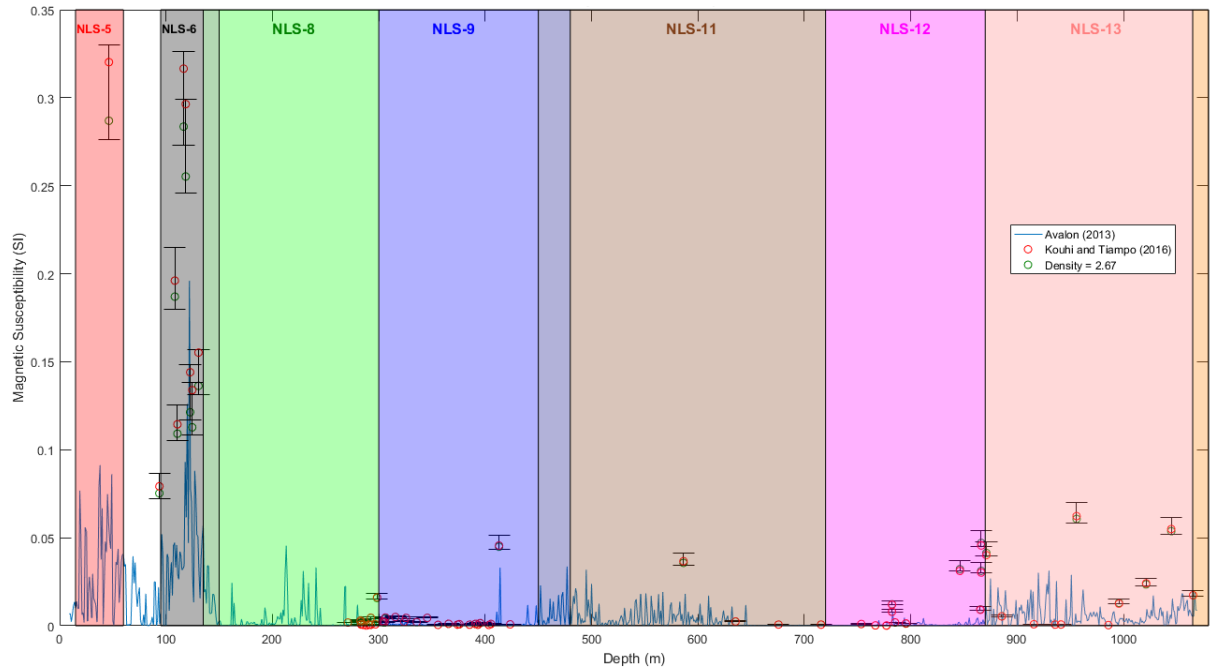


**Figure 4.3: Volume-based magnetic susceptibilities measured using the in-lab magnetic susceptibility meter (red circles). Green circles represent the susceptibilities using a constant density of  $2.67 \text{ g/cm}^3$  for sensitivity analysis. Lithological units are based from work by Möller and Williams-Jones (2016).**

## 4.4 Discussion

### 4.4.1 Geophysical Implications of the Mineralogy

Knowledge of the specific magnetic susceptibilities for each sample is important when relating the mineralogy to geophysics. A set of magnetic susceptibility values for samples where the mineralogy has been studied and interpreted can be an important basis for interpreting geophysical inversions. For example, the major alteration mineral in the upper units is magnetite, therefore high magnetic susceptibility values are expected here (Sheard *et al.*, 2012). From this study, samples in the upper 150 metres of the intrusion display the highest susceptibilities with values ranging from approximately 0.1 to 0.3 SI units. An exception to this trend is a sample from 93.75 metres depth, from the foyaite

unit (NLS-4) that hosts the upper and basal zones. This sample originates in the unit that hosts the highly susceptible layering, however it was formed in a sequence of layering that is sandwiched between the upper and basal zones that displays significantly less alteration (*Möller and Williams-Jones, 2016*). This is evident in its comparatively low magnetic susceptibility as well as the relative lack of magnetite upon visual inspection (**Figure 4.4**). This tie between the lithological unit and the magnetic susceptibility, and thus the estimated magnetite content, is important when interpreting geophysical models of the intrusion. While the resolution of such models may not detect each layering sequence within the foyaite unit, higher susceptibilities in this region can be attributed to those units that contain high concentrations of REE (NLS-5 and -6).

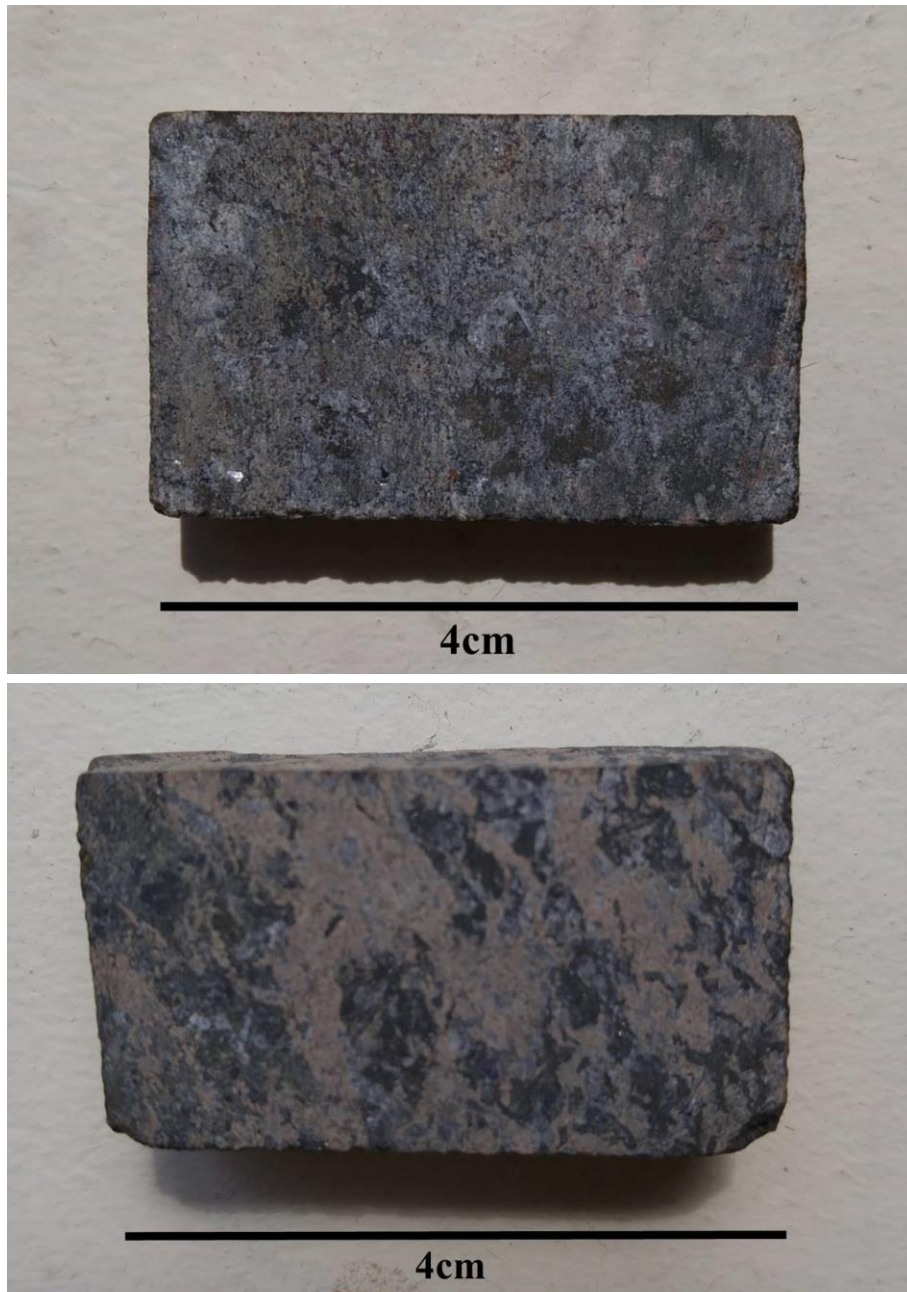


**Figure 4.4: Comparison of the visual mineralogy of a sample from 93.75 metres depth (top) and a sample from 118.5 metres depth (bottom). The top sample is from unit NLS-4 between the upper and basal zones while the bottom sample is from the basal zone (NLS-6). The bottom sample appears to contain significantly more magnetite by visual inspection. This is confirmed by the magnetic susceptibility measurements.**

Below the basal zone, magnetic susceptibilities vary from relatively low to negligible, with minor regions of high susceptibility, with values up to 0.05 SI. Samples with these higher susceptibilities appear to display magnetite forming rims around aegirine crystals (**Figure 4.5**). The geophysical importance of these regions relates to the allocation of deep-seated signal in magnetic susceptibility models. Geophysical inverse modelling solves for subsurface geophysical properties using measured data to constrain the models. Earlier chapters display models with relatively large susceptibility values at depth. Susceptibility measurements on samples from this drillhole can provide some insight that there may be pockets or layers that have been weakly altered to contain magnetite at depth. This may account for some of the extra magnetic signal, described in the results sections of both previous chapters, that is incorrectly allocated to padding cells at the bottom of the mesh.



**Figure 4.5:** A moderately susceptible sample from 1044.9 metres depth that shows potential evidence of aegirine altering to magnetite.

**Figure 4.6** is a density versus magnetic susceptibility plot for each sample that also displays the relationship between these variables, REE concentration and lithological unit. From this plot, a couple of interesting trends are evident. First, the relatively high densities and magnetic susceptibilities in samples from NLS-5 and -6 also contain high concentrations of REE as expected. The general trend displays magnetic susceptibility increasing with increases in density which implies that magnetite abundance could

potentially be a proxy for density as well as magnetic susceptibility. However, this trend only appears to fit for shallow units. Deeper units such as NLS-9 contain a similar range of densities to the shallower units, but with a lack of magnetic susceptibility increase. This suggests that there is much less magnetite at these depths, but another mineral is contributing to the density of these samples. All of the samples with the highest concentrations of REE are also highly susceptible. While a proportionally increasing relationship is apparent between REE concentrations and magnetic susceptibility, another factor affecting REE concentration may be density. It was noted above that REE concentration does not necessarily increase with denser samples, however in units where samples contain any significant magnetic susceptibility, it could be argued that these variables begin to increase proportionally.

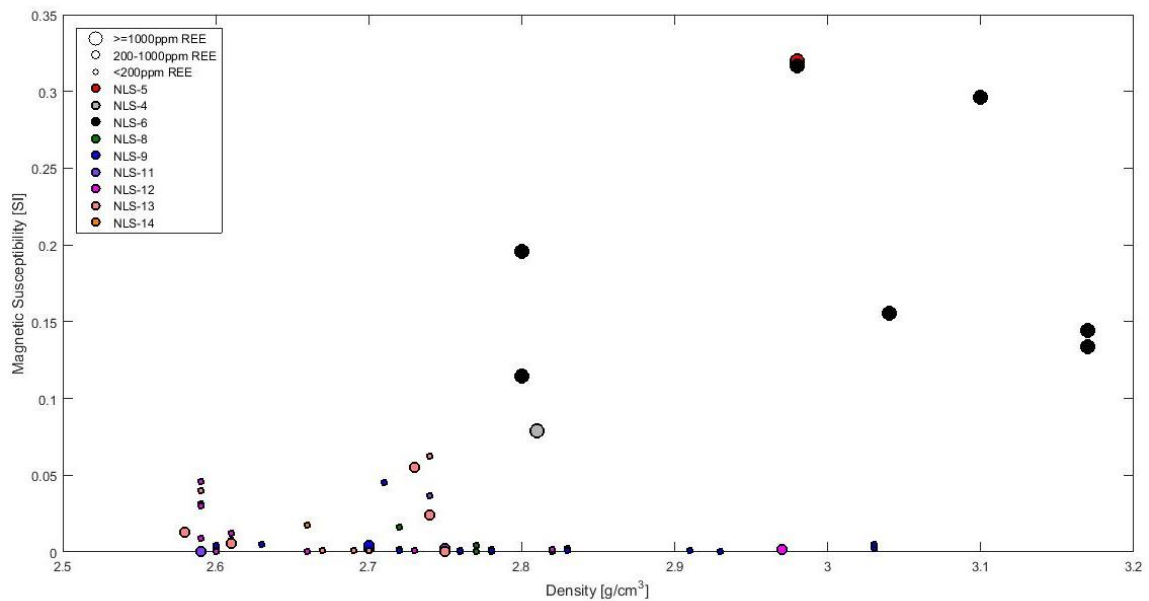


**Figure 4.6: Plot of density versus volume-based magnetic susceptibility for each sample. The approximate REE concentrations are represented by the sizes of the markers and the different colours represent the different lithological units.**

#### 4.4.2 Systematic Bias

**Figure 4.3** shows strong evidence for a systematic bias in the magnetic susceptibilities measured in the lab. Peaks in susceptibility occur in approximately the same positions in both datasets, however the magnitude of the measurements from the samples are systematically larger than the measurements from the core by a factor of approximately 1.5. **Figure 4.7** displays these values scaled down by this factor. There are a few potential sources that could account for this discrepancy. The first potential source that may result in some variation is the way in which the measurements are taken. The KT-9 instrument measurements were taken by placing the end of the instrument on the rounded exterior of the core. This could result in some systematic loss of signal due to coupling issues between the instrument and the curved surface of the core. The in-lab magnetic susceptibility meter measures the sample susceptibility as a whole by placing it in an enclosed field. Calibration error also could play a role, depending on how recently the portable instrument was calibrated using a standard; however, while potentially systematic, these errors are likely to be less significant. The lab instrument is calibrated prior to each use as described above. Finally, there may be error associated with the conversion from mass-based susceptibility and volume-based susceptibility. The inaccuracy of the density values for each sample plays a large role in this source of error. Due to the linear relationship between the sample density and the mass- to volume-based susceptibility conversion, changes in the density value assigned to the sample will change the susceptibility measurement proportionally. Assigning density values that were measured up to 2.5 metres away from the true sample depth is likely a source of random error and therefore cannot solely account for the systematic bias. Additionally,



sensitivity analysis on the effects of varying sample density also yields values higher than those obtained by *Avalon* (2013).

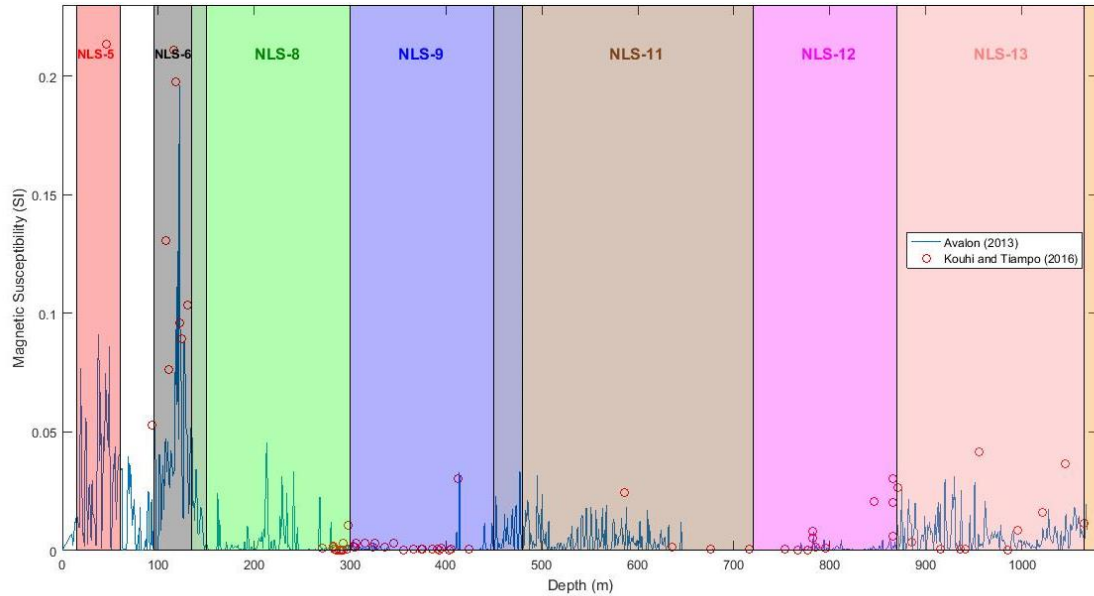


**Figure 4.7: Volume-based magnetic susceptibilities measured using the in-lab magnetic susceptibility meter, scaled down by a factor of 1.5. Lithological units are based from work by Möller and Williams-Jones (2016).**

While the majority of the susceptibility values from this study are larger than the values from previous measurements, the data point at 46.35 metres depth does not scale with the other values. Previous susceptibility measurements yielded values in the upper zone of as much as approximately 0.1 SI (*Avalon*, 2013). This data point represents the only sample within the upper zone unit and was measured at a value more than three times higher than previous measurements. A high susceptibility is anticipated, as the sample appears to contain significant amounts of magnetite (**Figure 4.8**). However, the difference between sample measurements and core measurements in this region also is significant. The

reason for this discrepancy is a target for future work, but it is interesting to note that this depth corresponds to the highest concentrations of REE (**Figure 4.9**).

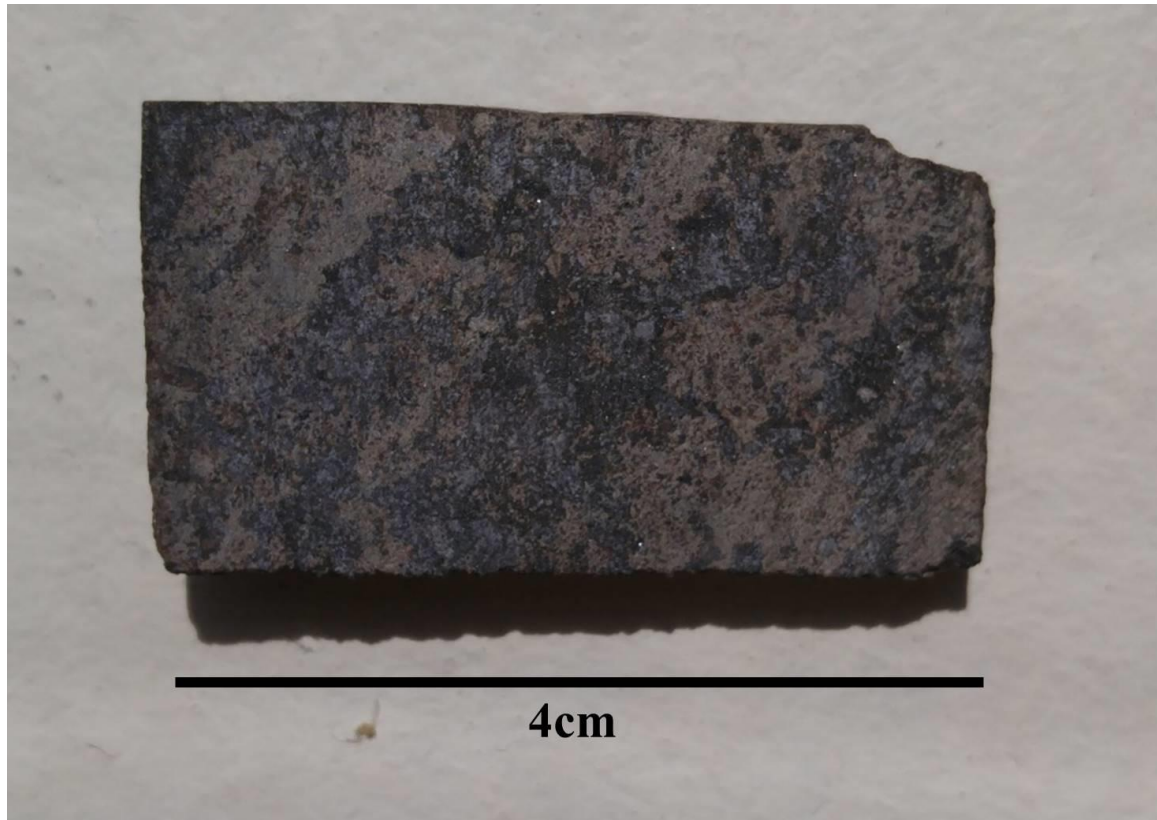


**Figure 4.8:** The only sample from within the upper zone (NLS-5). The measured magnetic susceptibility for this off-cut block is anomalously higher than previously measured by *Avalon* (2013). While most samples appear to be approximately 1.5 times higher in susceptibility than previously measured, this sample measured at values more than 3 times higher. Magnetite can be identified by visual inspection.

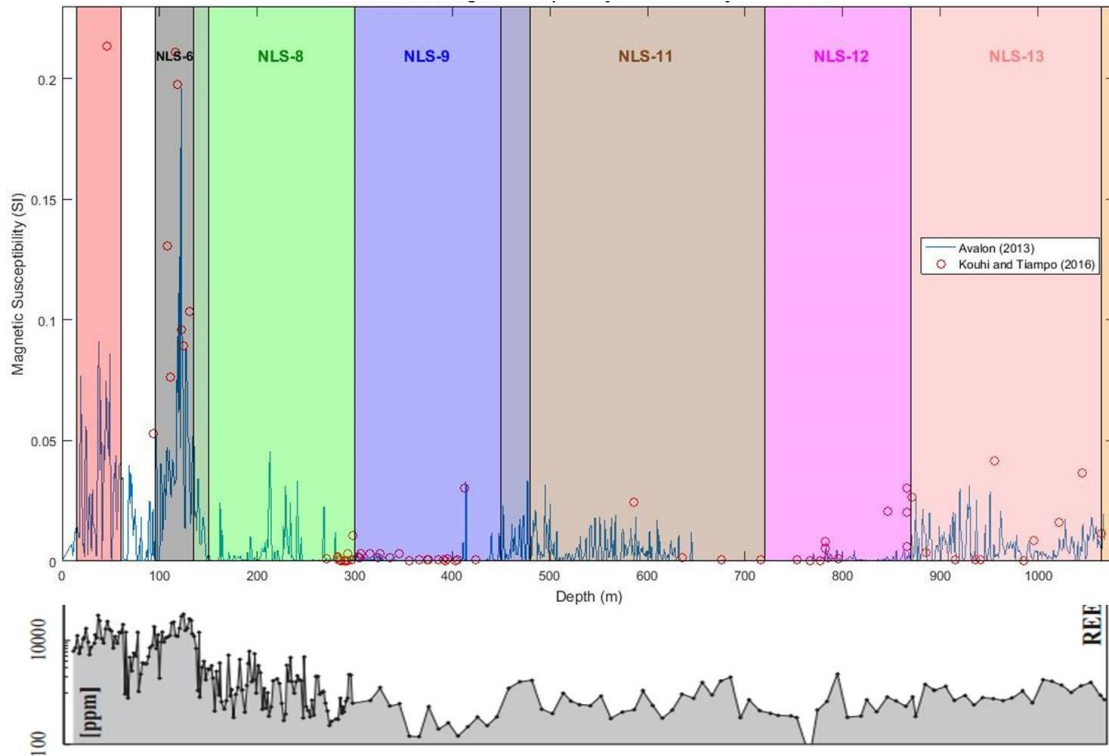


**Figure 4.9: Scaled down volume-based susceptibility measurements with REE abundance overlain below (modified from Möller and Williams-Jones (2016)).**

This trend of higher magnetic susceptibility than measured previously may play a role in future magnetic inversions. Increasing the measured susceptibilities would increase the expected values in inversion reference models and may result in the allocation of more deep-seated signal to these shallow units that host the deposit.

#### 4.4.3 Colour Analysis

In order to compare the overall mineralogy of the samples to their geophysical properties, this study attempted to quantify the colour of each sample using RGB colour values.

Multiple different methods of colour analysis were tested in order to visualize mineralogical trends in the geophysical data. The first method involved pulling the RGB

values from each individual pixel in a high resolution photograph and averaging these values to assign an overall colour to the sample (**Figure 4.10**). From the figure, it is evident that none of the samples bias toward any of the three RGB (red-green-blue) colours, resulting in different shades of grey. However, data points with higher magnetic susceptibilities appear to have darker overall colours which are likely a direct result of the amount of magnetite in these samples. As depth increases, the data points trend toward lighter shades of grey due to the increase in lighter minerals such as albite as well as the lack of magnetite.

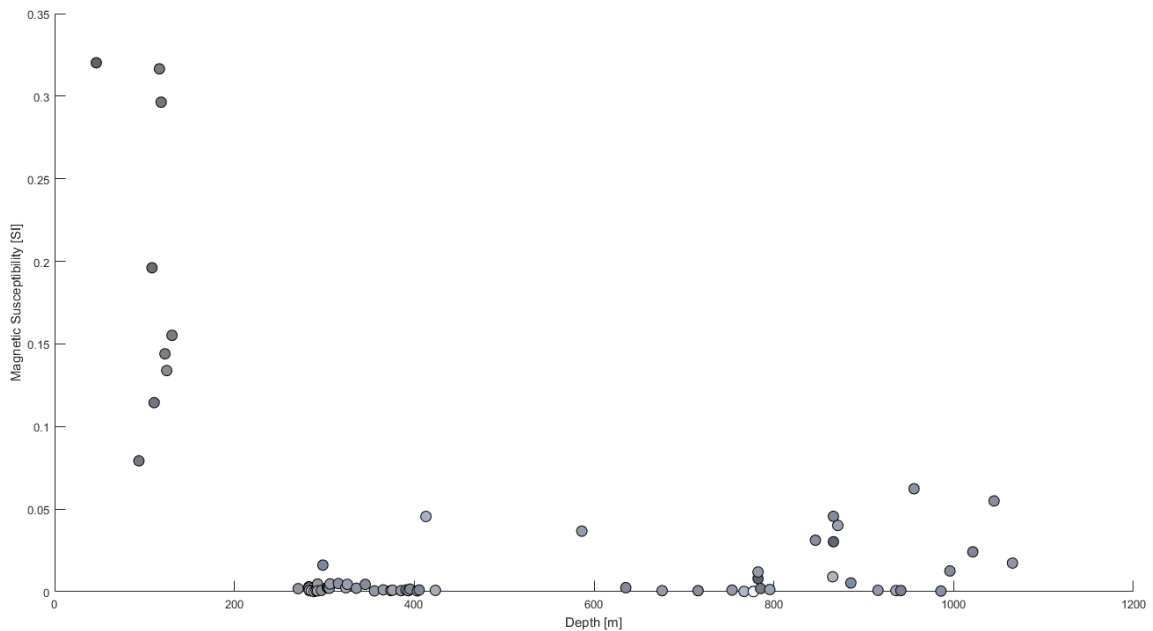


**Figure 4.10: Plot of magnetic susceptibility with depth for drillhole L09-194.**

**Marker colours were determined by the average red, green and blue values extracted from each image. Darker shades of grey represent minerals that were generally dominated by darker coloured minerals such as magnetite while lighter shades represent minerals that were dominated by minerals such as albite.**

In addition to averaging the RGB values for each pixel, another program was developed that assigns a mineral name to each pixel depending on a system of RGB value criteria. The criteria generally consist of a maximum threshold for all RGB values, as well as Boolean relationships between each of the three components. For example, magnetite is assigned to all black minerals, therefore the threshold for the RGB values is 65 (on a standard 0-255 RGB scale). This means that only pixels with all three components less than 65 will be considered. Next, from sampling multiple pixels where magnetite is present, it was determined that the blue component was always larger than both the red and green components. Therefore Boolean conditions were assigned such that this was also true. These images were broken up into a few basic minerals found in the samples: magnetite, aegirine, albite, sodalite, eudialyte (*Möller and Williams-Jones, 2016; Sheard et al., 2012*). Therefore in this simplified system any mineral that displays similar colour on the RGB value scale will be assigned as one of these minerals (**Table 1**). It should be noted that in the field of mineralogy, colour is not always a distinguishing feature, therefore there is a significant amount of error associated with this process. However, in a mineral system such as the Nechalacho deposit where each of the highlighted minerals have generally distinct colours, this could work as a first-pass technique of assigning mineral abundances. Magnetite is black, aegirine is green, albite is white, sodalite is blue, and altered eudialyte is yellow. **Figure 4.11** shows an original image that is compared to the colours assigned by the program to the mineral types to each pixel. There are a few discrepancies in the mineral assignment in addition to a few pixels where a mineral type could not be assigned (shown in red). However, the overall mineralogical geometry appears to match the sample very well as a preliminary technique.

**Table 4.2: A summary of the minerals included in RGB colour analysis methods.**

<b>Mineral</b>	<b>Chemical Formula</b>	<b>Assigned Colour</b>
Magnetite	$\text{Fe}_3\text{O}_4$	black
Aegirine	$\text{NaFeSi}_2\text{O}_6$	green
Albite	$\text{NaAlSi}_3\text{O}_8$	white
Sodalite	$\text{Na}_8(\text{AlSiO}_4)_6\text{Cl}_2$	blue
Eudialyte	$\text{Na}_{15}\text{Ca}_6(\text{Fe,Mn})_3\text{Zr}_3\text{SiO}(\text{O,OH,H}_2\text{O})_3(\text{Si}_3\text{O}_9)_2(\text{Si}_9\text{O}_{27})_2$ $(\text{OH,Cl})_2$	yellow
Other	N/A	red
Chemical Formula Reference: <a href="http://mindat.org">mindat.org</a>		



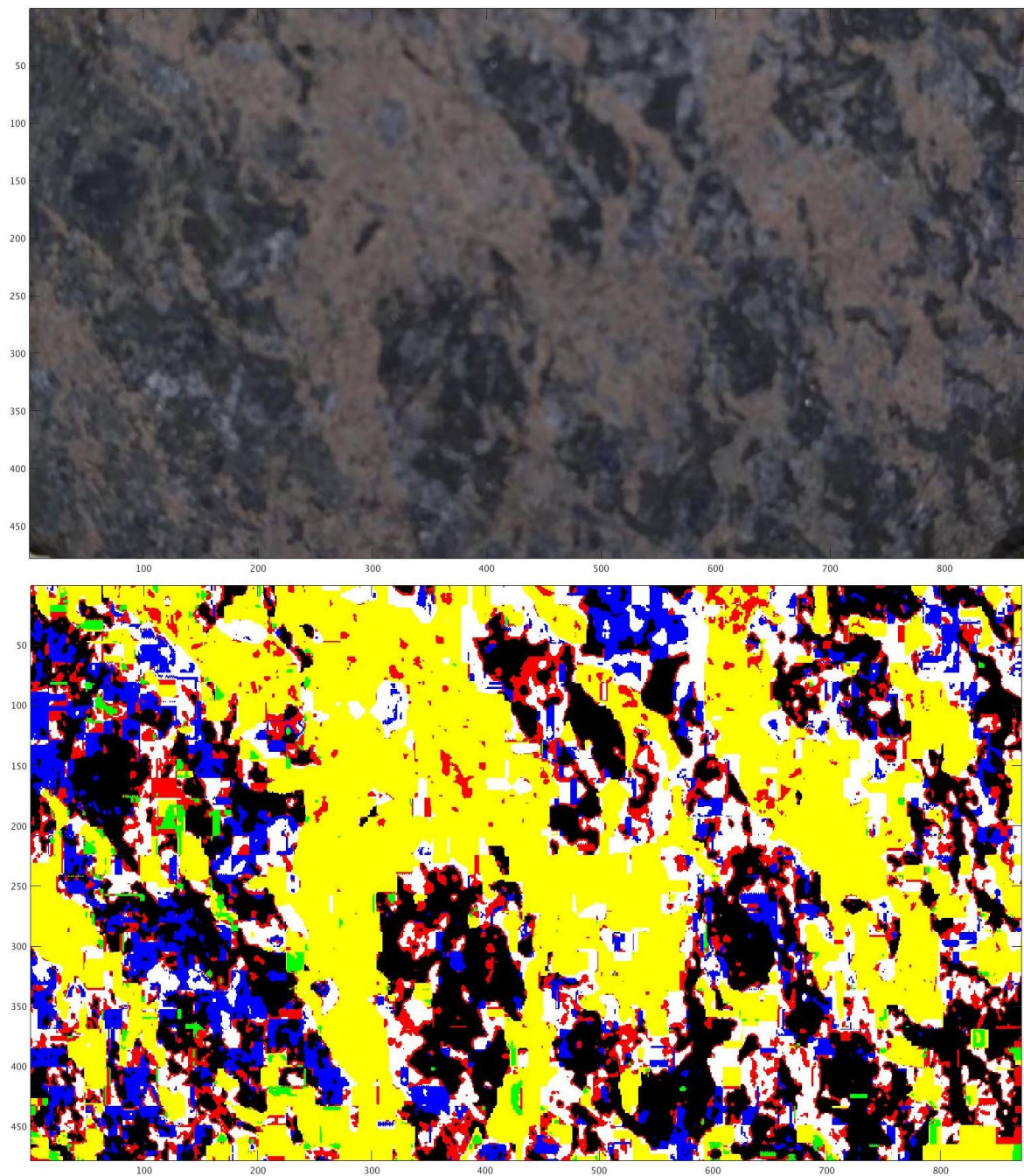


**Figure 4.11:** The original high resolution photograph (above) of a sample at 118.5 metres depth, and the reproduced image via computational colour analysis (below). This method uses colours to distinguish between different minerals. Black represents magnetite, green represents aegirine, white represents albite, blue

**represents sodalite, yellow represents eudialyte and red represents pixels that are unassigned.**

The output of the colour analysis program is a list of mineral abundances for the five minerals mentioned above. These abundances are plotted against the magnetic susceptibility of each sample in **Figure 4.12**, along with any unassigned pixel percentages that may be used as a proxy for the amount of error in each measurement. The susceptibility data points are plotted in colour based on their average RGB values described above unless there was a dominant colour component. For example, blue circles represent samples where the blue value was significantly higher than the red and green values. Note that there are several interesting trends in this data. The albite abundance increases with depth which results in a decrease in magnetic susceptibility as noted above. On the other hand, increases and decreases in eudialyte appear to be directly correlated with similar trends in susceptibility. Finally, magnetite abundances increase where high magnetic susceptibilities were measured as expected, with the exception of a couple of data points at depth. The majority of these outliers that occur with depth were noted when recording the mineral abundances and are due to incorrect mineral assignment where what appears to be nepheline appears as a dark grey. **Figure 4.13** shows the magnetic susceptibilities with the exception of four outlying points. From this plot, it appears that the preliminary mineral assignment is doing a very good job assigning a relative value to the abundance of magnetite because increases in abundance correlate very well with susceptibility highs with the exception of two data points at depth. These errors could be similar to the outliers that were removed above, or they could be associated with other dark-coloured minerals such as biotite contributing to the abundance. Another interesting point is that the high abundance of magnetite assigned to



the first data point. This is of interest because this is the sample that displayed much higher values of magnetic susceptibility than earlier measurements.

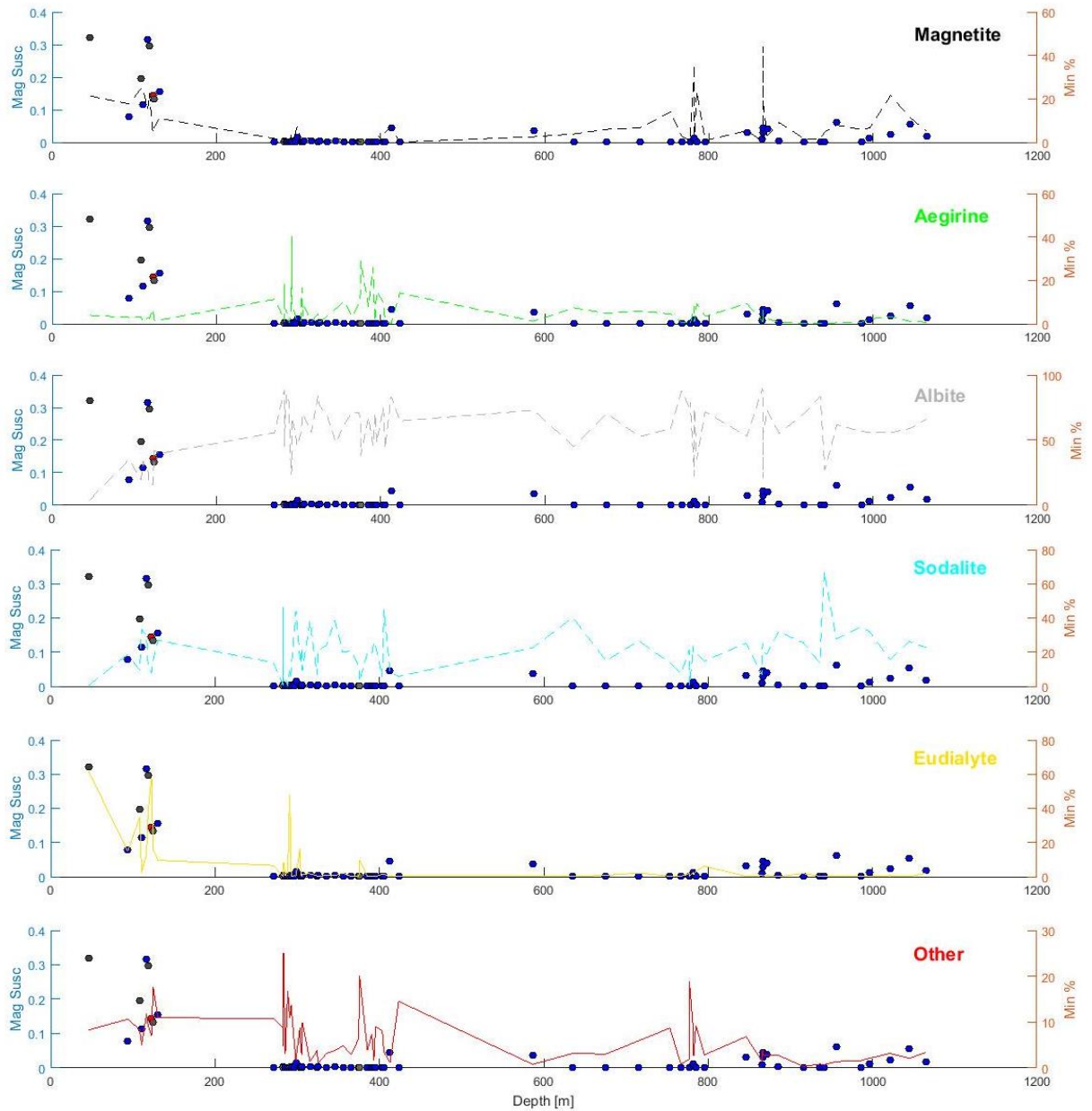


**Figure 4.12:** Mineral abundances as calculated from the computational colour analysis technique (coloured lines) versus depth for each sample are plotted on the right-hand y-axis. Magnetic susceptibilities are plotted (circles) versus depth on the left-hand y-axis. The filling colours for the circles represent the average RGB values for that sample unless the sample was dominated by a specific red, green or blue value (i.e. blue circles represent samples that had an average blue value significantly higher than its red or green values).

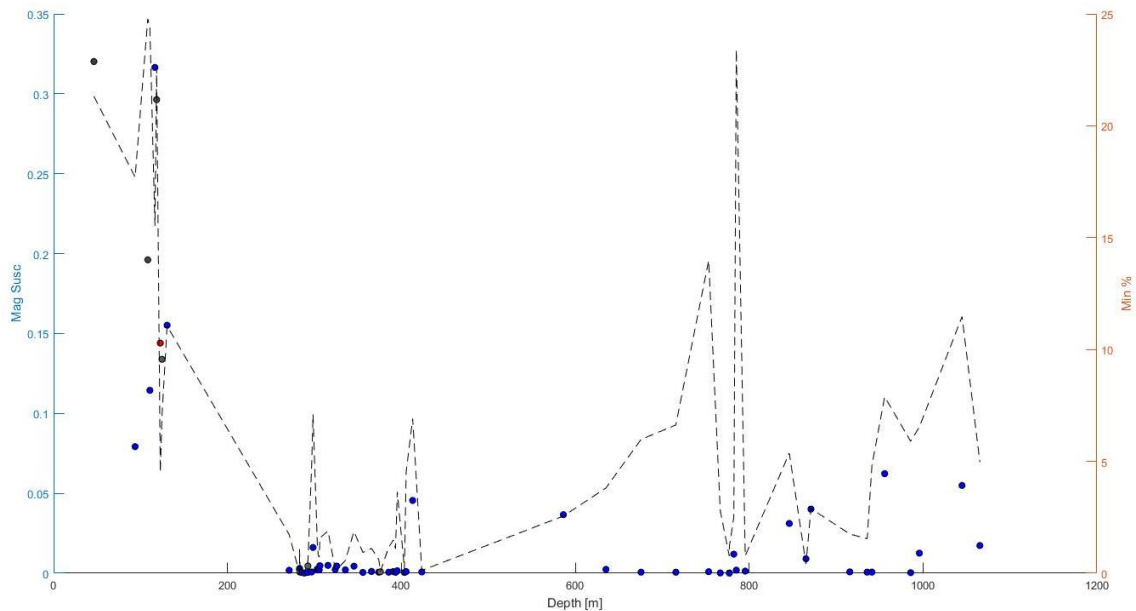


**Figure 4.13: Plot of the magnetic susceptibility (left-hand axis, circles, in SI units) and magnetite abundance (right-hand axis, dashed line) versus depth for the samples from drillhole L09-194. Abundances were calculated using computational colour analysis and exclude the four data points that were deemed outliers during the process.**

#### 4.4.4 Future Work

Future work to be completed as a continuation of this study would include further investigation of the systematic increase in values between field measurements and lab measurements. The first step in this process would be to obtain reliable density measurements for each sample. While methods exist for obtaining such measurements, traditional techniques cannot be used on these samples. An option for obtaining an accurate measurement of the volume and density is through the use of X-ray computed tomography (CT-scanning) (*McCausland et al.*, 2010). The CT-scanning technique is a non-destructive method, analogous to waveform tomography techniques used in

exploration seismology (*Pratt, 2015*). By using X-rays to scan the sample, CT-scanning can measure and digitize volume with resolutions between 20 and 100  $\mu\text{m}$  and can also be used to calculate bulk percentages of dense materials within the sample (*McCausland et al., 2010*). This also presents an interesting way to quantify the amount of dense materials, such as magnetite, in the samples and could lead to advanced studies of the geophysical properties of hydrothermal magnetite. Similar research could be performed on magmatic magnetite in another intrusion to assess potential differences in magnetic properties. Additional testing could also be completed to adapt the RGB conditions for mineral assignment in the colour analysis portion of this study. Enhancing the accuracy of these conditions could help increase the consistency of the calculated abundances and eliminate outliers that occur with depth. Another potential application and quality check for this method could be to assign densities to each pixel that are dependent on the mineral assignment. This could give important information about the density distribution within the sample and, additionally, could be used to compare a calculated bulk density to a measured bulk density for each sample in order to assess the accuracy of the RGB colour analysis. Finally, this could give some insight into what minerals are making up the unassigned minerals in the analysis.

## 4.5 Conclusion

Overall, this work has provided a confirmation of the quality of the previously measured magnetic susceptibility values. The values obtained here reproduced the trends in magnetic highs measured in original measurements by *Avalon (2013)*. The peaks of high magnetic susceptibility aligned reasonably well. However, a systematic increase in the magnitudes of these values by a factor of approximately 1.5 was observed throughout the

entire drillhole. These geophysical measurements were compared to mineralogical work by *Möller and Williams-Jones* (2016) that divided the intrusion into lithological units, as well as mineralogical knowledge of the hydrothermal alteration from *Sheard et al.* (2012) in order to integrate geophysical models with the subsurface geology. This study also provides a preliminary foundation for further research into the geophysical comparison of magmatic and hydrothermal magnetite. Finally, work with colour analysis using high resolution photographs has shown promise as a preliminary method of evaluating mineral abundances if the system is simplified to a subset of colour-distinct minerals.

## 4.6 References

**Avalon Rare Metals Inc., 2014.** Lithology and Magnetic Susceptibility Data. Prepared by Ben Webb.

**Hinze, W.J., von Frese, R.R.B., von Frese, R., and Saad, A.H., 2013.** Gravity and Magnetic Exploration: Principles, Practices and Applications. Cambridge University Press, Cambridge, UK, 512p.

**Kouhi, D.W., and Tiampo, K.F., 2016a.** Current Status of Magnetic Inversion Project at Thor Lake, N.W.T.; Open-File Report 2016-06, Northwest Territories Geological Survey, Yellowknife.

**Kouhi, D.W., and Tiampo, K.F., 2016b.** Implementation of Gravity Data for Isolated and Joint Inversion Methods at Thor Lake, N.W.T.; Pending Open-File Report, Northwest Territories Geological Survey, Yellowknife.

**McCausland, P.J.A., Brown, P.G., and Holdsworth, D.W., 2010.** Rapid, Reliable Acquisition of Meteorite Volumes and Internal Features by Laboratory X-Ray Micro-CT Scanning; 41<sup>st</sup> Lunar and Planetary Science Conference. Abstract #2584.

**Moller, V., and Williams-Jones, A.E., 2016.** Petrogenesis of the Nechalacho Layered Suite, Canada: Magmatic Evolution of a REE-Nb-rich Nepheline Syenite Intrusion; *Journal of Petrology*, v. 57, p. 229-276.

**Nichols, N., 2014.** KT-10 Instrument Magnetic Susceptibility Data.

**Pratt, G. R., 2015.** The Implications of Frequency Domain Modelling – Sampling and Wrap-Around; *in* *Waveform Tomography: An Introduction to Theory and Practice*, Western University, London, Canada, p. 6-30.

**Sheard, E. R., Williams-Jones, A.E., Heiligmann, M., Pederson, C., and Trueman, D. L., 2012.** Controls on the Concentration of Zirconium, Niobium, and the Rare Earth Elements in the Thor Lake Rare Metal Deposit, Northwest Territories, Canada; *Economic Geology*, v. 107, p. 51-104.

**Tiampo, K.F. and Nichols, N., 2014.** Preliminary Inversion, Blatchford Lake Intrusive Suite; Accelerated Masters Project Report by Nolan Nichols, University of Western Ontario, London, Canada.

## Chapter 5

### 5 General Discussion and Conclusions

The goal of this research was to model the geophysical properties of the subsurface at the Thor Lake region in the Northwest Territories. This modelling was achieved through constrained inverse modelling of airborne potential field data with the support of subsurface drillhole measurements. These models provide supplementary information on the geological features of the Nechalacho rare earth element deposit. The magnetic susceptibility and density models obtained were integrated to perform preliminary structural joint inversions. This geophysical information, combined with mineralogical work by *Möller and Williams-Jones* (2016) and *Sheard et al.* (2012), provides insight into the relationships between geological and geophysical properties.

#### 5.1 Model Improvements

Geological models of the Nechalacho deposit show a sub-horizontal layered region with high concentrations of rare earth elements (REE). These layers were expected to be substantially denser and highly altered in relation to the rest of the intrusion (*Sheard et al.*, 2012). Innovative lateral interpolation techniques for creating reference models from drillhole data have been successful in constraining the inversions in order to retrieve realistic models. Magnetic susceptibility and density models agree well with these studies, displaying anomalously high values in the shallow subsurface. Both models further validated prior geological work in regions with the highest concentrations of REE, but this modelling of geophysical properties indicates that the deposit may extend further north than previously estimated. Density modelling yields a densely packed layer with

relatively sharp boundaries and evidence of the fractional crystallization expected at depth within the intrusion. Both susceptibility and density models resolve a lower contact between the basal zone and the Nechalacho nepheline syenite. It is important to assess the limits of the model resolution when discussing lithological contacts in geological interpretation. With relatively flat-lying contacts, the resolution is controlled mainly by the vertical cell thickness, which is 10 metres in this case. However, when evaluating the ability of the model to resolve contacts that do not align with an axis, it gets more complicated. An angled contact, such as the contact between the upper/basal zones and the rooftop sodalite (or Thor Lake syenite), is difficult to identify because it will cut across the centre of multiple cells, and therefore may be washed out due to averaging. Therefore, this contact is estimated based on geological interpretation of the geophysical models and its exact position and trend is difficult to determine. In addition, the magnetic susceptibility model appears to map sections of the Hearne dyke swarm as well as the large Indin dyke that cross-cuts the area.

Core magnetic susceptibility values that were measured in the field (Avalon, 2013; Nichols, 2014) were validated with the use of in-lab instruments. Relationships between magnetic susceptibility measurements and sample mineralogy were analyzed with experimental computational techniques with promising results. This preliminary study represents a first-pass method of quantifying mineral abundances. In addition, trends between magnetic susceptibility, density, REE concentrations and mineral abundance further support the role of magnetite content in the Nechalacho deposit, and thus, the effectiveness of geophysical modelling.



Geological interpretations of the model delineate a combined region that includes the upper and basal zones. This region is relatively flat in geometry and extends for approximately 2000 metres in each direction with a thickness of approximately 300 metres, beginning from the surface in areas. Contacts with the rooftop sodalite and/or the Thor Lake syenite are inferred based on a graded contact in the geophysical models, and using prior knowledge of subsurface geology.

## 5.2 Structural Joint Inversion

While isolated inversion techniques yielded interesting results, the implementation of both datasets in cooperative inversions yielded positive, but subtle results. The structural cooperative inversion techniques used in this research aided in solving for more realistic geophysical models by eliminating small negative susceptibilities. However, when comparing the isolated models with joint models there are few additional differences. This may speak to the accuracy of the isolated models obtained. Both isolated and cooperative inversions delineate the upper and basal zones, as well as reasonable resolution of the lower contact between the basal zone and the Nechalacho nepheline syenite. Lateral contacts between the deposit and the Thor Lake syenite cannot be identified clearly due to the resolution of the models, however they can be inferred by relating knowledge of the geology of the deposit to the geophysical models obtained.

## 5.3 Newly Developed Techniques

For this thesis, multiple innovative techniques were tested and developed. A new technique of laterally interpolating between known data points proved to be extremely effective in enhancing the dataset for use in inverse modelling methods, as well as

predicting subsurface geology. This technique may have further applications in the mineral exploration industry where methods such as kriging have traditionally been used such as resource estimation, as well as applications in other fields such as statistics.

In addition to a lateral interpolation method, innovative inversion techniques such as the structural joint inversion method proposed by *Lelièvre et al.* (2009) were implemented and adapted. This joint inversion technique, as well as the other techniques for influencing the inverse problem via UBC-GIF software, were developed in this work and implemented successfully.

Finally, a technique that uses high-resolution photographs of samples to obtain modal percentages was developed and tested on specific samples. This first-pass method assigns mineral abundances to each sample in an automated manner based on colour using a simplified system of minerals. While further testing is necessary to assess the robust accuracy of this technique, preliminary studies yielded magnetite abundances that trend very closely with known magnetic susceptibility measurements. This method has the potential to be an excellent tool in the mineral exploration industry due to its ability to analyze large quantities of samples in a short period of time.

## 5.4 Future Work

Future work includes further experimentation with computational colour analysis.

Results shown here displayed the potential for quantifying minerals through their colours, however a larger database of colour variations in minerals is needed to extend this research, as well as mitigate some error in computation.

Additional in-lab sample measurements on other drill cores could help determine whether the higher magnetic susceptibilities measured in this work are uniform across the entire deposit. This has implications to any future magnetic or joint inversions that may be completed. Finally, further experimentation with the cooperative inversion problem could resolve the optimal intensity of adjusting the weighting coefficients.

## 5.5 References

**Avalon Rare Metals Inc., 2014.** Lithology and Magnetic Susceptibility Data. Prepared by Ben Webb.

**Lelièvre, P. G., Oldenburg, D. W., and Williams, N. C., 2009.** Integrating Geological and Geophysical Data Through Advanced Constrained Inversions; Exploration Geophysics, v. 40, p. 334-341.

**Möller, V., and Williams-Jones, A.E., 2016.** Petrogenesis of the Nechalacho Layered Suite, Canada: Magmatic Evolution of a REE-Nb-rich Nepheline Syenite Intrusion; Journal of Petrology, v. 57, p. 229-276.

**Nichols, N., 2014.** KT-10 Instrument Magnetic Susceptibility Data.

**Sheard, E. R., Williams-Jones, A.E., Heiligmann, M., Pederson, C., and Trueman, D. L., 2012.** Controls on the Concentration of Zirconium, Niobium, and the Rare Earth Elements in the Thor Lake Rare Metal Deposit, Northwest Territories, Canada; Economic Geology, v. 107, p. 51-104.

## Appendices

### Appendix A: Matlab Code

#### UBC-GIF\_Conversion.m

```
% UBC-GIF Conversion Codes V2.0
% Written by Derek Kouhi
% Last Updated: June 29, 2015

% This script takes drillhole measurements and bins/averages them into
% their appropriate cells to create a 3-D reference model. This
% reference model is then used to calculate maximum and minimum
% boundary constraints, as well as starting models.

%% Import Data and Recover Well Locations

% Important Variables:
%     new = list of well locations
%     all = data in the format: x,y,z,susc

clear new
clear new1
clear new2
clear data
clear data2
data = xlsread('BH_locations.xlsx',1,'A1:E65512');
data2 = xlsread('BH_locations.xlsx',1,'A65513:E113943');
count = 1;
for i = 1:length(data)
    if data(i,3) == 0
        new1(count,1) = data(i,1);
        new1(count,2) = data(i,2);
        count = count + 1;
    end
end
count = 1;
for i = 1:length(data2)
    if data2(i,3) == 0
        new2(count,1) = data2(i,1);
        new2(count,2) = data2(i,2);
        count = count + 1;
    end
end
count = 1;
for i = 1:length(data)
    if isfinite(data(i,4))
        all1(count,1) = data(i,1);
        all1(count,2) = data(i,2);
        all1(count,3) = data(i,5);
        all1(count,4) = data(i,4)/1000;
        count = count + 1;
    end
end
count = 1;
```

```

for i = 1:length(data2)
    if isfinite(data2(i,4))
        all2(count,1) = data2(i,1);
        all2(count,2) = data2(i,2);
        all2(count,3) = data2(i,5);
        all2(count,4) = data2(i,4)/1000;
        count = count + 1;
    end
end
new = [new1;new2];
all = [all1;all2];

clear count
clear i
clear new1
clear new2
clear all1
clear all2
clear data
clear data2
%% Input Dimensions and Set Mesh Layout

% Important Variables:
%     dim() = size of the model in the x,y,z directions
%     dimmodel = the total size of the model file (x*y*z)
%     x,y = cell sizes in the x and y directions
%     zcells = cell sizes in the depth domain
%     X,Y = gridded meshes

space = 25;
x = [413150,413950,414350,414550:space:418250,418450,418850,419650];
y =
[6883350,6884150,6884550,6884750:space:6889250,6889450,6889850,6890650]
;
zcells = [300:-12.5:-700,-725:-25:-1700];
dimx = length(x) - 1;
dimy = length(y) - 1;
dimz = length(zcells) - 1;
dimmodel = dimx*dimy*dimz;
[X,Y]=meshgrid(x,y);

clear count
clear i
clear space

%% Plot the Grid and Well Locations

% OPTIONAL CODE

close all;
figure('units','normalized','outerposition',[0 0 1 1])
plot(new(:,1),new(:,2),'.')
hold on;
plot(X,Y,'r')
plot(X',Y', 'r')
plot(new(:,1),new(:,2),'.')
title('X-Y Plane Grid and Drillhole Locations','FontSize',32);

```

```

xlabel('Easting','FontSize',20);
ylabel('Northing','FontSize',20);
legend('Drillholes','Grid Lines');
set(gca,'fontsize',18);
xt=get(gca,'xtick');
xt(2:2:end)=[];
set(gca,'xtick',xt);
curtick = get(gca, 'XTick');
set(gca, 'XTickLabel', cellstr(num2str(curtick(:))));
yt=get(gca,'ytick');
yt(1:2:end)=[];
set(gca,'ytick',yt);
curtick = get(gca, 'YTick');
set(gca, 'YTickLabel', cellstr(num2str(curtick(:))));

%% Sort the Data into Cells

% Important Variables:
%     timet = total time of the run
%     percentile = percentage of the highest values to use in the
model
%     model = the model created using the data

% Inputs

percentile = 0.5;

%
clc
timet = 0;
if percentile > 0.9 && percentile <= 1.0
    C = 1;
elseif percentile > 1.0 || percentile <= 0.0
    errordlg('The percentile must be between 0 and 1.0!');
    return
else
    C = 0;
end
for i = 1:dimy
    tic;
    disp(['y-index ',num2str(i),' of ',num2str(dimy)]);
    for j = 1:dimx
        for k = 1:dimz
            cellno = dimx*dimz*(i-1)+dimz*(j-1)+k;
            emin = x(j);
            emax = x(j+1);
            nmin = y(i);
            nmax = y(i+1);
            zmin = zcells(k+1);
            zmax = zcells(k);
%             m = 1;
%             while m <= length(all)
                indices = find(all(:,1) >= emin & all(:,1) <= emax &...
                    all(:,2) >= nmin & all(:,2) <= nmax &...
                    all(:,3) >= zmin & all(:,3) <= zmax);
%                 m = m + 1;
%             end
        end
    end
end

```

```

        if ~isempty(indices)
            addition(1,:) = all(indices,4);
            addition = sort(addition);
            start = length(addition)-
ceil(length(addition)*percentile)+C;
            if start < 1
                start = 1;
            end
            useadd = addition(start:length(addition));
            count = length(useadd);
            model(cellno,1) = sum(useadd)/count;
        else
            model(cellno,1) = 0;
        end
        clear addition
        clear useadd
        clear count
    end
end
time = toc;
timet = timet + time;
clc
disp(['Time for run: ',num2str(floor(time/60)),' minutes and
',num2str(((time/60)-floor(time/60))*60),' seconds']);
disp(['Estimated time remaining: ',num2str(floor(time*(dimy-
i)/3600)),' hours and ',...
num2str(((time*(dimy-i)/3600)-floor(time*(dimy-i)/3600))*60),'
minutes']);
end
clc
disp('*****MODEL COMPLETED*****');
disp(['Total Run Time: ',num2str(floor(timet/3600)),' hours, ',...
num2str(floor((timet/3600-floor(timet/3600))*60)),' minutes and
',...
num2str(timet-(floor(timet/3600))*3600-(floor((timet/3600-
floor(timet/3600))*60))*60),' seconds']);
clear count
clear emin
clear emax
clear nmin
clear nmax
clear zmax
clear zmin
clear percentile
clear start
clear time
clear timet
clear k
clear C
clear indices
clear i
clear j
clear cellno
clear p
dlmwrite([num2str(dimx),'x',num2str(dimy),'x',num2str(dimz),'_model.txt
'],...
model,'precision',7,'newline','pc');

```

```

%% Write the Model to a Text File

dlmwrite([num2str(dimx),'x',num2str(dimy),'x',num2str(dimz),'_model.txt'
'],...
    model,'precision',7,'newline','pc');

%% Create an Active Cell Matrix Based on the Model

% Important Variables:
%     active = the active cells matrix

active = zeros(length(model),1);
for i = 1:length(model)
    if model(i) > 0
        active(i) = 1;
    else
        active(i) = -1;
    end
end

dlmwrite([num2str(dimx),'x',num2str(dimy),'x',num2str(dimz),'_active.tx
t'],...
    active,'precision',7,'newline','pc');

clear i

%% Create a Starting Model

% Important Variables:
%     zeroval = the value to give to points that do not contain data
%     start_mod = the starting model

% Inputs

zeroval = 0.0001;

%

start_mod = zeros(length(model),1);
for i = 1:length(model)
    if model(i) == 0
        start_mod(i) = zeroval;
    else
        start_mod(i) = model(i);
    end
end

dlmwrite([num2str(dimx),'x',num2str(dimy),'x',num2str(dimz),'_start.txt'
'],...
    start_mod,'precision',7,'newline','pc');

clear i
clear zeroval

%% Create Maximum and Minimum Boundary Models

% Important Variables:

```



```

%      range = the value to +/- from the measured value to form the
range
%      maxnon = the value to assign for the maximum of cells with no
data
%      max_mod = the maximum boundary model
%      min_mod = the minimum boundary model

% Inputs

range = 0.05;
maxnon = 0.6;

%

max_mod = zeros(length(model),1);
min_mod = zeros(length(model),1);
for i = 1:length(model)
    if model(i) == 0
        max_mod(i) = maxnon;
        min_mod(i) = 0;
    else
        max_mod(i) = model(i)+range;
        min_mod(i) = model(i)-range;
        if min_mod(i) < 0
            min_mod(i) = 0;
        end
    end
end

dlmwrite([num2str(dimx),'x',num2str(dimy),'x',num2str(dimz),'_max.txt']
,...
        max_mod,'precision',7,'newline','pc');
dlmwrite([num2str(dimx),'x',num2str(dimy),'x',num2str(dimz),'_min.txt']
,...
        min_mod,'precision',7,'newline','pc');

clear i
clear range
clear maxnon

```

### upward\_cont.m

```

% upward_cont.m
% Written by Derek Kouhi
% July 2015
%
% This script takes airborne data and interpolates it onto a courser
grid
% using a biharmonic spline interpolation from MathWorks. The data is
% then upward continued using the mfilter function adapted from ES3320
% by Derek Kouhi and re-gridded back to a finer grid.

%%
% Import the airborne data for the region
magdata = xlsread('allmagdata.xlsx');

% Inputs:

```

```

% - width: the user-definted resolution for upward continuation
% - xi,yi: vectors define the grid over which the data will be
calculated

width = 200;
xi = 414300:width:418500;
yi = 6884500:width:6889500;

% Eliminate all data that does not lie between grid vector dimensions
count = 1;
for i = 1:length(magdata)
    if magdata(i,1) >= 414800 && magdata(i,1) <= 418000 && ...
        magdata(i,2) >= 6885000 && magdata(i,2) <= 6889000
        X(count,1) = magdata(i,1);
        Y(count,1) = magdata(i,2);
        Z(count,1) = magdata(i,3);
        count = count + 1;
    end
end

% Create a grid from the grid vectors and use a biharmonic spline
% interpolation function to reposition datapoints if necessary

[XI,YI] = meshgrid(xi,yi);
ZI = biharmonic_spline_interp2(X,Y,Z,XI,YI);
alldim = [X,Y,Z];
ppc = 0;

% Calculate the points per cell to help find parameters that avoid
aliasing

for i = 1:length(alldim)
    if alldim(i,1) >= 414800 && alldim(i,1) <= 414800+width &&
alldim(i,2) >= 6885000 && alldim(i,2) <= 6885000+width
        ppc = ppc + 1;
    end
end
disp(['This is approximately ',num2str(ppc),' points per cell.']);
clear alldim
clear ppc

% Plot the interpolated figure for reference

figure
imagesc(xi,yi,ZI);
set(gca,'YDir','normal')
colorbar;
clear count
clear i

% Upward continue the data using the mfilter function (see below)

howhigh = 5;
dec = 17.593;
inc = 81.196;
[upcon,rtp,uprtp] = mfilter(ZI,howhigh,inc,dec);
figure

```

```

imagesc(xi,yi,upcon);
set(gca,'YDir','normal')
colorbar;

% Rewrap the data into vector format and check the vector length
newmagdat = zeros(length(xi)*length(yi),1);
for i = 1:length(yi)
    for j = 1:length(xi)
        Xup(((j-1)*length(yi))+i,1) = XI(i,j);
        Yup(((j-1)*length(yi))+i,1) = YI(i,j);
        Zup(((j-1)*length(yi))+i,1) = upcon(i,j);
    end
end
fzero = find(Xup==0);
disp(['The number of zeros in this vector is:
',num2str(length(fzero))]);
disp(['The vector has a length of ',num2str(length(Xup)), ' which is
',...
    num2str(length(Xup)/(length(xi)*length(yi))), ' times the size it
should be.']);
clear fzero
clear i
clear j

% Interpolate the data onto a higher resolution grid

xi = 414800:50:418000;
yi = 6885000:50:6889000;
[XI,YI] = meshgrid(xi,yi);
Znorm = biharmonic_spline_interp2(X,Y,Z,XI,YI);
Zupcon = biharmonic_spline_interp2(Xup,Yup,Zup,XI,YI);

% Plot comparison plots for each anomaly
figure
imagesc(xi,yi,Znorm);
set(gca,'YDir','normal')
colorbar;
title(['Original Magnetic Anomaly on a
',num2str(length(xi)), 'x', num2str(length(yi)), ' Grid']);
figure
imagesc(xi,yi,Zupcon);
set(gca,'YDir','normal')
colorbar;
title(['Magnetic Anomaly Upward Continued by
',num2str(howhigh*1000), ...
    'm']);
Zfinal = Znorm - Zupcon;
figure
imagesc(xi,yi,Zfinal);
set(gca,'YDir','normal')
colorbar;
title(['Remaining Magnetic Anomaly on a
',num2str(length(xi)), 'x', num2str(length(yi)), ' Grid']);

% Put the data into the UBC-GIF observation file format

```

```

% Read an xls file containing x and y measurement locations in columns
1
% and 2, and altitude measurements in column 3.

elev = xlsread('elevation.xlsx');
finalmag = zeros(length(xi)*length(yi),1);
for i = 1:length(yi)
    for j = 1:length(xi)
        finalmag(((j-1)*length(yi))+i,1) = XI(i,j);
        finalmag(((j-1)*length(yi))+i,2) = YI(i,j);
        finalmag(((j-1)*length(yi))+i,4) = Zfinal(i,j);
    end
end
fzero = find(finalmag==0);
disp(['The number of zeros in this vector is:
',num2str(length(fzero))]);
disp(['The vector has a length of ',num2str(length(finalmag)), ' which
is ',...
    num2str(length(finalmag)/(length(xi)*length(yi))), ' times the size
it should be.']);
clear fzero
clear i
clear j
finalmag(:,3) = elev(:,3);
finalmag(:,5) = 5;

% Write the data to a text file to be used as the input observation
file
dlmwrite('thorlake_up.mag.txt',finalmag,'precision',7,'newline','pc');

function [output,output2,output3] = mfilter(data,dz,inc,dec);
% output = mfilter(data);
%
% This program was adapted by Derek Kouhi from a similar program
written
% for ES3320 at Western University (Taught by Dr. Gerhard Pratt).
% It applies a forward and inverse 2-D Fourier transform. A filter can
% be implemented after the forward transform. The units of dx and dy
% are km.

ic = sqrt(-1);
dx = 0.2;
dy = 0.2;
[m,n] = size(data);

[fftout,dbamp,u,v,k] = fft2d(data,dx,dy);
dec = dec*pi/180;
inc = inc*pi/180;
f = [cos(inc)*sin(dec),cos(inc)*cos(dec),sin(inc)];
a1 = f(3)^2-f(1)^2;
a2 = f(3)^2-f(2)^2;
a3 = -f(2)*f(1)-f(1)*f(2);
b1 = 2*f(1)*f(3);
b2 = 2*f(2)*f(3);

for i = 1:m

```

```

        for j = 1:n

%Upward Continuation filter
            filt(i,j) = exp(-dz*abs(k(i,j)));
%Reduction to the Pole filter
            filtrtp(i,j) =
abs(k(i,j)^2)/(a1*u(i,j)^2+a2*v(i,j)^2+a3*u(i,j)...
                *v(i,j)+ic*abs(k(i,j))*(b1*u(i,j)+b2*v(i,j)));

        end
    end

    filtdat = fftout .* filt;
    filtdat2 = fftout .* filtrtp;
    filtdat3 = fftout .* filt .* filtrtp;
%Output upward, rtp, both
    output = ifft2d(filtdat);
    output2 = ifft2d(filtdat2);
    output3 = ifft2d(filtdat3);

```

### grad\_attenuate.m

```

% grad_attenuate.m
% Written by Derek Kouhi
% September 2015

% This program takes the current best model from geophysical inversion,
% removes padding cells and calculates the gradient between each cell
in
% 3 dimensions. These gradients are used to adjust weighting
coefficients
% in subsequent inversions.

%% Unwrap a Model

% Important Variables:
%     inmodel = the model that is being unwrapped
%     unwrap = the unwrapped 3-D matrix (x,y,z)

clc
fileID = fopen('model3.txt','r');
formatSpec = '%f';
inmodel = fscanf(fileID,formatSpec);

ind = find(inmodel == -100);
inmodel(ind) = 0;
unwrap = zeros(dimx,dimy,dimz);
count = 1;
for i = 1:dimy
    for j = 1:dimx
        for k = 1:dimz
            unwrap(j,i,k) = inmodel(count);
            count = count + 1;
        end
    end
end

```

```

        end
    end
end

clear fileID
clear formatSpec
clear inmodel
clear count
clear i
clear j
clear k

%% Remove Padding

% Important Variables:
%     xypadding = the number of padded cells on either side on x-y
plane
%     zpadding = the number of cells padding the bottom in z-
direction
%     unwrap = the unwrapped 3-D matrix (x,y,z)
%     unpad = the unwrapped 3-D matrix with padding removed

% Inputs

xypadding = 3;
zpadding = 3;

%

clc
unpad = unwrap(xypadding+1:dimx-xypadding,xypadding+1:dimy-
xypadding,...
    1:dimz-zpadding);

%% Find the Gradient of the Unpadded Model

% Important Variables:
%     HX,HY,HZ = cell spacing in each direction (x,y,z)
%     unpad = the unwrapped 3-D matrix with padding removed
%     FX,FY,FZ = the gradient in each component

% Inputs

HX = 25;
HY = 25;
HZ = 10;

%

clc
[FX,FY,FZ] = gradient(unpad,HX,HY,HZ);
FX = FX/max(max(max(abs(FX)))));
FY = FY/max(max(max(abs(FY)))));
FZ = FZ/max(max(max(abs(FZ)))));

answer = input('Would you like to sample your gradient? (Y/N) ','s');
```

```

if answer == 'y' || answer == 'Y'
    znum = input('What z cell would you like to sample? ');
    if znum < 1 || znum > dimz
        error('Your chosen z cell is not within the bounds of the
model');
    end
    px = FX(:, :, znum);
    py = FY(:, :, znum);
    figure
    contour(unpad(:, :, znum))
    colorbar;
    hold on;
    quiver(px, py)
else return
end

clear znum
clear HX
clear HY
clear HZ
clear px
clear py
clear answer

%% Repad and Rewrap the Gradient Models

% Important Variables:
%     HX, HY, HZ = cell spacing in each direction (x, y, z)
%     unpad = the unwrapped 3-D matrix with padding removed
%     FX, FY, FZ = the gradient in each component

% Inputs

overzero = 0.01;

%

clc
FXrr = zeros(dimx-1, dimy, dimz);
FYrr = zeros(dimx, dimy-1, dimz);
FZrr = zeros(dimx, dimy, dimz-1);
FXrr(xypadding+1:dimx-xypadding, xypadding+1:dimy-xypadding, ...
1:dimz-zpadding) = FX;
FYrr(xypadding+1:dimx-xypadding, xypadding+1:dimy-xypadding, ...
1:dimz-zpadding) = FY;
FZrr(xypadding+1:dimx-xypadding, xypadding+1:dimy-xypadding, ...
1:dimz-zpadding) = FZ;

gradmodX = zeros(dimmodel-dimy*dimz, 1);
gradmodY = zeros(dimmodel-dimx*dimz, 1);
gradmodZ = zeros(dimmodel-dimx*dimy, 1);
for i = 1:dimy
    for j = 1:dimx-1
        for k = 1:dimz
            cellno = (dimx-1)*dimz*(i-1)+dimz*(j-1)+k;
            gradmodX(cellno, 1) = FXrr(j, i, k);
        end
    end
end

```

```

        end
    end
    for i = 1:dimy-1
        for j = 1:dimx
            for k = 1:dimz
                cellno = dimx*dimz*(i-1)+dimz*(j-1)+k;
                gradmodY(cellno,1) = FYrr(j,i,k);
            end
        end
    end
    for i = 1:dimy
        for j = 1:dimx
            for k = 1:dimz-1
                cellno = dimx*(dimz-1)*(i-1)+(dimz-1)*(j-1)+k;
                gradmodZ(cellno,1) = FZrr(j,i,k);
            end
        end
    end
    gradmodX = ones(dimmodel-dimy*dimz,1)*(1+overzero)-abs(gradmodX);
    gradmodY = ones(dimmodel-dimx*dimz,1)*(1+overzero)-abs(gradmodY);
    gradmodZ = ones(dimmodel-dimx*dimy,1)*(1+overzero)-abs(gradmodZ);

    gradmodS = ones(dimmodel,1)*0.0002;
    gradmodS(ind) = -1.0;
    weightmod = [gradmodS;gradmodX;gradmodY;gradmodZ];

    %%
    dlmwrite('weightmod.txt',weightmod,'precision',7,'newline','pc');

```

## lat\_interp.m

```

% lat_interp.m v2.0
% Written by Derek Kouhi
% Last Updated: June 10th 2016
%
% This program takes the magnetic susceptibility or density drillhole
% data and bins it into user-determined cells for inversion similar to
% UBC-GIF_Conversion.m. It implements lateral interpolation methods
% described in Kouhi and Tiampo (2016b) to create a weighted average
% reference model which is used to calculate maximum and minimum
boundary
% models. These models can be calculated using set +/- values
(default)
% or statistically using standard deviation. Magnetic and gravity
% codes are very similar, with slight distinctions.

%% Magnetic

% Import Data and Recover Well Locations

% Important Variables:
%     new = list of well locations
%     all = data in the format: x,y,z,susc

```



```

clear new
clear new1
clear new2
clear data
clear data2
data = xlsread('BH_locations.xlsx',1,'A1:E65512');
data2 = xlsread('BH_locations.xlsx',1,'A65513:E113943');
count = 1;
for i = 1:length(data)
    if data(i,3) == 0
        new1(count,1) = data(i,1);
        new1(count,2) = data(i,2);
        count = count + 1;
    end
end
count = 1;
for i = 1:length(data2)
    if data2(i,3) == 0
        new2(count,1) = data2(i,1);
        new2(count,2) = data2(i,2);
        count = count + 1;
    end
end
count = 1;
for i = 1:length(data)
    if isfinite(data(i,4))
        all1(count,1) = data(i,1);
        all1(count,2) = data(i,2);
        all1(count,3) = data(i,5);
        all1(count,4) = data(i,4)/1000;
        count = count + 1;
    end
end
count = 1;
for i = 1:length(data2)
    if isfinite(data2(i,4))
        all2(count,1) = data2(i,1);
        all2(count,2) = data2(i,2);
        all2(count,3) = data2(i,5);
        all2(count,4) = data2(i,4)/1000;
        count = count + 1;
    end
end
new = [new1;new2];
all = [all1;all2];

clear count
clear i
clear new1
clear new2
clear all1
clear all2
clear data
clear data2

% Input Dimensions and Set Mesh Layout

```

```

% Important Variables:
%     dim() = size of the model in the x,y,z directions
%     dimmodel = the total size of the model file (x*y*z)
%     x,y = cell sizes in the x and y directions
%     zcells = cell sizes in the depth domain
%     X,Y = gridded meshes

space = 20;
x = [413150,413950,414350,414550:space:418250,418450,418850,419650];
y =
[6883350,6884150,6884550,6884750:space:6889250,6889450,6889850,6890650]
;
zcells = [300:-12.5:-700,-725:-25:-1700];
dimx = length(x) - 1;
dimy = length(y) - 1;
dimz = length(zcells) - 1;
dimmodel = dimx*dimy*dimz;
[X,Y]=meshgrid(x,y);

clear count
clear i
clear space

% Laterally Interpolate and Sort the Data into Cells

% Important Variables:
%     timet = total time of the run
%     percentile = percentage of the highest values to use in the
model
%     model = the model created using the data
%     addition = the running sum of all weighted values for each cell
%     total = the total number of values added to addition
%     accurval = the running sum of all weighted accuracy values for
%               each cell

% Inputs

percentile = 0.1;

%
clc
timet = 0;
if percentile > 0.9 && percentile <= 1.0
    C = 1;
elseif percentile > 1.0 || percentile <= 0.0
    error('The percentile must be between 0 and 1.0!');
    return
else
    C = 0;
end
model = zeros(dimmodel,1);
addition = zeros(dimmodel,1);
total = zeros(dimmodel,1);
accurval = zeros(dimmodel,1);
standevadd = zeros(dimmodel,1);
totaldev = zeros(dimmodel,1);

```

```

accurvaldev = zeros(dimmodel,1);
for i = 1:dimy
    tic;
    disp(['y-index ',num2str(i),' of ',num2str(dimy)]);
    for j = 1:dimx
        for k = 1:dimz
            cellno = dimx*dimz*(i-1)+dimz*(j-1)+k;
            emin = x(j);
            emax = x(j+1);
            nmin = y(i);
            nmax = y(i+1);
            zmin = zcells(k+1);
            zmax = zcells(k);

            indices = find(all(:,1) >= emin & all(:,1) <= emax &...
                all(:,2) >= nmin & all(:,2) <= nmax &...
                all(:,3) >= zmin & all(:,3) <= zmax);

            if ~isempty(indices)
                %Implement percentile
                add1(1,:) = all(indices,4);
                add1 = sort(add1);
                standevadd(cellno,1) = standevadd(cellno,1) +
std(add1);

                start = length(add1)-ceil(length(add1)*percentile)+C;
                if start < 1
                    start = 1;
                end
                useadd = add1(start:length(add1));

                addition(cellno,1) = addition(cellno,1) +
4*sum(useadd);
                total(cellno,1) = total(cellno,1) + length(useadd);
                accurval(cellno,1) = accurval(cellno,1) +
4*length(useadd);
                totaldev(cellno,1) = totaldev(cellno,1) + 1;
                accurvaldev(cellno,1) = accurvaldev(cellno,1) + 4;

                %Interpolate to surrounding cells
                for w = -3:3
                    for v = -3:3
                        if (w~=v~=0)
                            if abs(w) >= abs(v)
                                if (cellno+w*dimx*dimz+v*dimz <=
dimmodel-3*dimx*dimz)

addition(cellno+w*dimx*dimz+v*dimz,1)=addition(cellno+w*dimx*dimz+v*dim
z,1)+(4-abs(w))*sum(useadd);
                                total(cellno+w*dimx*dimz+v*dimz,1)
= total(cellno+w*dimx*dimz+v*dimz,1) + length(useadd);

                                accurval(cellno+w*dimx*dimz+v*dimz,1) =
                                accurval(cellno+w*dimx*dimz+v*dimz,1) + (4-abs(w))*length(useadd);

                                standevadd(cellno+w*dimx*dimz+v*dimz,1)=standevadd(cellno+w*dimx*dimz+v
*dimz,1)+(4-abs(w))*std(add1);

```

```

totaldev(cellno+w*dimx*dimz+v*dimz,1) =
totaldev(cellno+w*dimx*dimz+v*dimz,1) + 1;

accurvaldev(cellno+w*dimx*dimz+v*dimz,1) =
accurvaldev(cellno+w*dimx*dimz+v*dimz,1) + (4-abs(w));
    end
    else
        if (cellno+w*dimx*dimz+v*dimz <=
dimmodel-3*dimx*dimz)

addition(cellno+w*dimx*dimz+v*dimz,1)=addition(cellno+w*dimx*dimz+v*dim
z,1)+(4-abs(v))*sum(useadd);
                                total(cellno+w*dimx*dimz+v*dimz,1)
= total(cellno+w*dimx*dimz+v*dimz,1) + length(useadd);

accurval(cellno+w*dimx*dimz+v*dimz,1) =
accurval(cellno+w*dimx*dimz+v*dimz,1) + (4-abs(v))*length(useadd);

standevadd(cellno+w*dimx*dimz+v*dimz,1)=standevadd(cellno+w*dimx*dimz+v
*dimz,1)+(4-abs(v))*std(add1);

totaldev(cellno+w*dimx*dimz+v*dimz,1) =
totaldev(cellno+w*dimx*dimz+v*dimz,1) + 1;

accurvaldev(cellno+w*dimx*dimz+v*dimz,1) =
accurvaldev(cellno+w*dimx*dimz+v*dimz,1) + (4-abs(v));
    end
    end
    end
    end
    end
    clear add1
    clear useadd
    end
    end
    time = toc;
    timet = timet + time;
    clc
    disp(['Time for run: ',num2str(floor(time/60)),' minutes and
',num2str(((time/60)-floor(time/60))*60),' seconds']);
    disp(['Estimated time remaining: ',num2str(floor(time*(dimy-
i)/3600)),' hours and ',...
        num2str(((time*(dimy-i)/3600)-floor(time*(dimy-i)/3600))*60),'
minutes']);
    end
    disp('Calculating Model.....');
    for ii = 1:dimmodel
        if accurval(ii)==0
            accurval(ii) = 1;
        end
        if total(ii)==0
            total(ii) = 1;
        end
    end
end
for ii = 1:dimmodel

```

```

        if accurvaldev(ii)==0
            accurvaldev(ii) = 1;
        end
        if totaldev(ii)==0
            totaldev(ii) = 1;
        end
    end
end
% Calculate the weighted average for susceptibility and accuracy values
model = addition./accurval;
avgacc = floor(accurval./total);
standev = standevadd./accurvaldev;
avgaccdev = floor(accurvaldev./totaldev);
clc
disp('*****MODEL COMPLETED*****');
disp(['Total Run Time: ',num2str(floor(timet/3600)),' hours, ',...
    num2str(floor((timet/3600-floor(timet/3600))*60)),' minutes and ',...
    num2str(timet-(floor(timet/3600))*3600-(floor((timet/3600-
floor(timet/3600))*60))*60),' seconds']);
clear count
clear emin
clear emax
clear nmin
clear nmax
clear zmax
clear zmin
clear percentile
clear start
clear time
clear timet
clear k
clear C
clear indices
clear i
clear j
clear cellno
clear p
disp('Writing Model to Text File..');
dlmwrite([num2str(dimx),'x',num2str(dimy),'x',num2str(dimz),'_magmod.tx
t'],...
    model,'precision',7,'newline','pc');
disp('COMPLETE');

% Create a Starting Model

% Important Variables:
%     zeroval = the value to give to points that do not contain data
%     start_mod = the starting model

% Inputs

zeroval = 0.0001;

%
disp('CREATING MODELS....');

start_mod = zeros(length(model),1);

```

```

for i = 1:length(model)
    if model(i) == 0
        start_mod(i) = zeroval;
    else
        start_mod(i) = model(i);
    end
end

disp('Writing starting model..');
dlmwrite([num2str(dimx), 'x', num2str(dimy), 'x', num2str(dimz), '_magstart.
txt'], ...
        start_mod, 'precision', 7, 'newline', 'pc');
disp('Starting model saved!');
clear i
clear zeroval

% Create Maximum and Minimum Boundary Models

% Important Variables:
%     range = the value to +/- from the measured value to form the
range
%     maxnon = the value to assign for the maximum of cells with no
data
%     max_mod = the maximum boundary model
%     min_mod = the minimum boundary model

% Inputs

% r1-r4 are the +/- values depending on the accuracy value of the cell
r1 = 0.01;
r2 = 0.075;
r3 = 0.05;
r4 = 0.025;

maxnon = 0.6;
minnon = 0;

%

max_mod = zeros(length(model),1);
min_mod = zeros(length(model),1);

% OPTIONAL CODE: takes a statistical approach to assigning max/min
values
%                 using standard deviations rather than set +/- values
% mult1 = 2.5;
% mult2 = 2;
% mult3 = 1.5;
% mult4 = 1;
%
% for i = 1:length(model)
%     if model(i) == 0 || standev(i) == 0
%         max_mod(i) = maxnon;
%         min_mod(i) = minnon;
%     else
%         if avgacc(i) == 1
%             max_mod(i) = model(i)+standev(i)*mult1;

```

```

%         min_mod(i) = model(i)-standev(i)*mult1;
%         if max_mod(i) > maxnon
%             max_mod(i) = maxnon;
%         end
%         if min_mod(i) < minnon
%             min_mod(i) = minnon;
%         end
%     elseif avgacc(i) == 2
%         max_mod(i) = model(i)+standev(i)*mult2;
%         min_mod(i) = model(i)-standev(i)*mult2;
%         if max_mod(i) > maxnon
%             max_mod(i) = maxnon;
%         end
%         if min_mod(i) < minnon
%             min_mod(i) = minnon;
%         end
%     elseif avgacc(i) == 3
%         max_mod(i) = model(i)+standev(i)*mult3;
%         min_mod(i) = model(i)-standev(i)*mult3;
%         if max_mod(i) > maxnon
%             max_mod(i) = maxnon;
%         end
%         if min_mod(i) < minnon
%             min_mod(i) = minnon;
%         end
%     elseif avgacc(i) == 4
%         max_mod(i) = model(i)+standev(i)*mult4;
%         min_mod(i) = model(i)-standev(i)*mult4;
%         if max_mod(i) > maxnon
%             max_mod(i) = maxnon;
%         end
%         if min_mod(i) < minnon
%             min_mod(i) = minnon;
%         end
%     end
% end
% end

% Calculate max/min boundary models using accuracy values
for i = 1:length(model)
    if model(i) == 0 || standev(i) == 0
        max_mod(i) = maxnon;
        min_mod(i) = minnon;
    else
        if avgacc(i) == 1
            max_mod(i) = model(i)+r1;
            min_mod(i) = model(i)-r1;
            if max_mod(i) > maxnon
                max_mod(i) = maxnon;
            end
            if min_mod(i) < minnon
                min_mod(i) = minnon;
            end
        elseif avgacc(i) == 2
            max_mod(i) = model(i)+r2;
            min_mod(i) = model(i)-r2;
            if max_mod(i) > maxnon

```

```

        max_mod(i) = maxnon;
    end
    if min_mod(i) < minnon
        min_mod(i) = minnon;
    end
elseif avgacc(i) == 3
    max_mod(i) = model(i)+r3;
    min_mod(i) = model(i)-r3;
    if max_mod(i) > maxnon
        max_mod(i) = maxnon;
    end
    if min_mod(i) < minnon
        min_mod(i) = minnon;
    end
elseif avgacc(i) == 4
    max_mod(i) = model(i)+r4;
    min_mod(i) = model(i)-r4;
    if max_mod(i) > maxnon
        max_mod(i) = maxnon;
    end
    if min_mod(i) < minnon
        min_mod(i) = minnon;
    end
end
end
end
for i = 1:length(model)
    if max_mod(i) == min_mod(i)
        max_mod(i) = maxnon;
        min_mod(i) = minnon;
    end
end
for i = 1:length(model)
    if round(max_mod(i),9) == round(min_mod(i),9)
        max_mod(i) = max_mod(i) + 0.01;
        min_mod(i) = min_mod(i) - 0.01;
    end
end

disp('Writing maximum model..');
dlmwrite([num2str(dimx),'x',num2str(dimy),'x',num2str(dimz),'_magmax.txt'],...
    max_mod,'precision',7,'newline','pc');
disp('Maximum model saved!');
disp('Writing minimum model..');
dlmwrite([num2str(dimx),'x',num2str(dimy),'x',num2str(dimz),'_magmin.txt'],...
    min_mod,'precision',7,'newline','pc');
disp('Minimum model saved!');

clear i
clear range
clear maxnon

% Create Active Cell Matrix (OPTIONAL)

active = ones(length(avgacc),1);

```



```

for i = 1:length(avgacc)
    if avgacc(i) == 4
        active(i) = -1;
    end
end

disp('Writing active cell matrix..');
dlmwrite([num2str(dimx), 'x', num2str(dimy), 'x', num2str(dimz), '_active_ma
g.txt'], ...
    active, 'precision', 7, 'newline', 'pc');
disp('Active cell matrix saved!');
clc
disp('~***MODELS COMPLETE***~');

%% Gravity Variation of Interpolation Code

% Import Data and Recover Well Locations

% Important Variables:
%     new = list of well locations
%     all = data in the format: x,y,z,susc

clear new
clear new1
clear new2
clear data
data = xlsread('BH_locations_den.xlsx');

count = 1;
for i = 1:length(data)
    if data(i,3) == 0
        new1(count,1) = data(i,1);
        new1(count,2) = data(i,2);
        count = count + 1;
    end
end

count = 1;
for i = 1:length(data)
    if isfinite(data(i,4))
        all1(count,1) = data(i,1);
        all1(count,2) = data(i,2);
        all1(count,3) = data(i,5);
        all1(count,4) = data(i,4);
        count = count + 1;
    end
end

% new = new1;
all = all1;

clear count
clear i
clear new1
clear all1
clear data

```

```

%% Input Dimensions and Set Mesh Layout

% Important Variables:
%     dim() = size of the model in the x,y,z directions
%     dimmodel = the total size of the model file (x*y*z)
%     x,y = cell sizes in the x and y directions
%     zcells = cell sizes in the depth domain
%     X,Y = gridded meshes

space = 20;
x = [413150,413950,414350,414550:space:418250,418450,418850,419650];
y =
[6883350,6884150,6884550,6884750:space:6889250,6889450,6889850,6890650]
;
zcells = [300:-12.5:-700,-725:-25:-1700];
dimx = length(x) - 1;
dimy = length(y) - 1;
dimz = length(zcells) - 1;
dimmodel = dimx*dimy*dimz;
[X,Y]=meshgrid(x,y);

clear count
clear i
clear space

% Sort the Data into Cells (rewrite)

% Important Variables:
%     timet = total time of the run
%     percentile = percentage of the highest values to use in the
model
%     model = the model created using the data

% Inputs

%
clc
timet = 0;
model = zeros(dimmodel,1);
addition = zeros(dimmodel,1);
total = zeros(dimmodel,1);
accurval = zeros(dimmodel,1);
for i = 1:dimy
    tic;
    disp(['y-index ',num2str(i),' of ',num2str(dimy)]);
    for j = 1:dimx
        for k = 1:dimz
            cellno = dimx*dimz*(i-1)+dimz*(j-1)+k;
            emin = x(j);
            emax = x(j+1);
            nmin = y(i);
            nmax = y(i+1);
            zmin = zcells(k+1);
            zmax = zcells(k);

            indices = find(all(:,1) >= emin & all(:,1) <= emax &...

```

```

        all(:,2) >= nmin & all(:,2) <= nmax &...
        all(:,3) >= zmin & all(:,3) <= zmax);

        if ~isempty(indices)
            addition(cellno,1) = addition(cellno,1) +
4*sum(all(indices,4));
            total(cellno,1) = total(cellno,1) + length(indices);
            accurval(cellno,1) = accurval(cellno,1) +
4*length(indices);

            for w = -3:3
                for v = -3:3
                    if (w~=v~=0)
                        if abs(w) >= abs(v)
                            if (cellno+w*dimx*dimz+v*dimz <=
dimmodel-3*dimx*dimz)
addition(cellno+w*dimx*dimz+v*dimz,1)=addition(cellno+w*dimx*dimz+v*dim
z,1)+(4-abs(w))*sum(all(indices,4));
                                total(cellno+w*dimx*dimz+v*dimz,1)
= total(cellno+w*dimx*dimz+v*dimz,1) + length(indices);

                                accurval(cellno+w*dimx*dimz+v*dimz,1) =
                                accurval(cellno+w*dimx*dimz+v*dimz,1) + (4-abs(w))*length(indices);
                                end
                                else
                                    if (cellno+w*dimx*dimz+v*dimz <=
dimmodel-3*dimx*dimz)
addition(cellno+w*dimx*dimz+v*dimz,1)=addition(cellno+w*dimx*dimz+v*dim
z,1)+(4-abs(v))*sum(all(indices,4));
                                            total(cellno+w*dimx*dimz+v*dimz,1)
= total(cellno+w*dimx*dimz+v*dimz,1) + length(indices);

                                            accurval(cellno+w*dimx*dimz+v*dimz,1) =
                                            accurval(cellno+w*dimx*dimz+v*dimz,1) + (4-abs(v))*length(indices);
                                            end
                                        end
                                    end
                                end
                            end
                        end
                    end
                end
            end
        end
        time = toc;
        timet = timet + time;
        clc
        disp(['Time for run: ',num2str(floor(time/60)), ' minutes and
',num2str(((time/60)-floor(time/60))*60), ' seconds']);
        disp(['Estimated time remaining: ',num2str(floor(time*(dimy-
i)/3600)), ' hours and ',...
            num2str(((time*(dimy-i)/3600)-floor(time*(dimy-i)/3600))*60), '
minutes']);
    end
    disp('Calculating Model.....');
    for ii = 1:dimmodel

```

```

        if accurval(ii)==0
            accurval(ii) = 1;
        end
        if total(ii)==0
            total(ii) = 1;
        end
    end
end
model = addition./accurval;
avgacc = floor(accurval./total);
clc
disp('*****MODEL COMPLETED*****');
disp(['Total Run Time: ',num2str(floor(timet/3600)),' hours, ',...
    num2str(floor((timet/3600-floor(timet/3600))*60)),' minutes and
    ',...
    num2str(timet-(floor(timet/3600))*3600-(floor((timet/3600-
    floor(timet/3600))*60))*60),' seconds']);
clear count
clear emin
clear emax
clear nmin
clear nmax
clear zmax
clear zmin
clear percentile
clear start
clear time
clear timet
clear k
clear C
clear indices
clear i
clear j
clear cellno
clear p
disp('Writing Model to Text File..');
modelsave = model; % Save a copy of calculated model
for i = 1:length(model)
    if model(i) == 0
        model(i) = 0;
    else
        model(i) = model(i) - 2.67; % Subtract average density
    end
end
end
dlmwrite([num2str(dimx),'x',num2str(dimy),'x',num2str(dimz),'_density.t
xt'],...
    model,'precision',7,'newline','pc');
disp('COMPLETE');

% Create a Starting Model

% Important Variables:
%     zeroval = the value to give to points that do not contain data
%     start_mod = the starting model

% Inputs

zeroval = 0;

```

```

%

start_mod = zeros(length(model),1);
for i = 1:length(model)
    if model(i) == 0
        start_mod(i) = zeroval;
    else
        start_mod(i) = model(i);
    end
end

dlmwrite([num2str(dimx),'x',num2str(dimy),'x',num2str(dimz),'_density_s
tart.txt'],...
        start_mod,'precision',7,'newline','pc');

clear i
clear zeroval

% Create Maximum and Minimum Boundary Models (rewrite)

% Important Variables:
%     range = the value to +/- from the measured value to form the
range
%     maxnon = the value to assign for the maximum of cells with no
data
%     max_mod = the maximum boundary model
%     min_mod = the minimum boundary model

% Inputs

r1 = 0.5;
r2 = 0.3;
r3 = 0.2;
r4 = 0.1;
maxnon = 1.0;
minnon = -1.0;

%

max_mod = zeros(length(model),1);
min_mod = zeros(length(model),1);
for i = 1:length(model)
    if model(i) == 0
        max_mod(i) = maxnon;
        min_mod(i) = minnon;
    else
        if avgacc(i) == 1
            max_mod(i) = model(i)+r1;
            min_mod(i) = model(i)-r1;
        elseif avgacc(i) == 2
            max_mod(i) = model(i)+r2;
            min_mod(i) = model(i)-r2;
        elseif avgacc(i) == 3
            max_mod(i) = model(i)+r3;
            min_mod(i) = model(i)-r3;
        elseif avgacc(i) == 4

```

```

        max_mod(i) = model(i)+r4;
        min_mod(i) = model(i)-r4;
    end
end
end

dlmwrite([num2str(dimx),'x',num2str(dimy),'x',num2str(dimz),'_max.txt']
,....
    max_mod,'precision',7,'newline','pc');
dlmwrite([num2str(dimx),'x',num2str(dimy),'x',num2str(dimz),'_min.txt']
,....
    min_mod,'precision',7,'newline','pc');

clear i
clear range
clear maxnon

% Create Active Cell Matrix (OPTIONAL)

active = ones(length(avgacc),1);
for i = 1:length(avgacc)
    if avgacc(i) == 4
        active(i) = -1;
    end
end
end

dlmwrite([num2str(dimx),'x',num2str(dimy),'x',num2str(dimz),'_active_de
ns.txt'],...
    active,'precision',7,'newline','pc');
```

## joint.m

```

% joint.m
% Written by Derek Kouhi
% June 2016
%
% This program takes the current best models for both datasets as
inputs
% and calculates their gradients. These values are then normalized
% and summed and used to inversely proportion weighting coefficients
% for subsequent inversions. Gradient method is similar to that
% of grad_attenuate.m

%% Input Dimensions and Set Mesh Layout

% Important Variables:
%     dim() = size of the model in the x,y,z directions
%     dimmodel = the total size of the model file (x*y*z)
%     x,y = cell sizes in the x and y directions
%     zcells = cell sizes in the depth domain
%     X,Y = gridded meshes
clear
clc
tic;
space = 20;
x = [413150,413950,414350,414550:space:418250,418450,418850,419650];
```

```

y =
[6883350,6884150,6884550,6884750:space:6889250,6889450,6889850,6890650]
;
zcells = [300:-10:-800,-820:-20:-1340];
% zcells = [300:-12.5:-700,-725:-25:-1700];
dimx = length(x) - 1;
dimy = length(y) - 1;
dimz = length(zcells) - 1;
dimmodel = dimx*dimy*dimz;
[X,Y]=meshgrid(x,y);

clear count
clear i
clear space

% Unwrap a Model

% Important Variables:
%     inmodel = the model that is being unwrapped
%     unwrap = the unwrapped 3-D matrix (x,y,z)

disp('Unwrapping magnetic model...      [1/6]');
fileID = fopen('mag2.txt','r');
formatSpec = '%f';
inmodel = fscanf(fileID,formatSpec);

fileID = fopen('191x231x137_magmax.txt','r');
formatSpec = '%f';
maxmag = fscanf(fileID,formatSpec);
fileID = fopen('191x231x137_magmin.txt','r');
formatSpec = '%f';
minmag = fscanf(fileID,formatSpec);

ind = find(inmodel == -100);
for i = 1:length(inmodel)
    if inmodel(i) < minmag(i)
        inmodel(i) = minmag(i);
    elseif inmodel(i) > maxmag(i);
        inmodel(i) = maxmag(i);
    end
end

dlmwrite('prevmag.txt',inmodel,'precision',7,'newline','pc');
unwrap = zeros(dimx,dimy,dimz);
count = 1;
for i = 1:dimy
    for j = 1:dimx
        for k = 1:dimz
            unwrap(j,i,k) = inmodel(count);
            count = count + 1;
        end
    end
end

magunwrap = unwrap;
disp('Magnetic model unwrapped!');

```

```

clear fileID
clear formatSpec
clear inmodel
clear minmag
clear maxmag
clear unwrap
clear count
clear i
clear j
clear k

disp('Unwrapping density model...      [2/6]');
fileID = fopen('den2.txt','r');
formatSpec = '%f';
inmodel = fscanf(fileID,formatSpec);

fileID = fopen('191x231x137_max.txt','r');
formatSpec = '%f';
maxden = fscanf(fileID,formatSpec);
fileID = fopen('191x231x137_min.txt','r');
formatSpec = '%f';
minden = fscanf(fileID,formatSpec);

for i = 1:length(inmodel)
    if inmodel(i) < minden(i)
        inmodel(i) = minden(i);
    elseif inmodel(i) > maxden(i);
        inmodel(i) = maxden(i);
    end
end

ind = find(inmodel == -100);
inmodel(ind) = 0;
dlmwrite('prevden.txt',inmodel,'precision',7,'newline','pc');
unwrap = zeros(dimx,dimy,dimz);
count = 1;
for i = 1:dimy
    for j = 1:dimx
        for k = 1:dimz
            unwrap(j,i,k) = inmodel(count);
            count = count + 1;
        end
    end
end

denunwrap = unwrap;
disp('Magnetic model unwrapped!');

clear fileID
clear formatSpec
clear inmodel
clear minden
clear maxden
clear unwrap
clear count
clear i

```



```

clear j
clear k

% Remove Padding

% Important Variables:
%     xypadding = the number of padded cells on either side on x-y
plane
%     zpadding = the number of cells padding the bottom in z-
direction
%     unwrap = the unwrapped 3-D matrix (x,y,z)
%     unpad = the unwrapped 3-D matrix with padding removed

% Inputs

xypadding = 3;
zpadding = 3;

%

disp('Removing padding...      [3/6]');
magunpad = magunwrap(xypadding+1:dimx-xypadding,xypadding+1:dimy-
xypadding,...
    1:dimz-zpadding);
denunpad = denunwrap(xypadding+1:dimx-xypadding,xypadding+1:dimy-
xypadding,...
    1:dimz-zpadding);
clear magunwrap
clear denunwrap

disp('Padding Removed!');

% Find the Gradient of the Unpadded Model

% Important Variables:
%     HX, HY, HZ = cell spacing in each direction (x,y,z)
%     unpad = the unwrapped 3-D matrix with padding removed
%     FX, FY, FZ = the gradient in each component

% Inputs

HX = 20;
HY = 20;
HZ = 10;

%

disp('Calculating gradients...      [4/6]');
[FXmag,FYmag,FZmag] = gradient(magunpad,HX,HY,HZ);
[FXden,FYden,FZden] = gradient(denunpad,HX,HY,HZ);
clear magunpad
clear denunpad
FXmag = FXmag/max(max(max(abs(FXmag)))));
FYmag = FYmag/max(max(max(abs(FYmag)))));
FZmag = FZmag/max(max(max(abs(FZmag)))));
FXden = FXden/max(max(max(abs(FXden)))));
FYden = FYden/max(max(max(abs(FYden)))));

```

```

FZden = FZden/max(max(max(abs(FZden))));
FX = abs(FXmag) + abs(FXden);
FY = abs(FYmag) + abs(FYden);
FZ = abs(FZmag) + abs(FZden);
FX = FX/max(max(max(abs(FX))));
FY = FY/max(max(max(abs(FY))));
FZ = FZ/max(max(max(abs(FZ))));
FX = FX*1;
FY = FY*1;
FZ = FZ*1;
% Set threshold for what gradients are included
delx = find(FX > 0.5);
dely = find(FY > 0.5);
delz = find(FZ > 0.5);
FX(delx) = 0.5;
FY(dely) = 0.5;
FZ(delz) = 0.5;
clear delx
clear dely
clear delz
delx = find(FX < 0.3);
dely = find(FY < 0.3);
delz = find(FZ < 0.3);
FX(delx) = 0.3;
FY(dely) = 0.3;
FZ(delz) = 0.3;
clear delx
clear dely
clear delz
clear FXmag
clear FYmag
clear FZmag
clear FXden
clear FYden
clear FZden

% Repad and Rewrap the Gradient Models

% Important Variables:
%     HX,HY,HZ = cell spacing in each direction (x,y,z)
%     unpad = the unwrapped 3-D matrix with padding removed
%     FX,FY,FZ = the gradient in each component

% Inputs

overzero = 0.3; % Sets the minimum weighting coefficient

%

disp('Creating weighting file and rewrapping...    [5/6]');
FXrr = zeros(dimx-1,dimy,dimz);
FYrr = zeros(dimx,dimy-1,dimz);
FZrr = zeros(dimx,dimy,dimz-1);
FXrr(xypadding+1:dimx-xypadding,xypadding+1:dimy-xypadding,...
    1:dimz-zpadding) = FX;
FYrr(xypadding+1:dimx-xypadding,xypadding+1:dimy-xypadding,...
    1:dimz-zpadding) = FY;

```

```

FZrr(xypadding+1:dimx-xypadding,xypadding+1:dimy-xypadding,...
    1:dimz-zpadding) = FZ;
clear FX
clear FY
clear FZ

gradmodX = zeros(dimmodel-dimy*dimz,1);
gradmodY = zeros(dimmodel-dimx*dimz,1);
gradmodZ = zeros(dimmodel-dimx*dimy,1);
for i = 1:dimy
    for j = 1:dimx-1
        for k = 1:dimz
            cellno = (dimx-1)*dimz*(i-1)+dimz*(j-1)+k;
            if k <= 41
                gradmodX(cellno,1) = FXrr(j,i,k);
            else
                gradmodX(cellno,1) = overzero;
            end
        end
    end
end
for i = 1:dimy-1
    for j = 1:dimx
        for k = 1:dimz
            cellno = dimx*dimz*(i-1)+dimz*(j-1)+k;
            if k <= 41
                gradmodY(cellno,1) = FYrr(j,i,k);
            else
                gradmodY(cellno,1) = overzero;
            end
        end
    end
end
for i = 1:dimy
    for j = 1:dimx
        for k = 1:dimz-1
            cellno = dimx*(dimz-1)*(i-1)+(dimz-1)*(j-1)+k;
            if k <=41
                gradmodZ(cellno,1) = FZrr(j,i,k);
            else
                gradmodZ(cellno,1) = overzero;
            end
        end
    end
end
gradmodX = ones(dimmodel-dimy*dimz,1)*(0.5+overzero)-abs(gradmodX);
gradmodY = ones(dimmodel-dimx*dimz,1)*(0.5+overzero)-abs(gradmodY);
gradmodZ = ones(dimmodel-dimx*dimy,1)*(0.5+overzero)-abs(gradmodZ);

gradmodS = ones(dimmodel,1)*0.0001;
gradmodS(ind) = -1.0;
weightmod = [gradmodS;gradmodX;gradmodY;gradmodZ];
disp('Weighting file created!');

disp('Saving weighting file...      [6/6]');
dlmwrite('weightmod2.txt',weightmod,'precision',7,'newline','pc');
disp('Weighting file saved!');

```

```

clc
disp('~***PROGRAM COMPLETE***~');
timet = toc;
disp(['Total Run Time: ',num2str(floor(timet/3600)),' hours, ',...
    num2str(floor((timet/3600-floor(timet/3600))*60)),' minutes and ',...
    num2str(timet-(floor(timet/3600))*3600-(floor((timet/3600-
floor(timet/3600))*60))*60),' seconds']);

```

## geo\_analysis.m

```

% geo_analysis.m
% Written by Derek Kouhi
% July 2016
% A script that takes mass- and volume-based magnetic susceptibility
% measurements at depth, along with their densities to create plots to
% find geological trends in the data.

%% Mass-Based Magnetic Susceptibility Analysis

% This section reads input mass-based susceptibility measurements at
% depth and plots them over their lithological units. Unit names and
% depth boundaries must be supplied.

% Input depth and mass-based susceptibility data via xls
data = xlsread('geology.xlsx');
depth = data(:,1);
msusc = data(:,2);

clear data

% Create a log-y plot of depth vs. magnetic susceptibility
figure('units','normalized','outerposition',[0 0 1 1])
semilogy(depth,msusc,'k.','MarkerSize',15);
hold on;
axis([0 1080 0 1000]);

% Identify the depth limits on each lithological unit (x-component)
% and plot as the area under a line. The y-component is arbitrary
% given the maximum height of the plot

%NLS-5
x = [15,60];
y = [1000,1000];
area(x,y,'FaceColor',[1 0 0],'FaceAlpha',0.3);
text(16,600,'NLS-5','Color',[1 0 0],'FontSize',10,'FontWeight','bold');
%NLS-6
x = [95,135];
y = [1000,1000];
area(x,y,'FaceColor',[0 0 0],'FaceAlpha',0.3);
text(96,600,'NLS-6','Color',[0 0 0],'FontSize',10,'FontWeight','bold');
%NLS-7
x = [135,150];
y = [1000,1000];
area(x,y,'FaceColor',[0 0.5 0],'FaceAlpha',0.3);
%NLS-8

```

```

x = [150,300];
y = [1000,1000];
area(x,y,'FaceColor',[0 1 0],'FaceAlpha',0.3);
text(200,600,'NLS-8','Color',[0 0.5
0],'FontSize',12,'FontWeight','bold');
%NLS-9
x = [300,450];
y = [1000,1000];
area(x,y,'FaceColor',[0 0 1],'FaceAlpha',0.3);
text(350,600,'NLS-9','Color',[0 0
1],'FontSize',12,'FontWeight','bold');
%NLS-10
x = [450,480];
y = [1000,1000];
area(x,y,'FaceColor',[0 0 0.5],'FaceAlpha',0.3);
%NLS-11
x = [480,720];
y = [1000,1000];
area(x,y,'FaceColor',[0.5 0.25 0.1],'FaceAlpha',0.3);
text(570,600,'NLS-11','Color',[0.5 0.25
0.1],'FontSize',12,'FontWeight','bold');
%NLS-12
x = [720,870];
y = [1000,1000];
area(x,y,'FaceColor',[1 0 1],'FaceAlpha',0.3);
text(770,600,'NLS-12','Color',[1 0
1],'FontSize',12,'FontWeight','bold');
%NLS-13
x = [870,1065];
y = [1000,1000];
area(x,y,'FaceColor',[1 0.5 0.5],'FaceAlpha',0.3);
text(950,600,'NLS-13','Color',[1 0.5
0.5],'FontSize',12,'FontWeight','bold');
%NLS-14
x = [1065,1080];
y = [1000,1000];
area(x,y,'FaceColor',[1 0.5 0],'FaceAlpha',0.3);

% Label the figure
xlabel('Depth (m)');
ylabel('Magnetic Susceptibility (m^3/kg)');
title('Mass-Based Magnetic Susceptibility by Lithological Unit');

%% Volume Based Magnetic Susceptibility Analysis

% This section reads input volume-based susceptibility measurements at
% depth, plots them over their lithological units and compares their
% values to previously measured susceptibilities. Unit names and
% depth boundaries must be supplied.

% Inputs:
% - drilldata: previous susceptibility measurements
% - vsusc: converted volume-based susceptibility data
% - vsuscens: converted susceptibility data using constant density
for
% sensitivity analysis

```

```

data = xlsread('geology.xlsx');
drilldata = xlsread('deephole_susc.xlsx');
vsusc = xlsread('geology2.xlsx');
vsuscsens = xlsread('geology3.xlsx');
depth = data(:,1);
drilldepth = drilldata(:,1);
drillsusc = drilldata(:,2);

clear data
clear drilldata

% Plot the previous magnetic data vs. new data for contrast
figure('units','normalized','outerposition',[0 0 1 1])
plot(drilldepth,drillsusc);
hold on;
axis([0 1080 0 0.35]);
plot(depth,vsusc,'ro');
plot(depth,vsuscsens,'o','Color',[0 0.5 0]);

% Identify the depth limits on each lithological unit (x-component)
% and plot as the area under a line. The y-component is arbitrary
% given the maximum height of the plot

%NLS-5
x = [15,60];
y = [0.35,0.35];
area(x,y,'FaceColor',[1 0 0],'FaceAlpha',0.3);
text(16,0.33,'NLS-5','Color',[1 0
0],'FontSize',10,'FontWeight','bold');
%NLS-6
x = [95,135];
y = [0.35,0.35];
area(x,y,'FaceColor',[0 0 0],'FaceAlpha',0.3);
text(96,0.33,'NLS-6','Color',[0 0
0],'FontSize',10,'FontWeight','bold');
%NLS-7
x = [135,150];
y = [0.35,0.35];
area(x,y,'FaceColor',[0 0.5 0],'FaceAlpha',0.3);
%NLS-8
x = [150,300];
y = [0.35,0.35];
area(x,y,'FaceColor',[0 1 0],'FaceAlpha',0.3);
text(200,0.33,'NLS-8','Color',[0 0.5
0],'FontSize',12,'FontWeight','bold');
%NLS-9
x = [300,450];
y = [0.35,0.35];
area(x,y,'FaceColor',[0 0 1],'FaceAlpha',0.3);
text(350,0.33,'NLS-9','Color',[0 0
1],'FontSize',12,'FontWeight','bold');
%NLS-10
x = [450,480];
y = [0.35,0.35];
area(x,y,'FaceColor',[0 0 0.5],'FaceAlpha',0.3);
%NLS-11
x = [480,720];

```

```

y = [0.35,0.35];
area(x,y,'FaceColor',[0.5 0.25 0.1],'FaceAlpha',0.3);
text(570,0.33,'NLS-11','Color',[0.5 0.25
0.1],'FontSize',12,'FontWeight','bold');
%NLS-12
x = [720,870];
y = [0.35,0.35];
area(x,y,'FaceColor',[1 0 1],'FaceAlpha',0.3);
text(770,0.33,'NLS-12','Color',[1 0
1],'FontSize',12,'FontWeight','bold');
%NLS-13
x = [870,1065];
y = [0.35,0.35];
area(x,y,'FaceColor',[1 0.5 0.5],'FaceAlpha',0.3);
text(950,0.33,'NLS-13','Color',[1 0.5
0.5],'FontSize',12,'FontWeight','bold');
%NLS-14
x = [1065,1080];
y = [0.35,0.35];
area(x,y,'FaceColor',[1 0.5 0],'FaceAlpha',0.3);

% Add labels and legend
xlabel('Depth (m)');
ylabel('Magnetic Susceptibility (SI)');
title('Volume-Based Magnetic Suscpetibility Comparison');
legend('Avalon (2013)','Kouhi and Tiampo (2016)','Density =
2.67','Location','Best');

% Scale the new measurements down by a factor of 1.5 and replot
figure('units','normalized','outerposition',[0 0 1 1])
plot(drilldepth,drillsusc);
hold on;
axis([0 1080 0 0.23]);
plot(depth,vsusc/1.5,'ro');

% Identify the depth limits on each lithological unit (x-component)
% and plot as the area under a line. The y-component is arbitrary
% given the maximum height of the plot

%NLS-5
x = [15,60];
y = [0.23,0.23];
area(x,y,'FaceColor',[1 0 0],'FaceAlpha',0.3);
text(16,0.21,'NLS-5','Color',[1 0
0],'FontSize',10,'FontWeight','bold');
%NLS-6
x = [95,135];
y = [0.23,0.23];
area(x,y,'FaceColor',[0 0 0],'FaceAlpha',0.3);
text(96,0.21,'NLS-6','Color',[0 0
0],'FontSize',10,'FontWeight','bold');
%NLS-7
x = [135,150];
y = [0.23,0.23];
area(x,y,'FaceColor',[0 0.5 0],'FaceAlpha',0.3);
%NLS-8
x = [150,300];

```

```

y = [0.23,0.23];
area(x,y,'FaceColor',[0 1 0],'FaceAlpha',0.3);
text(200,0.21,'NLS-8','Color',[0 0.5
0],'FontSize',12,'FontWeight','bold');
%NLS-9
x = [300,450];
y = [0.23,0.23];
area(x,y,'FaceColor',[0 0 1],'FaceAlpha',0.3);
text(350,0.21,'NLS-9','Color',[0 0
1],'FontSize',12,'FontWeight','bold');
%NLS-10
x = [450,480];
y = [0.23,0.23];
area(x,y,'FaceColor',[0 0 0.5],'FaceAlpha',0.3);
%NLS-11
x = [480,720];
y = [0.23,0.23];
area(x,y,'FaceColor',[0.5 0.25 0.1],'FaceAlpha',0.3);
text(570,0.21,'NLS-11','Color',[0.5 0.25
0.1],'FontSize',12,'FontWeight','bold');
%NLS-12
x = [720,870];
y = [0.23,0.23];
area(x,y,'FaceColor',[1 0 1],'FaceAlpha',0.3);
text(770,0.21,'NLS-12','Color',[1 0
1],'FontSize',12,'FontWeight','bold');
%NLS-13
x = [870,1065];
y = [0.23,0.23];
area(x,y,'FaceColor',[1 0.5 0.5],'FaceAlpha',0.3);
text(950,0.21,'NLS-13','Color',[1 0.5
0.5],'FontSize',12,'FontWeight','bold');
%NLS-14
x = [1065,1080];
y = [0.23,0.23];
area(x,y,'FaceColor',[1 0.5 0],'FaceAlpha',0.3);

% Add labels and legend
xlabel('Depth (m)');
ylabel('Magnetic Susceptibility (SI)');
title('Volume-Based Magnetic Suscpetibility Scaled Down by a Factor of
1.5');
legend('Avalon (2013)','Kouhi and Tiampo (2016)','Location','Best');

%% Rare Earth Concentration Analysis

% A plot comparing 4 key variables: density, magnetic susceptibility,
% lithological unit, and rare earth element concentration. This
section
% takes similar inputs to previous section, in addition to the
densities
% used to covert the mass-based data as well as approximate rare earth
% element concentrations.

% Input data
data = xlsread('geology.xlsx');
del = xlsread('geology4.xlsx');

```



```

vsusc = xlsread('geology2.xlsx');
dens = xlsread('geodens.xlsx');
depth = data(:,1);
REE = del(:,2);

clear data
clear del

% ih, im and il are indexing vectors for REE concentrations
ih = find(REE>=1000);
im = find(REE<1000 & REE>=200);
il = find(REE<200);

% Plot the outline of each point in a density vs susceptibility plot
figure('units','normalized','outerposition',[0 0 1 1])
plot(dens(ih),vsusc(ih),'ko','MarkerSize',10);
hold on;
plot(dens(im),vsusc(im),'ko','MarkerSize',6);
plot(dens(il),vsusc(il),'ko','MarkerSize',4);

% Create a matrix for each depth interval associated with lithology
ind = zeros(20,9);
id = [15,60,95,135,300,450,720,870,1065,2000];
for i = 1:length(id)-1
    delind = find(depth >= id(i) & depth < id(i+1));
    ind(1:length(delind),i) = delind;
    clear delind
end

% Remove zeros by setting to NaN
[del,del2] = find(ind == 0);
for i = 1: length(del)
    ind(del(i),del2(i)) = NaN;
end

% Set size values for each point based on REE concentration
reesize = zeros(length(depth),1);
for i = 1:length(depth)
    if REE(i) >= 1000
        reesize(i) = 100;
    elseif REE(i) < 1000 && REE(i) >= 200
        reesize(i) = 50;
    else
        reesize(i) = 20;
    end
end

% Plot each datapoint based on lithology (colour) and REE (size)
scatter(dens(ind((~isnan(ind(:,1))),1)),vsusc(ind((~isnan(ind(:,1))),1)),...
    reesize(ind((~isnan(ind(:,1))),1)), 'MarkerEdgeColor',[0 0 0],...
    'MarkerFaceColor',[1 0 0], 'LineWidth',1.5);
scatter(dens(ind((~isnan(ind(:,2))),2)),vsusc(ind((~isnan(ind(:,2))),2)),...
    reesize(ind((~isnan(ind(:,2))),2)), 'MarkerEdgeColor',[0 0 0],...
    'MarkerFaceColor',[0.7 0.7 0.7], 'LineWidth',1.5);

```

```

scatter(dens(ind((~isnan(ind(:,3))),3)),vsusc(ind((~isnan(ind(:,3))),3)
),...
    reesize(ind((~isnan(ind(:,3))),3),'MarkerEdgeColor',[0 0 0],...
        'MarkerFaceColor',[0 0 0],'LineWidth',1.5);
scatter(dens(ind((~isnan(ind(:,4))),4)),vsusc(ind((~isnan(ind(:,4))),4)
),...
    reesize(ind((~isnan(ind(:,4))),4),'MarkerEdgeColor',[0 0 0],...
        'MarkerFaceColor',[0 0.5 0],'LineWidth',1.5);
scatter(dens(ind((~isnan(ind(:,5))),5)),vsusc(ind((~isnan(ind(:,5))),5)
),...
    reesize(ind((~isnan(ind(:,5))),5),'MarkerEdgeColor',[0 0 0],...
        'MarkerFaceColor',[0 0 1],'LineWidth',1.5);
scatter(dens(ind((~isnan(ind(:,6))),6)),vsusc(ind((~isnan(ind(:,6))),6)
),...
    reesize(ind((~isnan(ind(:,6))),6),'MarkerEdgeColor',[0 0 0],...
        'MarkerFaceColor',[0.5 0.25 1],'LineWidth',1.5);
scatter(dens(ind((~isnan(ind(:,7))),7)),vsusc(ind((~isnan(ind(:,7))),7)
),...
    reesize(ind((~isnan(ind(:,7))),7),'MarkerEdgeColor',[0 0 0],...
        'MarkerFaceColor',[1 0 1],'LineWidth',1.5);
scatter(dens(ind((~isnan(ind(:,8))),8)),vsusc(ind((~isnan(ind(:,8))),8)
),...
    reesize(ind((~isnan(ind(:,8))),8),'MarkerEdgeColor',[0 0 0],...
        'MarkerFaceColor',[1 0.5 0.5],'LineWidth',1.5);
scatter(dens(ind((~isnan(ind(:,9))),9)),vsusc(ind((~isnan(ind(:,9))),9)
),...
    reesize(ind((~isnan(ind(:,9))),9),'MarkerEdgeColor',[0 0 0],...
        'MarkerFaceColor',[1 0.5 0],'LineWidth',1.5);

% Add labels and legend
legend('>=1000ppm REE','200-1000ppm REE','<200ppm REE',...
    'NLS-5','NLS-4','NLS-6','NLS-8','NLS-9','NLS-11','NLS-12',...
    'NLS-13','NLS-14','Location','NorthWest');
xlabel('Density [g/cm^3]');
ylabel('Magnetic Susceptibility [SI]');

```

## pixel\_test.m

```

% pixel_test.m
% Written by Derek Kouhi
% August 2016
% A program that searches through a high resolution image of a sample
% and assigns a mineral type on a pixel-by-pixel basis based on the
% RGB values of each pixel. The script then analyzes any trends in
% colour
% with respect to geophysical measurements.

%% Computational Colour Analysis

% Clear all past data from previous run
clear all
clc

% Read the image and display it for reference
RGB = imread('f4bz.JPG');
image(RGB)

```

```

% Create variables for each mineral
mag = 0;
aeg = 0;
alb = 0;
soda = 0;
eud = 0;
other = 0;
newpic = 255*zeros(size(RGB));

% Search image, pixel-by-pixel and assign a mineral to that pixel based
% on a set of RGB value conditions determined through experimentation
total = size(RGB,1)*size(RGB,2);
for i = 1:size(RGB,1)
    for j = 1:size(RGB,2)
        % pixel = impixel(RGB,i,j);
        pixel = [RGB(i,j,1) RGB(i,j,2) RGB(i,j,3)];
        % magnetite
        if pixel(1) <= 65 && pixel(2) <= 65 && pixel(3) <= 65 &&
pixel(3) > pixel(1) && pixel(3) > pixel(2)
            mag = mag + 1;
            newpic(i,j,:) = [0 0 0];
        % aegirine
        elseif pixel(1) <= 85 && pixel(2) <= 85 && pixel(3) <= 80 &&
pixel(3) < pixel(2) && pixel(2) >= pixel(1)-3
            aeg = aeg + 1;
            newpic(i,j,:) = [0 100 0];
        % sodalite
        elseif pixel(1) <= 90 && pixel(2) <= 90 && pixel(3) <= 100 &&
pixel(3) >= pixel(1)+4 && pixel(3) >= pixel(2)+4 && pixel(2) > pixel(1)
            soda = soda + 1;
            newpic(i,j,:) = [0 0 100];
        % eudialyte
        elseif pixel(1) <= 110 && pixel(2) <= 110 && pixel(3) <= 110 &&
pixel(1) > pixel(2) && pixel(1) > pixel(3)
            eud = eud + 1;
            newpic(i,j,:) = [255 255 0];
        % albite
        elseif pixel(1) >= 70 && pixel(2) >= 70 && pixel(3) >= 70 &&
pixel(3) > pixel(1) && pixel(3) > pixel(2)
            alb = alb + 1;
            newpic(i,j,:) = [220 220 220];
        % other
        else
            other = other + 1;
            newpic(i,j,:) = [255 0 0];
        end
    end
end

% Write mineral abundances as output
disp(['The proportions are as follows: '])
disp(['Magnetite = ',num2str(mag/total*100),'%'])
disp(['Aegirine = ',num2str(aeg/total*100),'%'])
disp(['Albite = ',num2str(alb/total*100),'%'])
disp(['Sodalite = ',num2str(soda/total*100),'%'])
disp(['Eudialyte = ',num2str(eud/total*100),'%'])

```

```

disp(['Other = ',num2str(other/total*100), '%.'])

% Output the average red, green and blue values for the image
disp(['R_avg = ',num2str(sum(sum(RGB(:,:,1)))/total),' G_avg = ',...
      num2str(sum(sum(RGB(:,:,2)))/total),' B_avg = ',...
      num2str(sum(sum(RGB(:,:,3)))/total)])

% Plot calculated image
figure
image(newpic)

%% Analyzing Trends in Colour Data

% Inputs
% - data: depth data for each sample
% - del: approximate REE concentrations for each sample
% - vsusc: volume-based magnetic susceptibilities for each sample
% - dens: densities for each sample
% - minperc: a matrix where each column represents a different mineral
%            percentage and each row represents a different sample
% - minrgb: a matrix that contains the average RGB values for each
sample

data = xlsread('geology.xlsx');
del = xlsread('geology4.xlsx');
vsusc = xlsread('geology2.xlsx');
dens = xlsread('geodens.xlsx');
minperc = xlsread('minperc.xlsx');
minrgb = xlsread('minrgb.xlsx');

depth = data(:,1);
REE = del(:,2);
mag = minperc(:,1);
aeg = minperc(:,2);
alb = minperc(:,3);
soda = minperc(:,4);
eud = minperc(:,5);
oth = minperc(:,6);

clear data
clear del

% Plot the average red, green and blue components of each sample
figure('units','normalized','outerposition',[0 0 1 1])
plot(depth,minrgb(:,1),'r');
hold on
plot(depth,minrgb(:,2),'g');
plot(depth,minrgb(:,3),'b');
xlabel('Depth [m]');
ylabel('RGB Value');
legend('R','G','B');

% Plot the average RGB values as the corresponding colour (shades of
grey)
figure('units','normalized','outerposition',[0 0 1 1])
scatter(depth,vsusc,30,minrgb/255,'filled','MarkerEdgeColor',[0 0 0]);
xlabel('Depth [m]');

```

```

ylabel('Magnetic Susceptibility [SI]');

% Search through the average RGB values for a dominant colour
thresh = 4; % User-set threshold for RGB values to be considered
dominant
for i = 1:length(depth)
    if minrgb(i,1) >= minrgb(i,2)+thresh && minrgb(i,1) >=
minrgb(i,3)+thresh
        colmin(i,:) = [1 0 0];
    elseif minrgb(i,2) >= minrgb(i,1)+thresh && minrgb(i,2) >=
minrgb(i,3)+thresh
        colmin(i,:) = [0 1 0];
    elseif minrgb(i,3) >= minrgb(i,1)+thresh && minrgb(i,3) >=
minrgb(i,2)+thresh
        colmin(i,:) = [0 0 1];
    elseif minrgb(i,1) >= minrgb(i,2)+thresh && minrgb(i,3) >=
minrgb(i,2)+thresh
        colmin(i,:) = [1 0 1];
    elseif minrgb(i,1) >= minrgb(i,3)+thresh && minrgb(i,2) >=
minrgb(i,3)+thresh
        colmin(i,:) = [1 1 0];
    elseif minrgb(i,2) >= minrgb(i,1)+thresh && minrgb(i,3) >=
minrgb(i,1)+thresh
        colmin(i,:) = [0 1 1];
    else
        colmin(i,:) = minrgb(i,:)/255;
    end
end

% Create a series of subplots displaying susceptibility vs mineral
% abundance

% Magnetite subplot
figure('units','normalized','outerposition',[0 0 1 1])
subplot(3,1,1)
yyaxis left
scatter(depth,vsusc,30,colmin,'filled','MarkerEdgeColor',[0 0 0]);
ylabel('Mag Susc');
hold on;
yyaxis right
plot(depth,mag,'k--');
ylabel('Min %');
text(1050,50,'Magnetite','Color','k','FontSize',15,'FontWeight','bold')
;

% Aegirine subplot
subplot(3,1,2)
yyaxis left
scatter(depth,vsusc,30,colmin,'filled','MarkerEdgeColor',[0 0 0]);
ylabel('Mag Susc');
hold on;
yyaxis right
plot(depth,aeg,'g--');
ylabel('Min %');
text(1050,50,'Aegirine','Color','g','FontSize',15,'FontWeight','bold');

% Albite subplot

```

```

subplot(3,1,3)
yyaxis left
scatter(depth,vsusc,30,colmin,'filled','MarkerEdgeColor',[0 0 0]);
ylabel('Mag Susc');
hold on;
yyaxis right
plot(depth,alb,'--','Color',[0.7 0.7 0.7]);
ylabel('Min %');
text(1050,85,'Albite','Color',[0.7 0.7
0.7],'FontSize',15,'FontWeight','bold');

% Sodalite subplot
figure('units','normalized','outerposition',[0 0 1 1])
subplot(3,1,1)
yyaxis left
scatter(depth,vsusc,30,colmin,'filled','MarkerEdgeColor',[0 0 0]);
ylabel('Mag Susc');
hold on;
yyaxis right
plot(depth,soda,'c--');
ylabel('Min %');
text(1050,70,'Sodalite','Color','c','FontSize',15,'FontWeight','bold');

% Eudialyte subplot
subplot(3,1,2)
yyaxis left
scatter(depth,vsusc,30,colmin,'filled','MarkerEdgeColor',[0 0 0]);
ylabel('Mag Susc');
hold on;
yyaxis right
plot(depth,eud,'Color',[1 0.87 0]);
ylabel('Min %');
text(1050,70,'Eudialyte','Color',[1 0.87
0],'FontSize',15,'FontWeight','bold');

% Other subplot
subplot(3,1,3)
yyaxis left
scatter(depth,vsusc,30,colmin,'filled','MarkerEdgeColor',[0 0 0]);
ylabel('Mag Susc');
hold on;
yyaxis right
plot(depth,oth,'r');
ylabel('Min %');
xlabel('Depth [m]');
text(1050,25,'Other','Color','r','FontSize',15,'FontWeight','bold');

```

## Curriculum Vitae

<b>Name:</b>	Derek Kouhi
<b>Post-secondary Education and Degrees:</b>	<p>The University of Western Ontario London, Ontario, Canada 2009-2014 B.Sc.</p> <p>The University of Western Ontario London, Ontario, Canada 2014-Present M.Sc.</p>
<b>Honours and Awards:</b>	<p>Dr. and Mrs. J.E. Fraser Memorial Scholarship 2009</p> <p>Scholarship of Distinction, UWO 2009</p> <p>3<sup>rd</sup> Place Imperial Barrel Award, Canada Region 2015</p> <p>Limion Scholarship, KEGS 2015</p> <p>Earth Science Graduate Student Teaching Award 2016</p>
<b>Related Work Experience</b>	<p>Teaching Assistant The University of Western Ontario 2014-2016</p> <p>Research Assistant The University of Western Ontario Summer 2014</p>

### **Publications:**

Kouhi, D.W., and Tiampo, K.F., 2016a. Current Status of Magnetic Inversion Project at Thor Lake, N.W.T.; Open-File Report 2016-06, Northwest Territories Geological Survey, Yellowknife.

Kouhi, D.W., and Tiampo, K.F., 2016b. Implementation of Gravity Data for Isolated and Joint Inversion Methods at Thor Lake, N.W.T.; Pending Open-File Report, Northwest Territories Geological Survey, Yellowknife.